

Università degli Studi di Milano

FACOLTÀ DI SCIENZE E TECNOLOGIE

Corso di Laurea in Fisica

TESI DI LAUREA MAGISTRALE



UNIVERSITÀ DEGLI STUDI DI MILANO

FACOLTÀ DI SCIENZE E TECNOLOGIE

**Energy equipartition and mass segregation
in globular clusters**

Candidato:

Stefano Torniamenti

Matricola 897325

Relatore:

Prof. Giuseppe Bertin

Correlatore:

Dott. Claudio Grillo

Contents

Abstract	v
1 Globular clusters	1
1.1 Basic phenomenology	1
1.1.1 Physical scales	1
1.1.2 Ages of globular clusters	3
1.1.3 Binary stars	5
1.2 Dynamics of globular clusters	6
1.2.1 Collisionless Boltzmann Equation	7
1.2.2 Moments of the distribution function	9
1.2.3 Time scales	11
1.2.4 Perturbations and their effects	12
1.3 Granularity of the gravitational field	13
1.3.1 Evaporation	14
1.3.2 Gravothermal catastrophe	15
1.3.3 Energy equipartition	19
1.3.4 Mass segregation	24
1.4 Recent discoveries	28
1.4.1 Internal kinematics	29
1.4.2 Multiple populations	33
1.4.3 Intermediate-Mass Black Holes?	33
2 Dynamical models	36
2.1 One-component models	36
2.1.1 Plummer model	36
2.1.2 Isothermal sphere	37
2.1.3 King models	39
2.1.4 $f_T^{(\nu)}$ models	41
2.2 Two-component models	44
2.2.1 Two-component King models	46

2.2.2	Two-component $f_T^{(\nu)}$ models	47
2.2.3	Mass segregation and energy equipartition in two-component models	49
2.2.4	Hydrostatic and Virial Equilibrium	54
2.3	The Spitzer “instability”	57
2.3.1	A discussion of the Spitzer criterion	60
2.4	The Vishniac criterion	62
2.4.1	A discussion of the Vishniac criterion	65
3	Energy equipartition and mass segregation in Monte Carlo simula- tions	72
3.1	Simulations	73
3.1.1	Hydrostatic and virial equilibrium	76
3.2	Energy equipartition and mass segregation	81
3.2.1	Energy equipartition	81
3.2.2	Mass segregation	83
3.3	Fitting the simulated states with self-consistent dynamical models .	85
3.3.1	Fit by one-component models	86
3.3.2	Two-component models	94
3.4	M/L ratio and comparison with observations	103
3.4.1	Application to observed globular clusters	106
4	Conclusions and perspectives	114
	Bibliography	116
A	Bootstrap estimate of standard error	122
B	Fit results	124
B.1	One-component models	124
B.1.1	One-component King models	124
B.1.2	One-component $f_T^{(\nu)}$ models	127
B.2	Two-component models	131
B.2.1	Two-component King models	131
B.2.2	Two-component $f_T^{(\nu)}$ models	139
	Ringraziamenti	152

Abstract

Two-body relaxation processes (collisions, that is star-star scattering) play a fundamental role in determining the structure and evolution of small stellar systems, like globular clusters. In this thesis I focus on two consequences of collisionality, that is energy equipartition and mass segregation, which are expected because globular clusters are populated by stars of different masses. As a result of energy equipartition, less massive stars should present greater velocity dispersions. Correspondingly, more massive stars are expected to be characterized by a more concentrated density distribution, a phenomenon usually referred to as mass segregation. In self-gravitating systems, the establishment of these processes is very complicated, because of their inhomogeneous nature and their self-consistent dynamics. The tendency toward equipartition may lead to interesting phenomena, only partially understood, that depend in a subtle manner on local and global effects (see Spitzer 1987 [49]). In particular, arguments have been provided in favor of the existence of an instability related to mass segregation (Spitzer 1969 [48]; Vishniac 1978 [61]), distinct from the so-called gravothermal catastrophe. Numerical experiments confirm this theoretical expectation only partially, suggesting that globular clusters can attain a condition of only partial energy equipartition (Trenti & van der Marel 2013 [58]; Bianchini et al. 2016 [12]). On the observational side, the difficulties in checking these phenomena by means of measurements with sufficient precision are being resolved by the enormous progress made with the advent of GAIA mission.

In this thesis I consider a set of numerical realistic simulations realized by means of Monte Carlo methods (Bianchini et al. 2016 [12]). Selected “snapshots” taken from these simulations are studied as simulated states. The structural and kinematic properties of these systems are analyzed by means of two-component models. For the purpose, I refer to isotropic King (1966) [34] models and to the truncated $f^{(\nu)}$ models (de Vita, Bertin, Zocchi 2016 [16]), conceived in the context of elliptical galaxies formation, but later adapted to globular clusters. The two components are light stars (collectively combining all main sequence stars) and heavy stars (giants, remnants, and binaries). This simplified dynamical framework allows me to address the issue of partial energy equipartition and mass segregation with simple analytic tools. I show that isotropic King models do not offer a good representation of these systems and, in particular, of their velocity distribution. On the other hand, two-component truncated $f^{(\nu)}$ models provide a reasonable description of simulated density, velocity dispersion and anisotropy profiles, especially for the

most relaxed systems. Curiously, this also implies that the slow cumulative effects of stellar encounters tend to generate anisotropic distribution functions similar to those predicted by the completely different process of collisionless violent relaxation.

In this thesis I also provide a critical discussion of the so-called Spitzer “instability” and of the related Vishniac criterion. I show that the application of these old conjectures is jeopardized by the lack of global energy equipartition. In addition, I show that the hypotheses at the basis of these conjectures are not well justified.

Finally, I address the issue of the local mass-to-light (M/L) ratio. The simple, two-component truncated $f^{(\nu)}$ models have difficulties in representing the existing (M/L) gradients, especially because significant gradients are associated with main-sequence stars, which are characterized by a sizable mass-spread and resulting segregation, whereas in the simple models main-sequence are lumped together into the light component. Finally, I quantify how gradients in the M/L ratio and in the mean mass profile influence the derivation of model parameters obtained in the observations. I show that a description of the mass distribution by means of the observed number density profile leads to an underestimate of the central density, whereas measures of the surface brightness profile lead to an overestimate of the concentration parameter.

This thesis is divided into three chapters. In the first chapter I introduce the main properties of globular clusters, with particular attention to some recent discoveries, and the effects of relaxation processes in these systems. In the second chapter I describe the dynamical models considered later in this thesis in the study of energy equipartition and mass segregation, focusing on two-components models. I also discuss the Spitzer “instability”. In the third chapter I describe the basic properties of a selected set of “snapshots” taken from realistic Monte Carlo simulations of globular clusters and make specific tests about the presence of energy equipartition and mass segregation in these systems. I then report the results of the fits performed on the density and the velocity dispersion profiles for these simulated states by means of one-component and two-component models. Finally, I describe how mass segregation influences observations by comparing gradients of the M/L profiles of the simulated states with those expected from the best-fit two component models.

Chapter 1

Globular clusters

1.1 Basic phenomenology

Globular clusters are compact groups of up to about a million stars and beyond, which are held together by their mutual gravitational attraction and are characterized by a nearly spherical spatial distribution. Our Galaxy hosts about 150 globular clusters, of which more than one half are within 10 kpc of the Galaxy center, but their distribution extends to much greater distances, well beyond 30 kpc [27]. The most visible globular cluster from Earth is ω Centauri (NGC 5139), in the constellation of Centaurus, with an apparent magnitude of $V = 3.68$. A photograph of this system is shown in Fig. 1.1. The image appears nearly circular, which is typical for globular clusters hosted by our Galaxy. If we define the ellipticity as $\epsilon = 1 - b/a$, where b and a are the minor and the major projected axis respectively, the distribution of ϵ seems to peak at $\epsilon \approx 0.05$, with maximum values of $\epsilon \approx 0.25$ [27]. Thus, to a first approximation, most globular clusters are nearly spherical: this symmetry will be one of the key points of the dynamical analysis of these objects in Sect. 1.2.

1.1.1 Physical scales

Typically, globular clusters exhibit a declining surface brightness profile. In the central regions the brightness is four orders of magnitude higher than in the outer parts (halo). While most systems show a central region (or core) within which the surface brightness changes slowly, in some systems it increases as we move in, down to the smallest radius resolved. Systems such as NGC 6624 are said to possess central cusps. This cluster is also one of the few that contain a strong X-ray burster source, presumably formed in the innermost region of the cluster. The presence of central cusps is probably connected with a process of core collapse, as described in



Figure 1.1: The globular cluster ω Centauri, with as many as ten million stars, in an image captured with the WFI camera from ESO’s La Silla Observatory. The image shows only the central part of the cluster — about the size of the full moon on the sky (half a degree). This color image is a composite of B, V, and I filtered images. Because WFI is equipped with a mosaic detector, there are two small gaps in the image that were filled with lower quality data from the Digitized Sky Survey. Image from www.eso.org.

Sect. 1.3.2.

Two length scales used to characterize the surface brightness profile are the core radius r_c , defined as the value of the radius at which the surface brightness is half of its central value, and the tidal radius r_t , at which the surface brightness vanishes, that is, is no longer measurable. The truncation is physically interpreted as due to tidal effects. For most globular clusters, r_c is between 0.3 and 10 pc and r_t/r_c ranges from 10 to 100. In ω Centauri $r_t \approx 30 \pm 2$ pc [49].

The distribution of the total luminosities of globular clusters is strongly peaked at a visual magnitude $M_V = -7.5$, as illustrated in Fig. 1.2 (van den Bergh 2008 [59]). This behavior is very different from that of another class of small stellar systems called dwarf spheroidals (filled blue squares), the luminosities of which are spread

out over a range of 10^5 . Another important difference between globular clusters and dwarf spheroidals is that the effective radii R_e , that is the projected radius that contains half of the luminosity of the cluster (indicated as R_h in Fig. 1.2) of the latter are typically one or two orders of magnitude larger than those of the former. The distributions of globular clusters and dwarf spheroidals in the (R_e, M_V) plane can be separated by the line:

$$M_V = 16.2 - 14.26 \log R_e. \quad (1.1)$$

This relation is referred to as the Shapley line.

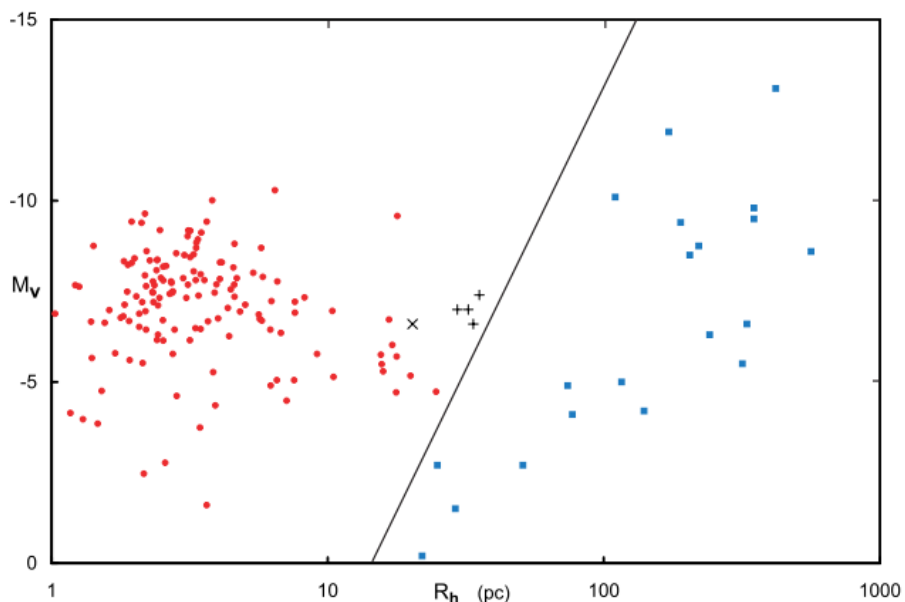


Figure 1.2: The figure shows a clear-cut separation between the distribution of Galactic globular clusters (filled red circles) and dwarf spheroidal companions to the Galaxy (filled blue squares). A line separating these two types of objects is given by Eq. (1.1) and is called Shapley line. Four luminous extended globular clusters in the outskirts of M31 are shown as plus signs. The extended cluster M33-EC1 is plotted as a cross. Figure from van den Bergh (2008) [59].

The total mass of globular clusters is generally estimated to be between $10^4 M_\odot$ and $10^6 M_\odot$.

1.1.2 Ages of globular clusters

Typically, ages of these systems are determined from their H-R diagrams, which show virtually no main-sequence stars with spectra earlier than a “turn-off” point, at which the stars leave the main sequence and evolve for the first time along the



Figure 1.3: This bright cluster is 47 Tucanae (NGC 104), shown in an image taken by ESO’s VISTA (Visible and Infrared Survey Telescope for Astronomy) from the Paranal Observatory in Chile. This cluster is located around 15 000 light-years away from us and contains millions of stars, some of which are exotic. This image was taken as part of the VISTA Magellanic Cloud survey, a project that is scanning the region of the Magellanic Clouds, two small galaxies that are close to the Milky Way. After ω Centauri this is the brightest globular cluster in the night sky, hosting tens of thousands of stars. Image from www.eso.org.

giant branch. As time goes on, the position of the turn-off, at which the hydrogen in the stellar core has been converted into helium, moves to stars of lower mass and later spectral type. Thus, in principle, the position of this point on the observed H-R diagram of a cluster can be used to determine the time since the stars, and presumably the entire cluster, were formed. In practice, the age is determined by fitting the points of each H-R diagram with one of a set of curves, computed with detailed stellar models and different assumed ages. The globular clusters of our Galaxy are estimated to be as old as about 10 Gyr. Therefore, these systems are very old and were likely born in the first phases of galaxy formation, because their ages are comparable with the age of the Universe. Consequently, globular clusters can be considered as the first “building blocks” of galaxies, since they are among the first recognizable stellar structures that were born on sub-galactic scales.

1.1.3 Binary stars

There is significant evidence that a substantial fraction of the stars populating globular clusters are binaries [28]. Binary stars play a fundamental role in the evolution of globular clusters for at least two important reasons. First, the evolution of stars in binaries, whether in a cluster or in the galactic field, can be very different from the evolution of the same stars in isolation. In a dense environment such as a globular cluster, this difference is exacerbated by dynamical encounters, which affect binaries much more than single stars. Secondly, binary stars crucially affect the dynamical evolution of globular clusters, providing (through inelastic collisions) the source of energy that supports them against gravothermal collapse, as we will see in Sect. 1.3.2.

Information on the presence of binaries in globular clusters was initially provided by X-ray observations. X-ray sources, in these systems, have a bimodal distribution of luminosity L_x , with the bright ones having L_x between 3×10^{35} erg/s and 3×10^{37} erg/s, whereas for the fainter, more numerous group, L_x is less than 10^{34} erg/s. The brighter sources are typically located within one core radius from the cluster center whereas the weaker sources are more widely distributed in the clusters where they are observed. The more luminous objects are interpreted as binaries, made of a compact object (a neutron star), and a main sequence star. The discovery of these sources was the first clear evidence for the presence of neutron stars as well as binaries in globular clusters. The weaker sources are likely to consist of a degenerate dwarf (with a mass somewhat less than that of the giants) as a compact emitting object, and again a main sequence companion that provides the gas accreting onto the X-ray emitting star.

Currently, it is possible to detect binaries in color-magnitude diagrams: unresolved binaries have similar colors to the other stars but are noticeably brighter. Eclipsing binaries, that is binaries observed photometrically by changes in brightness caused by an eclipse, were discovered later, many as by-product of searches for gravitational lenses. In recent years it has become possible to find evidence for radial velocity binaries, that is binaries observed spectroscopically by periodic changes in spectral lines, among the normal stars that have not yet evolved into giants.

At present, there are very few direct measurements of binary fractions¹ in clus-

¹The binary fraction is the ratio of the number of binaries to the total number of objects (single stars and binaries). It can be written:

$$f_{\text{binary}} = N_b / (N_s + N_b),$$

where N_s and N_b are the number of single stars and binaries, respectively.

ters. Observations of dense globular cluster cores typically yield binary fractions that are significantly smaller than in the solar neighborhood (where the fraction approaches 50%). Hubble Space Telescope (HST) observations of the core-collapsed cluster NGC 6397 yield a binary fraction of $\approx 5\%$ in the core and $\approx 1\%$ beyond the half-mass radius. For the non core-collapsed cluster 47 Tuc, the binary fraction is $\approx 13\%$. The core binary fraction generally ranges from a few percent to tens of percent, approaching 50% in some cases for less dense clusters [33].

For the primordial binary fraction in globular clusters, there are of course no direct measurements. However, there are no observational or theoretical arguments suggesting that the formation of binaries in dense stellar systems should be significantly different from that in other environments such as open clusters, the Galactic field, or star-forming regions. Observations of stars in low stellar density environments where dynamics are unimportant, such as the solar neighborhood, yield a binary fraction of 50% among solar-type stars, with an increasing trend with primary mass. Open clusters show similar large binary fractions [21].

Most dynamical interactions in dense cluster cores tend to destroy binaries (the possible exception is tidal capture, which may form binaries, but turns out to play a negligible role). Soft binaries² can be disrupted easily by any strong encounter with another passing star or binary. Hard binaries can be destroyed in binary-binary encounters, which typically eject two single stars and leave only one binary remaining, or produce physical stellar collisions and mergers. In addition, many binary stellar evolution processes lead to disruptions (e.g., following a supernova explosion of one of the stars) or mergers (e.g., following a common envelope phase).

1.2 Dynamics of globular clusters

A quantitative discussion of the dynamics of globular clusters is generally based on idealized models in which the effects of encounters between stars are ignored, at least on time scales longer than the dynamical time and shorter than the relevant relaxation time. Deflections associated with encounters can be regarded as perturbations that gradually induce cluster evolution along a sequence of these quasi-equilibrium models. In all these discussions relativistic effects are ignored as star velocities in these systems (a few km/s) are small compared to the speed of

²Theorists tend to distinguish between hard binaries and soft binaries. The former are binaries with binding energies greater than the typical star energy, which generally become more tightly bound (harden) as a result of encounters. The latter have binding energies smaller than the typical star energy in a cluster, and typically become less tightly bound (soften) or dissociate completely.

light. The basic assumption made in such idealized models is:

- (A) The granularity of the self-gravitating matter in the cluster can be ignored on the time scale of several dynamical time scales, and the gravitational potential can be taken as a slowly varying function of position (“mean potential theory”). This assumption makes it possible to consider the existence of stationary equilibrium states.

Once the hypothesis A is considered, it is useful to define a velocity distribution function $f(\mathbf{r}, \mathbf{v}, t)$, dependent on the position vector \mathbf{r} , the velocity \mathbf{v} and the time. This quantity is defined so that $f(\mathbf{r}, \mathbf{v}, t)d\mathbf{r}d\mathbf{v}$ represents the mass of stars at time t within the volume element $d\mathbf{r} \equiv dx dy dz$ centered at \mathbf{r} and within the velocity space element $d\mathbf{v} \equiv dv_x dv_y dv_z$, centered at \mathbf{v} . We can therefore define the mass density function as:

$$\rho(\mathbf{r}, t) = \int f(\mathbf{r}, \mathbf{v}, t)d\mathbf{v}. \quad (1.2)$$

In a discrete system, this quantity is meaningful if one can construct volume elements that are large enough to contain many stars, but small enough so that the relevant quantities are reasonably constant across each element. Under such conditions, $f(\mathbf{r}, \mathbf{v}, t)$ will be independent of the exact size and shape of the volume element used. Actually, it is difficult to define the instantaneous $f(\mathbf{r}, \mathbf{v}, t)$, even when the total number of stars N in the cluster is as great as 10^6 if all six dimensions in \mathbf{r} and \mathbf{v} are considered. This difficulty is reduced if, as we will assume, some symmetry exists and fewer dimensions enter the argument of the distribution function.

1.2.1 Collisionless Boltzmann Equation

The basic relationship that determines the evolution of f in a collisionless system is called *collisionless Boltzmann equation* or CBE (also known as *Vlasov equation* in plasma physics) and may be derived from conservation of f in phase space. It states that the one-star distribution function $f(\mathbf{r}, \mathbf{v}, t)$ evolves in the six-dimensional phase space under the action of the mean-field potential $\Phi(\mathbf{r}, t)$ according to the continuity equation of an incompressible fluid [7]:

$$\frac{\partial f}{\partial t} + \sum_i v_i \frac{\partial f}{\partial x_i} + \sum_i a_i \frac{\partial f}{\partial v_i} = 0, \quad (1.3)$$

where x_i denotes one of the three coordinates and a_i is the corresponding particle acceleration (assumed independent of \mathbf{v}). It is clear that Eq. (1.3) can be written as $Df/Dt = 0$, that is f is constant along a dynamical trajectory. For all the systems

we shall study, a_i is the result of a continuous (“mean”) gravitational potential Φ :

$$a_i = -\frac{\partial \Phi}{\partial x_i}. \quad (1.4)$$

We can also express f as a function of generalized coordinates and momenta in a standard Hamiltonian formulation and Eq. (1.3) can be conveniently rewritten in terms of Poisson brackets, much like the Liouville theorem (which generally applies only to the $6N$ -dimensional phase space):

$$\frac{\partial f}{\partial t} + \{f, H\} = 0. \quad (1.5)$$

Here $H = p^2/2 + \Phi$ represents the specific one-star Hamiltonian associated with the mean potential.

When weak collisionality is present, we may adopt the so-called Fokker-Planck description, which has on the right-hand-side of Eq. (1.3) a collisional term [7]:

$$\left(\frac{\partial f}{\partial t} \right)_c = \frac{\partial}{\partial \mathbf{v}} \left[\langle \frac{\Delta \mathbf{v}}{\Delta t} \rangle f \right] + \frac{1}{2} \frac{\partial^2}{\partial v_i \partial v_j} \left[\langle \frac{\Delta v_i \Delta v_j}{\Delta t} \rangle f \right], \quad (1.6)$$

where $\Delta \mathbf{v}$ is the specific variation of velocity due to collisions. The first term of Eq. (1.6) represents dynamical friction, and the second is a velocity-diffusion term. Fokker-Planck equation has an important application in the dynamics of globular clusters, in which the spherical geometry suggest a partitioning of phase space by use of energy and angular momentum so that friction and diffusion terms in velocity space are more conveniently reexpressed in the variables E and J [7] (see below).

To describe the system, we need to define the gravitational potential present in Eq. (1.3) through Eq. (1.4), that is we need to define the relation between this potential and the distribution function satisfying hypothesis A. If we deal with fully self-gravitating systems, in which the mean potential is completely determined by the stars described by f , Eq. (1.3) is supplemented by Poisson’s equation:

$$\Delta \Phi(\mathbf{r}, t) = 4\pi G \rho(\mathbf{r}, t) = 4\pi G \int f(\mathbf{r}, \mathbf{v}, t) d\mathbf{v}, \quad (1.7)$$

where ρ is defined by Eq. (1.2). In the self-consistent case, Eq. (1.3) and Eq. (1.7) trace a highly nonlinear problem because Φ is not to be considered as an assigned function but is determined by f . In the context of the dynamics of galaxies, the preceding equations are often referred to as the *fundamental equations of stellar dynamics*.

We can further simplify our idealized model by introducing two additional assumptions:

- (B) The gravitational potential Φ , the distribution function f , and the other properties of the system are independent of time.
- (C) The cluster has spherical symmetry: Φ is a function of r only and f is a function only of r , v_r , v_t , the modulus of \mathbf{r} , the radial and tangential components of the velocity respectively. This assumption is not a priori necessary but greatly simplifies the models and has a natural empirical justification, as suggested by Fig. 1.1 and Fig. 1.3. In reality, a globular cluster is always subject to the gravitational field of the host galaxy, which changes the shape of the cluster from spherical to ellipsoidal, with a structure stretched in the direction of the center of the galaxy, similarly to what happens in the case of terrestrial tides. For simplicity, we may initially ignore these complications associated with the external tidal field. The effect of the host galaxy is then quantified only by a truncation radius r_t , which is typically (but not necessarily) associated with tidal effects. It is worth noting that the truncation due to tidal effects is physically different from the picture of a system bounded by a reflecting wall.

As a result of assumption B, the energy of a star per unit mass, which we denote by E , is constant, and the angular momentum \mathbf{J} per unit mass is constant by virtue of assumption C. We define the energy (per unit mass) and the magnitude of the angular momentum (per unit mass):

$$E = \frac{1}{2}v^2 + \Phi(r), \quad (1.8)$$

$$J = |\mathbf{r} \times \mathbf{v}|. \quad (1.9)$$

The function f is always constant along a dynamical trajectory, given assumption A. In general, there are six integrals of motion that are constant along each dynamical trajectory. It follows directly from Eq. (1.3) that f must be function of these integrals, a result sometimes known as *Jeans' Theorem*. This allows us to write f as a function of the integrals of motion only. In spherical symmetry, self-consistent models are generally discussed in terms of a distribution function that depends on the energy and the magnitude of the angular momentum.

Poisson's equation [Eq. (1.7)], as a consequence of spherical symmetry C, becomes:

$$\frac{1}{r^2} \frac{d}{dr} \left[r^2 \frac{d\Phi(r)}{dr} \right] = 4\pi G\rho. \quad (1.10)$$

1.2.2 Moments of the distribution function

From the distribution function we can construct some fluid quantities, that is quantities from which information in the velocity space is integrated out. An exam-

ple of a fluid quantity is the mass density defined in Eq. (1.2). We can also define a mean fluid velocity $\mathbf{u}(\mathbf{r}, t) = \langle \mathbf{v} \rangle$:

$$\mathbf{u}(\mathbf{r}, t) = \frac{1}{\rho} \int \mathbf{v} f(\mathbf{r}, \mathbf{v}, t) d\mathbf{v}, \quad (1.11)$$

and a pressure tensor p_{ij} :

$$p_{ij} = \rho \langle (\mathbf{v} - \mathbf{u})_i ((\mathbf{v} - \mathbf{u})_j \rangle = \int (v_i - u_i)(v_j - u_j) f(\mathbf{r}, \mathbf{v}, t) d\mathbf{v}. \quad (1.12)$$

The pressure tensor can be expressed in terms of the velocity dispersion tensor

$$\sigma_{ij}^2 = \frac{1}{\rho} \int (v_i - u_i)(v_j - u_j) f(\mathbf{r}, \mathbf{v}, t) d\mathbf{v}, \quad (1.13)$$

so that $p_{ij} = \rho \sigma_{ij}^2$.

For a standard fluid the velocity dispersion tensor is a scalar (i.e., $\sigma_{ij}^2 = \sigma^2 \delta_{ij}$): this means that there is no preferential direction and the three Cartesian axes are equivalent. At the same time, in a stellar system the velocity dispersion tensor may not be proportional to the identity matrix and may be anisotropic. In general if the distribution function depends only on energy ($f = f(E)$, which is a consequence of hypothesis B), the velocity dispersion tensor is always proportional to the identity matrix and the system is isotropic. In fact, it is easy to show that in this case the mean fluid velocity in Eq. (1.11) vanishes ($\mathbf{u} = 0$) and, from Eq. (1.13):

$$\sigma_{ij}^2 = \langle (\mathbf{v} - \mathbf{u})_i (\mathbf{v} - \mathbf{u})_j \rangle = \langle v_i v_j \rangle = \sigma^2 \delta_{ij}. \quad (1.14)$$

If f depends also on J , the velocity dispersion tensor is anisotropic and:

$$\sigma_{ij}^2 = \begin{pmatrix} \sigma_{rr}^2 & 0 & 0 \\ 0 & \sigma_t^2 & 0 \\ 0 & 0 & \sigma_t^2 \end{pmatrix}, \quad (1.15)$$

with $\sigma_t^2 = \sigma_{\theta\theta}^2 = \sigma_{\phi\phi}^2$. We note that there is no distinction between the directions θ and ϕ , but only between the radial and tangential directions. For simplicity, in the following we will use the notation $\sigma_r^2 = \sigma_{rr}^2$, $\sigma_\theta^2 = \sigma_{\theta\theta}^2$, $\sigma_\phi^2 = \sigma_{\phi\phi}^2$.

The local degree of anisotropy in spherical stellar systems is generally quantified by the local anisotropy function:

$$\alpha(r) = 2 - \frac{\sigma_\theta^2(r) + \sigma_\phi^2(r)}{\sigma_r^2(r)}. \quad (1.16)$$

The condition $\alpha = 0$ corresponds to isotropy, whereas $\alpha = 2$ corresponds to full radial anisotropy.

1.2.3 Time scales

Before considering the dynamics of globular clusters we shall study the time scales that characterize these stellar systems.

- Age of the cluster, t_{age} .
- Dynamical time t_d (or crossing time). It is a measure of how long it takes for a star to cross the stellar system and can be defined as the ratio between the characteristic radius r of the orbit of a star and its typical velocity v_s :

$$t_d = \frac{r}{v_s} \sim \frac{1}{\sqrt{G\rho}}, \quad (1.17)$$

where G is the gravitational constant and ρ is the density of the cluster (which is, in general, not constant).

- Two-star relaxation time, t_r . It quantifies the effects of star-star collisions in changing the orbit of a star with respect to that determined by the smooth mean field generated by the whole stellar system. It measures the effects of the discreteness of the mass distribution. We can define the relaxation time as the time scale beyond which the relevant aspect of the scattering processes becomes significant in the course of the orbit of a reference star under consideration or, alternatively, the time required for deviations from a Maxwellian distribution to be significantly decreased. We report the definition of “time of relaxation” given by Spitzer (1987) [49]:

$$t_r = \frac{0.065 \sigma^3}{n m^2 G^2 \ln \Lambda} = 3.4 \times 10^9 \frac{[\sigma(km/s)]^3}{n(pc^{-3})[m(M_\odot)]^2 \ln \Lambda} yr, \quad (1.18)$$

where σ is the velocity dispersion, n is the numerical density, m is the mass of stars (this definition assumes that all the stars of the cluster have the same mass) and $\ln \Lambda$ is a constant, called the Coulomb logarithm. The relaxation time is not constant inside a cluster, as it is function of velocity dispersion and density, which are generally decreasing functions of the distance from the cluster center. In particular, it is expected to be smaller in the central regions of the system, where velocity dispersion rises, whereas in the outermost regions t_r can be as high as the age of the Universe.

For a globular cluster, a useful definition of central relaxation time is given by the core relaxation time, t_{rc} . For the definition of this quantity, we follow the approach of the Harris (2010) catalog [27], that contains basic parameters on

distances, velocities, metallicities, luminosities, colors, and dynamical parameters for 157 objects classified as globular clusters in the Milky Way galaxy. The core relaxation time is defined as [18], [44]:

$$t_{rc} = \frac{8.3 \times 10^6 \text{ yr}}{\log(0.4N)} \left(\frac{M_\odot}{\langle m \rangle} \right) \left(\frac{\rho_0}{M_\odot/\text{pc}^3} \right)^{1/2} \left(\frac{r_c}{\text{pc}} \right)^3, \quad (1.19)$$

where N is the number of stars in the cluster, $\langle m \rangle$ is the average stellar and ρ_0 is the density of the cluster inside the core radius. A definition of the relaxation time for a system as a whole is given by the half-mass relaxation time, defined as [49]:

$$t_{rh} = \frac{6.5 \times 10^8 \text{ yr}}{\log(0.4N)} \left(\frac{M}{M_\odot} \right)^{1/2} \left(\frac{M_\odot}{\langle m \rangle} \right) \left(\frac{r_h}{\text{pc}} \right)^{3/2}, \quad (1.20)$$

where M is the total mass of the cluster and r_h the half-mass radius, that is, the radius which contains half of the total mass of the system. The half-mass relaxation time changes relatively little during the evolution of some clusters and it is used as an estimation of the relaxation time of the whole system. By contrast, the core relaxation time t_{rc} decreases markedly during evolution.

We can combine the definitions of crossing time, Eq. (1.17), for the half-mass radius and of the half-mass relaxation time, Eq. (1.20), to obtain the scaling:

$$\frac{t_{rh}}{t_d} \sim \frac{N}{\ln N}, \quad (1.21)$$

which shows that large stellar systems are expected to be collisionless. For example typical relaxation times for elliptical galaxies are $t_{rh} \approx 10^{14}$ yr and for disk galaxies, even in central regions, the relaxation times typically exceeds 10^{10} . The dynamical time is often $t_d \approx 10^8$ yr. The ages of galaxies are comparable with the Hubble time (the age of the Universe), of the order of 10^{10} yr. For such systems $t_d \ll t_{age} \ll t_{rh}$. For globular clusters typical time scales are $t_d \approx 10^6$ yr, $t_{rh} \approx 10^{5-10}$ yr and $t_{age} > 10^{10}$ yr. This suggests that, in many cases, two-body interactions have had time to lead the system toward thermodynamic equilibrium. If we want to understand the present day structure of globular clusters we must consider the effects of long-time collisions for these systems.

1.2.4 Perturbations and their effects

A steady-state spherically symmetric model may provide a first description of the structure of globular clusters. The various effects neglected in these models

may be regarded as small perturbations. During the orbital period of a star in a cluster these effects are generally small, but over a period of many orbits they can produce gradual changes that make the system evolve along families of neighboring equilibria. We can also argue that such evolution leads to a state which may in many respects be independent of the initial conditions.

Perturbations result from the following three main factors:

- granularity of the gravitational potential within the cluster.
- gravitational field produced by mass external to the cluster, especially by the Galaxy.
- changes in the physical properties of the stars, as a result of stellar evolution and of direct impact between stars.

We are interested in the first factor, the quantitative aspects of which are treated in the following section (Sect. 1.3).

1.3 Granularity of the gravitational field

In a real cluster the gravitational field at any point will be constantly fluctuating. These fluctuations can be seen as continuous small changes on the time scale required for the nearest neighboring stars to pass by: this time interval is roughly that required to travel a distance $n^{-1/3}$, about the average distance between stars. There will be slower fluctuations resulting from a slight random excess of stars within regions where the total number of stars is large; these fluctuations have a relatively small amplitude, but produce an appreciable effect because of their longer time scale. Occasionally, there will be a transient fluctuation of larger amplitude as a star passes by relatively closely. Finally, at high densities, three single stars may interact to form a binary system, or a single star can interact with an existing binary. Close encounters involving four or more stars are also possible.

If we do not consider binary stars, the main effect produced by all these fluctuations in the gravitational field is to modify the stellar velocities, both in magnitude and in direction. The rate at which stellar velocities are modified by such fluctuations may be calculated by considering the velocity changes produced by a single encounter between two passing stars and summing these changes over all such encounters. Encounters between three single stars are relatively unimportant in a cluster. Moreover, close encounters between two stars, which produce relatively large changes in the stellar velocities, are generally unimportant; the cumulative

effect of many distant encounters, each producing only small changes in velocity, is greater by at least an order of magnitude [49]. Gravitational field fluctuations thus generate random walks in velocity space, characterized by mostly small step sizes. As a result, there will be a net diffusion in velocity space, in the direction of reducing existing deviations from this equilibrium, that is from the Maxwellian distribution function:

$$f = A \exp(-aE), \quad (1.22)$$

where A is a constant and a is the temperature parameter $a = m/(k_B T)$. When Eq. (1.22) holds, the system is said to be in *kinetic (thermal) equilibrium*.

The tendency toward a Maxwellian distribution produced by random two-body encounters has important consequences for the cluster. The possibility of finding a star within an energy interval ΔE at a given energy E is proportional both to $\exp(-aE)$ and to the volume of the phase space available for stars within ΔE :

$$P(E; \Delta E) \sim e^{-aE} \Delta E. \quad (1.23)$$

Hence one would expect that the tendency toward kinetic equilibrium would promote evolution in two directions: toward more tightly bound gravitational systems, with more negative E , and also toward expansion of the cluster volume, to increase the available phase space. Since the total energy must remain constant, this implies that some stars must move to higher energies to absorb the energy given up by the contracting core. There are different mechanisms by which a cluster composed of single stars evolves in the direction indicated by statistical arguments, that will be described in the following sections.

1.3.1 Evaporation

Evaporation is the departure from the cluster of stars the velocity of which exceeds the local velocity of escape, v_e . In a real cluster the tail of the Maxwellian distribution, at energies exceeding the escape energy E_e , will be depleted as a consequence of the tidal interaction with the host galaxy, but the fluctuations of the gravitational field will tend continually to drive some stars up to energies exceeding E_e , and these will quickly escape.

Evaporation can be studied in a simple spherical spatially truncated model by arguing that, when collisions bring a star above a certain energy level, the star will escape. In this context we can give a simple approximation for the tidal radius by considering the Galaxy as a point mass M_G situated at fixed distance r_G from the

cluster center. The tidal radius is given by:

$$r_T^3 = \frac{M_c}{3M_G} r_G^3. \quad (1.24)$$

A star moving radially along the line joining the centers will escape from the cluster if it can reach a distance from the cluster center greater than r_T (i.e., if its energy exceeds a certain value $E_T = \Phi(r_T)$) while stars moving in other directions and with some tangential velocities can remain bound with greater energies. This suggests that mass loss from globular clusters proceeds primarily through stars along radial orbits. As a consequence, the outermost parts of the system are expected to develop tangential pressure anisotropy. Evaporation can also be studied in a more realistic environment, in which the boundary of the system is defined by the three-dimensional structure of the so-called Roche lobe associated with tidal interaction [8].

Mass loss due to evaporation may be very significant: this process drives the system toward a less concentrated structure delaying core collapse (see Sect. 1.3.2) and, in some cases, it could lead to the disruption of the system itself. This process is expected to be stronger for low-mass clusters, as they have shorter relaxation times and thus evolve more quickly than massive clusters (Eq. (1.21)) and for clusters close to the Galactic Center, as confirmed by N -body simulations (Heggie & Vesperini, 1997 [30]).

1.3.2 Gravothermal catastrophe

In the 1950s, the study of self-gravitating isothermal spheres led to the discovery that gravity can produce a major change the Boyle law for isothermal configurations of ordinary gases at a given temperature. In particular, it was found that in the presence of self-gravity, for small values of the total volume V , the hyperbola characteristic of the Boyle law changes into a curve that spirals into a point in the plane (V, p_{ext}) , as shown in Fig. 1.4. Equilibrium configurations are possible only up to a maximum value of p_{ext} . All the points of this spiral along this line of isothermal self-gravitating equilibrium configurations beyond the point of maximum external pressure turn out to be unstable toward collapse.

This process was soon interpreted in terms of a heat flux that may originate from the innermost regions, dominated by self-gravity and associated with a negative specific heat, to the tenuous outer regions. According to the virial theorem, a self-gravitating isolated system has a total energy E_{tot} given by:

$$E_{tot} = -K = \frac{W}{2}, \quad (1.25)$$

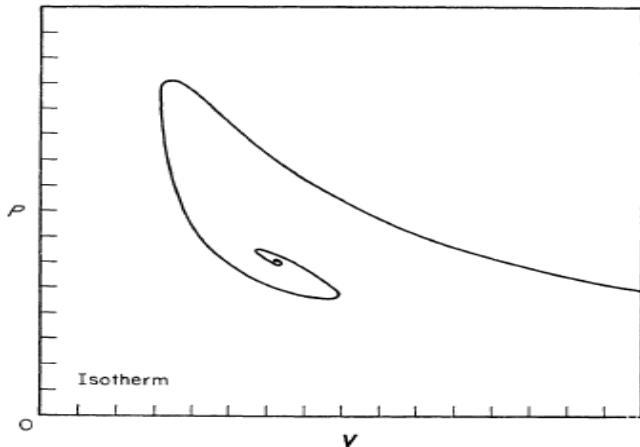


Figure 1.4: Isothermal equilibrium configurations for a self-gravitating system. For small values of the volume V , the equilibrium curve spirals around a point: equilibrium is possible up to a maximum value of pressure. All the equilibrium configurations on the spiral are unstable against gravitational collapse. Figure from Lynden-Bell & Wood (1968) [37].

where K is the total kinetic energy of the system and W is the total gravitational energy. From Eq. (1.25) we can see that, if the system loses energy (E_{tot} is negative, so its absolute value increases), W becomes more negative and K increases: the system becomes hotter as it loses energy and cools as it is heated (the system has negative specific heat). If such a bound system is in thermal contact with a heat sink (a colder system) at some constant temperature, an instability can result with heat flowing into the sink and the kinetic energies of the particles in the gravitationally bound system increasing steadily as the system contracts, losing energy. Within a single cluster this process can be important if the central core is so concentrated compared with the rest of the system that its dynamical equilibrium is practically that of an isolated system. The core is in thermal contact with the outer regions of the cluster, which can serve as a heat sink. Thus, it is possible for the core to lose energy to the outer regions, contract and heat up in the process. The increase of mean square random velocity in the core then encourages additional flow of heat from the core to the surrounding regions, increasing the rate of core collapse [49].

The above scenario of a gravothermal catastrophe gained much popularity in the context of stellar dynamics and, in particular, in the study of globular clusters. In fact, some of these relatively small stellar systems possess the desired degree of collisionality that is generically thought to be required for the phenomenon to occur (as far as the innermost regions are considered). In addition, some globular clusters, with relatively short relaxation times, are observed to possess a central cusp, distinct

from the core structure associated with the King models (introduced in Sect. 2.1.3). These clusters are naturally interpreted as systems that have suffered core collapse as a result of the gravothermal catastrophe [7]. However, we must keep in mind that globular clusters are truncated by tides in a way that is physically different from the picture of a sphere bounded by a reflecting wall. Therefore the application of the original discussion to stellar systems is not straightforward. As an example, Sormani & Bertin (2013) [47] observed that, by performing a linear modal analysis of an ideal, inviscid fluid model (assuming infinite thermal conductivity and isothermality), it is possible to prove that the onset of Jeans instability occurs exactly at the same point identified in the thermodynamical approach. The time scale for the instability has been found to be the dynamical time scale: there is a correspondence between the stability in the dynamical approach (in this context the nature of collapse is dynamical and not secular) and in the thermodynamical approach. This result strengthens the view that the applicability of different idealized models to describe the process of core collapse in systems made of a finite number of stars is more subtle than commonly reported.

Gravothermal oscillations

Direct N -body simulations ([28],[29]) show that, on the collisional time scale, core collapse can develop and it is eventually halted by binaries. Binaries can yield energy to the core in different ways: through the creation of binaries in three body interactions (three-body binaries) or in dissipative encounters between two single stars (tidal-capture binaries) or through binary-binary interactions. It seems that when the density in the core is high enough, binaries become active and start yielding energy to the core, in particular through binary-binary encounters of primordial binaries (binaries formed along with the single stars at the birth of the stellar system) that are expected to have accumulated in the core as consequence of mass segregation (Sect. 1.3.4). The total energy that binary-binary interactions in the core can release can be estimated to be of the order of $f_{binary}GN_cm^2/a$, where f_{binary} is the binary fraction, N_c is the number of objects in the core, m are the individual stellar masses and a is the semi-major axes. This is sufficient to halt the core if it exceeds the energy released by the core on its collapse time scale, which is in turn of the order of the energy of the core itself, $\sim N_c m \sigma_c^2$, where σ_c^2 is the velocity dispersion inside the core. Thus the collapse is halted if

$$f_{binary} \frac{Gm^2/a}{m\sigma_c^2} > 1. \quad (1.26)$$

As a consequence of the energy produced by binaries, the core energy becomes

less negative and it starts to expand (this is somehow similar to what happens to stars as they settle on the main sequence). During this core bounce, the thermal energy generated builds up in and around the core faster than it can be conducted away. This causes an expansion and cooling of the core and its immediate surroundings, because of the negative specific heat. If core collapse is sufficiently deep, the expanding core can actually cool to temperatures below that of its surroundings. At this point there is a temperature inversion, i.e. there is an inner region in which the temperature increases with radius (as shown in Fig. 1.5). At this stage, the

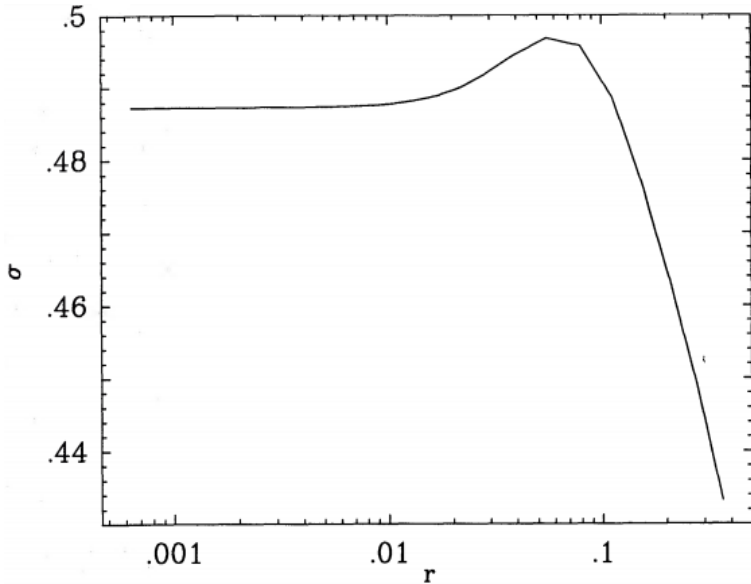


Figure 1.5: Velocity dispersion (“temperature”) profile in a gas model undergoing gravothermal expansion. As shown in N -body simulations [29], one of the characteristic signs of gravothermal expansion is the occurrence of a temperature inversion, that is, a region in which $d\sigma/dr > 0$, where $\sigma(r)$ is the velocity dispersion at distance r from the center of the system. From Heggie et al. (1994) [29].

warmest part of the system is outside the core, and this loses heat to both the core and the outer part of the entire system. The flux enhances the expansion of the core and its cooling, which reinforces the driving force behind the expansion (it is the gravothermal instability again, this time working in reverse). Eventually, the expanding core comes in thermal contact with the cooler parts of the cluster. When this happens, a normal distribution of temperature (decreasing monotonically from the center to the outside) is restored, and collapse of the core sets in once again. But this collapse is more-or-less like the first core collapse: the core overshoots, creates too much energy, and a temperature inversion, and the cycle recurs. This picture describes what are called gravothermal oscillations [28], represented in Fig. 1.6.

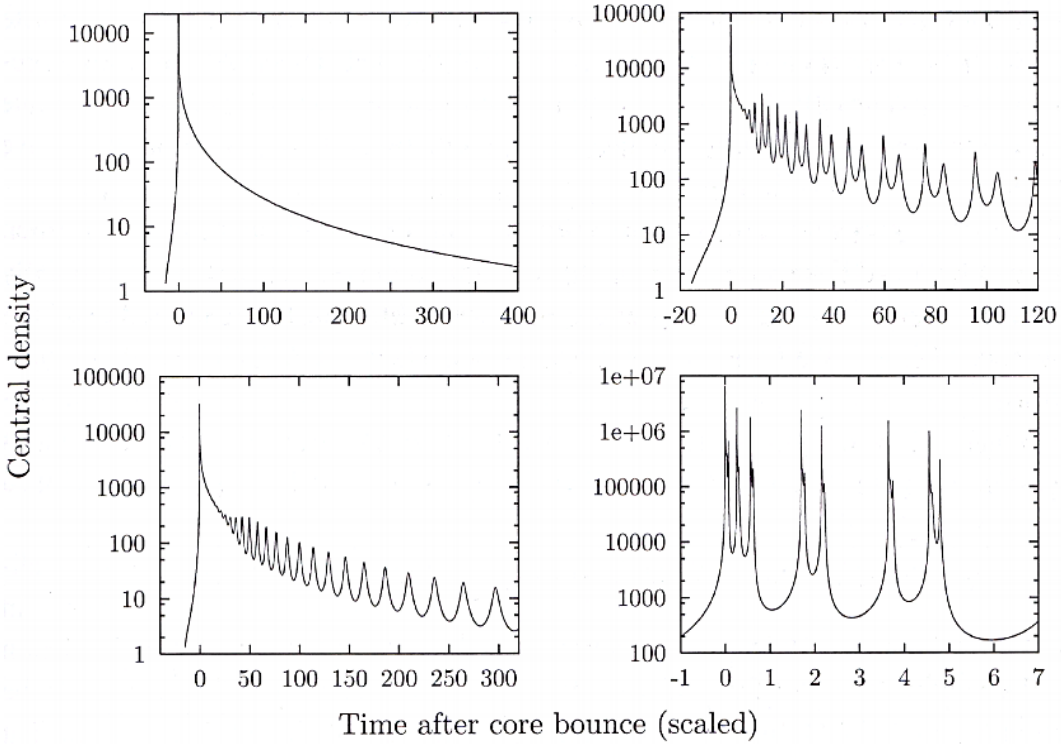


Figure 1.6: Period doubling and chaos in post-collapse expansion. Central density is plotted against time (in units of the initial half-mass relaxation time, with origin shifted to the time of core bounce) for models with $N = 6000$ (top left), $N = 8000$ (bottom left), $N = 10000$ (top right), $N = 50000$ (bottom right) particles. Image from Heggie & Hut (2003) [28].

1.3.3 Energy equipartition

In a realistic picture in which globular clusters are made of stars with different masses, another consequence of the granularity of the gravitational field is a tendency toward equipartition. We expect that, because of collisions, stars with different masses tend to erase their kinetic energy differences and reach a condition of thermodynamical equilibrium in which their temperatures (the mean kinetic energies) are constant. If we consider two generic components i and j , energy equipartition can be expressed as isothermality between them ($T_i = T_j$):

$$m_i \sigma_i^2 = m_j \sigma_j^2, \quad (1.27)$$

where m_i , m_j are the masses and σ_i^2 , σ_j^2 are the velocity dispersions associated with the i -th and j -th component. Velocity dispersions, as defined in Eq. 1.13, are local quantities, that is evaluated at a certain point (i.e., a certain distance r from the center in the case of spherical symmetry), and Eq. (1.27) expresses a condition of

local equipartition in which the two populations have locally the same temperature. However, we might define a global velocity dispersion Σ^2 , relative to the whole system or to a part of it (e.g., to the sphere of radius r_a), starting from the definition of kinetic energy $K = (1/2)M\Sigma^2$. In the case of spherical symmetry, the global velocity dispersion inside r_a for the i -th component is defined as:

$$\Sigma_i^2(r_a) = \frac{2K(r_a)}{M(r_a)} = \frac{\int_0^{r_a} \rho_i(r) \sigma_i^2(r) 4\pi r^2 dr}{\int_0^{r_a} \rho_i(r) 4\pi r^2 dr}, \quad (1.28)$$

where $K(r_a)$ and $M(r_a)$ are the kinetic energy and the mass of the system inside r_a . We might then refer to a condition of global equipartition as:

$$m_i \Sigma_i^2 = m_j \Sigma_j^2. \quad (1.29)$$

For many globular clusters, star-star collisions are important and might be thought to drive the system toward a state of global equipartition. In reality, global energy equipartition cannot be attained. In fact, the long relaxation times evaluated in the outermost parts of globular clusters are generally of the order of the age of the Universe. In addition, as pointed out by theoretical investigations (Spitzer, 1969 [48] and Vishniac, 1978 [61]) and many simulations ([58], [12]), only a condition of partial equipartition can be attained in real systems, even in the innermost regions.

Equipartition in kinematic observations

To study energy equipartition in real systems, it is necessary to determine whether the velocity distribution is mass dependent. As we will note in Sect. 1.4.1, until recently, star proper motions, which allow to determine the projected components of the velocity vector, have been measured for only a small number of globular clusters [5]. In the following we describe some examples of measures of energy equipartition obtained by means of proper motion.

For the cluster 47 Tucanae, proper motion data show a difference between *blue stragglers*³ and main sequence turn-off stars with similar magnitude. In particular, it has been observed that the velocity dispersion of 18 blue stragglers within $R < 20''$ (1 projected score radius) is smaller than that of bright red giants of similar luminosity, by a factor of about $\sqrt{2}$. This trend has been explained as due to the fact that the former are more massive than the latter [38].

³*Blue stragglers* are main sequence stars more luminous and bluer than stars at the main-sequence turn-off point for the cluster: they are typically younger and more massive than other stars of the cluster.

A direct measurement of global energy equipartition has been attempted for ω Centauri [58], where the projected global velocity dispersion inside the effective radius, $\Sigma_p = \Sigma_p(R_e, m)$, was measured for main-sequence stars with masses ranging from $0.3 M_\odot$ to $0.8 M_\odot$. It was observed that the dependency on mass is well fitted by a power-law of the kind $\Sigma_p(R_e, m) = m^{-\eta}$, with $\eta \approx 0.16 \pm 0.5$. Because in a condition of equipartition we would expect a power index $\eta = 0.5$, as suggested by Eq. 1.27, we can deduce that ω Centauri is in a state of only partial equipartition, as we would expect on the basis of its half-mass relaxation time (Eq. (1.20)) of 10 Gyr.

In a very recent investigation, Libralato et al. (2018) [36], analyzed the state of energy equipartition of NGC 362, which is characterized by a half-mass relaxation time $t_{rh} \approx 8.5 \times 10^8$ yr and a core relaxation radius $t_{rc} \approx 57.5 \times 10^6$ yr [27]. The authors considered all the main sequence stars from the center to beyond $2 R_e$ and divided them into 10 equally-populated mass bins of 2583 stars; for each bin they computed the projected velocity dispersion $\Sigma_p(2R_e, m)$ and the median mass of the stars. Also in this case the mass dependence was fitted by means of a power law, obtaining a value of $\eta = 0.114 \pm 0.012$. They also determined the radial variation of η , which is not expected to be constant because the level of relaxation in a globular cluster is not the same at all distances. The relevant sample was divided into 5 radial bins of $25''$ (the core radius is $0.18'$ [27]) each and a value of η has been measured for all the radial bins. The quantity η decreases monotonically with distance from the cluster center (Fig. 1.7). The innermost interval is characterized by $\eta \approx 0.4$. The estimate of η in the innermost radial bin may have been overestimated because it is obtained from stars covering a smaller mass range ($\Delta M \approx 0.2 M_\odot$) than in the remaining bins ($\Delta M \approx 0.3 M_\odot$). The other bins reveal that the level of energy equipartition decreases from $\eta \approx 0.25$ to $\eta \approx 0.08$ in the outer parts.

Equipartition in numerical simulations

The issue of understanding how energy equipartition operates in globular clusters has been explored mainly by means of numerical simulations. These have led to convincing evidence that collisional systems reach a state of only partial energy equipartition, even in the innermost regions. Pioneering work in this field was done by Spitzer & Hart (1971) [50] through simulations involving two-component systems. In present day simulations an increasing number of free parameters can be handled, and scientists prefer to include realistic mass functions. Trenti & van der Marel (2013) [58] performed a systematic N -body study to characterize the dependence of the global velocity dispersion on mass. They simulated systems with

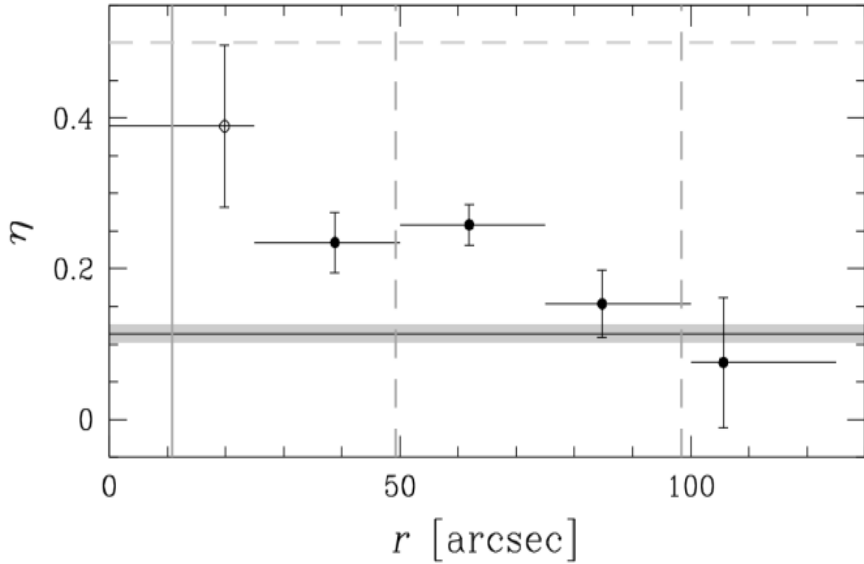


Figure 1.7: Decreasing trend of η with increasing projected distance from the center, R (here indicated as r). The black horizontal line represents the global value of η . Figure from Libralato et al. (2018) [36].

total number of particles which range from $N = 32768$ to $N = 65536$, with a realistic initial mass function⁴ (Salpeter, 1955 or Miller & Scalo, 1979). In their simulations they took into account stellar evolution and their code was initialized so as to obtain a final main-sequence turnoff at $0.8 M_{\odot}$. They also included a primordial binary fraction ranging from 0 to 0.1. One of the $N = 32768$ runs also contained a central Intermediate-Mass Black Hole IMBH (see Sect. 1.4.3), with the black hole mass set at 1% of the total cluster mass. The initial conditions in the position and velocity space were drawn from a King distribution function (King 1966 [34], see Sect. 2.1.3), with dimensionless central potential $\Psi = 3, 5, 7$. The simulated star clusters were tidally limited and particles experienced a tidal force from a point-like hosting galaxy, under the assumption that the cluster was in circular orbit at a distance selected so that the tidal radius was self-consistently defined by the

⁴The initial mass function (IMF) is an empirical function that describes the initial distribution of masses for a population of stars. The IMF is often stated in terms of a series of power laws, where the number of stars with masses in the range m to $m + dm$ within a specified volume of space, is proportional to $m^{-\alpha}$, where α is a dimensionless exponent:

$$dN/dm \propto m^{-\alpha}.$$

The IMF of stars more massive than our sun was first quantified by Edwin Salpeter in 1955, who favored an exponent of $\alpha = 2.35$. Later, Glenn E. Miller and John M. Scalo extended the work below one solar mass, suggesting that the IMF flattened (approached $\alpha = 1$) below one solar mass.

King density profile. All models filled their tidal radius initially. Simulations were generally run for $t > 15 t_{rh}(0)$, where $t_{rh}(0)$ is the initial half-mass relaxation time. Otherwise, they were stopped at earlier times, when 80% or more of the initial mass in the system had been evaporated (see Sect. 1.3.1).

The authors considered the dependence on mass of the projected global velocity dispersion, in order to allow a more direct comparison with observations. In their simulations, the dependence of the global projected velocity dispersion on mass at different radii (which contain from 30% to 90% of the total mass) is well-fitted by a power-law of the form $\Sigma_p(r, m) \propto m^{-\eta}$, both for single main-sequence stars and for compact remnants. The latter tend to have higher η than main-sequence stars (but still $\eta < 0.5$) due to their steeper (evolved) mass function. The result is that only partial energy equipartition develops in the simulations, despite the great variety of initial conditions considered. Central energy equipartition (inside the radius containing the inner 10% of the stars as seen in projection) is studied at the center of the system, where the projected central velocity dispersion $\sigma_0(m)$ is fitted by a power law of the form $\propto m^{-\eta}$, like in the case of global equipartition. The center can reach a maximum $\eta_{max} \approx 0.15$. No simulated system ever reaches a state close to complete equipartition, with $\eta = 0.5$.

A new characterization of equipartition in Monte-Carlo simulations

A new approach for characterizing energy equipartition has been introduced by Bianchini et al. (2016) [12] in view of applications to both simulations and observations. The article considered the set of Monte Carlo cluster simulations developed by Downing et al. (2010) [19] based on the Monte Carlo code of Giersz (1998) [22]. Initial conditions of these simulations are described in detail in Sect. 3.1. The properties of the simulated systems for three time snapshots, at 4, 7, and 11 Gyr. For each snapshot, the relaxation state of the system is described by the quantity $n_{rel} = t_{age}/t_{rc}$, where t_{rc} is the core relaxation time, defined in Eq. (1.19). The quantity n_{rel} denotes the number of relaxation times that a cluster has experienced. Higher values of n_{rel} thus correspond to more relaxed stellar systems. All the snapshots are pre-core collapse with respect to gravothermal catastrophe (see Sect. 1.3.2).

To quantify the mass dependence of the kinematics, a projected velocity dispersion profile is constructed, as a function of stellar mass. The analysis is restricted to stars within the projected half-light radius $6 R_e$ and includes all the stars within the mass range $0.1 - 1.8 M_\odot$. The projected quantities are considered for a direct comparison with observations. A simple analytical expression is adopted to describe

the establishment of partial equipartition:

$$\Sigma_p(R_e, m) = \begin{cases} \Sigma_0 \exp\left(-\frac{1}{2} \frac{m}{m_{eq}}\right) & \text{if } m \leq m_{eq} \\ \Sigma_{eq} \left(\frac{m}{m_{eq}}\right)^{-1/2} & \text{if } m > m_{eq} \end{cases} \quad (1.30)$$

The quantities Σ_0 and Σ_{eq} are two velocity scales. The parameter m_{eq} quantifies the level of partial energy equipartition reached by the system. For $m > m_{eq}$ the system is characterized by full global energy equipartition inside R_e ($\Sigma(R_e, m) \propto m^{-1/2}$). Following the power-law assumption proposed by Trenti & van der Marel (2013) [58], the slope of the function is then:

$$\eta(m) = -\frac{d \ln \Sigma_p(R_e, m)}{d \ln m} = \begin{cases} \frac{1}{2} \frac{m}{m_{eq}} & \text{if } m \leq m_{eq} \\ \frac{1}{2} & \text{if } m > m_{eq} \end{cases} \quad (1.31)$$

This profile can describe the differential behavior of equipartition, that is reached more efficiently in the higher-stellar mass regime. According to Eq. (1.30), systems with lower values of m_{eq} are thus closer to full energy equipartition. Bianchini et al. (2016) observed a correlation between m_{eq} and n_{rel} (Fig. 1.8), with decreasing m_{eq} for increasing n_{rel} (see Tab. 1.1). Clusters with $n_{rel} > 20$ reach an asymptotic maximum degree of equipartition characterized by $m_{eq} = 1.5$ (see Tab. 1.1), not a state of complete equipartition. These clusters have $\log T_{rc} < 8.5$ and are usually referred to as relaxed globular clusters.

1.3.4 Mass segregation

Tendency towards equipartition has significant consequences on the evolution and the structure of globular clusters. As the temperature of the heavier stars approaches that of the lighter stars, the heavies will tend to acquire lower random velocities and will sink towards the center of the cluster. On the other hand lighter stars, which acquire higher random velocities, will move outwards and populate the outermost regions of the cluster. The system will thus tend to be characterized by a stratification in mass, usually called mass segregation.

Mass segregation in observed clusters

Measurements of mass segregation require the acquisition of data on stellar positions and luminosities (on the main sequence, luminosity correlates with mass). A clear evidence of mass stratification - which we expect mainly in the central, more crowded regions - has been obtained in several globular clusters thanks to high-quality Hubble Space Telescope (HST) data. Such observations have confirmed

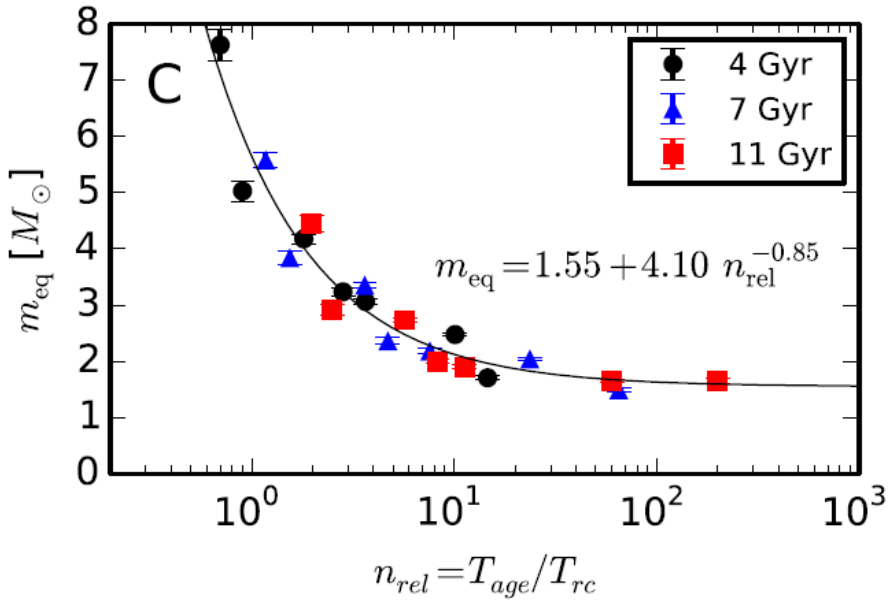


Figure 1.8: Relation between the level of energy equipartition reached by a cluster, m_{eq} , and its relaxation condition, n_{rel} . Well relaxed clusters (characterized by $n_{rel} > 20$) reach a maximum degree of energy equipartition of $m_{eq} = 1.55$. The solid line is the best fit interpolation for the $m_{eq} - n_{rel}$ correlation. Figure from Bianchini et al. (2016) [12].

the qualitative picture that massive stars are preferentially found in the core. Star classes with different masses, studied in different regions of the H-R diagram, show different radial distribution functions. This effect has been observed by comparing binaries and main sequence stars and by comparing *blue stragglers* and turn-off stars and is generally interpreted as mass segregation.

In a detailed analysis, Anderson (1997) [2], used data coming from HST/FOC (*Faint Object Camera*) and HST/WFPC2 (*Wide Field and Planetary Camera 2*) to bring out the presence of mass segregation in the nuclei of three galactic globular clusters: M92, 47 Tucanae e ω Centauri. He determined the luminosity functions⁵ for each cluster at two different distances from the center. These function were then fitted with the predicted luminosity functions on the basis of multi-components Michie-King models, with and without considering the presence of mass segregation between the different stellar classes. M92 and 47 Tucanae show a good agreement

⁵The luminosity function represents the number of stars (per unit volume) with absolute magnitude (M) in a luminosity interval ($M, M + dM$):

$$LF(M) = dN(M)/dM$$

with observational data and models characterized by mass segregation. This is probably due to the fact that the two systems show similar structural and concentration parameters and they are both relaxed systems, with central relaxation times of about 100 Myr. In contrast, ω Centauri exhibits a mild mass segregation, as would be natural in a system characterized by a central relaxation time of 6 Gyr.

Mass segregation effects on M/L

A feature strictly connected with mass segregation is the variation of the M/L ratio inside a globular cluster. Red giants and stellar (“dark”) remnants segregate toward the center of a cluster. They are responsible for opposite variations of the M/L: dark remnants increase the M/L, whereas bright red giants lower it. The combined effect of their segregation can either increase or decrease the M/L ratio in the central regions, generating a radial gradient in its profile. Other processes should also be taken into account in the study of radial variations of the M/L ratio. Stellar evolution has the effect of increasing the value of M/L since the ratio between high-mass stars (characterized by low M/L) and low-mass stars (characterized by high M/L) decreases with time, while massive stars gradually evolve into stellar remnants. Another effect which has to be considered is the preferential escape of low-mass stars (see Sect. 1.3.1). All these effects may jeopardize the application of dynamical models if a constant M/L ratio is assumed.

Bianchini et al. (2017) [10] studied the effect of mass segregation on the ratio M/L. They considered the simulations introduced in Sect. 3.1 and investigated the connection between the relaxation state of a cluster and the radial variation of M/L. They constructed the M/L profiles for all the snapshots, using a radial binning with logarithmic spacing. The M/L was computed by considering all the objects (stars and stellar remnants) in each spatial bin, and referring to the V-band luminosity. In Fig. 1.9, we can observe the M/L profiles as a function of radius, in units of the corresponding half-light radius. Profiles are color-coded according to their relaxation state n_{rel} . A clear dependence of the shape of the M/L profile of a cluster on its relaxation state is observed. Less relaxed clusters (lower n_{rel} , red colors) display a central peak (reaching values of M/L up to $25 M_\odot/L_\odot$ within $0.1 R_e$) that progressively flattens down for more relaxed clusters (higher n_{rel} , blue colors). For the most relaxed clusters a slight increase in M/L occurs in the outer part. As expected for mass segregated systems, we note that the profiles cannot be considered constant with radius, not even in the case of dynamically young clusters. In fact, systems with low n_{rel} (with ages of the same order of their relaxation time) are the ones that exhibit the strongest radial variation, namely a central peak. The

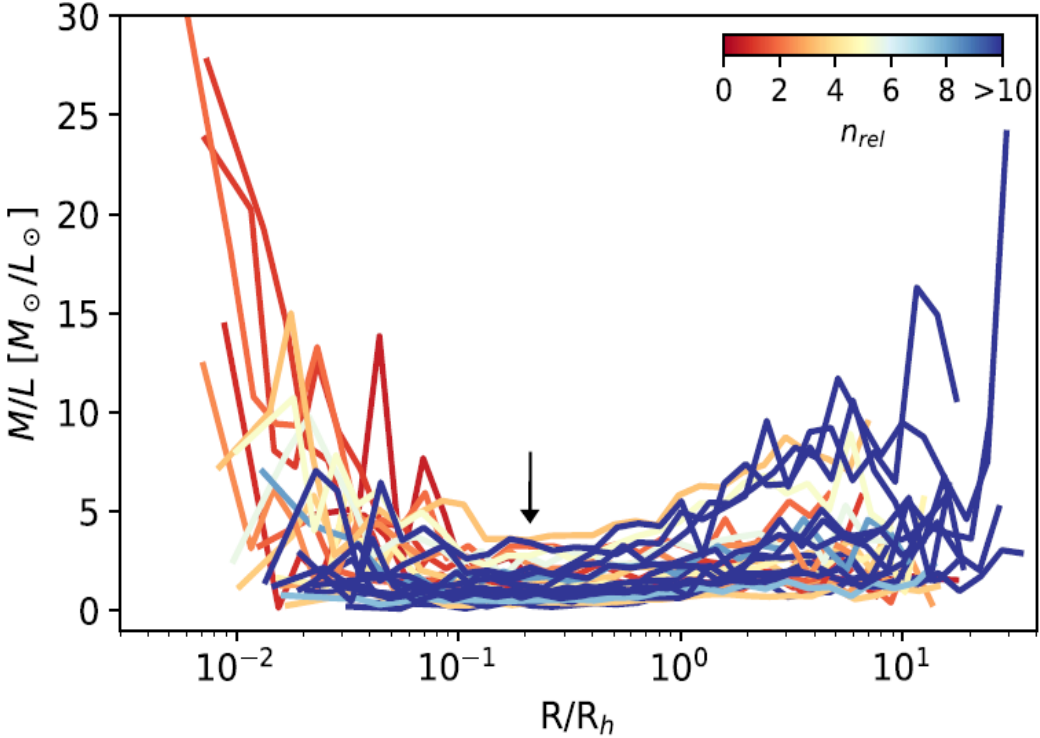


Figure 1.9: M/L profiles (in the V band) as a function of radius (in unit of the half-light radius R_e , here indicated as R_h) for all simulations. The profiles are colour-coded proportionally to their relaxation states indicated by n_{rel} . Redder profiles correspond to dynamically younger clusters, while bluer profile dynamically older ones. We can see that dynamically young clusters tend to show a central increase of the M/L ratio, while more relaxed system have a flatter M/L profile. Figure from Bianchini et al. (2017) [10].

presence of a minimum is due to the gradual mass segregation of stars with low M/L (giant stars and high mass main-sequence stars) toward the cluster center, whereas the increase in the outer parts is due to the presence of low-mass main sequence stars, characterized by higher M/L. Interestingly, the profiles show a common minimum around $0.2\text{--}0.3 R_e$, as indicated by a black arrow in Fig. 1.9. To interpret the central peak in the M/L profiles (within $0.1R_e$) and its relation with the relaxation states of the clusters, we have to consider the combined role of dark remnants (high-M/L neutron stars and stellar black holes) and bright stars (low-M/L red giant stars). Less relaxed clusters have a higher fraction of dark remnants than more relaxed clusters in their core. This is due to the fact that, while a cluster reaches a more advanced state of dynamical evolution, the number of stellar encounters that the dark remnants have experienced is higher, and therefore they have probably experienced a higher number of dynamical ejections.

In Tab. 1.1 we report the equipartition parameter m_{eq} , introduced in Eq.[1.30] and the V-band M/L ratios for the 4, 7 and 11 Gyr snapshots: the global M/L, the M/L ratio within the half-light radius R_e and the M/L ratio within $0.1 R_e$, in solar units.

Table 1.1: Relaxation states and M/Ls. Table from Bianchini et al. (2017) [10].

	n_{rel}			m_{eq}			M/L global			M/L($< R_e$)			M/L($< 0.1R_e$)		
	4 Gyr	7 Gyr	11 Gyr	4 Gyr	7 Gyr	11 Gyr	4 Gyr	7 Gyr	11 Gyr	4 Gyr	7 Gyr	11 Gyr	4 Gyr	7 Gyr	11 Gyr
Sim 1	2.8	4.4	8.3	3.24	2.37	2.00	1.04	1.61	2.22	0.85	1.23	1.84	0.92	2.09	2.17
Sim 2	1.8	3.6	5.70	4.18	3.36	2.37	1.15	1.95	2.95	0.98	1.72	2.51	1.67	2.48	3.81
Sim 3	0.9	1.50	2.5	5.03	3.84	2.92	1.19	1.66	2.59	1.08	1.52	2.35	1.69	2.59	2.82
Sim 4	0.7	1.20	2.0	7.63	5.58	4.46	1.38	2.05	3.26	1.34	1.88	3.12	2.58	4.80	5.60
Sim 5	14.6	64.9	200.2	1.71	1.50	1.66	0.85	1.22	1.78	0.44	0.69	1.29	0.43	0.30	1.44
Sim 6	10.1	23.6	60.1	2.48	2.04	1.65	1.05	1.55	2.20	0.8	1.15	1.61	0.84	1.09	0.81
Sim 7	3.6	7.6	11.2	3.07	2.19	1.90	0.73	1.00	1.40	0.55	0.70	1.02	0.54	0.59	0.99

Based on the above-described simulations, if we can independently determine the relaxation state of a cluster, we may thus anticipate its M/L profile and therefore remove some of the degeneracies (such as the mass-anisotropy degeneracy) in the structure of the cluster and disentangle the dynamical effects of stellar dark remnants from those of other dark components (e.g. intermediate-mass black holes or dark matter halos).

1.4 Recent discoveries

Until recently, globular clusters were generally assumed to be single population, isotropic stellar systems, formed by a single starburst in the early Universe. This traditional picture of the internal dynamics of globular clusters has now been revolutionized by a series of discoveries about their chemical, structural, and kinematic properties. The empirical evidence that their velocity space is much more complex than earlier assumed provides fresh new curiosity about many aspects of collisional gravitational dynamics. Such renew interest in dynamics is coupled with the recent discovery of chemical abundance anomalies, suggesting that not all stars in a cluster were born in a single homogeneous population. Globular clusters may also soon reveal the presence of massive black holes that would provide a “missing link” in the populations and growth of cosmic supermassive black holes. Globular clusters may also host populations of smaller (i.e. stellar-mass) black holes, potential progenitors for sources of gravitational wave emission. Finally, reconstructing the evolution of structural, kinematic and chemical properties of globular clusters would lead to important information about the assembly history of the Milky Way, including its dark matter component.

With the arrival of data from GAIA mission, we are entering the era of high-precision kinematics. The space observatory GAIA is now measuring distances, positions and proper motions of thousands of stars in the globular clusters of our Galaxy, with unprecedented accuracy. This new generation of data, coupled with astrometric measurements by the Hubble Space Telescope and other photometric and spectroscopic ground-based surveys (e.g., the GAIA-ESO survey), will enable us to probe the full six-dimensional “phase-space” properties of globular clusters. Therefore, we are about to enter a new golden age for the study of the internal dynamics of these stellar systems.

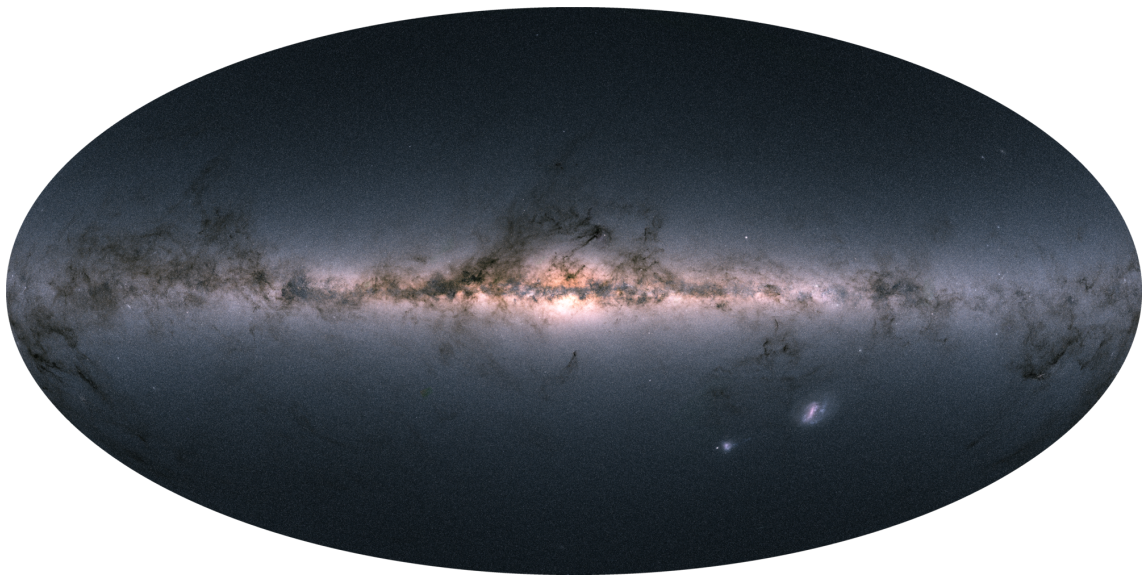


Figure 1.10: Gaia’s all-sky view of our Milky Way Galaxy and neighbouring galaxies, based on measurements of nearly 1.7 billion stars. The map shows the total brightness and color of stars observed by the satellite in each portion of the sky between July 2014 and May 2016. The bright horizontal structure that dominates the image is the Galactic plane, the flattened disc that hosts most of the stars in our home Galaxy. Figure from sci.esa.int/gaia.com.

1.4.1 Internal kinematics

Until recently, almost all of what was known about the internal motions within globular clusters was based on spectroscopic line-of-sight (LOS) velocity measurements. These suffer from some intrinsic limitations. First of all only brighter (more massive) stars can be analyzed spectroscopically. Moreover, in the crowded central regions of the cluster core, spectroscopy is limited by source confusion. Integral-field

spectroscopy is affected by the shot noise from the bright sources. In addition, LOS measurements are limited to measuring only one component of the velocity vector.

A significant improvement beyond the above limitations is possible when proper-motion (PM) measurements can be performed. Proper motions have the potential to provide several advantages over LOS velocity studies: (1) no spectroscopy is required, so the more plentiful fainter stars can be studied; (2) stars are measured individually, in contrast with integrated light measurements, which contain a disproportionate contribution from bright giants; and (3) two components of the velocity vector are measured instead of just one. Proper motions are small and difficult to measure with ground-based telescopes. The stable environment of space makes the Hubble Space Telescope (HST) and the new space observatory GAIA excellent astrometric tools for the study of proper motions. Hubble Space Telescope has executed only a very limited number of programs specifically aimed at the study of proper motions in globular clusters, in particular of NGC 104 (47 Tucanae), NGC 7078 (M15), NGC 6266, and NGC 5139 (ω Centauri, Anderson & van der Marel, 2010) [5]. The study of proper motions by means of HST allowed to reveal some new interesting aspects, such as the presence of rotation [3], [9], [6] and anisotropy (see below).

A great improvement is expected to come from GAIA mission. GAIA will provide positional and velocity (on the plane of sky) measurements with the accuracies needed to produce a stereoscopic and kinematic census of about one billion stars in our Galaxy and throughout the Local Group. This amounts to about 1 per cent of the Galactic stellar population. The first release included celestial positions of 1.1 billion stars, the parallax and proper motion for a subset of two million, plus additional information on 3000 variable stars and 2000 distant quasars.

Anisotropy

A direct measurement of the degree of velocity anisotropy (defined in Sect. 1.2.2) can be obtained by studying the ratio between velocity dispersions in two directions in the plane of sky as functions of the projected radial distance from the center of the cluster. In Fig. 1.11 we report the anisotropy profile determined for 47 Tuc by Bellini et al. (2017) [6]. The center of the cluster is isotropic, with increasing radial anisotropy moving outward. It is worth noting that this trend agrees with what is seen in a sample of 22 globular cluster [6].

Isotropy in the innermost regions can be interpreted as a consequence of two-body relaxation processes. The development of velocity anisotropy can be interpreted as the combined result of the formation mechanism of globular clusters (e.g., violent

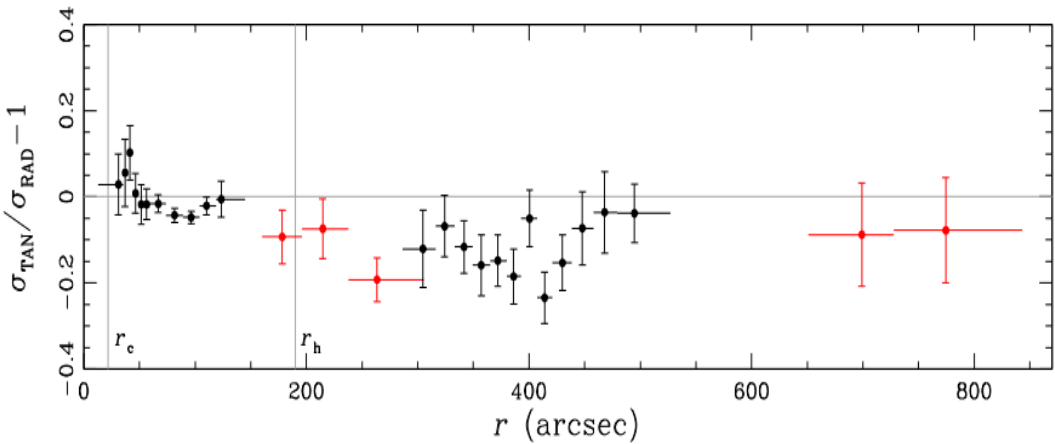


Figure 1.11: Deviation from isotropy (gray horizontal line) in 47 Tuc as a function of the projected radius R , here indicated as r . The horizontal line at 0 indicates an isotropic system. The center of the cluster is isotropic, with increasing radial anisotropy moving outward. Red points are computed using WFPC2 data, for which systematic effects cannot be quantified. Core and half-light radii (Harris, 1996 values) (R_c and R_e respectively) are marked by the two vertical lines in all panels. Figure from Bellini et al. (2017). [6]

relaxation, Lynden-Bell (1967) [37]) and their subsequent long-term dynamical evolution. Violent relaxation can generate significant anisotropy, with radial orbits dominating outside the half-mass radius. In addition, dynamical evolution can also naturally determine the development of radial anisotropy. Numerical investigations (pioneering studies from Hénon (1971) [31], Spitzer & Hart (1971) [50], Spitzer & Shapiro (1972) [51] and, more recent studies from Bianchini et al. (2017) [11], Zocchi et al. (2016) [63]) have shown that pressure anisotropy can arise in a collisional system, even if the initial conditions isotropic. During their evolution, isolated globular clusters tend to develop a structure composed of two distinct regions, a dense core and a halo, as a consequence of the process described in Sect. 1.3.2. The core-halo structure has important implications on the velocity distribution of the system. Strong relaxation in the core (because of its high density) forces isotropy and continues to produce high-energy stars whose orbits extend into the halo. Owing to the low density in the halo, stars which travel in it interact mainly with stars in the core rather than with other halo stars: they do not experience collisions and return to the core, producing very radial orbits on average. Halo stars that are initially not on radial orbits do not go into the core and their velocity distribution does not evolve spherically. Therefore radial orbits tend to dominate the halo and velocity anisotropy increases as the halo grows, penetrating into the innermost region as the

core collapses [54].

Recently Tiongco et al. (2016) [55] and Zocchi et al. (2016) [63] have studied the evolution of the velocity anisotropy of globular clusters in a tidal field, showing that the field can play a significant role in shaping the velocity anisotropy. As the evolution proceeds, the external tidal field has the effect of suppressing the anisotropy, and the system may eventually become fully isotropic. This happens for two main reasons: first, mass loss has the effect of exposing the deeper parts of the systems, where deviations from isotropy are more modest [24]; second, the tidal torque induces isotropy in the velocity dispersion of the outer regions of the cluster [43]. Figure 1.12 illustrates the evolution of anisotropy obtained from N -body

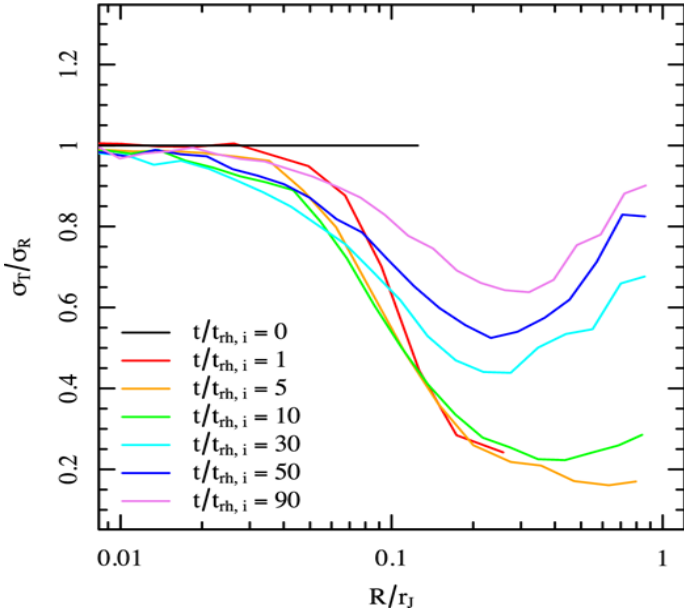


Figure 1.12: Time evolution of the radial profile of σ_t/σ_r for an initially isotropic model. The projected radius is normalized to the tidal radius, here indicated as r_J . Each line is the median of the profiles obtained from four realizations. The imposed isotropic profile of the King model at $t = 0$ is shown.

simulations of an initially isotropic cluster in the presence of a tidal field performed by Tiongco et al. (2016) [55]. The cluster is initialized with an isotropic King model, and, as it evolves and expands, it develops a strong radial anisotropy in the outer regions. As the system continues its evolution and starts to lose mass, a minimum in the ratio σ_t/σ_r forms (corresponding to a maximum in the radial anisotropy) while the outermost regions become increasingly less radially anisotropic.

1.4.2 Multiple populations

Chemical composition in globular clusters is determined mostly from spectroscopic studies, which show that stars in globular clusters are mostly Population II stars, that is old and with low metallicities⁶. For decades globular clusters have been thought to be systems made of stars with the same initial chemical composition, that is stellar populations were thought to be very homogeneous. Recent studies of globular clusters have shown that they are not simple stellar populations, being rather made of multiple components of stars. The most convincing evidence comes from the observation of different chemical compositions for different stars and the presence of two or more branches in the evolutionary sequences of the H-R diagram. The suggested interpretation is that different stellar population have formed in successive epochs.

The first who suspected that the main sequence would split in globular clusters was Jay Anderson who considered the case of ω Centauri in his PhD thesis [2], but his result was based on only one external WFPC2 field, and this finding was so unexpected that he decided to wait for more data and more accurate photometry. Later, Bedin et al. (2004) [4] confirmed the main sequence split in ω Centauri in WFPC2 field and in an additional ACS (Advanced Camera for Surveys) field located 17' from the cluster center. In reality, the scenario in ω Centauri is even more complex; as is already evident in the color-magnitude diagram of Bedin et al. (2004) the three main sequences of the cluster spread into a sub-giant branch (SGB) made of five distinct components characterized by different metallicities and ages. These results reinforced the idea that ω Centauri could be a peculiar object, not even a globular cluster, but a remnant of a dwarf galaxy. The case of ω Centauri stimulated a number of investigations that showed that the multiple population scenario is not a peculiarity of a single object. Piotto et al. (2007) [45] showed that also the color-magnitude of NGC 2808 is splitted into three main sequences. In general, the multiple population phenomenon differs from cluster to cluster.

1.4.3 Intermediate-Mass Black Holes?

Globular clusters are candidates to host Intermediate-Mass Black Holes (IMBH), that is black holes with mass of $M_\bullet \approx 10^3 M_\odot$. Black holes in this mass range should

⁶Metallicity is the ratio between the abundance of iron with respect to the Sun. It is usually expressed as [Fe/H]:

$$[Fe/H] = \log(N_{Fe}/N_H) - \log(N_{Fe}/N_H)_{sun}$$

represent a natural link between solar mass black holes, the number of which in globular clusters seems to be higher than expected, and Super-Massive black holes (with mass $M_\bullet > 10^6 M_\odot$), found in the nucleus of most galaxies, in particular in the Local Group. At the present day, we do not have convincing proof of the existence of IMBHs; some studies led to controversial results, as the central dispersion velocity gradients could be interpreted not only as due to the presence of an IMBH but also in terms of different dynamical processes.

Noyola et al. (2008) [42] observed that the surface brightness profile of ω Centauri shows a continuous rise toward the center, in contrast with previous measurements that found a flat core. The shape of the profile is similar to that expected for star clusters containing black holes in their centers. They also measured a line-of-sight velocity dispersion for two regions, one at the center of the cluster and the other $14''$ away (core radius is $2.37'$ for this cluster [27]), detecting a rise in velocity dispersion from 18.6 km/s for the outer field to 23 km/s for the central one. They compared the observed velocity dispersion profile with a series of isotropic models containing black holes of various masses and found that a black hole of $4 \times 10^3 M_\odot$ is necessary to match observations.

Later, van der Marel & Anderson (2010) [60] presented a detailed dynamical analysis of the star-counts, surface-brightness, and kinematic data available for the same cluster, with a particular focus on new HST data available. Based on the observed profile of the projected density, their models used the Jeans equation to yield predictions for the projected profiles of line-of-sight velocity dispersion as function of projected distance R from the cluster center, in each of the three orthogonal coordinate directions (line of sight, proper motion radial, and proper motion tangential). They found out that models with a core provide a good fit to the kinematic data without any dark mass: in these models the presence of the central peak in velocity dispersion is due to the presence of radial anisotropy in the center of the system. Since a core is also consistent with the observed density profile, this seems to imply that the presence of an IMBH is not required in ω Centauri. Differences in the results seem to be due to different positions of the cluster center considered by the two groups. The case of ω Centauri shows that IMBH detection can be accompanied by a combination of subtle effects which complicate kinematic analysis.

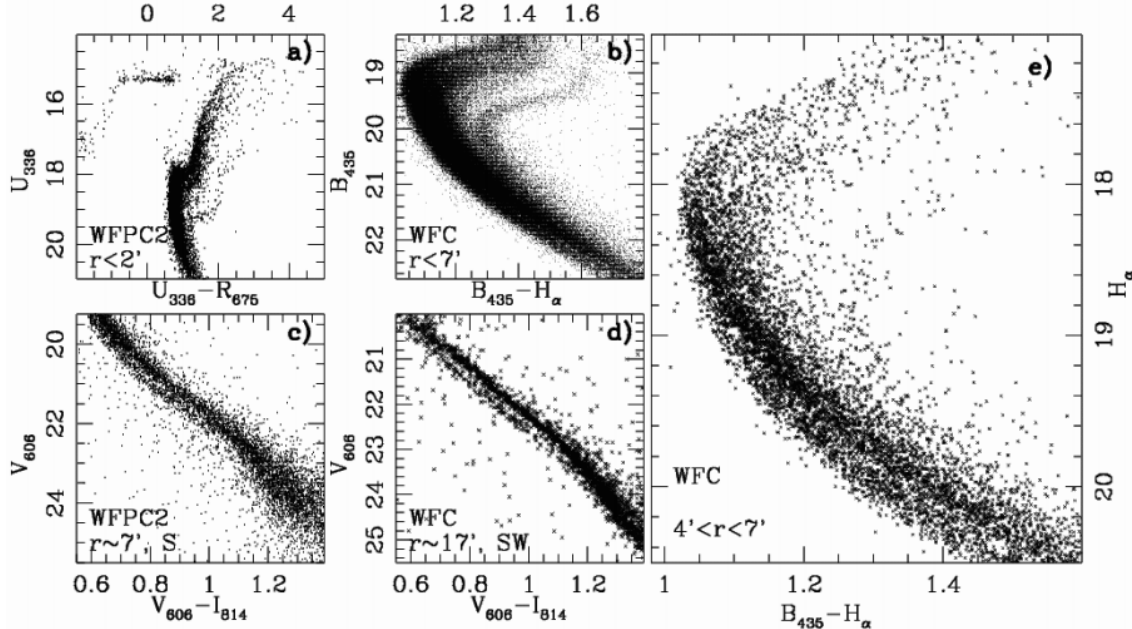


Figure 1.13: A collection of color-magnitude diagrams from WFPC2 and ACS data of ω Centauri. For each color-magnitude diagram, the label indicates the distances of the field from the cluster center. The left part of the figure shows four color-magnitude diagrams: the two upper panels focus on the turnoff stars, and the lower ones on the main-sequence stars. Panel (a) shows the original WFPC2 color-magnitude diagram that first discovered the lower turnoff (LTO) sequence. Panel (b) shows the same sequence (from WFC data) with many more details and more stars, from a larger region of the cluster. Panel (c) shows the original color-magnitude diagram from Anderson (1997) [2], where the double main sequence (DMS) was first identified. The main sequence appears to bifurcate into two distinct sequences, with a region between the two that is almost devoid of stars. Panel (d) shows another color-magnitude diagram from ACS/WFC images, which also shows the anomalous DMS in a different field, at $R = 17'$ from the center. Panel (e) shows the subsample of the stars plotted in panel (b), located at projected radial distances $R > 4'$. Figure from Bedin et al. (2004) [4]

Chapter 2

Dynamical models

A quantitative discussion of globular clusters requires the introduction of realistic dynamical models which satisfy assumptions A, B, C introduced in Sect. 1.2. These models are useful for theoretical investigations of dynamical mechanisms as initial conditions in the computations of detailed numerical models, and to fit observed clusters. In particular, by means of these models, parametric fits to the luminosity and kinematic profiles of globular clusters allow us to measure important structural properties, such as the M/L ratio. We introduce some specific models, starting with one-component models, in which all stars have the same mass m (mass density is equal to $m n(r)$, where n is the numerical density)¹. One-component models describe observed clusters with the smallest number of free parameters. Of course, in order to take into account fundamental aspects of the relaxation process such as energy equipartition (Sect. 1.3.3) and mass segregation (Sect. 1.3.4), multi-components models are required.

2.1 One-component models

2.1.1 Plummer model

A simple class of spherical isotropic models can be constructed by assuming a power-law dependence of the relevant distribution function on energy per unit mass:

$$f(E) = \begin{cases} k_1(-E)^p & \text{for } E < 0 \\ 0 & \text{for } E \geq 0, \end{cases} \quad (2.1)$$

¹In practice, the assumption of a single mass is not required. The models assume that the stellar population is homogeneous throughout the cluster.

where k_1 is a constant and the gravitational potential $\Phi(r)$ introduced in Eq. (1.8) is taken to vanish at the cluster surface. From Eq. (2.1) we can compute the smoothed mass density, defined in Eq. (1.2):

$$\rho(r) = k_2[-\Phi(r)]^{p+3/2}, \quad (2.2)$$

where k_2 is a constant. The Poisson equation Eq. (1.10) becomes the same as the equation for a polytropic sphere with index $n = p + 3/2$. Analytic solutions are known for $n = 0$ (uniform sphere), $n = 1$, and $n = 5$. Despite its infinite radius, the polytrope with $n = 5$ gives a reasonable description of the surface brightness profile of real clusters with a compact core and an extended outer envelope. For this reason, it is sometimes used as a starting point for simulations (e.g., by Bianchini et al. (2016) [12], see Sect 3.1). Because this model was used by Plummer (1911) [46] in an attempt to fit the observed light distributions of clusters, it is often called the Plummer model. Its physical properties can be expressed by simple formulas [7]:

$$\rho(r) = \frac{3Mb^2}{4\pi} \frac{1}{(b^2 + r^2)^{5/2}}, \quad (2.3)$$

$$\Phi(r) = -\frac{GM}{(b^2 + r^2)^{1/2}} = -2\sigma^2(r), \quad (2.4)$$

where σ^2 is the mean square velocity. The integrated mass is given by

$$M(r) = M \frac{r^3}{(b^2 + r^2)^{3/2}}. \quad (2.5)$$

so that the half-mass radius occurs at $r_h \approx 1.3b$. The projected density $\rho_p(R)$ is given by:

$$\rho_p(R) = \frac{M}{\pi} \frac{b^2}{(b^2 + R^2)^2}. \quad (2.6)$$

The radius containing half of the projected mass equals $R_e \approx b$ [49].

2.1.2 Isothermal sphere

A physical model based on the role of relaxation in globular clusters might consider a distribution function suggested by statistical equilibrium:

$$f(E) = A \exp(-aE), \quad (2.7)$$

where the energy per unit mass is $E = (1/2)v^2 + \Phi(r)$ and A and a are positive constants related to the total mass and the velocity dispersion. A spherical system

in which Eq.(2.7) holds exactly is called an *isothermal sphere*. The mass density for such a distribution function is:

$$\rho(r) = 4\pi A \exp[-a\Phi(r)] \int_0^\infty v^2 e^{-av^2/2} dv = 4\pi\sqrt{2} \frac{A}{a^{3/2}} \Gamma\left(\frac{3}{2}\right) \exp(\psi) = \frac{\tilde{A}}{a^{3/2}} \exp(\psi) \quad (2.8)$$

where $\Gamma(a) = \int_0^\infty t^{a-1} e^{-t} dt$ is the gamma function and $\tilde{A} = 4\sqrt{2}\pi A \Gamma(3/2)$. Here we have introduced the dimensionless potential $\psi = -a\Phi(r)$. The density depends on the radial coordinate only implicitly through the potential. The velocity dispersion can be evaluated by means of Eq.(1.13):

$$\sigma^2(r) = \frac{2}{a} \frac{\Gamma(5/2)}{\Gamma(3/2)} = \frac{3}{a}, \quad (2.9)$$

which is constant (isothermality). The fully self-consistent problem requires the solution of the Poisson equation (Eq. (1.10)), which we express in dimensionless form by rescaling the radial coordinate $r \rightarrow \xi = r/\lambda$, with $\lambda = \sqrt{a^{1/2}/(4\pi G \tilde{A})}$:

$$\frac{1}{\xi^2} \frac{d}{d\xi} \left(\xi^2 \frac{d\psi}{d\xi} \right) = -\exp(\psi). \quad (2.10)$$

If we look for a solution with finite central density, the natural boundary conditions are $\psi(0) = \Psi$ and $(d\psi/d\xi)(0) = 0$. Close to the center, the potential well can be approximated by a parabola with

$$\psi \sim \Psi - \frac{1}{6} \exp(\Psi) \xi^2. \quad (2.11)$$

As ξ increases, ψ approaches asymptotically, with slow oscillations, a singular solution of Eq. 2.10:

$$\psi = -\ln\left(\frac{\xi^2}{2}\right). \quad (2.12)$$

This form of ψ corresponds to the dimensionless density profile:

$$\hat{\rho} = \exp(\psi) = \frac{2}{\xi^2} = \frac{2\lambda^2}{r^2}. \quad (2.13)$$

Thus the integrated mass of the singular solution:

$$M(r) = \int_0^r \rho(r') 4\pi r'^2 dr' = 8\pi \frac{\tilde{A}}{a^{3/2}} \lambda^2 r, \quad (2.14)$$

which increases linearly with radius. This last equation shows that mass associated with an isothermal sphere increases indefinitely, as result of the tail of the Maxwellian velocity distribution, and makes this model inapplicable for describing the global profiles of stellar systems. However, this model could represent a good description for the inner regions of clusters as they are believed to be nearly isothermal.

2.1.3 King models

A simple velocity distribution function that resolves the problem of infinite mass of the isothermal sphere is obtained by introducing a truncation radius r_t , so that f vanishes for $E > E_t = \Phi(r_t)$:

$$f^K(E) = \begin{cases} A [\exp(-aE) - \exp(-aE_t)] & \text{for } E < E_t \\ 0 & \text{for } E \geq E_t, \end{cases} \quad (2.15)$$

where A , a are positive constants and E_t represents the boundary energy above which stars do not belong to the system and are ignored. The physical basis for this truncation is the presence of a galactic tidal field, which pulls stars out of the cluster beyond the tidal radius r_T (Eq. (1.24)). Mathematically, the truncation radius r_t may be smaller than the relevant tidal radius; in this case the model is said to underfill the tidal volume. Models based on this distribution function have been computed and compared with observed clusters by King [34] and thus are generally called King models. We introduce the dimensionless escape energy ψ , defined as:

$$\psi(r) = -a[\Phi(r) - \Phi(r_t)]. \quad (2.16)$$

The condition $E < \Phi(r_t)$ can be written as $av^2/2 < \psi$. The density profile (for $r < r_t$, i.e. $\psi > 0$) associated with the distribution function is given by

$$\rho(r) = \frac{\tilde{A}}{a^{3/2}} \exp(\psi) \gamma\left(\frac{5}{2}, \psi\right) = \frac{\tilde{A}}{a^{3/2}} \hat{\rho}(\psi), \quad (2.17)$$

with $\tilde{A} = (8/3)\pi\sqrt{2}A \exp[-a\Phi(r_t)]$. The function γ is the incomplete gamma function defined as $\gamma(s, x) = \int_0^x t^{s-1} e^{-t} dt$. The dimensionless mass density is $\hat{\rho}(\psi) = \exp(\psi) \gamma(5/2, \psi)$ and, like for the isothermal sphere (Eq.(2.8)), it depends on the radial coordinate only through the potential. The velocity dispersion can be written as

$$\sigma^2(r) = \frac{6}{5a} \frac{\gamma(7/2, \psi)}{\gamma(5/2, \psi)}. \quad (2.18)$$

It should be emphasized that despite a 's being constant, the velocity dispersion associated in the King models is not constant. The velocity dispersion decreases monotonically with radius and vanishes at the truncation radius. The presence of the truncation present in Eq.(2.15) implies a truncation in the velocity space, brings the system out of thermodynamical equilibrium, and makes the velocity dispersion depend on the position.

The self-consistency relation implied by the Poisson equation, by a suitable rescaling of the radial coordinate $r \rightarrow \xi = r/\lambda$, with $\lambda = \sqrt{a^{1/2}/(4\pi G \tilde{A})}$, can

be written as:

$$\frac{1}{\xi^2} \frac{d}{d\xi} \left(\xi^2 \frac{d\psi}{d\xi} \right) = -\hat{\rho}(\psi), \quad (2.19)$$

which is to be integrated with boundary conditions $\psi(0) = \Psi$ and $(d\psi/d\xi)(0) = 0$. Integrating Eq. (2.19) determines the dimensionless radius r_t/λ as the location where ψ vanishes. Thus a one-to-one correspondence is found between Ψ and r_t/λ . A commonly used scale for this problem is

$$r_0 = \sqrt{\frac{9a^{1/2}}{4\pi G \tilde{A} \hat{\rho}(\Psi)}} = \frac{3}{\sqrt{\hat{\rho}(\Psi)}} \lambda. \quad (2.20)$$

King models are thus a one-parameter family of models, identified by the value of Ψ or, more often, by the value of the concentration index

$$c = \log(r_t/r_0). \quad (2.21)$$

The radius r_0 is sometimes confused with the core radius r_c . With the definition of Eq. (2.20), the identification is correct for the isothermal sphere, and it is reasonable for concentrated King models, whereas at low values of Ψ , the ratio r_0/r_c changes significantly with Ψ .

Application of these models to interpret the photometric profiles of globular clusters has been successful. The globular clusters of our Galaxy are generally well fitted by King models with concentration parameters in the range $0.5 < c < 2$ (see Fig. 2.1); some are even more concentrated, but they are generally interpreted as systems in a post-core-collapse phase because of the onset of the gravothermal catastrophe (see Sect. 1.3.2), which is known to take place at $\Psi \gtrsim 7.4$. Unfortunately, so far the comparison between models and data has been limited mainly to a fit to the available photometric profiles. Only recently attention has been drawn to the need for a combined test of photometric and kinematic data.

Regardless of their success, King models exhibit several internal inconsistencies. The models are meant to describe tidally truncated stellar systems, but in their original form they are spherical, in spite of the stretching that tides are expected to impose. The models are chosen to reflect the conditions of a collisionally relaxed state, but actually, outside their half-mass radius, globular clusters and the models themselves are associated with very long relaxation times (Harris 2010) [27]. These models are generally applied as one-component models, that is, they are suited to describe stellar systems made of a single homogeneous stellar population, yet, if collisional relaxation is at work, it should generate significant mass segregation, with heavier stars characterized by a distribution more concentrated than that of lighter stars. With respect to this last inconsistency, a more realistic generalization to two-component King models is presented in Sect. 2.2.1.

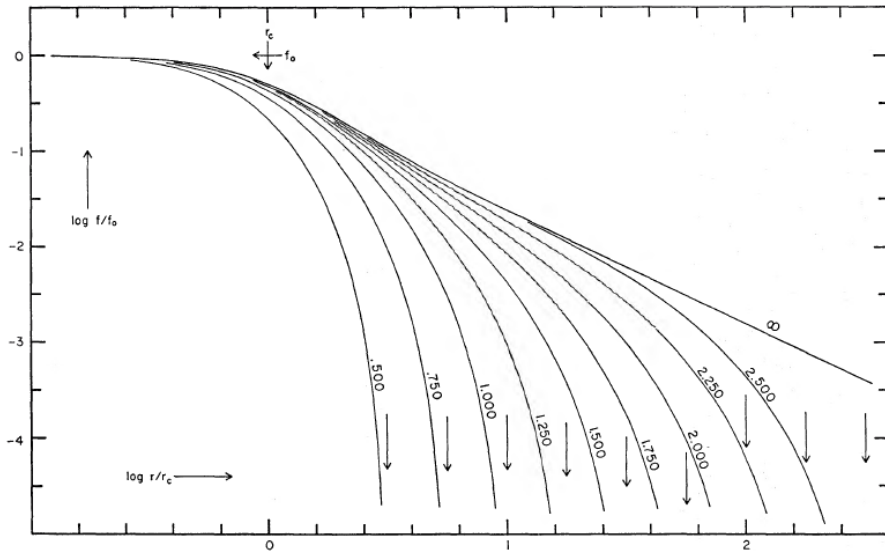


Figure 2.1: Projected density profiles for the King models. The curves show the logarithm of the projected density (normalized to its central value) for selected values of the concentration parameter c (marked along the curve). For each case, an arrow provides the location of the relevant truncation radius. Figure from King (1966) [34].

2.1.4 $f_T^{(\nu)}$ models

Many large globular clusters are characterized by long relaxation times (e.g., ω Centauri, NGC 2419), comparable to the age of the Universe even in their central regions [27]. Because in these clusters collisions have not had time to act, we expect them to be far from thermodynamical equilibrium, so that their description in terms of King models may not be very adequate. In contrast, these systems might be described by means of models originally conceived for less relaxed systems such as, for example, elliptical galaxies. Studies of the dynamics of elliptical galaxies have focused mainly on the picture of galaxy formation by incomplete violent relaxation from collisionless collapse. There are ways to translate this picture into an appropriate choice of the relevant distribution function to represent the current state of ellipticals. One particular choice, which reflects a conjecture on the statistical foundation of the relevant distribution function (see Stiavelli & Bertin (1987) [52]), corresponds to a family of partially relaxed models called $f^{(\nu)}$ models, constructed from:

$$f^{(\nu)}(E, J) = \begin{cases} A \exp \left[-aE - d \left(\frac{J^2}{|E|^{3/2}} \right)^{\nu/2} \right] & \text{for } E < 0 \\ 0 & \text{for } E \geq 0, \end{cases} \quad (2.22)$$

where A , a , and d are positive constants and J is the magnitude of the specific angular momentum. In particular, d is related to the anisotropy scale of the system. In principle, ν is any positive real number; in practice, a given value of $\nu \approx 1$ is taken and thus ν should be considered as a fixed parameter. Self-consistent models based on this distribution function define a family of anisotropic, non-truncated models. The presence of anisotropy (as suggested by the presence of a second integral of the motion in the distribution function) is natural in systems formed via incomplete violent relaxation, which have the characteristic signature of radially-biased pressure anisotropy for less bound stars.

The use of the $f^{(\nu)}$ models is preferred to other options (for example to the use of King-Michie models, Michie (1963) [40]) because the $f^{(\nu)}$ models are based on a specific physical justification and have been shown to perform well both in interpreting the observations of bright ellipticals and the properties of the products of incomplete violent relaxation found in numerical simulations of collisionless collapse (over a range of nine orders of magnitude in the computed density profiles, with an excellent matching of the properties of the generated pressure anisotropy profiles; see Trenti, Bertin, van Albada (2005) [57]).

In a recent investigation Zocchi, Bertin, Varri (2012) [62] used this class of spherical $f^{(\nu)}$ models to study a sample of Galactic globular clusters under different relaxation conditions and compared their performance to that of standard spherical King models. This exploratory investigation indicates that for less relaxed clusters (e.g. NGC 2419, ω Centauri) the use of $f^{(\nu)}$ models is encouraged because they can match significant velocity gradients inside the half-light radius, as opposed to King models. However, these models, being non-truncated, are at a disadvantage in describing the outer parts of the available photometric profiles.

Truncated $f^{(\nu)}$ models

In order to incorporate the effects of a tidal truncation, a truncation to the $f^{(\nu)}$ was introduced by de Vita, Bertin, Zocchi (2016) [16]. They considered models with $\nu = 1$ and argued:

$$f_T^{(\nu)}(E, J) = \begin{cases} A \exp \left[-aE - \frac{dJ}{|E-E_t|^{3/4}} \right] & \text{for } E < E_t \\ 0 & \text{for } E \geq E_t. \end{cases} \quad (2.23)$$

For $J \neq 0$, the distribution function vanishes at the cut-off energy E_t together with all its derivatives. The self-consistent problem can be written in a dimensionless form by means of the dimensionless potential $\psi(r) = -a[\Phi(r) - \Phi(r_t)]$, the dimensionless

radius $\xi = ra^{1/4}d$ and dimensionless velocity $\omega^2 = (a/2)v^2$. The mass density associated with the $f_T^{(\nu)}$ distribution function is:

$$\hat{\rho}(\xi, \psi) = \frac{A}{a^{3/2}} \int_0^\pi \int_0^{\sqrt{\psi}} \hat{f}_T^{(\nu)}(\xi, \psi, \omega, \zeta) \omega^2 \sin \zeta d\zeta d\omega = \frac{A}{a^{3/2}} \hat{\rho}(\xi, \psi), \quad (2.24)$$

where

$$\hat{f}_T^{(\nu)}(\xi, \psi, \omega, \zeta) = 4\sqrt{2}\pi \exp \left[-\omega^2 + \psi - \frac{\sqrt{2}\xi\omega \sin \zeta}{|\omega^2 - \psi|^{3/4}} \right], \quad (2.25)$$

and ζ is the angle between the position vector \mathbf{r} and the velocity vector \mathbf{v} of a single star. In this case, dependence on radial coordinate is not only implicit through ψ but also explicit, as opposed to King models (Eq. (2.17)). The resulting dimensionless form of the Poisson equation (Eq. (1.10)) is given by:

$$\frac{d^2}{d\xi^2} \psi + \frac{2}{\xi} \frac{d}{d\xi} \psi = -\frac{1}{\gamma} \hat{\rho}(\xi, \psi) \quad (2.26)$$

where the dimensionless parameter $\gamma = ad^2/(4\pi G A)$ has been introduced. This differential equation is integrated under the boundary conditions $\psi(0) = \Psi$ and $(d\psi/d\xi)(0) = 0$ out to the dimensionless truncation radius ξ_t , where the dimensionless potential vanishes. Hence, the self-consistent problem for the dimensionless potential reduces to a family of second-order differential equations defined by two structural parameters: the central dimensionless potential Ψ and γ .

For non-truncated $f^{(\nu)}$ distribution functions, γ is determined as an eigenvalue $\gamma = \gamma(\Psi)$ in order to satisfy the condition of Keplerian decay of the gravitational potential ($\Phi \sim -1/r$) at large radii. For models with $\nu \approx 1$, in the range $0 \leq \Psi \leq 15$, the function $\gamma(\Psi)$ presents a pronounced peak at $\Psi \approx 5.5$; for higher values of Ψ , γ decreases, reaches about half of its peak value at $\Psi \approx 10$, and then stays approximately constant (as illustrated by Fig. 2.2). In truncated models γ is left as a free parameter. However, since, for a given Ψ , there is a maximum value γ_{max} beyond which the models do not present any truncation. The parameter space thus is confined to the region under the curve $\gamma(\Psi)$ found for the non-truncated models. For a given Ψ , the non-truncated models are recovered in the limit $\gamma \rightarrow \gamma_{max}$.

In the natural spherical coordinates, the velocity dispersion tensor is diagonal with $\sigma_\theta^2 = \sigma_\phi^2$. We thus consider a radial and a tangential component ($\sigma_T^2 = \sigma_\theta^2 + \sigma_\phi^2$) of the velocity dispersion tensor:

$$\sigma_r^2(\xi, \psi) = \frac{2}{a} \frac{1}{\hat{\rho}} \int_0^\pi \int_0^{\sqrt{\psi}} \hat{f}_T^{(\nu)}(\xi, \psi, \omega, \zeta) \omega^4 \cos^2 \zeta \sin \zeta d\zeta d\omega, \quad (2.27)$$

$$\sigma_T^2(\xi, \psi) = \frac{2}{a} \frac{1}{\hat{\rho}} \int_0^\pi \int_0^{\sqrt{\psi}} \hat{f}_T^{(\nu)}(\xi, \psi, \omega, \zeta) \omega^4 \sin^3 \zeta d\zeta d\omega, \quad (2.28)$$

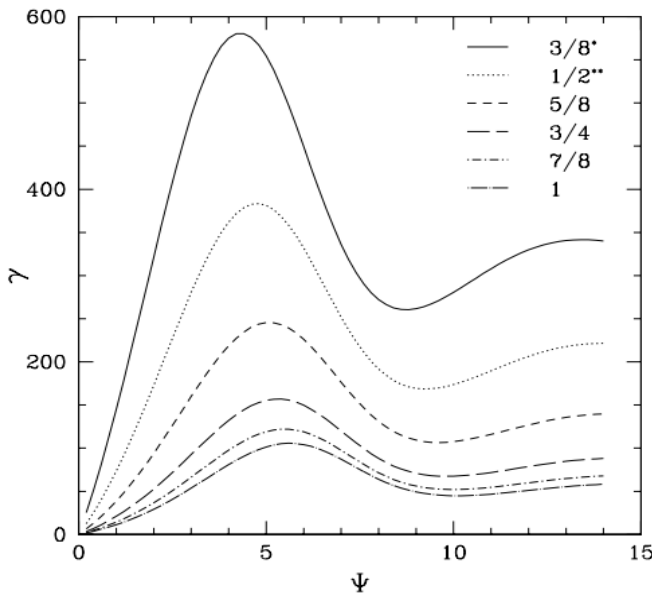


Figure 2.2: Relation $\gamma(\Psi)$ for the $f^{(\nu)}$ family of models, for selected values of ν . To fit the adopted frame, the γ values corresponding to $\nu = 3/8$ have been multiplied by a factor 1/6 and the ones corresponding to $\nu = 1/2$ by a factor 2/3. Figure from Trenti & Bertin (2005) [56].

where we have used the relations $v_r^2 = v^2 \cos^2 \zeta$ and $v_T^2 = v_\theta^2 + v_\phi^2 = v^2 \sin^2 \zeta$.

As expected, according to the picture of violent relaxation, these models are characterized by an isotropic core and a radially-biased anisotropic envelope. The radial extent of the anisotropic core can be measured by means of the anisotropy radius r_α , defined as the radius at which $\alpha(r_\alpha) = 1$, with the local anisotropy parameter α defined in Sect. 1.2.2). At fixed Ψ , models with higher γ are characterized by lower values of r_α/r_h , as shown in Fig. 2.3.

Curiously, in our study of some simulations initialized by isotropic models we will find (see Sect. 3.3.1) that the slow cumulative effect of star encounters may produce radially biased anisotropic systems, similar in phase space to the result of violent relaxation. This result has also bee discussed in several recent papers [11], [55], [63].

2.2 Two-component models

Models introduced in Sect. 2.1 are suited to describe stellar systems made of a single homogeneous stellar population. However, in the presence of significant collisionality, stars with different masses, should be characterized by different distributions, as a consequence of energy equipartition (see Sect. 1.3.3) and mass

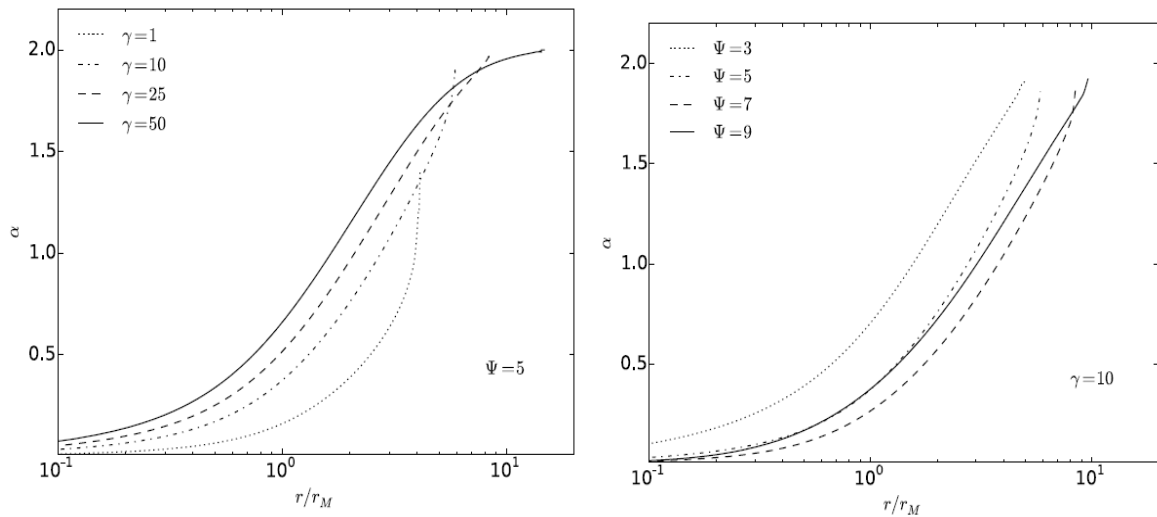


Figure 2.3: The left frame shows the anisotropy profile $\alpha(r)$ for selected values of γ at fixed Ψ . Models with higher γ are characterized by lower values of r_α/r_h (here the half-mass radius is indicated as r_M). The right frame shows the anisotropy profile for selected values of Ψ at fixed γ . Where a curve terminates, the truncation radius is reached. Figure from de Vita, Bertin, Zocchi (2016) [16].

segregation (see Sect. 1.3.4). Thus a more realistic framework for the modeling of globular cluster is often sought in terms of multi-component models, in which the distribution function is given by:

$$f = \sum_{i=1}^N f_i, \quad (2.29)$$

with f_i the distribution function for the i -th component. A second, physically separate reason to address the issue of multi-component models is given by the relatively recent finding that globular clusters host multiple stellar populations. As explained in Sect. 1.4.2, in many observed cases, the suggested interpretation is that clusters have been the site of multiple generations of stars, so that the stars can be divided into the groups of the first and the second generation, and these groups may be associated with different dynamical properties, such as concentration or degree of anisotropy.

Multi-components models have been constructed with a large number of components to allow for a better fitting to photometric profiles of globular clusters (e.g., $N = 10$ for Da Costa & Freeman (1976) [15], see Sect. 2.2.3). Sometimes an approach based on two or three components has been preferred for simpler studies of dynamical mechanisms; by means of simpler models it is possible to attain analytic conclusions on processes such as the Spitzer “instability” (Sect. 2.3). Here, much

as was done by Spitzer [48], we focus on two-component models, in which we distinguish a population of lighter stars (let m_1 be the representative mass of its individual stars and M_1 its associated total mass) from a second population of heavier stars (with $m_2 > m_1$ and, in general $M_2 < M_1$), so that the total mass of the cluster is $M = M_1 + M_2$.

2.2.1 Two-component King models

Starting from the King models described in the Sect. 2.1.3, we introduce the two distribution functions ($i = 1, 2$):

$$f_i^K(E) = \begin{cases} A_i [\exp(-a_i E) - \exp(-a_i E_t)] & \text{for } E < E_t \\ 0 & \text{for } E \geq E_t, \end{cases} \quad (2.30)$$

where A_i and a_i are positive constants and E_t is the escape energy ($E_t = \Phi(r_t)$). The truncation radius, r_t , is assumed to be the same for all the components. As for the one-component models, we rescale the problem to a dimensionless form. We do so, by referring to a length scale and to an energy scale based on the constants associated with the lighter component; we define the dimensionless potential $\psi = -a_1[\Phi(r) - E_t]$ and the dimensionless radius $\xi = r/\lambda$, with $\lambda = \sqrt{a_1^{1/2}/(4\pi G \tilde{A}_1)}$. Mass density for each component is:

$$\rho_i(r) = \frac{\tilde{A}_i}{a_i^{3/2}} \exp\left(\frac{a_i}{a_1}\psi\right) \gamma\left(\frac{5}{2}, \frac{a_i}{a_1}\psi\right) = \frac{\tilde{A}_i}{a_i^{3/2}} \hat{\rho}_i(\psi), \quad (2.31)$$

where $\tilde{A}_i = (8/3)\pi\sqrt{2}A_i \exp[-a_i\Phi(r_i)]$ and $\hat{\rho}_i(\psi) = \exp(a_i/a_1\psi)\gamma(5/2, a_i/a_1\psi)$. The velocity dispersion for each component can be written as:

$$\sigma_i^2(r) = \frac{6}{5a_i} \frac{\gamma(7/2, a_i/a_1\psi)}{\gamma(5/2, a_i/a_1\psi)}. \quad (2.32)$$

The resulting dimensionless Poisson equation is:

$$\frac{1}{\xi^2} \frac{d}{d\xi} \left(\xi^2 \frac{d\psi}{d\xi} \right) = - \left(\hat{\rho}_1(\psi) + \frac{\tilde{A}_2 a_1^{3/2}}{\tilde{A}_1 a_2^{3/2}} \hat{\rho}_2(\psi) \right), \quad (2.33)$$

to be solved under the boundary conditions $\psi(0) = \Psi$ and $(d\psi/d\xi)(0) = 0$. After the rescaling, we are left with three independent constants. To reduce the number of parameters and thus to simplify the mathematical work, we can make the following assumption:

- We consider models in which the total masses associated with the two components are in a given ratio M_1/M_2 . This can be seen as a requirement on the

ratio of normalization factors \tilde{A}_1/\tilde{A}_2 . In practice, for a globally self-consistent model this constraint can be written as

$$\frac{\tilde{A}_1 a_1^{-3/2}}{\tilde{A}_2 a_2^{-3/2}} \frac{\int_0^{\xi_t} \hat{\rho}_1(\xi) \xi^2 d\xi}{\int_0^{\xi_t} \hat{\rho}_2(\xi) \xi^2 d\xi} = \frac{M_1}{M_2}. \quad (2.34)$$

For a desired mass ratio, the equation is basically a relation between the constant $\tilde{A}_2 a_2^{-3/2}$ in terms of $\tilde{A}_1 a_1^{-3/2}$ but, due to the dependence on $\hat{\rho}_i$ in Eq. (2.34), solutions have to be worked out iteratively.

- We choose a given value for the single-mass ratio m_1/m_2 and impose partial energy equipartition in the central regions of the system by means of a dimensionless parameter η , following Trenti & van der Marel (2013) [58] (see Sect. 1.3.3). Partial central equipartition is imposed by means of the relation:

$$\frac{\sigma_1(0)}{\sigma_2(0)} = \left[\frac{a_2 \gamma(7/2, \Psi) \gamma(5/2, a_i/a_1 \Psi)}{a_1 \gamma(5/2, \Psi) \gamma(7/2, a_i/a_1 \Psi)} \right]^{1/2} = \left(\frac{m_1}{m_2} \right)^{-\eta}. \quad (2.35)$$

Full energy equipartition would correspond to $\eta = 1/2$. In the case of the simulated systems introduced in Sect. 3.1, η will be chosen according to the value of the velocity dispersion profile in their central regions.

In summary, two-component King models depend on five constants. With our assumptions, we reduced the number of free constants to three. Two of them are used to rescale the Poisson equation to a dimensionless form, the remaining one define an independent dimensionless parameter, $\Psi = -a_1(\Phi(0) - E_t)$, as in the one-component case.

2.2.2 Two-component $f_T^{(\nu)}$ models

Two-component $f_T^{(\nu)}$ models can be introduced in a similar way. We consider the distribution function [16]:

$$f_{T,i}^{(\nu)}(E, J) = \begin{cases} A_i \exp \left[-a_i(E - E_t) - d_i \frac{J}{|E - E_t|^{3/4}} \right] & \text{for } E < E_t \\ 0 & \text{for } E \geq E_t \end{cases}, \quad (2.36)$$

where A_i , a_i and d_i are positive constants for the i -th component. Also in this case we have assumed a common truncation energy, E_t . To rescale the problem to a dimensionless form, we refer to energy and length scales associated to the lighter component. The dimensionless radius is defined as $\xi = r a_1^{1/4} d_1$ and the dimensionless potential $\psi = -a_1(\Phi - E_t)$. The mass density of each component is given by:

$$\rho_i(\xi, \psi) = \frac{A_i}{a_i^{3/2}} \int_0^\pi \int_0^{\sqrt{a_i/a_1 \psi}} \hat{f}_{T,i}^{(\nu)}(\xi, \psi, \omega, \zeta) \omega^2 \sin \zeta d\zeta d\omega = \frac{A_i}{a_i^{3/2}} \hat{\rho}_i(\xi, \psi), \quad (2.37)$$

where

$$\hat{f}_{T,i}^{(\nu)}(\xi, \psi, \omega, \zeta) = 4\sqrt{2}\pi \exp \left[-\omega^2 + \frac{a_i}{a_1}\psi - \frac{d_i a_i^{1/4}}{d_1 a_1^{1/4}} \frac{\sqrt{2}\xi\omega \sin \zeta}{|\omega^2 - a_i/a_1\psi|^{3/4}} \right]. \quad (2.38)$$

The radial and tangential velocity dispersions for each component are:

$$\sigma_{r,i}^2(\xi, \psi) = \frac{2}{a_i} \frac{1}{\hat{\rho}_i} \int_0^\pi \int_0^{a_i/a_1\sqrt{\psi}} \hat{f}_{T,i}^{(\nu)}(\xi, \psi, \omega, \zeta) \omega^4 \cos^2 \zeta \sin \zeta d\zeta d\omega, \quad (2.39)$$

$$\sigma_{T,i}^2(\xi, \psi) = \frac{2}{a_i} \frac{1}{\hat{\rho}_i} \int_0^\pi \int_0^{\sqrt{a_i/a_1\psi}} \hat{f}_{T,i}^{(\nu)}(\xi, \psi, \omega, \zeta) \omega^4 \sin^3 \zeta d\zeta d\omega. \quad (2.40)$$

The resulting dimensionless form of the Poisson equation (Eq. (1.10)) is given by:

$$\frac{1}{\xi^2} \frac{d}{d\xi} \left(\xi^2 \frac{d\psi}{d\xi} \right) = -\frac{1}{\gamma} \left(\hat{\rho}_1 + \frac{A_2}{A_1} \frac{a_1^{3/2}}{a_2^{3/2}} \hat{\rho}_2 \right), \quad (2.41)$$

where $\gamma = a_1 d_1^2 / (4\pi G A_1)$. To reduce the number of parameters, we can make the following assumptions:

- We consider models with fixed total mass ratio M_1/M_2 :

$$\frac{A_1 a_2^{3/2}}{A_2 a_1^{3/2}} \frac{\int_0^{\xi_t} \hat{\rho}_1(\xi) \xi^2 d\xi}{\int_0^{\xi_t} \hat{\rho}_2(\xi) \xi^2 d\xi} = \frac{M_1}{M_2}. \quad (2.42)$$

The procedure requires iteration.

- We chose a given value for the single-mass ratio m_1/m_2 and impose partial energy equipartition in the central regions of the system by means of a dimensionless parameter η , like in Sect. 2.2.1. In this case, partial central equipartition is imposed by means of the relation:

$$\frac{\sigma_1(0)}{\sigma_2(0)} = \left[\frac{a_2}{a_1} \frac{\gamma(5/2, \Psi)\gamma(3/2, a_2/a_1\Psi)}{\gamma(3/2, \Psi)\gamma(5/2, a_2/a_1\Psi)} \right]^{1/2} = \left(\frac{m_1}{m_2} \right)^{-\eta}. \quad (2.43)$$

Note that at $r = 0$ the distribution function of the i-th component is simple, because the dependence on J drops out and $\Phi = \Phi(0)$, so that Eq. 2.43 is expressed in closed form only in terms of the relevant constants and of the concentration parameter $\Psi = -a_1(\Phi(0) - E_t)$.

- Following De Vita, Bertin & Zocchi (2016) [16], we assume that the radial scales which define the size of the radially biased anisotropic outer envelope are the same for the two components, that is:

$$d_2 a_2^{1/4} = d_1 a_1^{1/4}. \quad (2.44)$$

This qualitative argument was meant to recognize that one of the possible causes of radially-biased pressure anisotropy is incomplete violent relaxation, which is a collisionless relaxation process that acts in the same way on stars of different masses. In the simulations that we are going to consider (see Sect. 3.1), the initial velocity distribution is isotropic (it is drawn from a Plummer model, see Sect. 2.1.1) and anisotropy slowly develops in the course of time because of collisionality by means of the process described in Sect. 1.4.1. Here we keep this assumption in order to simplify our calculations.

The self-consistent problem for two-component $f_T^{(\nu)}$ models depends on seven constants. Two of them are used to rescale the Poisson equation to a dimensionless form, and three are fixed by our assumptions. The remaining two define two independent dimensionless parameters. As in the one-component models, we use as independent structural parameters $\Psi = -a_1(\Phi(0) - E_t)$ and $\gamma = a_1 d_1^2 / (4\pi G A_1)$.

2.2.3 Mass segregation and energy equipartition in two-component models

Concentration parameters

For the two-component King models introduced in Sect. 2.2.1 the ratio between central densities is given by

$$\frac{\rho_1(0)}{\rho_2(0)} = \frac{A_1 a_2^{3/2}}{A_2 a_1^{3/2}} \frac{e^\Psi \gamma(5/2, \Psi)}{e^{a_2/a_1 \Psi} \gamma(5/2, a_2/a_1 \Psi)}, \quad (2.45)$$

whereas for the two-component $f_T^{(\nu)}$ models (Sect. 2.2.2) it corresponds to:

$$\frac{\rho_1(0)}{\rho_2(0)} = \frac{A_1 a_2^{3/2}}{A_2 a_1^{3/2}} \frac{e^\Psi \gamma(3/2, \Psi)}{e^{a_2/a_1 \Psi} \gamma(3/2, a_2/a_1 \Psi)}. \quad (2.46)$$

Under the conditions listed in the previous sections, these quantities are expected to fall below unity from a simple picture of mass segregation, in which the central parts should be dominated by the heavier components. There are several ways of defining the concentration of a given density profile. De Vita, Bertin, Zocchi (2016) [16] considered two possible definitions; the ratio r_{h1}/r_{h2} of the half-mass radii of the two components and the ratio of the density contrasts of the lighter component $\rho_1(0)/\rho_1(r_{h1})$ to that of the heavier component $\rho_2(0)/\rho_2(r_{h2})$. They plotted these quantities for different values of Ψ and γ (Fig. 2.4) and noticed that only r_{h1}/r_{h2} exceeds unity for all the models considered. Thus they argue that r_{h1}/r_{h2} is the more natural parameter to be used to describe the relative concentration of the two

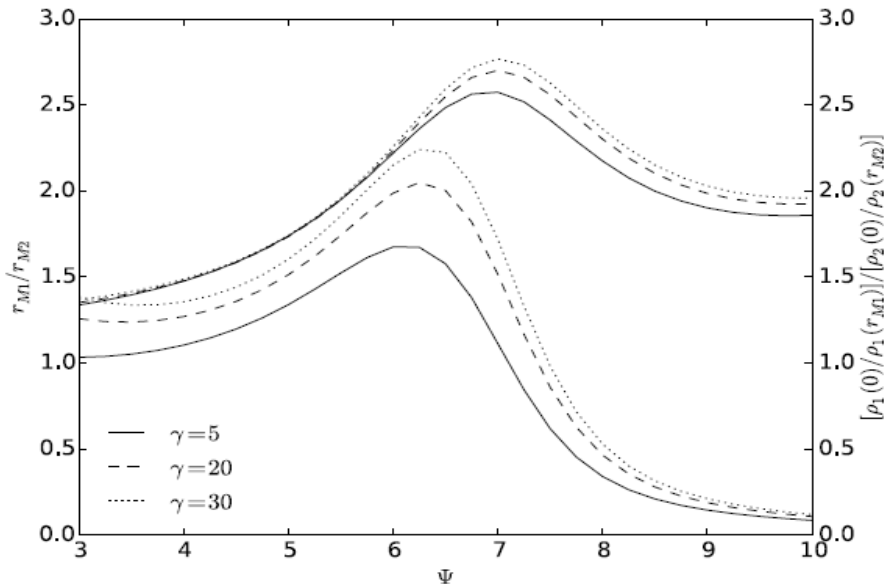


Figure 2.4: Relative concentrations of the two components of $f_T^{(\nu)}$ models as a function of Ψ , for selected values of γ . The upper set of curves represents the ratio r_{h1}/r_{h2} of the half-mass radius of the lighter component to the half-mass radius of the heavier component. The lower set represents the ratio of the density contrast parameters $[\rho_1(0)/\rho_1(r_{h1})]/[\rho_2(0)/\rho_2(r_{h2})]$. Figure from De Vita, Bertin, Zocchi (2016) [16].

components. I repeated the same procedure for the two-component King models, evaluating the two different concentration estimates for different values of Ψ . The result is illustrated in Fig. 2.5. Also in this case, r_{h1}/r_{h2} exceeds unity for all the models considered whereas the density contrast $[\rho_1(0)/\rho_1(r_{h1})]/[\rho_2(0)/\rho_2(r_{h2})]$ falls below unity at sufficiently high values of Ψ , confirming the statement that the former quantity is a more natural parameter to describe the relative concentration of the two components in these models.

Isothermal approximation

Multi-component models represent a simple tool to take into account energy equipartition. Traditionally, application of multi-component models has been constructed as an extension of King models. In such models global equipartition (Eq. (1.29)) cannot hold because the relevant distribution function is not a Maxwellian. As noted earlier, in Sect. 1.3.3, a global equipartition would be unrealistic for globular clusters because in their outer regions the relaxation time is too long. However, a certain degree of equipartition is naturally expected to occur where the relaxation

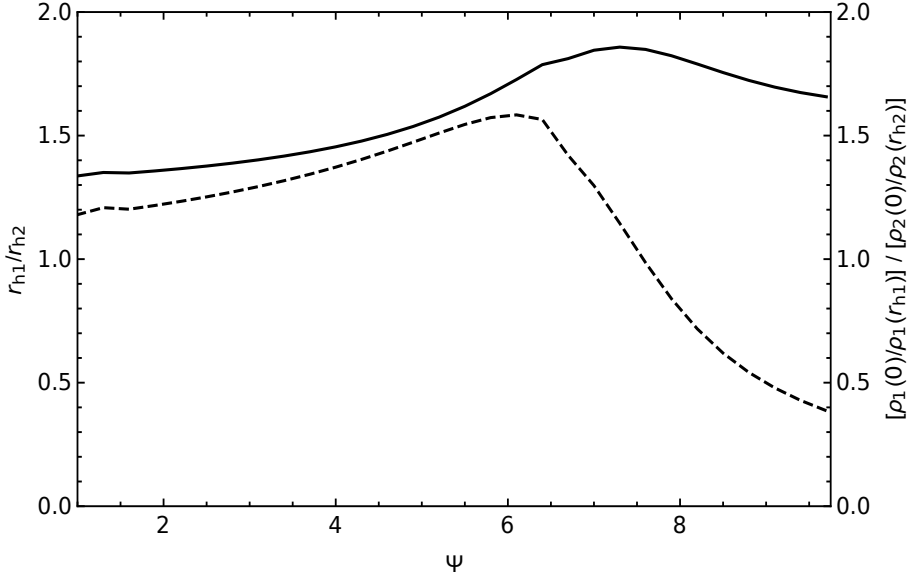


Figure 2.5: Relative concentrations of the two components of King models as a function of Ψ . The solid line represents the ratio r_{h1}/r_{h2} of the half-mass radius of the lighter component to the half-mass radius of the heavier component. The dashed line represents the ratio of the density contrast parameters $[\rho_1(0)/\rho_1 r_{h1}]/[\rho_2(0)/\rho_2 r_{h2}]$.

time is shortest. Partial central energy equipartition can be correctly implemented by means of Eq. (2.35) (or Eq. (2.43), if we consider $f_T^{(\nu)}$ models) with a suitable choice of η .

Some authors (e.g. Da Costa & Freeman (1976) [15]; Gunn & Griffin (1979) [26]) tried to impose full energy equipartition setting:

$$a_i/a_j = m_i/m_j. \quad (2.47)$$

Such assumption is often referred to as *isothermal approximation* (or *IA*) [41]. This notation and the related choice reflect the fact that $a/m = 1/(k_B T)$ in a Maxwell-Boltzmann distribution function (Eq. (2.7)).

One of the first examples of application of the *isothermal approximation* was given by Da Costa & Freeman (1976) [15]. Because a single-mass King model could not give a satisfactory description of the brightness profile of globular cluster M3, the authors referred to a multi-component approach based on ten components. Each component was meant to represent a class of stars the luminosity of which was inferred from the luminosity function of the cluster. A representative mass value was assigned to each class of stars to obtain an appropriate M/L ratio. In order to limit the number of free parameters, Da Costa & Freeman decided to impose Eq. (2.47). For M3, the core relaxation time (Eq. (1.19)) is about $t_{rc} \approx 1.0 \times 10^8 \text{ yr}$, and

$t_{rh} \approx 1.0 \times 10^{10}$ yr [27]. A model for the cluster was constructed by varying the A_i parameters and the central potential. Density profiles obtained were then projected along the line-of-sight and, by means of the M/L ratio of each class, a brightness profile for every component was constructed and compared to the data. The best-fit model is illustrated in Fig. 2.6; we notice a much better agreement with data with respect to the one-component best-fit model. No kinematic test was made on the system.

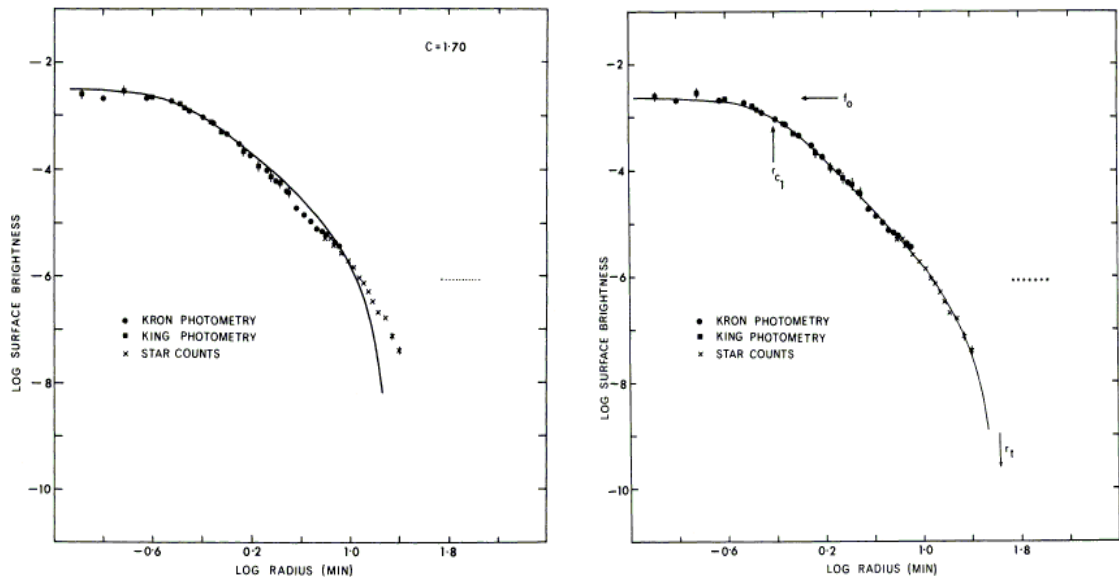


Figure 2.6: Comparison between best-fit models of the photometric profile of M3. In the left panel the best-fit result one-component model is illustrated. The right panel shows performance of the best-fit result with ten components. A better agreement of the multi-component model with data is evident. Units for surface brightness is the number of stars with magnitude 10.00 in the V-band per arcsec². Figure from Da Costa & Freeman (1976) [15].

As pointed out by various authors (e.g. Merritt (1981) [39]; Kondrat'ev & Ozerov (1982) [35]; Miocchi (2006) [41]), strictly speaking, the choice of a_i parameters made by Da Costa & Freeman does not actually imply central equipartition between stars of different mass in King models. To show this, I considered the two-component King models introduced in Sect. 2.2.1 and, instead of imposing central energy equipartition by means of Eq. (2.35), I considered $a_2/a_1 = m_2/m_1 = 2$. I solved the self-consistent problem (Eq. (2.33)) with different values of Ψ between $1 < \Psi < 6$. The ratio of velocity dispersions at the center of the system can be

evaluated directly from Eq.(2.32):

$$\frac{\sigma_1^2(0)}{\sigma_2^2(0)} = \frac{a_2}{a_1} \frac{\gamma(7/2, \Psi)\gamma(5/2, a_2/a_1\Psi)}{\gamma(5/2, \Psi)\gamma(7/2, a_2/a_1\Psi)}. \quad (2.48)$$

I also computed global velocity dispersion (defined in Eq. 1.28) inside the half-mass radius r_h and inside r_t . In case of full equipartition, as supposed by Da Costa & Freeman, the ratio of velocity dispersions would be expected to be equal to m_2/m_1 , at least at the center of the model. Results of my calculation are presented in Fig. 2.7. Setting $a_2/a_1 = m_2/m_1$ does not imply energy equipartition for multi-

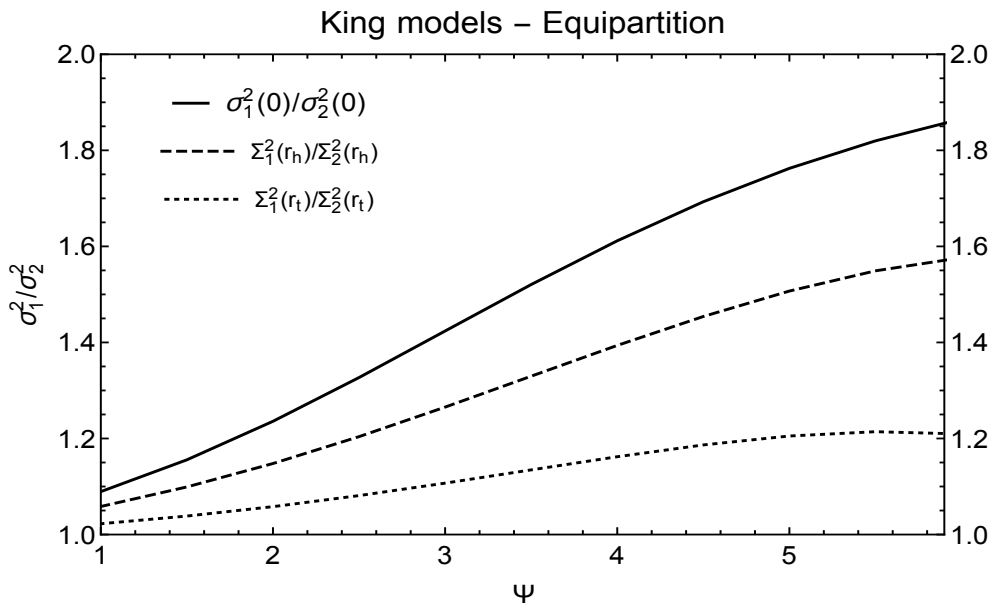


Figure 2.7: Ratio between velocity dispersions in two-component King models for the case $m_2 = 2m_1$. The solid line represents the local velocity dispersion ratio at the center of the system. The dashed line represents the global velocity dispersion ratio at the half-mass radius. The dotted line represents global velocity dispersion ratio at r_t . We can notice that strict equipartition can't be attained either locally or globally inside the system. A condition of energy equipartition would be recovered locally at the center of the system for very large values of Ψ .

component King models, either in local sense, at the center, or in the global sense; the so-called *isothermal approximation* would imply energy equipartition in case of Maxwell-Boltzmann distributions, but it does not so for King models. Deviation from equipartition is due to the presence of a truncation term in the King distribution function. The central ratio of velocity dispersions in Fig 2.7 tends to approach a condition of energy equipartition for large values of Ψ . In fact, if we consider King models with $\Psi \gg 1$ the presence of the truncation term has a negligible role at

the center where isothermality is recovered. In the limit for $\Psi \rightarrow \infty$, Eq. (2.48) becomes:

$$\lim_{\Psi \rightarrow \infty} \frac{\sigma_1^2(0)}{\sigma_2^2(0)} = \lim_{\Psi \rightarrow \infty} \frac{a_2}{a_1} \frac{\gamma(7/2, \Psi)\gamma(5/2, a_2/a_1\Psi)}{\gamma(5/2, \Psi)\gamma(7/2, a_2/a_1\Psi)} = \frac{a_2}{a_1} \frac{\Gamma(7/2)}{\Gamma(5/2)} \frac{\Gamma(5/2)}{\Gamma(7/2)} = \frac{a_2}{a_1}, \quad (2.49)$$

which follows directly from the definition of incomplete gamma function ($\lim_{x \rightarrow \infty} \gamma(s, x) = \Gamma(s)$). In this case $a_i/a_j = m_i/m_j$ implies $\sigma_1^2(0) = \sigma_2^2(0)$ (so that the so-called *isothermal approximation* implies energy equipartition at the center of the system). As to global equipartition, deviation from equipartition is evident both inside r_h and r_t , also for large Ψ .

2.2.4 Hydrostatic and Virial Equilibrium

A general property of self-gravitating systems without bulk motions ($\mathbf{u} = 0$) is hydrostatic equilibrium. This condition consists of a balance between the pressure gradient and the mean gravitational field. Hydrostatic equilibrium can be derived directly by integrating Eq. (1.3) in velocity space, that is by considering one of the moment equations of the collisionless Boltzmann equation. We focus on hydrostatic equilibrium in spherical systems. In spherical coordinates, if we multiply by v_r Eq. (1.3) and integrate over velocity space we obtain:

$$\begin{aligned} & \rho \frac{\partial u_r}{\partial t} + \frac{\partial}{\partial r} (\rho \langle v_r v_r \rangle) + \frac{1}{r} \frac{\partial}{\partial \theta} (\rho \langle v_\theta v_r \rangle) + \frac{1}{r \sin \theta} \frac{\partial}{\partial \phi} (\rho \langle v_\phi v_r \rangle) + \\ & - \frac{1}{r} (\langle v_\theta^2 \rangle + \langle v_\phi^2 \rangle) + \rho \frac{\partial \Phi}{\partial r} + 2 \frac{\rho}{r} \langle v_r v_r \rangle + \rho \cot \theta \frac{\langle v_\theta v_r \rangle}{r} = 0, \end{aligned} \quad (2.50)$$

where $\langle v_i v_j \rangle = \sigma_{ij}^2 + u_i u_j$ are the second moments of velocity. If we consider stationarity ($\partial/\partial t = 0$) and spherical symmetry ($\partial/\partial \theta = \partial/\partial \phi = 0$), $u_\theta = u_\phi = 0$ and $\cot \theta = 0$ (no angular dependence), Eq. (2.50) becomes:

$$\frac{\partial}{\partial r} (\rho \langle v_r v_r \rangle) - \frac{\rho}{r} (\langle v_\theta^2 \rangle + \langle v_\phi^2 \rangle) + \rho \frac{\partial \Phi}{\partial r} + 2 \frac{\rho}{r} \langle v_r v_r \rangle = 0. \quad (2.51)$$

Hydrostatic equilibrium is recovered under the assumption of no bulk motions (so that $u_r = 0$). In this case, Eq. (2.51) gives:

$$\frac{d}{dr} [\rho(r) \sigma_r^2(r)] + \rho(r) \alpha(r) \frac{\sigma_r^2(r)}{r} = -\rho(r) \frac{d\Phi(r)}{dr} = -\frac{GM(r)}{r^2} \rho(r), \quad (2.52)$$

where α is the local anisotropy parameter, defined in Eq. (1.16). This is an equilibrium condition obtained directly from the collisionless Boltzmann equation (Eq. (1.3)). All models introduced in Sect. 2.1 and in Sect. 2.2 are based on the *Jeans theorem* (i.e. they are solutions of collisionless Boltzmann equation), thus they must

be in hydrostatic equilibrium. In particular, we prove this condition analytically for King models. As these models are isotropic, $\alpha = 0$ and the left-hand side of Eq. (2.52) becomes:

$$\frac{1}{\rho} \frac{d}{dr} (\rho \sigma^2) = \frac{2}{5} \frac{\tilde{A}}{a^{5/2} \lambda} \frac{d}{d\xi} \left[e^\psi \gamma \left(\frac{7}{2}, \psi \right) \right] = \frac{2}{5} \frac{\tilde{A}}{a^{5/2} \lambda} \frac{d\psi}{d\xi} \frac{d}{d\psi} \left[e^\psi \gamma \left(\frac{7}{2}, \psi \right) \right], \quad (2.53)$$

where we have used the definitions (2.17) and (2.18). The derivative of incomplete γ function is given by $(\partial/\partial x)\gamma(s, x) = x^{(s-1)}e^{-x}$ [1]:

$$\frac{1}{\rho} \frac{d}{dr} (\rho \sigma^2) = \frac{2}{5} \frac{\tilde{A}}{a^{5/2} \lambda} e^\psi \frac{d\psi}{d\xi} \left[\gamma \left(\frac{7}{2}, \psi \right) + \psi^{5/2} e^\psi \right] = \frac{\tilde{A}}{a^{5/2} \lambda} e^\psi \gamma \left(\frac{5}{2}, \psi \right) \frac{d\psi}{d\xi}, \quad (2.54)$$

where in the last step we have used the relation $\gamma(s+1, x) = s\gamma(s, x) - x^s e^{-x}$ [1]. The right-hand-side of Eq. (2.52) can be written as

$$-\rho \frac{d\Phi}{dr} = \frac{\tilde{A}}{a^{5/2} \lambda} \hat{\rho} \frac{d\psi}{d\xi} = \frac{\tilde{A}}{a^{5/2} \lambda} e^\psi \gamma \left(\frac{5}{2}, \psi \right) \frac{d\psi}{d\xi}, \quad (2.55)$$

which is exactly the result obtained in Eq. (2.54). We conclude that the King models satisfy hydrostatic equilibrium as expected. In the case of multi-component models, Eq. (2.52) is satisfied by each component, that is by each f_i .

Kondrat'ev & Ozernoy (1982) [35] claimed that the *isothermal appproximation*, as formulated by Da Costa & Freeman (1976) [15], was inconsistent with the assumption of isothermal equilibrium. They proposed an alternative distribution function characterized by a parameter β , equal for all components, which, in their opinion, would enforce hydrostatic equilibrium:

$$f_i(E) = \begin{cases} A_i \left(\exp \left(-\frac{m_i}{\beta_h} E \right) - \exp \left(-\frac{m_i}{\beta_h} E_t \right) \right) & \text{for } E < E_t \\ 0 & \text{for } E \geq E_t. \end{cases} \quad (2.56)$$

Note that β_h has the dimensions of energy. As shown above in this section, multi-component King models satisfy hydrostatic equilibrium, independently of the *isothermal approximation*. In fact, Konrat'ev & Ozernoy result was made on incorrect normalization in the definition of velocity dispersions. Moreover, constant β_h in the distribution function (Eq. (2.56)) plays exactly the same role as *isothermal approximation* Eq. (2.47): $\beta_h = m_i/a_i$. The assumption expressed by Eq. (2.47) is exactly the same as requiring a constant β_h .

Virial Theorem

Virial equations can be obtained by taking moments of the fluid equations with respect to the spatial coordinates and by integrating over the volume occupied by

the system under investigation. Here we report the second order virial equations, obtained by integrating over dV the j -th of the fluid equations multiplied by x_i . The time-dependent equations can be written as [7]:

$$\frac{1}{2} \frac{d^2 I_{ij}}{dt^2} = 2T_{ij} + W_{ij} + \Pi_{ij}, \quad (2.57)$$

where the inertia tensor I_{ij} , the kinetic-energy tensor K_{ij} and the gravitational-energy tensor W_{ij} are given by

$$I_{ij} = \int \rho x_i x_j dV, \quad (2.58)$$

$$T_{ij} = \frac{1}{2} \int \rho u_i u_j dV \quad (2.59)$$

$$W_{ij} = \int \rho x_i \frac{\partial}{\partial x_j} \left(G \int \frac{\rho(\mathbf{x}')}{|\mathbf{x} - \mathbf{x}'|} dV' \right) dV, \quad (2.60)$$

and the pressure contribution is given by

$$\Pi_{ij} = \int p_{ij} dV. \quad (2.61)$$

We obtain the standard scalar virial constraint $W + 2K = 0$ (Eq.(1.25)), with $K = T + \Pi/2$, for a stationary system by taking the trace of the preceding tensor relations in the time-independent case. The total kinetic energy includes a part associated with the kinetic energy of random motions (i.e. the pressure term) and a part associated with the kinetic energy of fluid motions. The virial condition (Eq. (1.25)) states, at equilibrium, how energy is present in various forms. A cold system is one for which the balance is primarily between W and the kinetic energy of fluid motions T , whereas a hot system is one for which the balance is mostly between W and the internal kinetic energy in the form of random motions.

We now define a virial coefficient as

$$\kappa = \frac{2K}{|W|}, \quad (2.62)$$

which, for a system in virial equilibrium, should equal unity. For the models introduced in Sect. 2.1 and Sect. 2.2, the virial equilibrium condition can be used to test the accuracy of the numerical code used in the construction of the models. For our spherical models, the virial condition is given by

$$\kappa = \frac{\int_0^{r_t} \rho(r) \sigma^2(r) r^2 dr}{G \int_0^{r_t} M(r) \rho(r) r dr} = 1, \quad (2.63)$$

for one-component models, and

$$\kappa = \frac{\int_0^{r_t} [\rho_1(r) \sigma_1^2(r) + \rho_2(r) \sigma_2^2(r)] r^2 dr}{G \int_0^{r_t} [M_1(r) + M_2(r)][\rho_1(r) + \rho_2(r)] r dr} = 1, \quad (2.64)$$

in the case of two-component models. For accurate codes, deviations from unity of the order of $10^{-5} - 10^{-7}$ are expected.

Hydrostatic and virial equilibrium conditions can be used as tests in the field of numerical simulations. In Sect. 3.1.1 we will use them to prove the quality of the Monte Carlo simulations under consideration.

2.3 The Spitzer “instability”

We consider the problem of thermodynamical equilibrium in a cluster in which more massive stars become more concentrated in the inner regions as a result of tendency toward energy equipartition. We examine, under some simplifying assumptions, which conditions have to be satisfied for attain thermal equilibrium, characterized by global energy equipartition to be established. The hypotheses and results here reported have been discussed by Spitzer (1969) [48] and reworked by Cova (2014) [14].

To simplify the discussion, stars of only two masses, m_1 and m_2 (as usual index 1 refers to the lighter population) are considered. The total masses of the two populations of stars are M_1 and M_2 . The virial equilibrium for a two-component system implies:

$$2K_1 + W_1 + W_{21} = 0, \quad (2.65)$$

$$2K_2 + W_2 + W_{12} = 0. \quad (2.66)$$

The meaning of the terms introduces above (in Eq. (2.65) and Eq. (2.66)) is the following:

- K_1, K_2 are the kinetic energies of the individual components (1 and 2, respectively).
- W_1, W_2 are the gravitational energies of the individual components (1 and 2, respectively).
- W_{12}, W_{21} are exchange energies; they represent the gravitational energies associated with the interaction of component 1 on component 2 and vice-versa.

Virial equations (Eq. (2.65) and Eq. (2.66)) can be simplified by making some assumptions. We consider the case in which the total mass of the light component is much larger than that of the heavy component, $M_1 \gg M_2$. In addition, we consider the case in which $m_2 \gg m_1$; as a consequence we expect that, because of mass segregation, the density of heavy stars at the center of the system, $\rho_2(0)$, should be

much larger than density of light stars, $\rho_1(0)$. This assumption, as we will see later (in Sect. 2.3.1), has been criticized by Merritt (1981) [39].

It is now possible to estimate the exchange terms: as $M_2 \ll M_1$, the interaction term of the heavy component on the light one will be negligible, that is $W_{21} \approx 0$. Thus Eq. (2.65) becomes $2K_1 = -W_1$. Under spherical symmetry, it can be written:

$$M_1 \Sigma_1^2 = 4\pi \int_0^\infty \rho_1 r^3 \frac{d\Phi_1}{dr} dr \approx \frac{GM_1^2}{r_{h1}}. \quad (2.67)$$

where r_{h1} is the half-mass radius of the light component, where Σ_1^2 is the global square velocity dispersion of the light component (defined in Eq. (1.28)).

In order to estimate the term W_{12} , we can assume that the density of light stars is constant in the very small region where most of heavier stars are located, that is $\rho_1(r) \approx \rho_1(0) \equiv \rho_{01}$. The gravitational potential Φ_1 associated with a constant density ρ_{01} is given by $\Phi_1 = (2\pi/3)G\rho_{01}r^2$. We can now calculate W_{12} :

$$W_{12} = -4\pi \int_0^\infty \rho_2 r^3 \frac{d\Phi_1}{dr} dr = -4\pi \int_0^\infty \rho_2 r^3 \left[\frac{4\pi}{3} G \rho_{01} r \right] dr. \quad (2.68)$$

If we note that

$$M_2 = \int_0^\infty 4\pi \rho_2 r^2 dr, \quad (2.69)$$

the exchange term can be rewritten as:

$$W_{12} = -\frac{4\pi}{3} M_2 G \rho_{01} \langle r_2^2 \rangle, \quad (2.70)$$

where we have indicated with $\langle r_2^2 \rangle$ the mean value of r^2 for stars of mass m_2 . We now write the virial equation for the heavy component as:

$$\Sigma_2^2 = \frac{GM_2}{r_{h2}} + \frac{4\pi}{3} G \rho_{01} \langle r_2^2 \rangle, \quad (2.71)$$

where Σ_2^2 is the square velocity dispersion of the second component, defined in Eq. (1.28).

In order to find a criterion for the establishment thermodynamical equilibrium, we assume a condition of energy equipartition by means of the relation:

$$m_1 \Sigma_1^2 = m_2 \Sigma_2^2. \quad (2.72)$$

This is a condition of global energy equipartition (like Eq. (1.29)), as it involves global estimates of velocity dispersion. This condition, as already anticipated in Sect. 2.2.3, cannot be considered realistic for globular clusters for a number of reasons. We may expect that an equipartition condition can be realized only in the innermost regions where a distribution close to Maxwell-Boltzmann distribution

is likely to be established (as in the case of concentrated King models). Spitzer discussion [48] would remain unchanged by confining its relevance to the innermost regions, as suggested by Merritt (1981) [39]. However, as shown by means of many numerical simulations [58] [12], even in the innermost regions a condition of only partial energy equipartition can be attained (see Sect. 1.3.3), thus making Spitzer assumption not realistic for globular clusters. If we substitute in Eq. (2.72) relations obtained for Σ_1^2 (Eq. (2.67)) and Σ_2^2 (Eq. (2.71)):

$$\frac{m_1 M_1}{r_{h1}} = m_2 \left(\frac{M_2}{r_{h2}} + \frac{4\pi}{3} \rho_{01} \langle r_2^2 \rangle \right); \quad (2.73)$$

If ρ_{h1} represents the mean density of the stars of mass m_1 within the sphere of radius r_{h1} , we can write $(1/2)M_1 = (4\pi/3)\rho_{h1}r_{h1}^3$ so that:

$$m_1 \frac{M_1}{r_{h1}} = m_2 \left(\frac{M_2}{r_{h2}} + \frac{1}{2} M_1 \frac{\rho_{01}}{\rho_{h1}} \frac{\langle r_2^2 \rangle}{r_{h1}^3} \right). \quad (2.74)$$

We then introduce a dimensionless parameter α , similar to that introduced by Spitzer²

$$\alpha = \frac{1}{2} \frac{\rho_{01}}{\rho_{h1}} \frac{\langle r_2^2 \rangle}{r_{h1}^2}, \quad (2.75)$$

and write Eq. (2.74) in the form:

$$m_1 \frac{M_1}{r_{h1}} = m_2 \left(\frac{M_2}{r_{h2}} + M_1 \alpha \frac{r_{h2}^2}{r_{h1}^3} \right). \quad (2.76)$$

From the definition of the half-mass radius, we have $(r_{h2}/r_{h1})^3 = (M_2/M_1)(\rho_{h1}/\rho_{h2})$ and obtain:

$$\frac{M_2}{M_1} \left(\frac{m_2}{m_1} \right)^{3/2} = \frac{(\rho_{h1}/\rho_{h2})^{1/2}}{(1 + \alpha \rho_{h1}/\rho_{h2})^{3/2}} \equiv S. \quad (2.77)$$

Equation (2.77) derives from the assumptions of virial and thermodynamical equilibrium, without considering any dynamical model explicitly.

By varying ρ_{h1}/ρ_{h2} and keeping α constant, S assumes a maximum value $S_{max} = 0.24\alpha^{-1/2}$. By considering a Maxwellian distribution with a parabolic potential resulting from the assumption of constant ρ_{01} , we find $\langle r_{h2} \rangle/r_{h2} = 1.13$. The ratio ρ_{01}/ρ_{h1} entering in the definition of α is instead more variable, and increases from 2.5 to 4.4 for polytropes with index n between 3 and 5; in his discussion Spitzer [48] chooses $\rho_{01}/\rho_{h1} = 3.5$. These values lead to $\alpha \approx 2.2$ and $S_{max} \approx 0.16$. Equation (2.77) thus expresses a necessary equilibrium condition for systems in global equipartition of energy:

$$\frac{M_2}{M_1} \left(\frac{m_2}{m_1} \right)^{3/2} = S < S_{max} = 0.16. \quad (2.78)$$

²Spitzer uses a numerical factor 5/4 instead of 1/2: 5/4 is suggested by numerical studies on globular clusters, performed by Spitzer on the basis of observed data [49].

The criterion expressed in Eq. 2.78 is often called Spitzer instability, even if it expresses an equilibrium condition and not a stability condition.

We stress that this result is valid when m_2 is much greater than m_1 , so that we can assume that heavy population is so concentrated at the center that the approximation $\rho_1(r) \approx \rho_1(0)$ is applicable. In addition, we have considered the case $M_1 \gg M_2$ in which the effect of the gravitational potential of the heavy stars on most of the light stars can be considered negligible ($W_{21} \approx 0$). We notice that this derivation is based on heuristic considerations which ignore self-consistency. As we will see in Sect. 2.3.1, when self-consistency is considered, this criterion is no longer applicable.

We can now wonder what happens if condition expressed in Eq. (2.78) is not fulfilled. In this case Spitzer argues that heavy stars should continue to lose energy to the light ones and, if the total mass of the heavy component is sufficiently high, he imagines a situation in which the nucleus of the cluster goes on contracting because of a failed redistribution of kinetic energy. Falling in towards the center, heavy stars will tend to acquire kinetic energy, increasing the departure from equipartition condition and determining a successive collapse of the nucleus [49]. It is important to notice that this collapse is different from a gravothermal collapse (Sect. 1.3.2), because the latter process does not require the presence of stars with different masses.

2.3.1 A discussion of the Spitzer criterion

The Spitzer criterion suggests that virial and thermal equilibrium is impossible to be attained simultaneously by some configurations. The specification, expressed by Eq. (2.78) depends on the assumption that the dimensionless parameter α can be considered approximately constant. Spitzer focuses on a value of $\alpha \approx 2.2$ starting from polytropic models, with relatively small variations of the relevant polytropic index. As shown by Merritt (1981) [39], this assumption is not always justified. In particular, Merritt observes that the ratio ρ_{01}/ρ_{h1} could vary significantly and that the values considered by Spitzer are representative only of less concentrated clusters (see Tab. 2.1).

In order to test the validity of the Spitzer result (Eq. (2.78)), Merritt rewrote Eq. (2.76) (using equipartition condition in Eq. (2.72)) in the following way:

$$\alpha \tilde{R}^3 - \tilde{\Sigma}^2 \tilde{R}^2 + \tilde{M} = 0, \quad (2.79)$$

where he introduced the quantities $\tilde{R} = r_{h2}/r_{h1}$, $\tilde{\Sigma}^2 = \Sigma_2^2/\Sigma_1^2 = m_1/m_2$ and $\tilde{M} = M_2/M_1$. He then studied the relation in the $(\log \tilde{M}, \log \tilde{R})$ plane for the value $\alpha = 2.2$ and $\tilde{\Sigma}^2 = 0.1$. It is reasonable to suppose that there exists a minimum value for

Ψ	ρ_{01}/ρ_{h1}
1	2.39
2	2.72
3	3.14
4	3.84
5	5.91
6	9.23
7	19.1
8	78.6
9	4.39
10	1.88×10^3
12	1.46×10^4
15	1.91×10^5

Table 2.1: Variation of ρ_{01}/ρ_{h1} for one-component King models. Table from Merritt (1981) [39]

α (Eq. (2.75)), as ρ_{01}/ρ_{h1} cannot be less than unity and $\langle r_{h2} \rangle/r_{h2}$ is generally approximately constant. Equation (2.79) implies, together with the existence of a minimum value for α , the existence of a maximum for \tilde{M} , which Merritt calls \tilde{M}_0 . This fact might suggest that the initial interpretation of Spitzer could be justified by substituting α with its minimum value α_{min} . He also constructed a set of two-component self-consistent King models, for which he studied the relation between \tilde{M} and \tilde{R} by setting $\tilde{m} = m_2/m_1 = 10$. We can notice that the mass ratio is higher than values which are found in our definition of components in Sect. 3.3.2, where $\tilde{m} = 2$. In Fig. 2.8, \tilde{R} is shown as a function of \tilde{M} for fixed $\tilde{\Sigma}^2 = 0.1$, both for solutions of Eq. (2.79) (thin lines) and for two-component King models (thick lines). Solutions for two-component King models are not limited to a maximum value of \tilde{M} ; curves obtained for constant α tend to separate from that based on Eq. (2.79) and continue for higher values, where solutions tend to converge to a unique curve. Thus, the request for self-consistency, by means of the choice of King distribution functions, allows the existence of systems in thermal and virial equilibrium for every value of \tilde{M} . In Sect. 3.3.2 we will see how the application of the Spitzer criterion to realistic simulated systems actually leads to inconclusive results, because it is based on assumptions which are not realized in real systems.

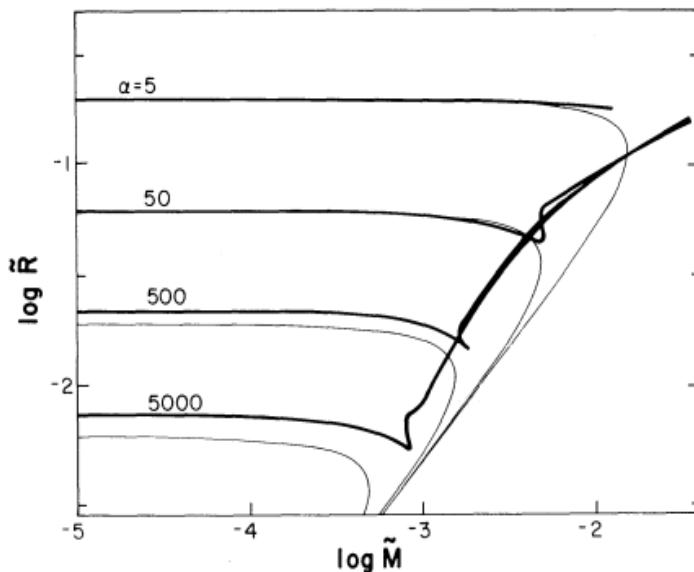


Figure 2.8: Thick lines represent equilibrium configurations for two-components King models with $\tilde{m} = m_2/m_1 = 10$. Ratio between velocity dispersion was set to $\tilde{\Sigma}^2 = 0.1 = m_1/m_2$. Thin lines represent solutions to Eq. (2.79) with $\alpha \approx 2.2$. We can see that equilibrium configurations for two-components King models are not limited do a maximum value of \tilde{M} for sufficiently high values of α , as opposed to solution of Eq. (2.79). Figure from Merritt (1981) [39].

2.4 The Vishniac criterion

Vishniac (1978) [61] attempted to generalize the analysis by Spitzer to systems containing a continuous distribution of masses, deriving a necessary but not sufficient condition for isothermal equilibrium in a globular cluster. The assumptions and results reported here are taken from Vishniac (1978) [61].

We consider a spherical symmetric system characterized by a continuous spectrum of mass. The basic assumption is that the density profile of stars with mass m is proportional to a single function $\alpha[r/R(m)]$, where $R(m)$ is the characteristic length scale factor for stars with mass m . The function $\alpha(x)$ is taken to be the same for all masses; this corresponds to the assumption that all stellar mass groups have homologous density profiles (see Sect. 2.4.1).

We consider the following assumptions: $R(m)$ is a continuous function which decreases with mass. Although Vishniac does not give an explicit definition of $R(m)$, this represents the length scale for stars with mass m and thus we realistically expect that stars with higher masses are more concentrated and characterized by a lower value of $R(m)$. We also assume that the function $\alpha(x)$ is a decreasing function of x ,

that is the density profile is a decreasing function of radius. Finally, we assume that $g(m)$, that in this case represents the mass spectrum, presents a minimum mass, which we call m_1 .

Let the mass contained in stars with masses in the range $(m, m+dm)$ be $g(m)dm$. Moreover let $\rho_m(r)dm$ be the mass density at radius r of stars with masses in the range $(m, m + dm)$. The function $\alpha[r/R(m)]$ is defined by the following relation:

$$\rho_m(r) = \frac{g(m)}{R^3(m)} \alpha[r/R(m)], \quad (2.80)$$

with $\alpha(x)$ which satisfies the normalization condition:

$$1 = 4\pi \int_0^\infty x^2 \alpha(x) dx. \quad (2.81)$$

Equation (2.81) requires that, for every interval $(m, m + dm)$, the volume integral of $P(r, m) = \rho_m(r)/g(m)$, that is the probability of finding a star with mass m at a distance between r e $r + dr$, is normalized to 1.

We may apply the virial theorem to each group of stars of mass $(m, m + dm)$ to obtain the average kinetic energy K_m of stars in this range of mass:

$$2K_m = 4\pi \int_0^\infty \frac{GM(r)m}{r} \rho_m(r) r^2 dr. \quad (2.82)$$

where $M(r)$ is the mass contained inside a sphere of radius r , which, from Eq. (2.80), can be written:

$$M(r) = \int_0^\infty g(m') dm' \int_0^{r/R(m')} 4\pi x^2 \alpha(x) dx, \quad (2.83)$$

By substituting Eq. (2.80) inside Eq. (2.82) and writing $K_m = (1/2)m\Sigma^2(m)$, where $\Sigma^2(m)$ is the velocity dispersion of all stars of mass m , we obtain:

$$m\Sigma^2(m) = \frac{4\pi Gm}{R^3(m)} \int_0^\infty M(r) \alpha[r/R(m)] r dr. \quad (2.84)$$

We may substitute Eq. (2.83) inside Eq. (2.84) and integrate by parts to obtain:

$$K_V \equiv \frac{m\Sigma^2(m)}{G} = \frac{4\pi Gm}{R(m)} \int_0^\infty g(m') \left[f(\infty) - \int_0^\infty f\left(x \frac{R(m')}{R(m)}\right) x^2 4\pi \alpha(x) dx \right] dx, \quad (2.85)$$

where

$$f(a) \equiv \int_0^a x \alpha(x) dx. \quad (2.86)$$

The assumption that the cluster is in a state of thermal equilibrium is expressed by means of the request that $K_V = m\Sigma^2(m)/G$ is not a function of m . The cluster

will be unable to reach equilibrium if $g(m)$ is such that there do not exist functions $\alpha(x)$ and $R(m)$ that satisfy reasonable constraints and for which K_V is constant. We can easily notice that, like in Spitzer derivation (Sect. 2.3), $\Sigma^2(m)$ is a velocity dispersion defined starting from the virial theorem and thus a global quantity for the system (it is calculated on all the stars of the system inside a certain, infinitesimal, range of mass). Energy equipartition condition is, in this case, a global condition, which is not realistic for globular clusters, even in the innermost regions, where only partial energy equipartition is expected.

In order to establish constraints on the function $R(m)$, we consider some inequalities generated by equation (2.85) (hereafter ' $'$ $\equiv d/dm$):

$$\left(\frac{K_V}{mR^2(m)} \right)' = -\frac{4\pi R'}{R^4(m)} \int_0^\infty g(m') \left\{ 3 \int_0^\infty \int_{xR(m')/R(m)}^\infty y\alpha(y) dy 4\pi x^2 \alpha(x) dx - \frac{R^2(m')}{R^2(m)} \int_0^\infty \alpha[xR(m')/R(m)] \alpha(x) 4\pi x^4 dx \right\} dm', \quad (2.87)$$

which can be written, integrating by parts:

$$K_V \left[\frac{1}{mR^2(m)} \right]' = -\frac{4\pi R'}{R^4(m)} \int_0^\infty g(m') \left\{ \int_0^\infty \left[3 \int_0^x 4\pi y^2 \alpha(y) dy - 4\pi x^3 \alpha(x) \right] x \alpha[xR(m')/R(m)] dx \right\} \frac{R^2(m')}{R^2(m)} dm', \quad (2.88)$$

Now:

$$3 \int_0^x y^2 4\pi \alpha(y) dy = x^3 4\pi \alpha(x) - \int_0^x y^3 4\pi \alpha'(y) dy \geq x^3 4\pi \alpha(x), \quad (2.89)$$

where we have used the assumption $\alpha(x) \leq 0$. So, because $R'(m) < 0$, we see that Eq. (2.88):

$$\left(\frac{1}{mR^2(m)} \right)' > 0. \quad (2.90)$$

As m_1 is the mass of the least massive star of the system, Eq. (2.90) implies that:

$$\frac{R(m)}{R(m_1)} < \left(\frac{m}{m_1} \right)^{3/2}. \quad (2.91)$$

From the virial theorem (Eq. (2.85)) we can find a lower bound on K_V :

$$K_V < \frac{8\pi}{3} \frac{m_1 M}{R(m_1)} f(\infty). \quad (2.92)$$

From the virial theorem (Eq. (2.85)) we can also find a lower bound on K_V :

$$K_V > \frac{4\pi m}{R(m)} M > \left[f(\infty) - \int_0^\infty f(x) x^2 4\pi \alpha(x) dx \right], \quad (2.93)$$

where $M_>$ is the mass contained in stars with mass greater than m . Using the bounds on K established in Eq. (2.92) and Eq. (2.93), we can find:

$$\tilde{R} > \beta \tilde{m} \tilde{M}, \quad (2.94)$$

with $\tilde{m} = m/m_1$, $\tilde{R} = R(m)/R(m_1)$, $\tilde{M} = M_>/M$ and:

$$\beta = \frac{3}{2} \frac{\int_0^\infty \int_x^\infty y \rho(y) dy 4\pi x^2 \rho(x) dx}{\int_0^\infty x \rho(x) dx}. \quad (2.95)$$

The constant β is a function of the assumed profile $\alpha(x)$ but does not vary greatly. For $\alpha(x)$ constant for $x \leq 1$ and zero for $x > 1$ we obtain $\beta = 0.6$. For $\alpha \propto (1-x)^N$ for $x \leq 1$ we obtain $\beta \approx 0.57$ if $N = 1$ and $\beta \rightarrow 0.47$ when $N \rightarrow \infty$. Choosing $\alpha \propto e^{(-x)}$ we get $\beta \approx 0.47$. The narrow range of values suggests that $\beta \approx 0.5$ should be an adequate approximation. Finally we can combine Eq. (2.94) and Eq. (2.91) to obtain the so-called Vishniac criterion:

$$1 > \beta \tilde{m}^{3/2} \tilde{M}, \quad (2.96)$$

which is directly analogous to Spitzer result (1969) [48] (see Sect. 2.3).

2.4.1 A discussion of the Vishniac criterion

Vishniac criterion in the two-component case

With the formalism introduced in Sect. 2.4 we can write, for a two-components system with masses m_1 and m_2 :

$$g(m) = M_1 \delta(m - m_1) + M_2 \delta(m - m_2), \quad (2.97)$$

$$\rho_m(r) = \rho_1(r) \delta(m - m_1) + \rho_2(r) \delta(m - m_2), \quad (2.98)$$

where ρ_1 and ρ_2 are mass densities of the two components. The total mass is

$$M_{tot} = \int_0^\infty g(m) dm = M_1 + M_2. \quad (2.99)$$

By integrating over m , we have the total density profile:

$$\rho(r) = \int_0^\infty \rho_m(r) dm = \frac{M_1}{R_1^3} \alpha\left(\frac{r}{R_1}\right) + \frac{M_2}{R_2^3} \alpha\left(\frac{r}{R_1} \frac{R_1}{R_2}\right) = \rho_1(r) + \rho_2(r), \quad (2.100)$$

where $\rho_1(r) = M_1/R_1^3 \alpha(r/R_1)$ and $\rho_2(r) = M_2/R_2^3 \alpha(r/R_2)$. We now derive Vishniac criterion in the discrete case with two components. The mean kinetic energies for the two components can be written, following Vishniac derivation:

$$m_1 \Sigma_1^2 = \frac{4\pi G m_1}{R_1^3} \int_0^\infty M(r) \alpha(r/R_1) r dr, \quad (2.101)$$

$$m_2 \Sigma_2^2 = \frac{4\pi G m_2}{R_2^3} \int_0^\infty M(r) \alpha(r/R_2) r dr, \quad (2.102)$$

where Σ_i^2 is the global velocity dispersion (defined in Eq. (1.28)) of the i -th component, and $M(r)$ is the total mass contained inside r . We can define:

$$K_{V,1} = \frac{m_1 \Sigma_1^2}{G} = \frac{4\pi m_1}{R_1^3} \int_0^\infty M(r) \alpha(r/R_1) r dr, \quad (2.103)$$

$$K_{V,2} = \frac{m_2 \Sigma_2^2}{G} = \frac{4\pi m_2}{R_2^3} \int_0^\infty M(r) \alpha(r/R_2) r dr. \quad (2.104)$$

Vishniac assumption of global energy equipartition becomes $K_{V,1} = K_{V,2}$. In addition, the request that $R'(m) < 0$ can now be written as $R_1 > R_2$. We now consider:

$$\begin{aligned} \frac{K_{V,1}}{m_1 R_1^2} - \frac{K_{V,2}}{m_2 R_2^2} &= \frac{4\pi}{R_1^5} \int_0^\infty r M(r) \left[\alpha(r/R_1) - \left(\frac{R_1}{R_2} \right)^5 \alpha(r/R_2) \right] dr \\ &< M_{tot} \frac{4\pi}{R_1^5} \int_0^\infty r \left[\alpha(r/R_1) - \left(\frac{R_1}{R_2} \right)^5 \alpha(r/R_2) \right] dr. \end{aligned} \quad (2.105)$$

If we calculate:

$$\int_0^\infty r \alpha(r/R_1) dr = R_1^2 \int_0^\infty x \alpha(x) dx = R_1^2 f(\infty), \quad (2.106)$$

where $f(\infty) = \int_0^\infty x \alpha(x) dx$, and

$$\int_0^\infty r \alpha(r/R_2) dr = R_2^2 \int_0^\infty x \alpha(x) dx = R_2^2 f(\infty), \quad (2.107)$$

thus Eq. (2.105) can be written:

$$\frac{K_{V,1}}{m_1 R_1^2} - \frac{K_{V,2}}{m_2 R_2^2} < M_{tot} \frac{4\pi}{R_1^3} f(\infty) \left[1 - \left(\frac{R_1}{R_2} \right)^3 \right] < 0, \quad (2.108)$$

as $R_1 > R_2$. Equation (2.108) implies, in condition of equipartition ($K_{V,1} = K_{V,2}$):

$$\frac{1}{m_1 R_1^2} - \frac{1}{m_2 R_2^2} < 0, \quad (2.109)$$

and thus

$$\frac{R_2}{R_1} < \left(\frac{m_2}{m_1} \right)^{-1/2}, \quad (2.110)$$

which is analogous to Eq. (2.91). We can now consider an upper bound to $K_{V,1}$:

$$\begin{aligned} K_{V,1} &= \frac{4\pi m_1}{R_1^3} \int_0^\infty M(r) \alpha(r/R_1) r dr < \frac{4\pi m_1}{R_1^3} M_{tot} \int_0^\infty \alpha(r/R_1) r dr \\ &< \frac{4\pi m_1}{R_1} M_{tot} f(\infty) \end{aligned} \quad (2.111)$$

On the other hand, we can find a lower bound to $K_{V,2}$:

$$\begin{aligned}
 K_{V,2} &= \frac{4\pi m_2}{R_2^3} \int_0^\infty [M_1(r) + M_2(r)] \alpha(r/R_2) r dr \\
 &> \frac{4\pi m_2}{R_2^3} \int_0^\infty M_2(r) \alpha(r/R_2) r dr = \frac{4\pi m_2}{R_2^3} \int_0^\infty \left(\int_0^r 4\pi r'^2 \rho_2(r') dr' \right) \alpha(r/R_2) r dr \\
 &= \frac{4\pi m_2}{R_2^6} M_2 \int_0^\infty \left(\int_0^r 4\pi r'^2 \alpha(r'/R_2) dr' \right) \alpha(r/R_2) r dr = \\
 &= \frac{4\pi m_2}{R_2} M_2 \int_0^\infty \left(\int_0^x 4\pi x'^2 \alpha(x') dx' \right) \alpha(x) x dx.
 \end{aligned} \tag{2.112}$$

In condition of global energy equipartition ($K_{V,1} = K_{V,2}$) we can combine Eq. (2.112) and Eq. (2.111) to obtain:

$$\frac{R_2}{R_1} > \beta_1 \frac{m_2}{m_1} \frac{M_2}{M_{tot}}, \tag{2.113}$$

where we have defined β_1 as:

$$\beta_1 = \frac{\int_0^\infty \left(\int_0^x 4\pi x'^2 \alpha(x') dx' \right) \alpha(x) x dx}{f(\infty)}. \tag{2.114}$$

Combining Eq. (2.113) with Eq. (2.110) we obtain:

$$1 > \beta_1 \left(\frac{m_2}{m_1} \right)^{3/2} \frac{M_2}{M_{tot}}, \tag{2.115}$$

which is analogous to the result found by Vishniac (Eq. (2.96)). If $M_1 \gg M_2$, then $M_{tot} \approx M_1$ and Eq. (2.115) gives the result found by Spitzer (Eq. (2.78)).

Homology of density profiles

A key hypothesis in Vishniac derivation is that the form factor $\alpha(x)$ does not depend on mass. This hypothesis implies that density profiles of two generic components are homologous, that is we can obtain the density profile of each component by rescaling and normalizing the density profile of the other component. Merritt (1981) [39] suggested that this condition cannot be considered realistic for real systems, making Vishniac result not clearly justified. We thus wonder if there exists a physically-based distribution function which implies homologous density profiles.

We first observe that the gravitational potential $\Phi(r)$ is an increasing monotonic function of the radial coordinate r , which implies a one-to-one relationship between Φ and r . We can thus use Φ as a radial coordinate. Homology condition on density profile can be rewritten as:

$$\rho_m(\Phi) = H(m) \Theta[\Phi/\Phi_m], \tag{2.116}$$

with $\Theta(x)$ equal for all the masses. The fact that more massive stars are more concentrated can be expressed as:

$$\frac{d\Phi_m}{dm} < 0. \quad (2.117)$$

We now define $f_m dm$ as the distribution function (normalized to mass density) for stars in the mass range $(m, m+dm)$. We first consider isotropic systems; in this case it is possible to apply Abel inversion to obtain the distribution function in terms of mass density:

$$f_m(E) = \frac{1}{2\pi^2\sqrt{2}} \left[\int_E^0 \frac{d^2\rho_m}{d\Phi^2} \frac{d\Phi}{\sqrt{\Phi-E}} - \frac{1}{\sqrt{-E}} \left(\frac{d\rho_m}{d\Phi} \right)_{\Phi=0} \right]. \quad (2.118)$$

We can substitute Eq.[2.116] inside Eq.[2.118] to obtain:

$$f_m(E) = \frac{H(m)}{2\pi^2\sqrt{2}\Phi_m^{3/2}} \left[\int_{E/\Phi_m}^0 \frac{d^2\Theta}{dx^2} \frac{dx}{\sqrt{x-E/\Phi_m}} - \frac{1}{\sqrt{-E/\Phi_m}} \left(\frac{d\Theta}{dx} \right)_{x=0} \right] = F(m)\zeta(E/\Phi_m). \quad (2.119)$$

The form obtained for the distribution function is coherent with that of multi-components King models (Eq.[2.30]) (note that in that case every component was labeled by a discrete index i whereas in this case we use a continuous index m). In effect, if we generalize profiles described in Sect. 2.2.1 to a continuous index m , density profile for every component of mass m is:

$$\rho_m(\psi) = \frac{\tilde{A}_m}{a_m^{3/2}} \exp\left(\frac{a_m}{a_1}\psi\right) \gamma\left(\frac{5}{2}, \frac{a_m}{a_1}\psi\right), \quad (2.120)$$

which can be written as:

$$\rho_m(\psi) = H(m)\Theta(\psi/\psi_m), \quad (2.121)$$

By comparison with Eq.[2.120] we have:

$$H(m) = \frac{\tilde{A}_m}{a_m^{3/2}}, \quad (2.122)$$

$$\Theta(\psi/\psi_m) = \exp\left(\frac{a_m}{a_1}\psi\right) \gamma\left(\frac{5}{2}, \frac{a_m}{a_1}\psi\right), \quad (2.123)$$

with $\psi_m = a_1/a_m$. The fact that more massive stars are more concentrated to the center can be expressed as:

$$\frac{d\psi_m}{dm} < 0, \quad (2.124)$$

as, for smaller values of ψ_m , values of central densities (Eq.[2.120] for $\psi = \Psi$) raise. Homology condition requires that $\Theta(x)$ is the same for all masses. For King models homology condition is satisfied if we express density profiles as functions of ψ .

I studied if the condition expressed in Eq. (2.124) is verified in King models. I considered two-component King models and studied the variation of $\psi_2 = a_1/a_2$ as a function of the mass of the second component by solving Eq. (2.35) in case of central energy equipartition ($\eta = 0.5$) with different values of m_2/m_1 from 1 to 10. The result is represented in Fig. 2.9. We note that a_1/a_2 is a monotonic decreasing function of m_2/m_1 . The assumption that the heavy component is more concentrated, as expressed by Eq. (2.124), is thus fulfilled.

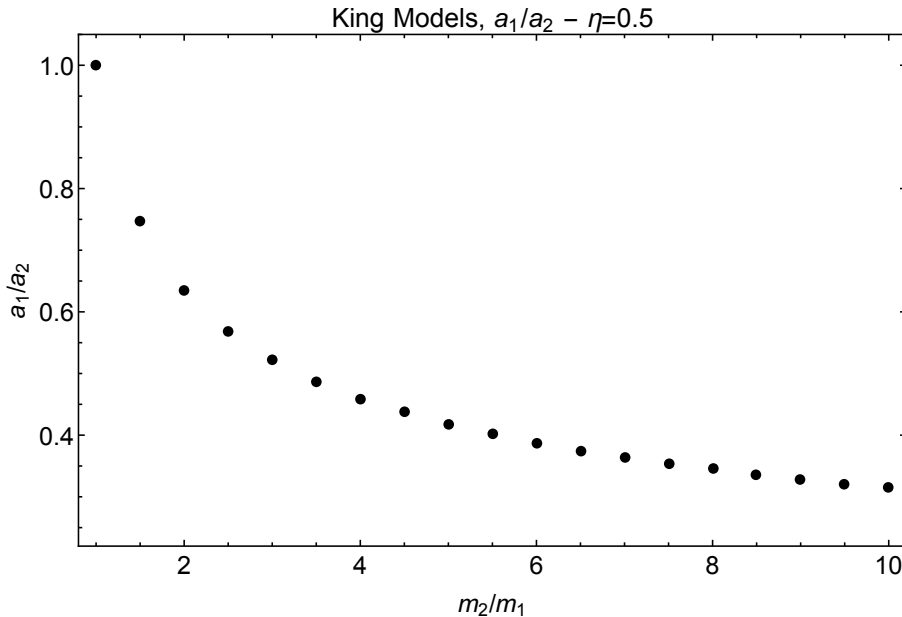


Figure 2.9: The ratio a_1/a_2 for different values of mass ratio m_2/m_1 . We note that a_1/a_2 is a decreasing function of mass. The assumption that the heavy component is more concentrated, as expressed by Eq. (2.124), is thus fulfilled.

I also studied if the two-component models that we will use in the study of realistic simulations in Sect. 3.3.2 fulfill the homology condition assumed by Vishniac. Let $\rho_1(r)$ and $\rho_2(r)$ be given functions, for example those produced by the construction of the two-component self-consistent King or $f_T^{(\nu)}$ models. Vishniac's ansatz, for the two component case, leads to:

$$\rho_1(r) = \frac{M_1}{R_1^3} \alpha(r/R_1), \quad (2.125)$$

and

$$\rho_2(r) = \frac{M_2}{R_2^3} \alpha(\lambda r/R_2), \quad (2.126)$$

where we set $\lambda \equiv R_1/R_2 > 0$. In other words, there should exist a suitable characteristic scale R_2 , i.e. a suitable λ , such that for all the values of r :

$$\rho_2(r) = \left(\frac{M_2}{m_1} \right) \lambda^3 \rho_1(\lambda r). \quad (2.127)$$

We can argue that two-component King or anisotropic models violate this conjecture, so that the positive-definite integral:

$$D_0(\lambda) = \int_0^\infty \left[\rho_2(r) - \frac{M_2}{M_1} \lambda^3 \rho_1(\lambda r) \right]^2 dr \quad (2.128)$$

is expected not to vanish (for any $\lambda > 0$).

Other definition of “violation” may also be acceptable. For example, if we wish to emphasize the role of the 3-dimensional distribution, we might refer to:

$$D_1(\lambda) = \int_0^\infty \left[\rho_2(r) - \frac{M_2}{M_1} \lambda^3 \rho_1(\lambda r) \right]^2 4\pi r^2 dr. \quad (2.129)$$

Vishniac’s ansatz is supplemented by a requirement on $R'(m)$. Thus, if $D_0(\lambda)$ happened to be reasonably small for some λ , we expect that, if $m_1 < m_2$, the optimal λ is larger than unity.

I considered two-component King models under the assumption of central energy equipartition (Eq. (2.35) with $\eta = 0.5$) and with $m_2/m_1 = 2$ and $M_1/M_2 = 2$. I solved the self-consistent problem by setting $\Psi = 5$ and obtained the density profiles of the two components. I then evaluated D_0 and D_1 by applying Eq. (2.128) and Eq. (2.129). The integral $D_0(\lambda)$ presents a minimum in $\lambda_{min,0} = 2.08$, with $D_0(\lambda_{min,0}) = 101$. The integral $D_1(\lambda)$ presents a minimum in $\lambda_{min,1} = 1.98$, with $D_1(\lambda_{min,1}) = 36$. The profiles of the second component and of the first component normalized and rescaled by $\lambda_{min,0}$ (left panel) and $\lambda_{min,1}$ (right panel) are plotted in Fig. 2.10. As illustrated, the density profiles of the King models have approximately similar shapes only up to the half-mass radius and thus they cannot be considered homologous. Thus King models profiles, if expressed as functions of the radial coordinate, do not fulfill the condition of homology.

I repeated the same procedure by considering the two-component $f_T^{(\nu)}$ models introduced in Sect. 2.2.2, under the assumption of central energy equipartition (Eq. (2.43)). I solved the self-consistent problem by setting $\Psi = 5$ and $\gamma = 40$ and obtained the density profiles of the two components. I then evaluated D_0 and D_1 , obtaining, from the first calculation, $\lambda_{min,0} = 3.10$ and $D_0(\lambda_{min,0}) = 6.65 \times 10^4$ and from the second calculation $\lambda_{min,1} = 3.59$ and $D_1(\lambda_{min,1}) = 867$. The profiles of the second component and of the first component normalized and rescaled by $\lambda_{min,0}$ (left panel) and $\lambda_{min,1}$ (right panel) are plotted in Fig. 2.11. Also for the $f_T^{(\nu)}$ models, the values of D_0 and D_1 do not vanish for some λ . The homology condition is not fulfilled. In this case, as illustrated in Fig. 2.11, the differences between the two profiles are even more evident, with very large discrepancies outside the half-mass radius.

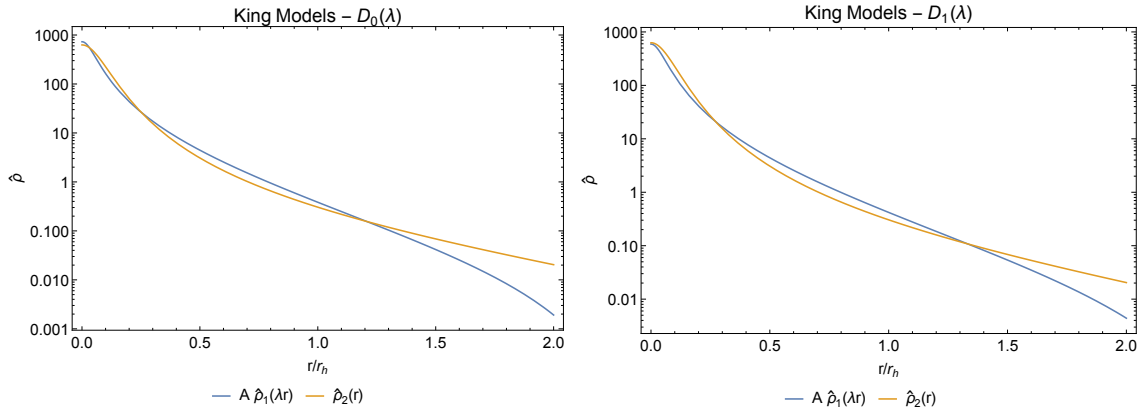


Figure 2.10: The King models density profiles of the second component (yellow line) and of the first component (blue line) normalized and rescaled by $\lambda_{min,0}$ (left panel) and $\lambda_{min,1}$ (right panel).

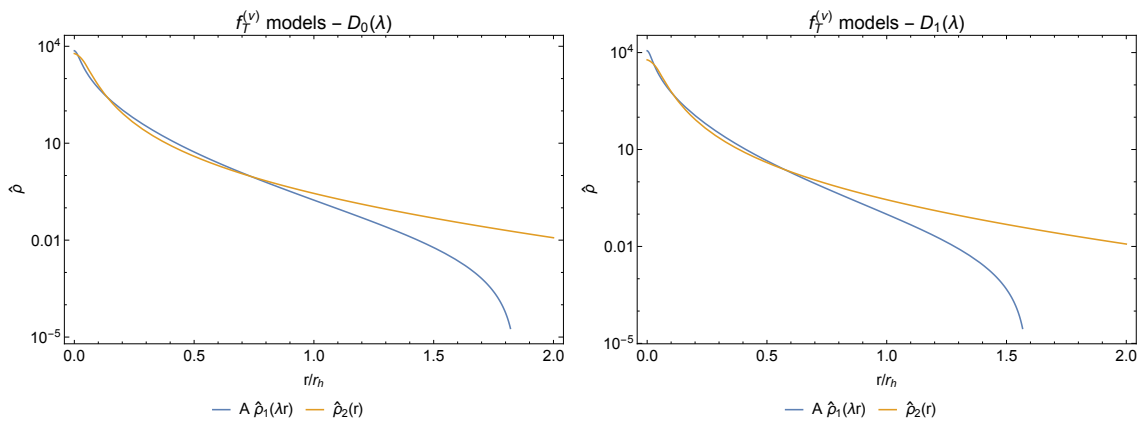


Figure 2.11: The $f_T^{(\nu)}$ models density profiles of the second component (yellow line) and of the first component (blue line) normalized and rescaled by $\lambda_{min,0}$ (left panel) and $\lambda_{min,1}$ (right panel).

Chapter 3

Energy equipartition and mass segregation in Monte Carlo simulations

Several different techniques have been developed for computing cluster evolution in phase space. To model the evolution of real stellar systems and make meaningful comparisons with observations, one has to take into account the complex interaction between stellar evolution, stellar dynamics and the environment. A possible method to deal with the dynamics of the stars consists in the direct integration of the dynamical equations for N mass points. This way of proceeding, sometimes referred to as *N-body* calculation, can be applied to almost any situation, including transient perturbations by external masses with no simple symmetry. An important application of such technique is to the dynamics of collapsing cores (e.g., see Bianchini et al. (2017) [13]), when the formation of binary stars by three-body encounters becomes important. The great disadvantage of this technique is the generally prohibitive amount of cpu time ($\sim N^2$) required if N becomes large.

For globular clusters, aside from some complex situations (e.g., those that may develop after core collapse), phase space diffusion produced by distant two-body encounters plays the dominant role in their evolution. In this case one may consider a kind of codes, the so-called Monte Carlo codes, that are faster with respect to *N-body* codes but properly incorporate the standard relaxation processes. At the same time, because they are much “lighter” than direct *N-body* codes, Monte Carlo codes offer a way to introduce more degrees of freedom as, for example, the physical processes that are important during stellar evolution. Monte Carlo methods were developed by Hénon (1971) [31] and Spitzer (1975) [49] and substantially improved by Stodółkiewicz (1986) [53] and Giersz (1998) [22] (see also [23], [25], [32]).

In this thesis I consider a set of Monte Carlo cluster simulations, developed and performed by Downing et al. (2010) [19] and used by Bianchini et al. (2016) [12] and Bianchini et al. (2017) [10] in their study of energy equipartition and mass segregation. These authors focused on projected quantities to make useful comparisons with observations. In this thesis I consider intrinsic quantities for a more direct comparison with models. Simulation data (i.e., the output of simulations) were kindly shared by P. Bianchini. The simulations include a Kroupa (2001) initial mass function¹ with different amounts of primordial binaries. By means of a relatively high number of particles they include the main characteristics of stellar evolution and provide a realistic description of the long-term evolution of globular clusters with a single stellar population. The initial and final properties of these systems are described in detail in Sect. 3.1.

3.1 Simulations

Initial conditions of simulations under consideration are described by Downing et al. (2010) [19] and Bianchini et al. (2016) [12]. All the simulations have their initial mass and velocity distributions drawn from a Plummer (1911) [46] isotropic model (see Sect. 2.1.1), to which a cutoff was performed at 150 pc. Details of the initial conditions of the simulations are summarized in Tab. 3.1. Simulations from

Table 3.1: Initial state of simulations. Table from Bianchini et al. (2016) [12].

	f_{binary} [%]	r_t/r_h	N	M_{tot} [M_\odot]
Sim 1 (10low75)	10	75	5×10^5	3.62×10^5
Sim 2 (50low75)	50	75	5×10^5	5.07×10^5
Sim 3 (10low37)	10	37	5×10^5	3.62×10^5
Sim 4 (50low37)	50	37	5×10^5	5.07×10^5
Sim 5 (10low180)	10	180	5×10^5	3.62×10^5
Sim 6 (50low180)	50	180	5×10^5	5.07×10^5
Sim 7 (10low75-2M)	10	75	20×10^5	7.26×10^5

Sim 1 to Sim 6 contain an initial number of 5×10^5 stars, with different binary fractions (10% or 50%) and concentration values, quantified by the ratio of the

¹The Kroupa (2001) mass function has the form of a composite power law:

$$dN/dm \propto m^{-\alpha},$$

with $\alpha = 0.3$ for $m < 0.08 M_\odot$, $\alpha = 1.3$ for $0.08 M_\odot < m < 0.5 M_\odot$, and $\alpha = 2.3$ for $m > 0.5 M_\odot$.

intrinsic truncation radius and the intrinsic half-mass radius r_t/r_h amounting to 75, 37 or 180. Sim 7 initially contains 2×10^6 particles, with a binary fraction of 10%. Note that for a galactic mass $M_G \approx 10^{11} M_\odot$ and cluster masses of the order of $5 \times 10^5 M_\odot$ (as indicated in Tab. 3.1) distances of clusters from the center of galaxies (which could be estimated in first approximation by means of Eq. (1.24)) are of the order of 12 – 13 kpc. This condition makes simulations relatively isolated, so that the observed effects are due mainly to internal cluster dynamics. The tidal cutoff is not held constant during the evolution of the cluster but is re-calculated at each time-step according to the current cluster mass, which can vary as consequence of dynamical evaporation (see Sect. 1.3.1) and stellar evolution (e.g. during supernova explosions the emitted gas is removed from the system)

Systems were made evolved for 11 Gyr and their properties were studied at three snapshots from the initial time, at 4, 7, 11 Gyr. Table 3.2 reports projected properties of simulations at the three snapshots considered: the concentration c , defined as $c = \log(R_t/R_c)$, with R_t the projected truncation radius and R_c the projected core radius; the projected effective radius R_e ; the logarithm of the half-mass relaxation time t_{rh} (evaluated by means of Eq. (1.20)) and the logarithm of the core relaxation time t_{rc} (evaluated by means of Eq. (1.19)).

Table 3.2: Projected properties of the simulation states. Table from Bianchini et al. (2017) [10].

	c			R_e [pc]			R_c [pc]			$\log t_{rh}$			$\log t_{rc}$		
	4 Gyr	7 Gyr	11 Gyr	4 Gyr	7 Gyr	11 Gyr	4 Gyr	7 Gyr	11 Gyr	4 Gyr	7 Gyr	11 Gyr	4 Gyr	7 Gyr	11 Gyr
Sim 1	1.52	1.46	1.45	4.01	4.23	4.92	2.74	3.12	3.15	9.38	9.49	9.54	9.15	9.17	9.12
Sim 2	1.42	1.38	1.34	4.89	5.92	6.06	3.42	3.62	3.89	9.47	9.58	9.66	9.35	9.29	9.29
Sim 3	1.26	1.21	1.16	7.04	8.16	9.05	4.92	5.52	6.07	9.66	9.76	9.82	9.65	9.66	9.65
Sim 4	1.21	1.16	1.12	8.84	8.96	10.92	5.54	6.11	6.47	9.71	9.80	9.88	9.76	9.78	9.74
Sim 5	1.81	1.95	2.06	1.53	1.90	2.69	1.33	0.96	0.75	9.17	9.26	9.35	8.44	8.03	7.74
Sim 6	1.73	1.74	1.79	2.96	3.10	3.05	1.64	1.56	1.34	9.25	9.35	9.42	8.60	8.47	8.26
Sim 7	1.52	1.52	1.51	2.57	2.62	2.90	1.73	1.87	1.85	9.42	9.50	9.57	9.04	9.04	8.99

Energy equipartition and mass segregation have been studied in these systems by Bianchini et al. (2016) [12] and Bianchini et al. (2017) [10] and their main results were described in Sect. 1.3.3 and Sect. 1.3.4 respectively. For my study of energy equipartition and mass segregation, I initially considered eight snapshots. As I want to study relaxation effects, I focused on all the snapshots of more relaxed simulations (Sim 5 and Sim 6 at 4 Gyr, 7 Gyr and 11 Gyr) and on two other snapshots at 11 Gyr, that is Sim 1 at 11 Gyr and Sim 3 at 11 Gyr. At my disposal I have complete information about mass, luminosity (in the V-band), type (the evolutionary phase), position and velocity of single stars. In case of a binary system, I have information about mass, luminosity (in the V-band), type of the two components and about

position and velocity of the center of mass. I always consider the reference system of the center of mass of the cluster. All the simulations show typical values for the velocity of the center of mass of the order of $v_{cm} \sim 10^{-2} - 10^{-3}$ km/s. Table 3.3 reports binary fraction, the intrinsic ratio r_t/r_h , total number, total mass and relaxation parameter, defined as $n_{rel} = t_{age}/t_{rc}$, for each simulation considered. All

Table 3.3: Properties of the simulation states.

	f_{binary} [%]	r_t/r_h	N	M_{tot} [M_\odot]	n_{rel}
Sim 1, 11 Gyr	2.95	11.27	4.69×10^5	1.73×10^5	8.3
Sim 3, 11 Gyr	5.60	6.90	4.52×10^5	1.73×10^5	2.5
Sim 5, 4 Gyr	3.66	13.95	4.46×10^5	1.75×10^5	14.6
Sim 6, 4 Gyr	12.24	11.95	5.36×10^5	2.35×10^5	10.1
Sim 5, 7 Gyr	3.54	18.21	4.32×10^5	1.65×10^5	64.9
Sim 6, 7 Gyr	11.83	15.33	5.20×10^5	2.20×10^5	23.6
Sim 5, 11 Gyr	3.44	16.13	4.11×10^5	1.54×10^5	200.2
Sim 6, 11 Gyr	11.49	13.78	5.00×10^5	2.07×10^5	60.1

the snapshots relative to Sim 6 present a higher number of stars (column 4) with respect to the initial state as a consequence of the high initial number of binaries. Binary systems are destroyed by encounters, producing single stars and increasing the number of stars in the simulations. Most of the mass is lost because of dynamical evaporation. A fraction of the total mass is also lost because of stellar evolution, but this contribution is important only in the first few million years, when a high number of massive stars is present.

I initially identified four main groups of stars: main sequence single stars; giant single stars, which include stars labeled as Hertzsprung gap, giant branch, core helium, first AGB, second AGB, helium main sequence, helium Hertzsprung gap and helium giant branch; single remnants, which include carbon-oxygen white dwarfs, oxygen-neon white dwarfs, neutron stars and black holes; binaries. Table 3.4 reports the number and relative contribution to the total number, mass and luminosity of stars of each type. Main sequence stars (MS) dominate the number and mass percentage and constitute a good part of the luminosity of the system (about 25 – 30%). Giants represent a negligible part of the mass of the clusters but, despite their very small number, dominate the luminosity of the system. Remnants are a relevant part of the mass of the system (between 15 – 25%) but do not contribute to luminosity. Finally, binary mass is important particularly in Sim 6, which has been initialized with a high binary fraction (50%).

Figure 3.1 illustrates the mass spectra for four simulations. All the spectra

Table 3.4: Number, mass and luminosity percentage of each class of stars.

	Number percentage [%]				Mass percentage [%]				Luminosity percentage [%]			
	MS	Giants	Remnants	Binaries	MS	Giants	Remnants	Binaries	MS	Giants	Remnants	Binaries
Sim 1, 11 Gyr	84.92	0.33	11.80	2.95	69.61	0.77	23.55	6.07	31.28	62.19	0.006	6.53
Sim 3, 11 Gyr	82.08	0.31	12.01	5.60	64.05	0.67	23.40	11.89	31.97	63.61	0.004	4.41
Sim 5, 4 Gyr	87.67	0.40	8.27	3.66	74.60	1.14	17.09	7.16	26.77	69.24	0.003	3.99
Sim 6, 4 Gyr	78.76	0.36	8.63	12.24	61.03	0.93	16.24	21.80	24.90	62.23	0.006	12.86
Sim 5, 7 Gyr	85.25	0.39	10.82	3.54	70.81	0.96	21.50	6.74	24.20	72.55	0.005	3.24
Sim 6, 7 Gyr	76.70	0.35	11.12	11.83	58.41	0.78	20.27	20.54	24.46	61.20	0.004	14.34
Sim 5, 11 Gyr	82.85	0.36	13.35	3.44	67.16	0.79	25.71	6.34	27.48	69.14	0.004	3.38
Sim 6, 11 Gyr	74.60	0.32	13.59	11.49	55.69	0.65	24.16	19.51	25.61	61.64	0.007	12.74

present a general decreasing behavior with a secondary peak at about $0.6 M_{\odot}$. The presence of the secondary peak is due to the formation of a large number of white dwarfs as a consequence of stellar evolution.

3.1.1 Hydrostatic and virial equilibrium

Before addressing the objectives of this thesis, I checked if simulations in the sample considered fulfill the conditions of hydrostatic and virial equilibrium (see Sect. 2.2.4). I first verified the virial equilibrium condition by calculating the parameter κ defined in Eq. (2.62). If the models captured by the snapshots are in approximate equilibrium condition, this parameter should be very close to unity (as explained in Sect. 2.2.4). I first evaluated the total kinetic energy as the sum of all the kinetic energies of stars, K_i :

$$K = \sum_i^N K_i = \frac{1}{2} m_i v_i^2, \quad (3.1)$$

where m_i is the star (or binary) mass and v_i is the velocity. A direct evaluation of the total gravitational energy would require too much time as the time to evaluate all the distances between two stars $\sim N^2$. Thus, I evaluated the total gravitational energy as:

$$W = -4\pi G \int_0^{r_t} M_{tot}(r) \rho_{tot}(r) r dr. \quad (3.2)$$

I constructed the total density profile $\rho_{tot}(r)$ for each simulation (for a detailed description of this procedure see Sect. 3.3.1) and evaluated $M_{tot}(r)$, the mass contained inside a certain radius r . Values of $\kappa - 1$, reported in Tab. 3.5, are all of the order of 10^{-4} . Thus the virial equilibrium condition is found to be satisfied in all the models considered.

In order to check the establishment of hydrostatic equilibrium, I defined a hydrostatic coefficient in analogy to the virial coefficient. The hydrostatic coefficient can

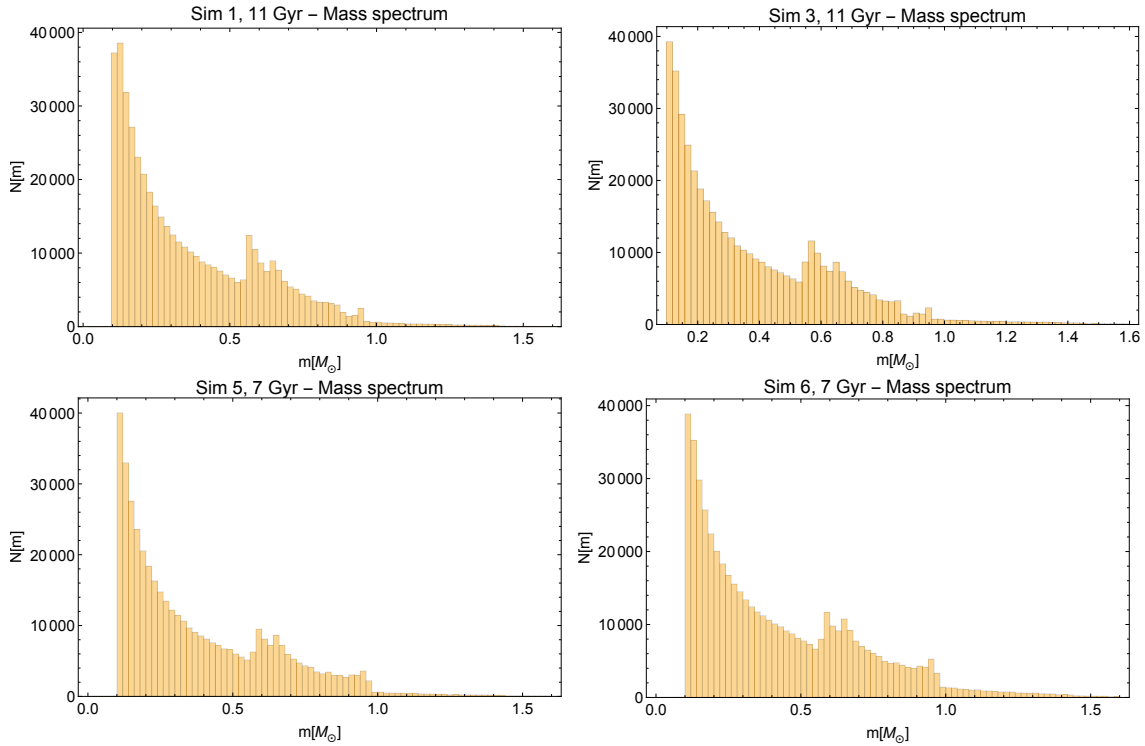


Figure 3.1: Mass spectra of four simulations: Sim 1 at 11 Gyr (left upper panel), Sim 3 at 11 Gyr (right upper panel), Sim 5 at 7 Gyr (left lower panel), Sim 6 at 7 Gyr (right lower panel). There is a secondary peak at about $0.6 M_{\odot}$, which is the typical mass at which white dwarfs form.

Table 3.5: Virial coefficients

	Sim 1, 11 Gyr	Sim 3, 11 Gyr	Sim 5, 4 Gyr	Sim 5, 7 Gyr	Sim 5, 11 Gyr	Sim 6, 4 Gyr	Sim 6, 7 Gyr	Sim 6, 11 Gyr
$\kappa - 1$	4.50×10^{-4}	-2.59×10^{-4}	2.18×10^{-4}	3.66×10^{-4}	1.37×10^{-4}	1.31×10^{-4}	1.57×10^{-4}	2.51×10^{-4}

be defined as the ratio between the moduli of the left-hand-side and the right-hand-side of hydrostatic equilibrium condition (Eq. (2.52)). Because for a multi-mass system hydrostatic condition must be fulfilled by each mass component (analogously, it must be fulfilled by any f_i in multi-components models, as seen in Sect. 2.2.4), I defined the hydrostatic coefficient for stars of mass m as:

$$H_m(r) = \frac{|(d/dr) [\rho_m(r)\sigma_{r,m}^2(r)] + \rho_m(r)\alpha_m(r)\sigma_{r,m}^2(r)/r|}{GM_{tot}(r)\rho_m(r)/r^2}, \quad (3.3)$$

where ρ_m , $\sigma_{r,m}^2$ and α_m are the density, the radial velocity dispersion and the anisotropy of stars with mass m . In case of hydrostatic equilibrium, $H_m(r)$ is expected to be very close to unity for every value of r and for every mass m .

To check the establishment of hydrostatic equilibrium, I divided the system in narrow mass bins of width $0.05 M_{\odot}$ centered in $0.12 M_{\odot}$, $0.22 M_{\odot}$, $0.57 M_{\odot}$ and $0.62 M_{\odot}$. I evaluated $H_m(r)$ for every mass bin at different radii. The values of

$H_m(r) - 1$ for the four mass bins are represented in Fig. 3.2 and Fig. 3.3.

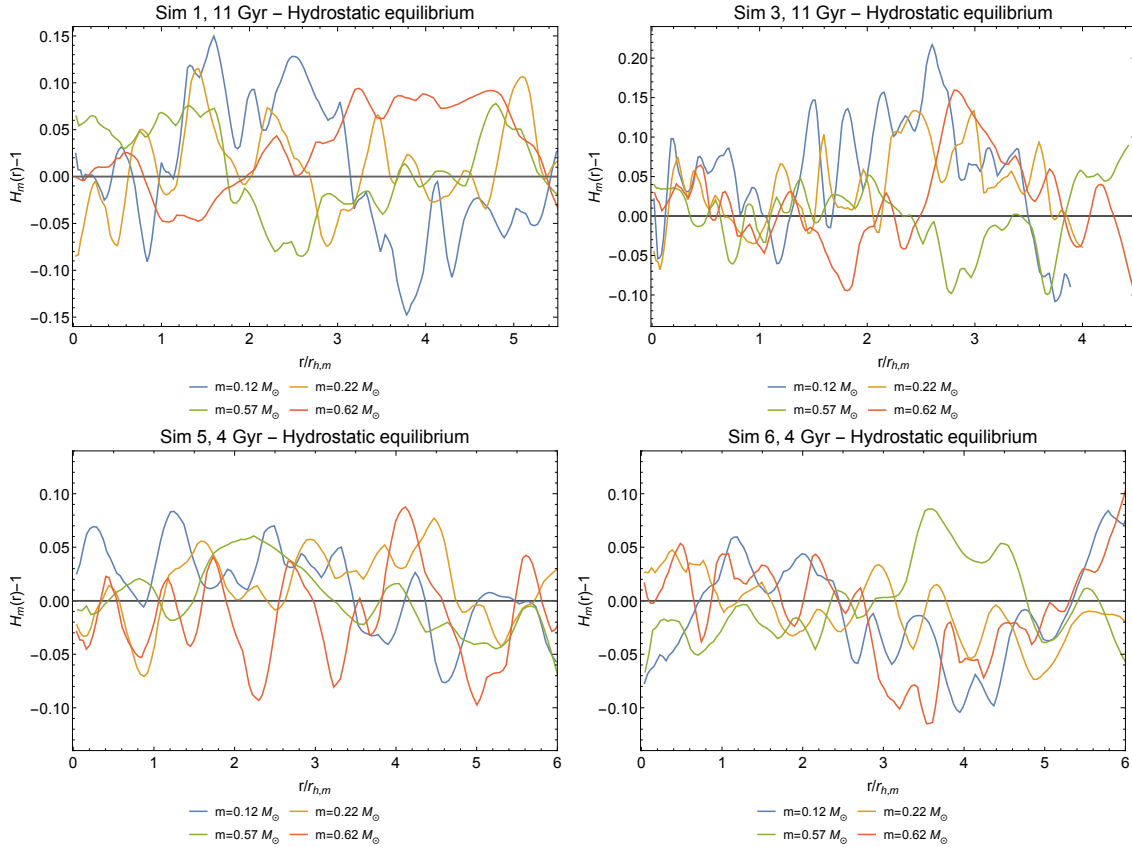


Figure 3.2: Values of $H_m(r) - 1$ as a function of radius for four simulations: Sim 1 at 11 Gyr (left upper panel), Sim 3 at 11 Gyr (right upper panel), Sim 5 at 4 Gyr (left lower panel), Sim 6 at 4 Gyr (right lower panel). The radial coordinate was rescaled, for each mass bin, to the half-mass radius of the stars in that bin, $r_{h,m}$. For all the systems represented, hydrostatic equilibrium condition is fulfilled.

Hydrostatic equilibrium condition is fulfilled by all the snapshots except two, Sim 5 at 11 Gyr and Sim 6 at 11 Gyr, which exhibit an anomalous decreasing behavior, with values of $H_m(r)$ lower than the expected $H_m(r) = 1$. These systems cannot be considered in hydrostatic equilibrium.

I tried to analyze the possible causes of this anomaly. I first constructed histograms for the radial velocity distributions of the anomalous simulations and compared them to those of their previous snapshots, as shown in Fig. 3.4. In the anomalous systems, almost all (except for few hundreds) stars have positive radial velocities, as opposed to the others, consistent with hydrostatic equilibrium, for which radial velocity distribution has approximately vanishing mean value. I considered two possible reasons that might explain positive radial velocities.

First, this could be simply a problem in the generated output. This would explain

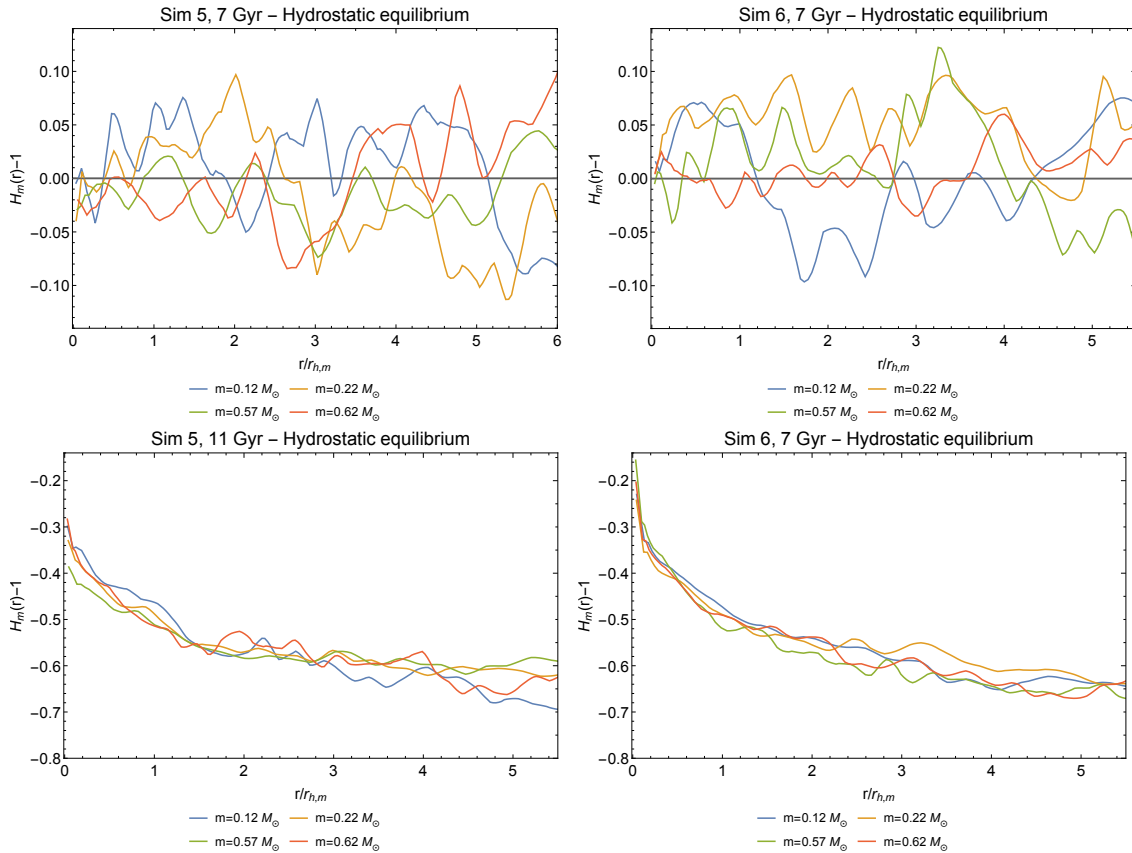


Figure 3.3: Values of $H_m(r) - 1$ as a function of radius for four simulations: Sim 5 at 7 Gyr (left upper panel), Sim 6 at 7 Gyr (right upper panel), Sim 5 at 11 Gyr (left lower panel), Sim 6 at 11 Gyr (right lower panel). The radial coordinate was rescaled, for each mass bin, to the half-mass radius of stars in that bin, $r_{h,m}$. Systems in the upper panels fulfill the condition of hydrostatic equilibrium whereas those in the lower panels exhibit a monotonically decrease, with values always lower than the equilibrium value. For these systems hydrostatic equilibrium condition is not fulfilled.

why these systems turn out to be in virial equilibrium, as the virial test considers only the moduli of velocities. To verify this possibility, I repeated the hydrostatic equilibrium test by assuming that the output consists of the moduli of the radial velocities and that the mean radial velocity of the system is actually zero. I then defined another coefficient, $H'_m(r)$ as:

$$H'_m(r) = \frac{|(d/dr)(\rho_m \langle v_{r,m} v_{r,m} \rangle) + \rho_m(r) \alpha_m(r) \sigma_{r,m}^2(r)/r + 2\rho_m \langle v_{r,m} \rangle \langle v_{r,m} \rangle / r|}{GM_{tot}(r)\rho_m(r)/r^2}, \quad (3.4)$$

with $\langle v_{r,m} v_{r,m} \rangle = \sigma_{r,m}^2 + \langle v_{r,m} \rangle \langle v_{r,m} \rangle$. Under the assumption of an output error, the square radial velocity dispersion $\sigma_{r,m}^2$ would be given by the second moment of

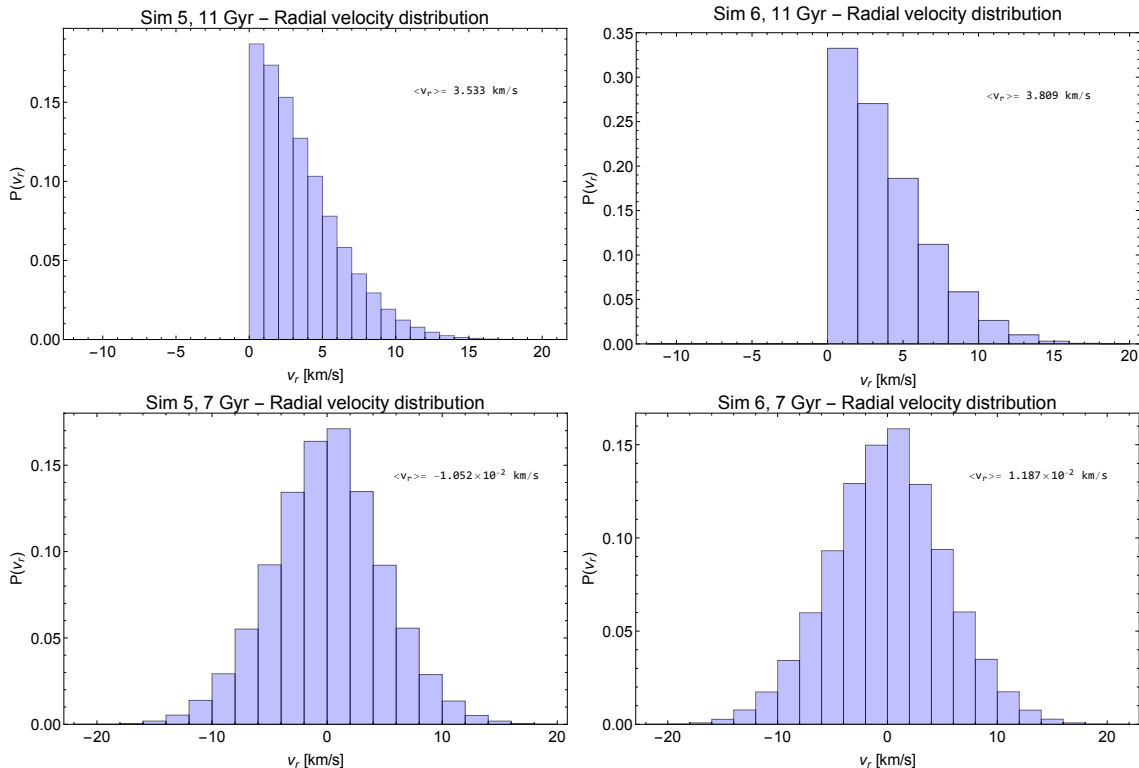


Figure 3.4: Normalized radial velocity distributions, $P(v_r)$. We can observe that two simulations which do not fulfill hydrostatic equilibrium, that is Sim 5 at 11 Gyr (left upper panel) and Sim 6 at 11 Gyr (right upper panel) have almost all positive radial velocities, as opposed to Sim 5 at 7 Gyr (left lower panel) and Sim 6 at 7 Gyr (right lower panel) in which mean radial velocity is very close to zero.

velocities $\langle v_{r,m} v_{r,m} \rangle$, with $\langle v_{r,m} \rangle$ close to zero. I repeated the same procedure as described above for the study of hydrostatic equilibrium and found that, for the two simulations considered, the value of $H'_m(r) - 1$ remains close to 0 throughout the systems considered, as can be seen in Fig. 3.5. However, if there was an output error of this kind, we would expect that all the velocities were positive; anomalous simulations, instead, contain some hundred of stars with negative radial velocities.

The fact that $H'_m(r)$ is very close to unity throughout the anomalous system can also be explained as due to a radial expansion. In fact, $H'_m(r)$ is the ratio between the moduli of the left-hand-side and the right-hand-side of the momentum equations in radial coordinates (Eq. (2.51)) without the assumption of zero mean radial velocity. On the other hand, the anomalous models are the most relaxed states (see Tab. 3.3) and therefore they may have undergone a core collapse according to the process described in Sect. 1.3.2. These simulations may thus be in a post-collapse expansion phase. Thus, a radial expansion due to gravothermal catastrophe is another possible explanation for the velocity distributions in Sim 5 at 11 Gyr and Sim 6 at 11 Gyr.

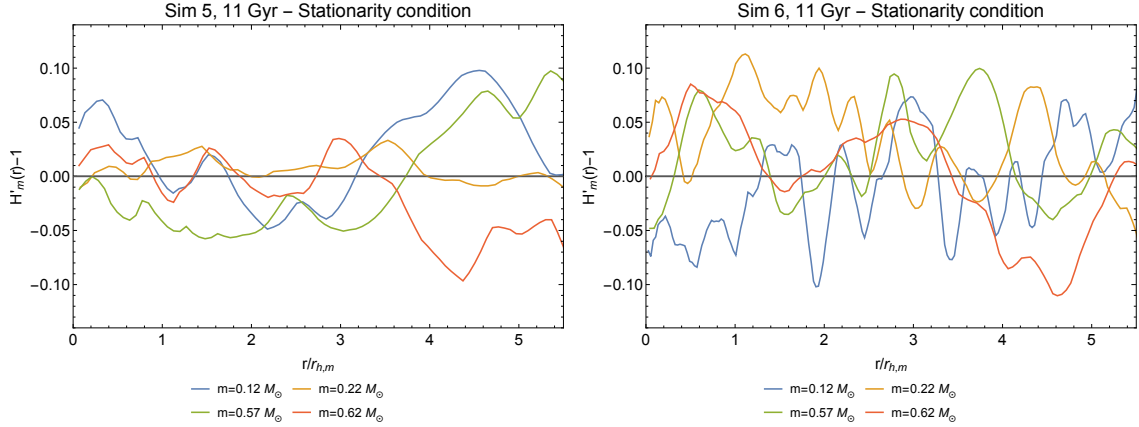


Figure 3.5: Values of $H'_m(r) - 1$ as a function of radius for Sim 5 at 11 Gyr (left panel) and Sim 6 at 11 Gyr (right panel). A condition of stationarity is recovered.

However, as explained in Sect. 1.3.2, in this case the expansion would affect only the stars in the core and, even if the all system would be expanding, it is difficult to explain why the virial coefficient is so close to unity.

As this test on hydrostatic equilibrium cannot clarify the cause of the anomalous velocity distribution found in Sim 5 at 11 Gyr and Sim 6 at 11 Gyr, I simply decided to rule Sim 5 at 11 Gyr and Sim 6 at 11 Gyr out of the sample.

3.2 Energy equipartition and mass segregation

3.2.1 Energy equipartition

Equipartition in the simulations under consideration was studied by Bianchini et al. (2016) [12]. In particular, this article pointed out that such systems reach a state of only partial energy equipartition, which is quantified by means of the parameter m_{eq} (see Sect. 1.3.3). In their study of equipartition, Bianchini et al. (2016) considered all the stars inside the effective radius R_e , thus referring to the concept of global equipartition. As already anticipated in Sect. 1.3.3, real systems cannot fulfill a condition of global energy equipartition because this would be possible only in presence of global thermodynamical equilibrium. In principle, a condition close to energy equipartition could be reached only in the central regions, where systems are more relaxed.

I tried to check if, by restricting the study of energy equipartition to more central regions, a state close to energy equipartition is indeed approached. In my study, energy equipartition is characterized by means of the quantity $m\Sigma^2(r, m)$, where $\Sigma^2(r, m)$ is defined as the statistical variance of velocities calculated on all the stars

of mass m inside a sphere of radius r ; in the case of energy equipartition this parameter would be expected to be constant for different values of mass. I divided the system in narrow mass bins of width $5.6 \times 10^{-2} M_\odot$ centered from $0.11 M_\odot$ to $0.9 M_\odot$ and assigned a representative value of mass to each bin by taking the mean mass. I then evaluated $m\Sigma^2(r, m)$ by considering all the stars of each mass bin inside $0.2r_{h,m}$, $0.5r_{h,m}$, $r_{h,m}$ and $2r_{h,m}$, where $r_{h,m}$ is the half-mass radius of the stars belonging to the mass bin centered in m . I then divided $m\Sigma^2(r, m)$ by $m_0\Sigma^2(r, m_0)$, where m_0 is the central mass of the first bin, $m_0 = 0.11 M_\odot$. As illustrated in Fig. 3.6, the ratio $\tilde{m}\tilde{\Sigma}^2(r, m) = m\Sigma^2(r, m)/(m_0\Sigma^2(r, m_0))$ shows an increasing trend as we move to higher masses, confirming that systems are not in a state of full energy equipartition. In the central regions the slope of the curve is smaller than that at higher radii, suggesting that the system is closer to a state of energy equipartition. We also note that more relaxed and less relaxed systems, as indicated by the parameter n_{rel} (see Tab. 3.3), have a similar behavior, also in central regions; this suggests that a condition of only partial energy equipartition can be fulfilled, even in more relaxed systems.

As the systems under consideration are not in a state of energy equipartition, the Vishniac condition (expressed by Eq. (2.96)) is expected to fail. In order to test Vishniac result, I evaluated the quantities \tilde{m} and \tilde{M} , as defined in Sect. 2.4, for different values of m . I determined β by means of its definition in Eq. (2.95) (with density profiles constructed as explained in Sect. 3.3.1). I obtained typical values of $\beta \approx 0.4$, in good agreement with his assumption of $\beta \approx 0.5$. If Vishniac criterion is fulfilled, the quantity $\beta\tilde{m}^{3/2}\tilde{M}$ should be smaller than unity. In Fig. 3.7, I plot $\beta\tilde{m}^{3/2}\tilde{M}$ as a function of mass: this quantity has values > 1 in almost all the mass spectrum and falls below unity only for very low values of all the simulated systems. The fact that $\beta\tilde{m}^{3/2}\tilde{M} < 1$ at low masses is due to the fact that $\beta\tilde{m}^{3/2}\tilde{M} \approx \beta < 1$ near m_1 , but very few stars fall in this range of mass. The shape of the profiles in Fig. 3.7 suggests a progressive approach to equipartition (condition of $\beta\tilde{m}^{3/2}\tilde{M} < 1$) by heavy stars, in agreement with what found by Bianchini et al. (2016) [12]. However, even for Sim 5 at 7 Gyr, the percentage of mass of stars which fulfill Vishniac criterion is smaller than 1%. We can conclude that Vishniac criterion is not fulfilled by all the systems that we have considered. In addition, density profiles of systems under consideration are well described by $f_T^{(\nu)}$ models (as we will see in Sect. 3.3.2), which do not fulfill the homology condition required to derive Vishniac criterion. This undermines the application of this criterion to these systems, the hypotheses which it is based on cannot be considered fully realistic.

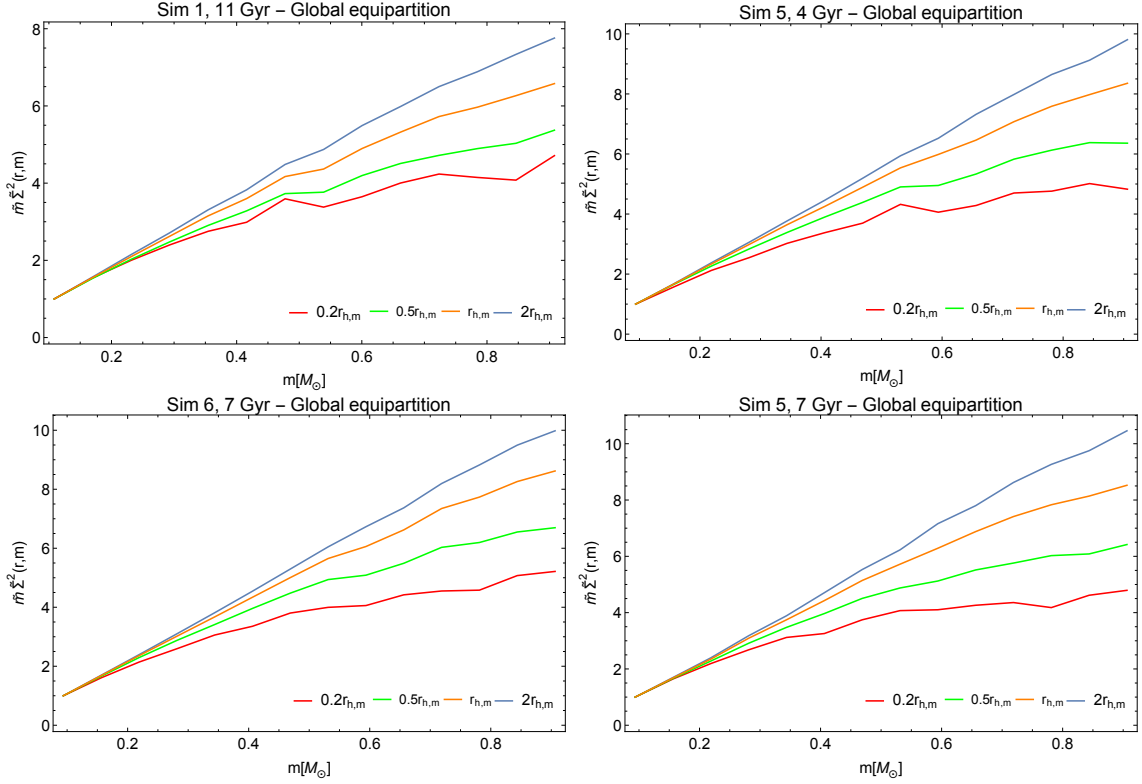


Figure 3.6: Values of $\tilde{m}\tilde{\Sigma}^2(r, m) = m\Sigma^2(r, m)/(m_0\Sigma^2(r, m_0))$ for four simulated states: Sim 1 at 11 Gyr (left upper panel), Sim 5 at 4 Gyr (right upper panel), Sim 6 at 7 Gyr (left lower panel), Sim 5 at 7 Gyr (right lower panel). This quantity has been evaluated inside four different radii, $0.2r_{h,m}$ (red line), $0.5r_{h,m}$ (green line), $r_{h,m}$ (orange line) and $2r_{h,m}$ (blue line). Note that $\tilde{m}\tilde{\Sigma}^2(r, m)$ is not constant even for most relaxed systems (lower panels) and even in central regions.

3.2.2 Mass segregation

I divided the system into radial shells and, for each shell, I calculated the mean mass, $\bar{m}(r)$. I repeated the same procedure considering the four classes of stars defined in Sect. 3.1 separately. In Fig. 3.8 and Fig. 3.9 the mean mass is shown to have a monotonic decline in all the simulations under consideration, even for the least relaxed system, Sim 3 at 11 Gyr. In addition, all the classes of stars defined in Sect. 3.1 present mass segregation separately, with the exception of giant stars. These are not affected by mass segregation as the giant phase in a star life is very short and thus, at each snapshot, only a group of stars in a restricted range of mass is in this evolution stage. The fact that main sequence stars exhibit mass segregation can have important implications for the comparison between models and observations, as we will see in Sect. 3.4.

Mass segregation can also be described considering the variation of the half-mass

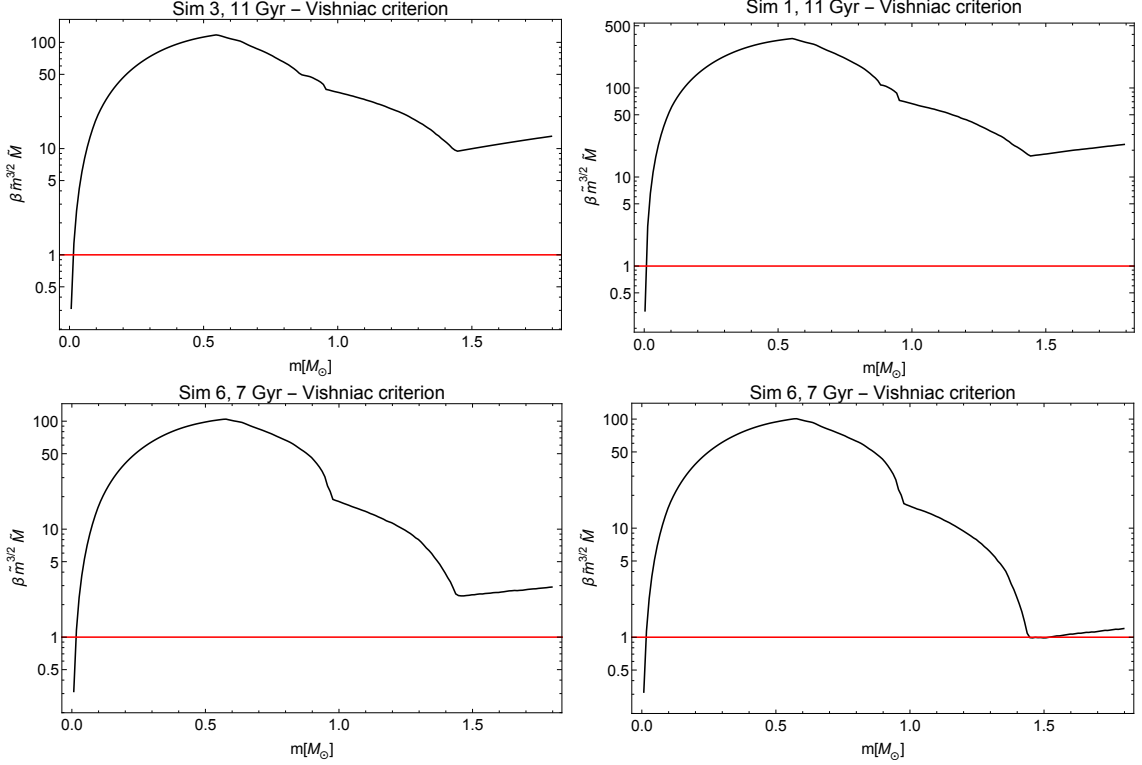


Figure 3.7: The Vishniac criterion tested in four simulated states: Sim 3 at 11 Gyr (left upper panel), Sim 1 at 11 Gyr (right upper panel), Sim 6 at 7 Gyr (left lower panel), Sim 5 at 7 Gyr (right lower panel).

radius for stars of a certain mass, $r_{h,m}$, as a function of mass (see also Fig. 9 in de Vita et al. (2016) [16] and related discussion). For a mass-segregated system, we expect a decreasing trend with mass. In Fig 3.10 this trend can be observed, also for less relaxed systems. We can also observe that the gradient is small in all the half-mass radius profiles at about $0.6 M_\odot$. As noted above, in Sect. 3.1, this is the typical mass at which white dwarfs form, in many cases after undergoing a severe mass loss. If, after loosing a great quantity of mass, white dwarfs do not have time to relax dynamically, they will be characterized by the same mass distribution as objects with their original mass and, as a consequence, they will exhibit a lower half-mass radius. We can conclude that mass segregation affects all the systems considered, even those with very small n_{rel} .

3.3. FITTING THE SIMULATED STATES WITH SELF-CONSISTENT DYNAMICAL MODELS

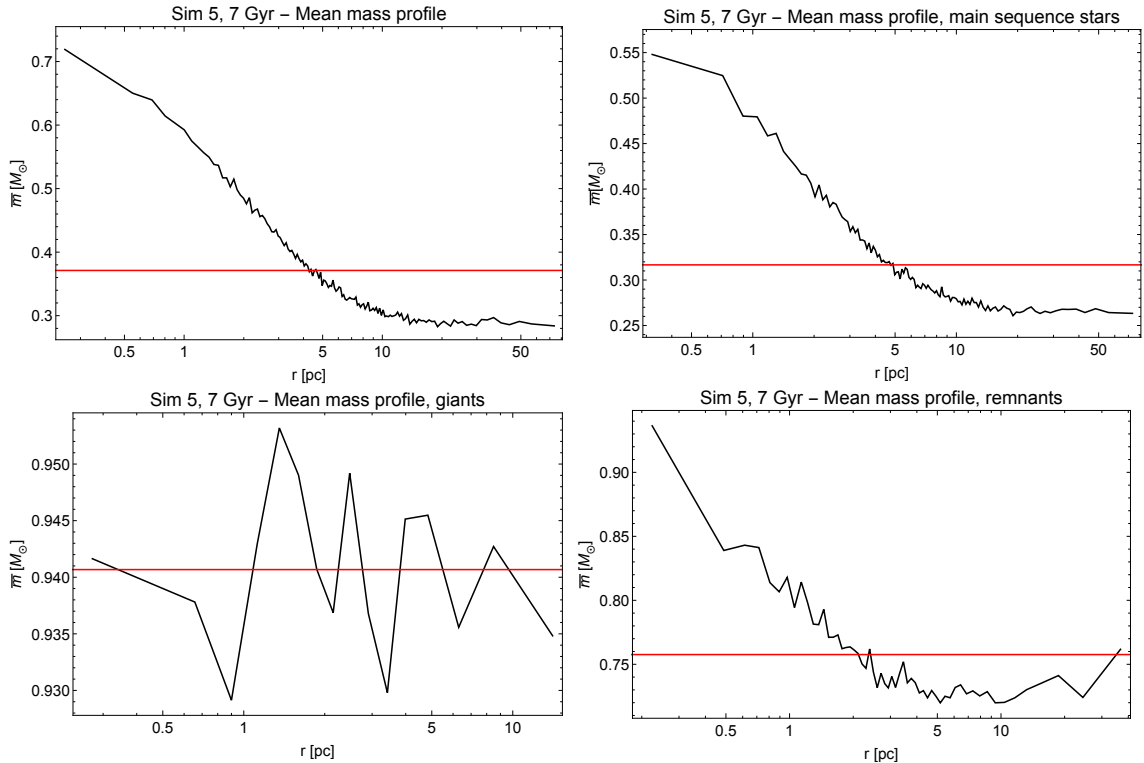


Figure 3.8: Mean mass profiles for the most relaxed simulation state of our sample, Sim 5 at 7 Gyr. The left upper panel shows the variation of the mean mass considering all the classes of stars. The right upper panel shows the main sequence stars mean mass profile. The left lower panel shows giant mean mass profile. The line is jagged because of the very small number of stars in the giant phase. The right lower panel shows remnant mean mass profile. Red lines represent the mean mass of the component, evaluated considering all the stars of the simulated system.

3.3 Fitting the simulated states with self-consistent dynamical models

I performed a fit to the simulated states by means of King models, isotropic models traditionally applied to the study of globular clusters (see Sect. 2.1.3), and anisotropic $f_T^{(\nu)}$ models, which have been constructed to describe partial relaxed systems formed by violent relaxation (see Sect. 2.1.4). The model that best fits the simulated systems is determined by means of a chi-square test on density and velocity dispersion profiles. For the method used to perform the chi-square test I refer to Zocchi et al. (2012) [62].

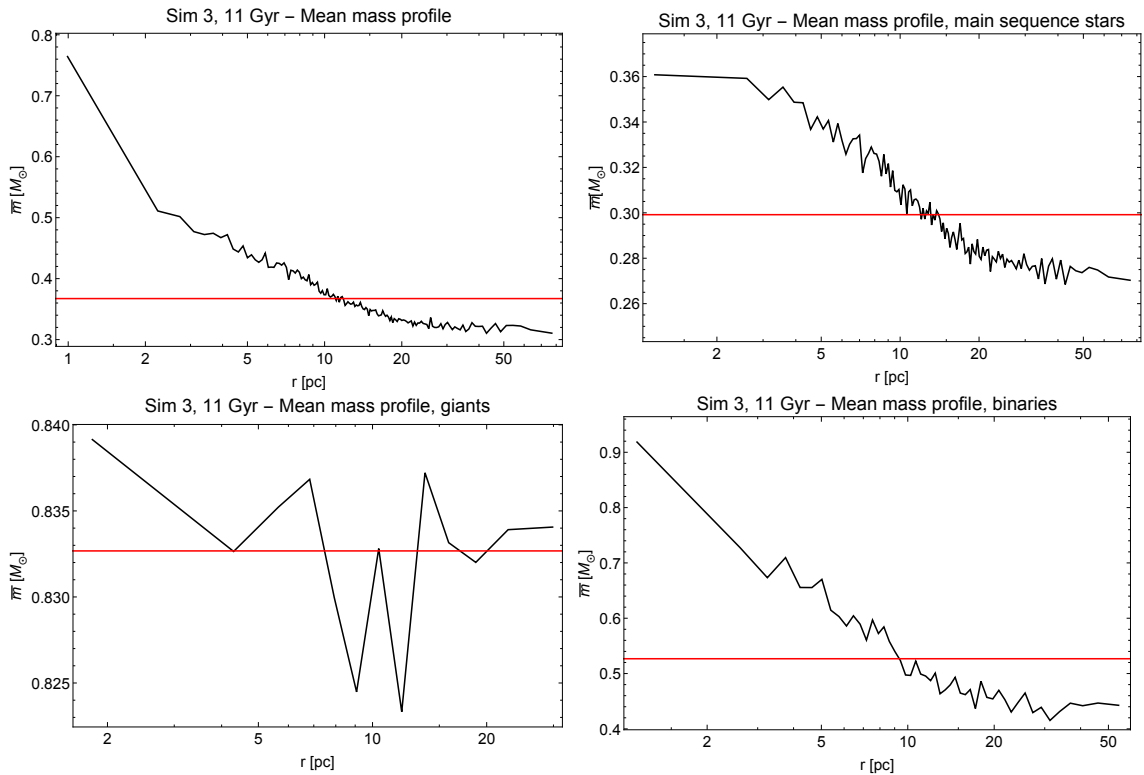


Figure 3.9: Mean mass profiles for the least relaxed simulation state of our sample, Sim 3 at 11 Gyr. See caption of Fig. 3.8. In this case the mean mass profile of remnants (right lower panel) is replaced by the mean mass profile of binaries.

3.3.1 Fit by one-component models

Construction of profiles

Best-fit one-component models are those that best represent the total density and velocity dispersion profiles. These profiles are constructed by dividing the systems into radial shells such that the number of stars in the various shells is constant, with at least 3000 stars. The number of shells N_{shells} in which the system is divided for the construction of the profiles and the number of stars in each shell N_{stars} are reported in Tab 3.6. Density profiles are constructed by dividing the mass in

Table 3.6: Shell construction for one-component models.

	Sim 1, 11 Gyr	Sim 3, 11 Gyr	Sim 5, 7 Gyr	Sim 6, 7 Gyr	Sim 5, 4 Gyr	Sim 6, 4 Gyr
N_{shells}	152	145	140	168	145	175
N_{stars}	3083	3118	3087	3098	3085	3061

stars contained in each shell by the volume of the shell, $V_{shell} = (4\pi/3)(r_{sup,shell}^3 - r_{inf,shell}^3)$, where $r_{sup,shell}$ and $r_{inf,shell}$ are the upper and the lower radii of the shell. The radial distance associated with the i-th shell r_i is the mean distance of stars

3.3. FITTING THE SIMULATED STATES WITH SELF-CONSISTENT DYNAMICAL MODELS

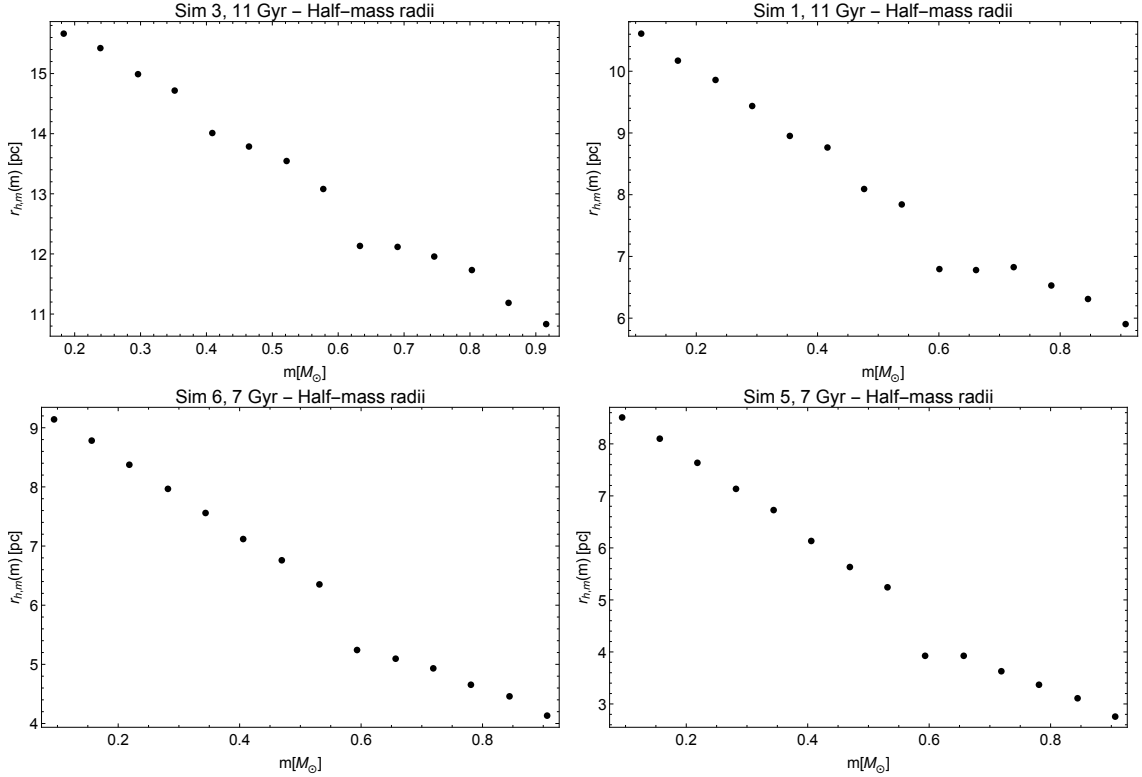


Figure 3.10: The variation of the half-mass radius with mass. All the simulations show a decreasing trend with mass, with no substantial differences between less relaxed systems (Sim 3 at 11 Gyr, left upper panel) and more relaxed systems (Sim 5 at 7 Gyr, right lower panel). This means that mass segregation sets in efficiently after very few relaxation times. The right upper panel represents Sim 1 at 11 Gyr and the left lower panel represents Sim 6 at 7 Gyr.

belonging to the shell. Velocity dispersion profiles are constructed by evaluating the square root of the total variance of the velocities of the stars in each shell. In order to perform a chi-square analysis, it is necessary to associate an error to the values of density and velocity dispersion in each shell. In my profiles, radial errors are simply the width of each shell (but they do not enter the chi-square analysis). Density and velocity dispersion uncertainties, instead, are determined by means of a bootstrap resampling, as described in Appendix A. In particular, the uncertainty on the value of a quantity is determined as the bootstrap estimate of standard error (Eq. [A.4]). Uncertainties obtained in this way are very small, typically of the order of 1%. Once the best-fit models are found, they can be used to try to match other quantities of these systems, such as the anisotropy profiles. The anisotropy profiles of the simulated states are obtained by evaluating for each shell the value of local anisotropy function $\alpha(r)$ (no uncertainty is associated in this case), as defined in Eq. (1.16). In Fig. 3.11 an example of total density, velocity dispersion and anisotropy

profiles, for Sim 1 at 11 Gyr, is shown. The anisotropy profile shows an increasing

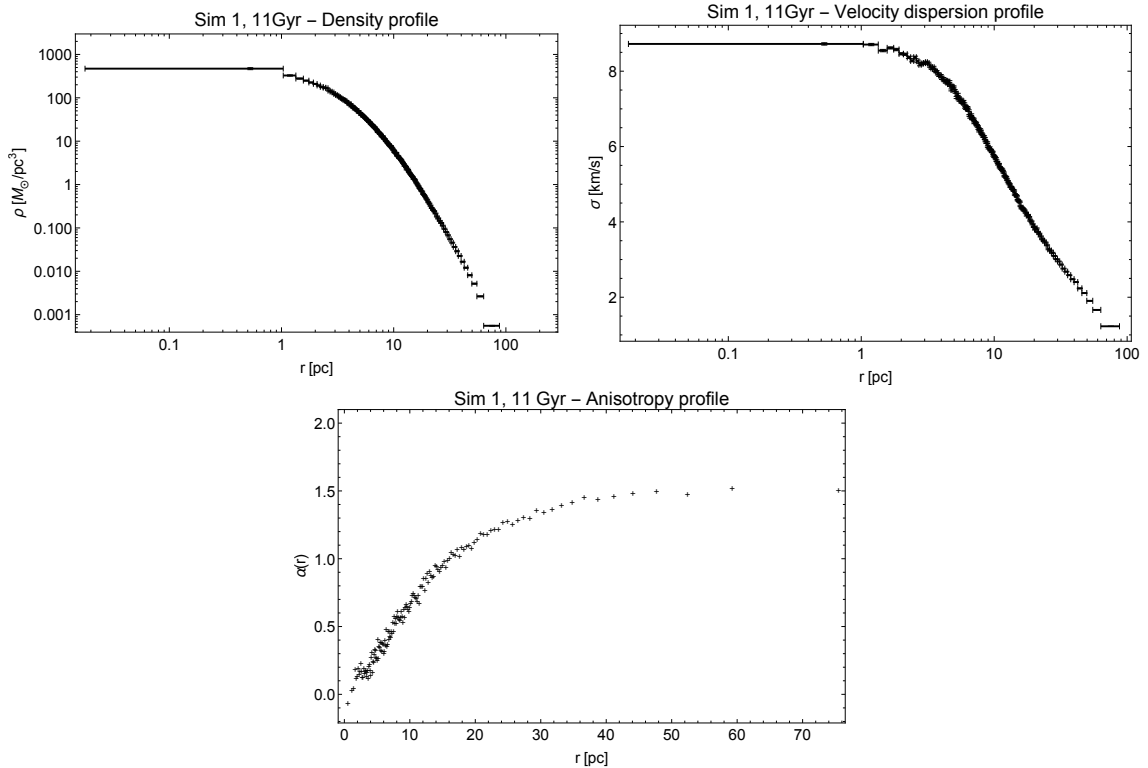


Figure 3.11: The density (left upper panel), velocity dispersion (right upper panel) and anisotropy (lower panel) profiles for Sim 1 at 11 Gyr.

trend with radius, as a consequence of the development of the core-halo structure described in Sect. 1.3.2 because the system was initialized by means of an isotropic Plummer model. More relaxed systems show higher values of α in the outermost regions, suggesting that the slow cumulative effects of relaxation processes drive the system toward a velocity distribution similar to that generated by collisionless violent relaxation, which is the physical basis under which $f^{(\nu)}$ models were originally constructed.

Fitting procedure

The best-fit model is obtained by means of a chi-square analysis by minimizing the quantity $\chi_{tot}^2 = \chi_{\rho_{tot}}^2 + \chi_{\sigma_{tot}^2}^2$, with the density chi-square defined as

$$\chi_{\rho_{tot}}^2 = \sum_{i=1}^{N_{shells}} \left[\frac{\rho_{tot}(r_i) - \rho_s \hat{\rho}(r_i/\lambda)}{\delta \rho_i} \right]^2, \quad (3.5)$$

where $\rho_{tot}(r_i)$ is the value of the total density of the i -th shell, $\delta \rho_i$ is the density error associated with the i -th shell and $\hat{\rho}$ is the dimensionless density of the model

considered. In order to compare simulated states with models, it is necessary to assign two scales, the density scale ρ_s and the length scale λ . The velocity dispersion chi-square is defined as:

$$\chi_{\sigma_{tot}}^2 = \sum_{i=1}^{N_{shells}} \left[\frac{\sigma_{tot}(r_i) - \sigma_s \hat{\sigma}(r_i/\lambda)}{\delta\sigma_i} \right]^2, \quad (3.6)$$

where $\sigma_{tot}(r_i)$ is the value of velocity dispersion in the i -th shell, $\delta\sigma_i$ is the velocity dispersion error associated with the i -th shell and $\hat{\sigma}$ is the dimensionless velocity dispersion of the model considered. Also in this case, to compare simulations with models, it is necessary to determine two scales, the velocity dispersion scale σ_s and the length scale λ . The goodness of the fit is determined by evaluating the reduced χ_{tot}^2 :

$$\tilde{\chi}_{tot}^2 = \frac{\chi_{tot}^2}{2N_{shell} - \lambda_{free}}, \quad (3.7)$$

where λ_{free} is the total number of free parameters in our models. The denominator in Eq. (3.7) represents the number of degrees of freedom N_{free} in the model considered. Similarly, we find $\tilde{\chi}_{\rho_{tot}}^2$ and $\tilde{\chi}_{\sigma_{tot}}^2$ by dividing each quantity by the corresponding number of degrees of freedom.

I point out that this is meant to be a formal analysis which has the objective to determine which model is able to give a better description of the simulated states under consideration, and not to give an accurate determination of the relevant parameters of the models under consideration.

Setting the scales

In order to compare simulated systems to models we need to set the scales λ , ρ_s and σ_s in Eq. (3.5) and Eq. (3.6). This can be done by setting two scales of the problem. The length scale λ is determined by equating the half-mass radius of the simulated states under consideration, $r_{h,sim}$, to the half-mass ratio of the model $\lambda\xi_h$:

$$\lambda = \frac{r_{h,sim}}{\xi_h}. \quad (3.8)$$

The mass scale M_s can be easily set by equating the total mass of the simulated state M_{sim} to the mass of the model $M_s \hat{M}$, where \hat{M} is the dimensionless mass of the model, to find:

$$M_s = \frac{M_{sim}}{\hat{M}}. \quad (3.9)$$

The relations which allow to determine ρ_s and σ_s depend on the model considered, as will be seen below. Values of $r_{h,sim}$ and M_{sim} for the sample of the simulated states are recorded in Tab. 3.7.

Table 3.7: Half-mass radii and total masses of the simulated states.

	Sim 1, 11 Gyr	Sim 3, 11 Gyr	Sim 5, 7 Gyr	Sim 6, 7 Gyr	Sim 5, 4 Gyr	Sim 6, 4 Gyr
$r_{h,sim} [pc]$	7.89	12.91	4.81	5.64	4.35	4.99
$M_{sim} [M_\odot]$	1.73×10^5	1.73×10^5	1.65×10^5	2.20×10^5	1.75×10^5	2.35×10^5

Residuals and error on the best-fit parameters

The i-th residual for the density profile is calculated as

$$\frac{\Delta\rho}{\rho}(r_i) = \frac{\rho_{tot}(r_i) - \rho_s \hat{\rho}(r_i/\lambda)}{\rho_{tot}(r_i)}, \quad (3.10)$$

and the i-th residual for the velocity dispersion profile is calculated as

$$\frac{\Delta\sigma}{\sigma}(r_i) = \frac{\sigma_{tot}(r_i) - \sigma_s \hat{\sigma}(r_i/\lambda)}{\sigma_{tot}(r_i)}. \quad (3.11)$$

Formal errors on parameters are calculated from of the Hessian matrix:

$$H_{ij} = \frac{\partial^2 \chi_{tot}^2}{\partial x_i \partial x_j}, \quad (3.12)$$

where x_i are the free parameters of the fit. Then we calculate the covariance matrix:

$$[E] = 2[H]^{-1}. \quad (3.13)$$

Finally the error on parameter x_i can be found as:

$$\delta x_i = (E_{ii})^{1/2}. \quad (3.14)$$

For example, in the case of the parameter Ψ for both King and $f_T(\nu)$ models:

$$\delta\Psi = \left[\frac{2}{\partial^2 \chi_{tot}^2 / \partial \Psi^2} \right]^{1/2}. \quad (3.15)$$

One-component King models

One-component King models have only one free parameter, Ψ ($\lambda_{free} = 1$). In this case, with notation introduced in Sect. 2.1.3, $\rho_s = \tilde{A}/a^{3/2}$ and $\sigma_s = a^{-1/2}$. The length scale of the system, expressed as a function of a and \tilde{A} , is

$$\lambda = \sqrt{\frac{a^{1/2}}{4\pi G \tilde{A}}}, \quad (3.16)$$

and the total mass is:

$$M = \frac{\tilde{A}}{a^{3/2}} \lambda^3 4\pi \int_0^{\xi_t} \hat{\rho}(\psi) \xi^2 d\xi = \frac{\tilde{A}}{a^{3/2}} \hat{M}, \quad (3.17)$$

where $\hat{\rho}(\psi)$ is defined in Eq. (2.17). Thus, for King models, $M_s = \tilde{A}\lambda^3/a^{3/2}$. These relations allow to determine the values of a and \tilde{A} for given λ and M_s :

$$a = \frac{\lambda}{4\pi GM_s}, \quad (3.18)$$

$$\tilde{A} = [M_s(4\pi G\lambda)^3]^{-1/2}. \quad (3.19)$$

By combining Eq. (3.18) and Eq. (3.19) with Eq. (3.8) and Eq. (3.9), we find the values of a and \tilde{A} for a fit of a model to a simulation state and thus ρ_s and σ_s . Best-fit values of Ψ for King models are reported in Tab. 3.8. The set of simulated states

Table 3.8: Best-fit results for one-component King models

	Ψ	$\tilde{\chi}_{\rho_{tot}}^2$	$\tilde{\chi}_{\sigma_{tot}}^2$	$\tilde{\chi}_{tot}^2$	N_{free}
Sim 3, 11 Gyr	5.850 ± 0.005	32.04	114.71	73.12	289
Sim 1, 11 Gyr	6.761 ± 0.005	81.80	242.02	161.38	303
Sim 6, 4 Gyr	7.151 ± 0.004	143.53	469.08	305.43	349
Sim 5, 4 Gyr	7.399 ± 0.005	143.38	496.77	318.96	289
Sim 6, 7 Gyr	7.507 ± 0.003	159.22	374.67	266.15	335
Sim 5, 7 Gyr	7.717 ± 0.006	127.29	502.052	313.54	279

has been listed from the least relaxed (Sim 3 at 11 Gyr) to the most relaxed (Sim 5 at 7 Gyr). We find a trend of increasing Ψ for more relaxed systems. The values of $\tilde{\chi}_{tot}^2$ are very high, in particular for the kinematic comparison; this is partly due to the low values of the formal uncertainties, but suggests a bad agreement between models and simulations. Apparently, King models appear to perform slightly better for less relaxed cases. The best-fit density and velocity dispersion profiles for Sim 3 at 11 are plotted in Fig. 3.12. The density profile seem to be fitted reasonably well, at variance with the kinematic profile. One-component King models cannot reproduce the central peak of velocity dispersion. This is probably related to the fact that King models have isotropic velocity distributions, whereas the simulated states have significant pressure anisotropy.

In the same format, in Fig. 3.13, we show the best-fit profiles for Sim 6 at 7 Gyr. The relevant plots for the remaining cases are found in Appendix B.1.1. In general, one-component King models are found to provide a poor representation of the simulated states, because the models exhibit an exceedingly sharp density truncation in the outer parts and an excessively high central density peak, and they are unable to match the qualitative behavior of the velocity dispersion profile.

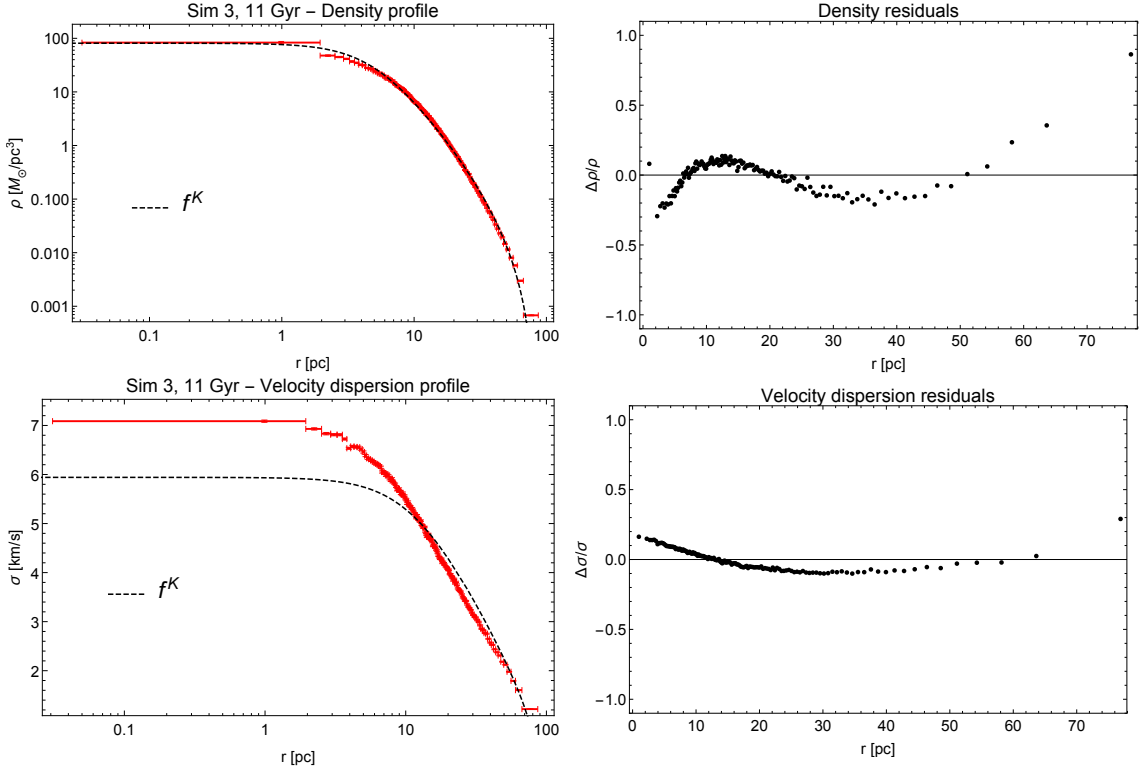


Figure 3.12: Best-fit profiles and residuals for Sim 3 at 11 Gyr for one-component King models. The upper panels shows the density profile (left) and the density residuals (right). The lower panel illustrates the velocity dispersion profile (left) and the velocity dispersion residuals (right).

One-component $f_T^{(\nu)}$ models

The $f_T^{(\nu)}$ models are characterized by two free parameters, Ψ and γ . The density and velocity dispersion scales are, with notation introduced in Sect. 2.1.4, $\rho_s = A/a^{3/2}$ and $\sigma_s = a^{-1/2}$. The length scale is:

$$\lambda = \frac{1}{da^{1/4}}, \quad (3.20)$$

whereas total mass is given by:

$$M = \frac{A}{a^{3/2}} \lambda^3 4\pi \int_0^{\xi_t} \hat{\rho}(\xi, \psi) \xi^2 d\xi = \frac{A}{a^{3/2}} \lambda^3 \hat{M}, \quad (3.21)$$

where $\hat{\rho}(\xi, \psi)$ is defined in Eq. (2.24), so that $M_s = A\lambda^3/a^{3/2}$. We can now determine, for a given γ , the values of a , d and A :

$$a = \frac{\lambda}{M_s 4\pi G \gamma}, \quad (3.22)$$

$$d = \left[\frac{M_s}{\lambda^5} (4\pi G \gamma) \right]^{1/4}; \quad (3.23)$$

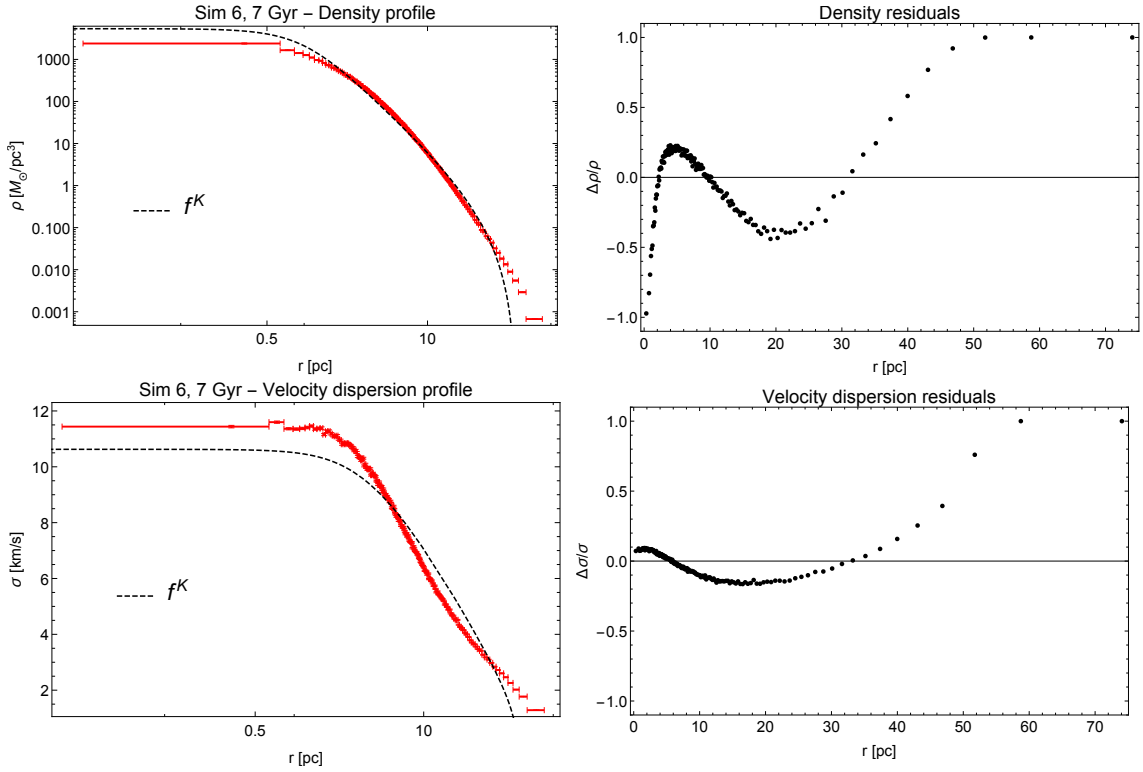


Figure 3.13: Best-fit profiles and residuals for Sim 6 at 7 Gyr for one-component King models. The upper panels shows the density profile (left) and density residuals (right). The lower panel illustrates the velocity dispersion profile (left) and velocity dispersion residuals (right).

$$A = [M_s(4\pi G \lambda \gamma)^3]^{-1/2}. \quad (3.24)$$

By combining Eq. (3.22) and Eq. (3.24) with Eq. (3.8) and Eq. (3.9) we can find the values of a and A for a fit of a model to the simulated state and thus ρ_s and σ_s . Best-fit results for $f_T^{(\nu)}$ models are reported in Tab. 3.9. By comparing χ^2_{tot} obtained with these models with that in Tab. 3.8, we notice a significant improvement with respect to King models. Also here there is a trend of higher Ψ for more relaxed systems.

The best-fit result for Sim 1 at 11 Gyr is presented in Fig. 3.14. The $f_T^{(\nu)}$ density profile is able to give a good representation of that of the simulated state, with differences only in the central shell. As to the velocity dispersion profile, the model cannot reproduce the central peak that characterizes the simulation but its shape is in better agreement with respect to the best-fit King model. The best-fit profiles for the other five simulated states are shown in Appendix B.1.2. In general, the $f_T^{(\nu)}$ models present a milder density truncation with respect to King models, but they fail to reproduce the central kinematic peak exhibited by the simulated states.

Interestingly, the $f^{(\nu)}$, as shown in Fig. 3.15, give a good description of the pres-

Table 3.9: Best-fit results for one-component $f_T^{(\nu)}$ models

	Ψ	γ	$\tilde{\chi}_{\rho_{tot}}^2$	$\tilde{\chi}_{\sigma_{tot}}^2$	$\tilde{\chi}_{tot}^2$	N_{free}
Sim 3, 11 Gyr	5.03 ± 0.01	26.0 ± 0.2	5.44	41.44	23.36	288
Sim 1, 11 Gyr	5.46 ± 0.01	55.6 ± 0.3	2.88	41.68	22.20	302
Sim 6, 4 Gyr	5.26 ± 0.02	76.8 ± 0.2	3.00	49.93	26.39	348
Sim 5, 4 Gyr	5.92 ± 0.01	80.0 ± 0.3	5.15	56.26	30.60	288
Sim 6, 7 Gyr	6.20 ± 0.01	58.0 ± 0.2	6.93	49.93	28.35	334
Sim 5, 7 Gyr	7.06 ± 0.01	52.4 ± 0.2	10.83	55.91	33.25	278

sure anisotropy for relaxed systems (like Sim 6 at 7 Gyr) whereas Sim 1 at 11 Gyr presents a lower degree of radial anisotropy with respect to that of model. This supports the view that collisions drive the system toward a velocity distribution similar to that generated by violent relaxation. This is probably also the reason behind the better agreement between velocity dispersions of these profiles with respect to that of isotropic King models.

We can conclude that one-component $f_T^{(\nu)}$ models give a good description of simulations, with the exception of velocity dispersions in the central regions, and are able to reproduce even the anisotropy profile in case of more relaxed systems. In general, these models are a far better representation of simulated systems with respect to King models.

3.3.2 Two-component models

Definition of the two components

As already anticipated in Sect. 2.2, multi-component models represent a simple way to incorporate central energy equipartition and mass segregation. In particular, I refer to the two-component models introduced in Sect. 2.2. First, I have divided the systems into a light component, with mass m_{light} , and a heavy component, with mass m_{heavy} . In Sect. 3.1 (in particular, see Tab. 3.4) I identified four classes of stars: single main sequence stars, single giant stars, single remnants and binaries. In Tab. 3.10 I report, for each component, the mean star mass. Mean masses of giants, remnants and binaries are always more than twice the mean mass of main sequence stars. I have thus identified the main sequence stars with the light component (with mass $m_{light} = \bar{m}_{MS}$) and have combined the other classes into the heavy component (with m_{heavy} equal to the mean mass of stars belonging to these three classes).

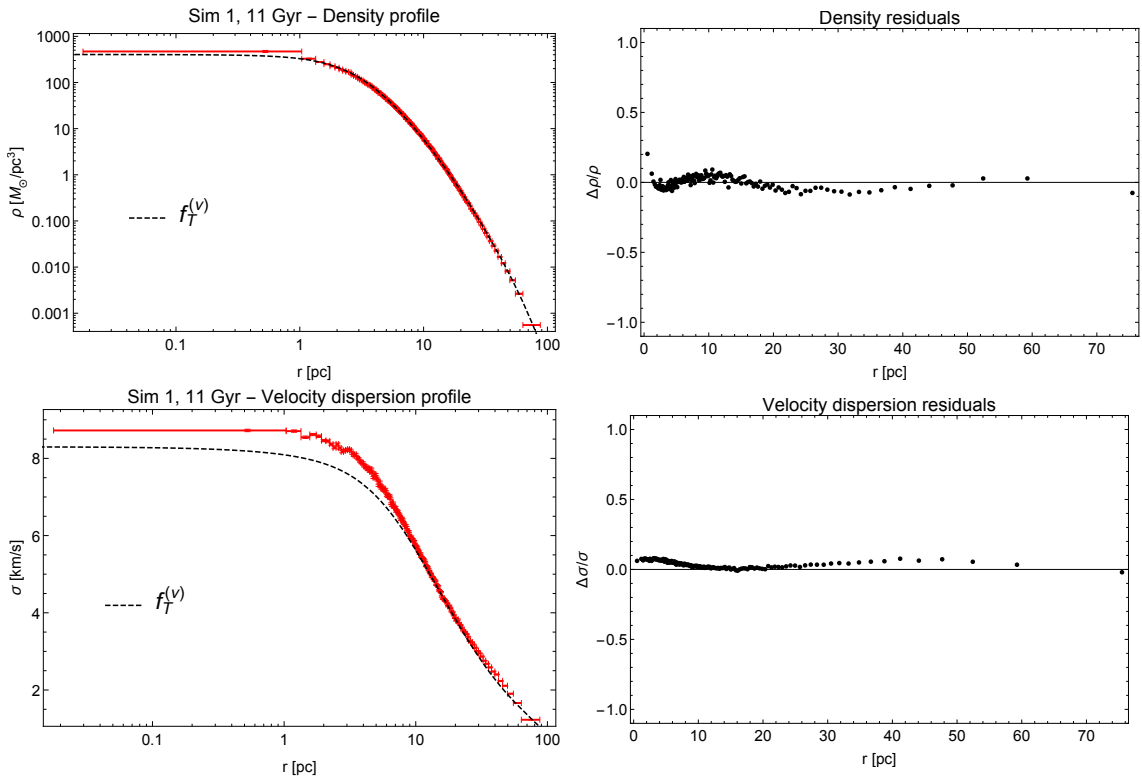


Figure 3.14: Best-fit profiles and residuals for Sim 1 at 11 Gyr for one-component $f_T^{(\nu)}$ models. The upper panels shows the density profile (left) and the density residuals (right). The lower panel illustrates the velocity dispersion profile (left) and the velocity dispersion residuals (right).

In Tab. 3.11 I report the total masses of all the classes of stars. In particular, the last column reports the value of S , which represents the maximum value of $M_{\text{heavy}}/M_{\text{light}}(m_{\text{heavy}}/m_{\text{light}})^{3/2}$ in the conjecture of the Spitzer ‘‘instability’’ (Eq. (2.78)). According to Spitzer (see Sect. 2.3), the maximum value of S for a system in global energy equipartition should be $S_{\max} = 0.16$. Therefore, the components that I have just defined violate Spitzer criterion by about an order of magnitude. To be sure, these systems do not fulfill the global equipartition condition. In addition, as reported in Tab. 3.13, the condition $M_{\text{heavy}} \ll M_{\text{light}}$ and $m_{\text{heavy}} \gg m_{\text{light}}$ is not really viable. In conclusion, the Spitzer criterion is not applicable to the present test.

Fitting procedure

For two-component models, the chi-square test described in Sect. 3.3.1 is performed on the density and velocity dispersion profiles of the two components separately. I first constructed light and heavy component profiles following the same

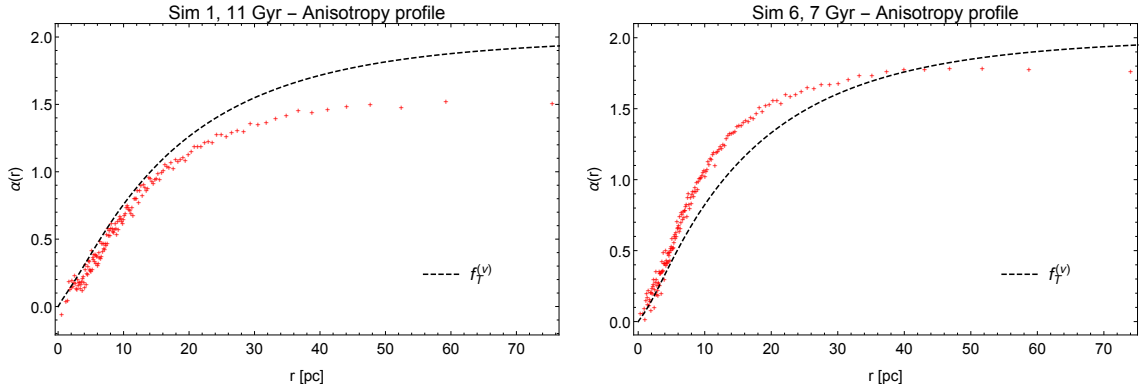


Figure 3.15: Anisotropy profiles of Sim 1 at 11 Gyr (left panel) and Sim 6 at 7 Gyr (right panel) compared with those from the best-fit one-component $f_T^{(\nu)}$ models.

Table 3.10: Definition of the components and values of their mean masses.

	Light stars	Heavy stars			
	$\bar{m}_{MS} [M_\odot]$	$\bar{m}_{giants} [M_\odot]$	$\bar{m}_{remn} [M_\odot]$	$\bar{m}_{bin} [M_\odot]$	$\bar{m}_{heavy} [M_\odot]$
Sim 1, 11 Gyr	0.30	0.85	0.74	0.76	0.74
Sim 3, 11 Gyr	0.30	0.83	0.75	0.81	0.77
Sim 5, 7 Gyr	0.32	0.94	0.76	0.73	0.75
Sim 6, 7 Gyr	0.32	0.94	0.77	0.73	0.75
Sim 5, 4 Gyr	0.33	1.12	0.81	0.77	0.81
Sim 6, 4 Gyr	0.34	1.12	0.82	0.78	0.80

procedure as in Sect. 3.3.1. The number of shells in which simulations were divided ($N_{shells,light}$ for the light component and $N_{shells,heavy}$ for the heavy component) are reported in Tab. 3.12, together with the number of stars contained in each ($N_{stars,light}$ and $N_{stars,heavy}$). I put at least 3000 stars in each light component shell and at least 1300 heavy stars in each heavy component shell. The two snapshots relative to Sim 6 present higher values of $N_{shell,heavy}$ because of their high binary fraction (see Tab. 3.1).

Table 3.11: Total masses of the components and Spitzer criterion.

	Light stars	Heavy stars				$S (S_{max} = 0.16)$
	$M_{MS} [M_\odot]$	$M_{giants} [M_\odot]$	$M_{remn} [M_\odot]$	$M_{bin} [M_\odot]$	$M_{heavy} [M_\odot]$	
Sim1, 11 Gyr	1.20×10^5	1.33×10^3	4.07×10^4	1.05×10^4	5.25×10^4	1.68
Sim3, 11 Gyr	1.11×10^5	1.16×10^3	4.06×10^4	2.06×10^4	6.23×10^4	2.31
Sim 5, 7 Gyr	1.17×10^5	1.58×10^3	3.54×10^4	1.11×10^4	4.81×10^4	1.52
Sim 6, 7 Gyr	1.29×10^5	1.71×10^3	4.46×10^4	4.52×10^4	9.15×10^4	2.55
Sim 5, 4 Gyr	1.31×10^5	2.00×10^3	2.99×10^4	1.25×10^4	4.44×10^4	1.28
Sim 6, 4 Gyr	1.43×10^5	2.18×10^3	3.81×10^4	5.12×10^4	9.15×10^4	2.33

Table 3.12: Bin construction of the two-component models fit.

	Sim 1, 11 Gyr	Sim 3, 11 Gyr	Sim 5, 7 Gyr	Sim 6, 7 Gyr	Sim 5, 4 Gyr	Sim 6, 4 Gyr
$N_{\text{shells},\text{light}}$	130	120	121	132	128	138
$N_{\text{stars},\text{light}}$	3083	3118	3087	3098	3056	3061
$N_{\text{shells},\text{heavy}}$	51	60	47	80	41	84
$N_{\text{stars},\text{heavy}}$	1386	1350	1356	1515	1341	1354

For each simulated case I have evaluated $\chi^2_\rho = \chi^2_{\rho_{\text{light}}} + \chi^2_{\rho_{\text{heavy}}}$ and $\chi^2_\sigma = \chi^2_{\sigma_{\text{light}}} + \chi^2_{\sigma_{\text{heavy}}}$, where

$$\chi^2_\rho = \sum_{i=1}^{N_{\text{shell},\text{light}}} \left[\frac{\rho_{\text{light}}(r_i) - \rho_{s,1}\hat{\rho}_1(r_i/\lambda)}{\delta\rho_{i,\text{light}}} \right]^2 + \sum_{i=1}^{N_{\text{shell},\text{heavy}}} \left[\frac{\rho_{\text{heavy}}(r_i) - \rho_{s,2}\hat{\rho}_2(r_i/\lambda)}{\delta\rho_{i,\text{heavy}}} \right]^2, \quad (3.25)$$

$$\chi^2_\sigma = \sum_{i=1}^{N_{\text{shell},\text{light}}} \left[\frac{\sigma_{\text{light}}(r_i) - \sigma_{s,1}\hat{\sigma}_1(r_i/\lambda)}{\delta\sigma_{i,\text{light}}} \right]^2 + \sum_{i=1}^{N_{\text{shell},\text{heavy}}} \left[\frac{\sigma_{\text{heavy}}(r_i) - \sigma_{s,2}\hat{\sigma}_2(r_i/\lambda)}{\delta\sigma_{i,\text{heavy}}} \right]^2, \quad (3.26)$$

and minimized $\chi^2_{\text{tot}} = \chi^2_\rho + \chi^2_\sigma$. For the models I use the same notation as in Sect. 2.2, indicating with the index 1 the quantities associated with the light component of the model ($\hat{\rho}_1$ and $\hat{\sigma}_1$) and with index 2 quantities associated with the heavy component ($\hat{\rho}_2$ and $\hat{\sigma}_2$). In this case, $N_{\text{free}} = 2N_{\text{shell},\text{light}} + 2N_{\text{shell},\text{heavy}} - \lambda_{\text{free}}$.

The i-th residual for the density profile of the j-th component is calculated as

$$\left(\frac{\Delta\rho}{\rho}(r_i) \right)_j = \frac{\rho_j(r_i) - \rho_{s,j}\hat{\rho}_j(r_i/\lambda)}{\rho_j(r_i)}, \quad (3.27)$$

and the i-th residual for the velocity dispersion profile of the j-th component is calculated as

$$\left(\frac{\Delta\sigma}{\sigma}(r_i) \right)_j = \frac{\sigma_j(r_i) - \sigma_{s,j}\hat{\sigma}_j(r_i/\lambda)}{\sigma_j(r_i)}. \quad (3.28)$$

Setting the scales

The presence of an additional component increases the number of scales. However, as we saw in Sect. 2.2.1 and in Sect. 2.2.2, we can consider some physical assumptions to reduce the problem to the same number of free parameter as in the one-component case. In particular, we can assign the ratio between the total masses, $M_{\text{light}}/M_{\text{heavy}}$, to set the ratio between the density scales $\rho_{s,2}/\rho_{s,1}$ (by means of Eq. (2.34) in the case of King models and Eq. (2.42) in the case of $f_T^{(\nu)}$ models). The ratio between the velocity dispersion scales, $\sigma_{s,2}/\sigma_{s,1}$, can be set by means of the assumption of central partial energy equipartition (Eq. (2.35) in the case of the King models and Eq. (2.43) for the $f_T^{(\nu)}$ models). The value of η , which quantifies

the degree of central energy equipartition, has been chosen by considering the ratio between the velocity dispersions of the two components in the central shells. As we can see from Tab. 3.13, more relaxed systems present higher values of η , suggesting that relaxation drives these systems toward a condition of central energy equipartition, but values close to $\eta = 0.5$ are never attained. Table 3.13 also lists the ratios between the single masses and total masses of the two components components.

Table 3.13: Basic parameters for two-component models.

	Sim 1, 11 Gyr	Sim 3, 11 Gyr	Sim 5, 7 Gyr	Sim 6, 7 Gyr	Sim 5, 4 Gyr	Sim 6, 4 Gyr
m_{heavy}/m_{light}	2.46	2.57	2.38	2.34	2.42	2.37
M_{light}/M_{heavy}	2.29	1.78	2.43	1.40	2.94	1.57
η	0.232	0.191	0.270	0.269	0.259	0.230

As the problem now presents the same number of free parameters as for one-component models, only the length and the mass scales of the light component need to be set. This can be done in the same way as for one-component models. The length scale can be set by dividing the half-mass radius of the light component of the simulation, $r_{h,light}$, by the dimensionless value of the light component half-mass radius obtained from the model $\xi_{h,1}$:

$$\lambda = \frac{r_{h,light}}{\xi_{h,1}}. \quad (3.29)$$

The mass scale of the light component, $M_{s,1}$ can be set by equating the total mass of the light component M_{light} in the simulated system to the mass of the light component in the model $M_{s,1}\hat{M}_1$, to find:

$$M_{s,1} = \frac{M_{light}}{\hat{M}_1}. \quad (3.30)$$

Values of $r_{h,light}$ and M_{light} for the sample of simulated cases are shown in Tab. 3.14.

Table 3.14: Physical scales for the two-component models.

	Sim 1, 11 Gyr	Sim 3, 11 Gyr	Sim 5, 7 Gyr	Sim 6, 7 Gyr	Sim 5, 4 Gyr	Sim 6, 4 Gyr
$M_{light} [M_\odot]$	1.20×10^5	1.11×10^5	1.17×10^5	1.29×10^5	1.31×10^5	1.43×10^5
$r_{h,light}$ [pc]	8.84	14.11	5.79	6.75	4.93	5.68

Two-component King models

In the two-component King models, the scale length is (for notation, we refer to Sect. 2.2.1):

$$\lambda = \sqrt{\frac{a_1^{1/2}}{4\pi G \tilde{A}_1}}. \quad (3.31)$$

In this case, the scales can be set in the same way as for one-component models (Sect. 3.3.1), with a and \tilde{A} replaced by a_1 and \tilde{A}_1 . We thus have:

$$a_1 = \frac{\lambda}{4\pi GM_{s,1}}, \quad (3.32)$$

$$\tilde{A}_1 = [M_{s,1}(4\pi G\lambda)^3]^{-1/2}. \quad (3.33)$$

By combining Eq. (3.32) and Eq. (3.33) with Eq. (3.29) and Eq. (3.30) we can find the value of a_1 and \tilde{A}_1 for a given comparison between model and simulation and thus $\rho_{s,1} = \tilde{A}_1/a_1^{3/2}$ and $\sigma_{s,1} = a_1^{-1/2}$.

Best-fit concentration parameters are recorded in Tab. 3.15. As for one-component

Table 3.15: Concentration parameter for the best-fit two-component King models.

	Ψ	$\tilde{\chi}_{\rho_1}^2$	$\tilde{\chi}_{\sigma_1}^2$	$\tilde{\chi}_{\rho_2}^2$	$\tilde{\chi}_{\sigma_2}^2$	$\tilde{\chi}_{tot}^2$	N_{free}
Sim 3, 11 Gyr	4.700 ± 0.002	68.44	99.95	31.12	36.24	67.09	359
Sim 1, 11 Gyr	5.165 ± 0.003	104.06	357.93	53.56	162.53	195.59	361
Sim 6, 4 Gyr	4.651 ± 0.003	156.59	689.87	45.19	219.91	312.14	443
Sim 5, 4 Gyr	5.651 ± 0.004	160.24	712.63	86.34	157.21	358.92	337
Sim 6, 7 Gyr	4.855 ± 0.004	164.17	671.29	67.80	217.85	312.82	423
Sim 5, 7 Gyr	5.680 ± 0.003	201.66	735.86	49.67	150.21	364.36	335

models, values of $\tilde{\chi}_{tot}^2$ are very high, of the order of some hundreds. Also in this case the kinematic comparison gives the worst result, in particular for the first component ($\tilde{\chi}_{\sigma_1}^2$). The values of $\tilde{\chi}_{tot}^2$ for two-component King models $\tilde{\chi}_{tot}^2$ are even higher than for one-component King models.

In Fig. 3.16 and Fig. 3.17 the best-fit two-component King models is shown for Sim 3 at 11, which presents the lowest value of χ_{tot}^2 . There is little agreement between models and simulated systems, except for the density profile of the heavy component. The light component density profile model overshoots in the central regions and exhibits a truncation that is too sharp. The velocity dispersion profiles, as already noted for one-component models, do not really match those of the simulated states. In Fig. 3.18 I show the total profiles obtained from best-fit mode, by defining the total density as

$$\rho(r) = \rho_1(r) + \rho_2(r), \quad (3.34)$$

and the total velocity dispersion as

$$\sigma(r) = \sqrt{\frac{\rho_1(r)\sigma_1^2(r) + (m_1/m_2)\rho_2(r)\sigma_2^2(r)}{\rho_1(r) + (m_1/m_2)\rho_2(r)}}, \quad (3.35)$$

3.3. FITTING THE SIMULATED STATES WITH SELF-CONSISTENT DYNAMICAL MODELS

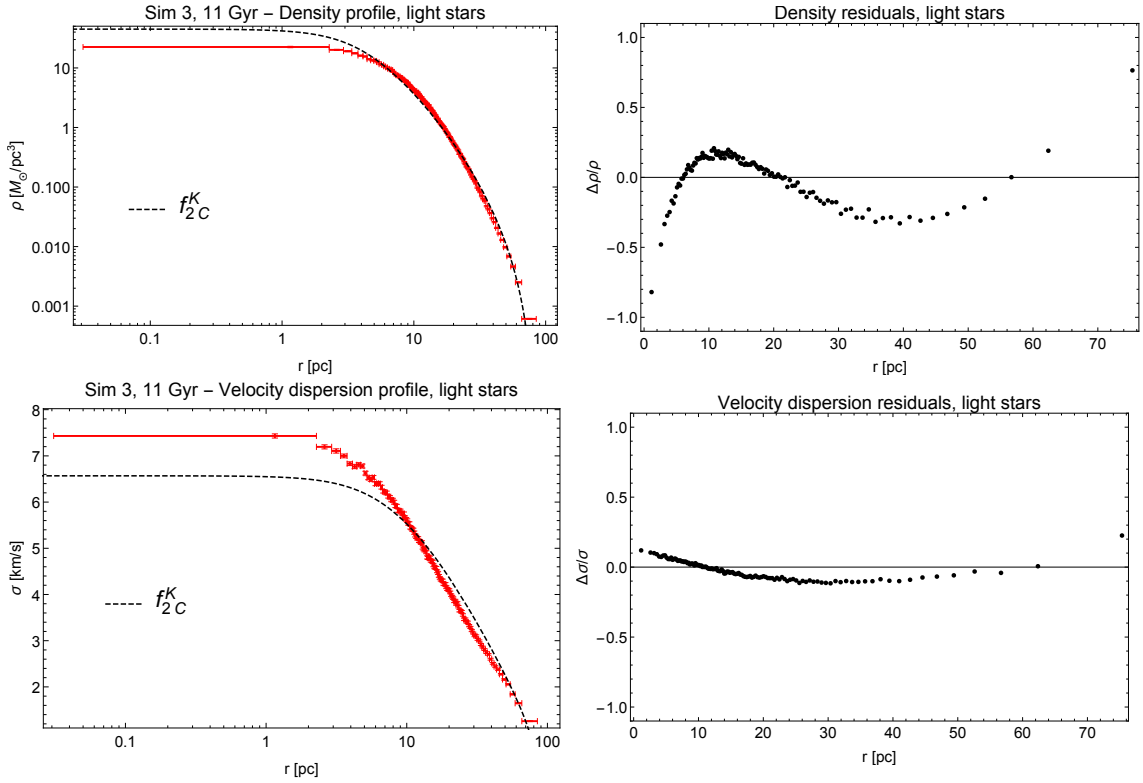


Figure 3.16: Best-fit profiles and residuals for the light component for Sim 3 at 11 Gyr from two-component King models. In the upper panels we show the density profile (left) and the density residuals (right). In the lower panel we show the velocity dispersion profile (left) and the velocity dispersion residuals (right).

where m_1/m_2 is set equal to m_{light}/m_{heavy} of the simulated states under consideration. Total velocity dispersion is obtained by weighting the velocity dispersion of each component by its number density. Also for total profiles there is little agreement between profiles and data.

The complete set of results for the two-component King models is recorded in Appendix B.2.1. The King models present a truncation that is too sharp, and the central densities predicted by these models are too high with respect to those of the simulated states. In addition, the velocity dispersion profiles of the models are too flat in the central regions and decrease too rapidly in the outermost regions. We conclude that, even by introducing a second component, the King models cannot be used to give a proper description of the systems under consideration.

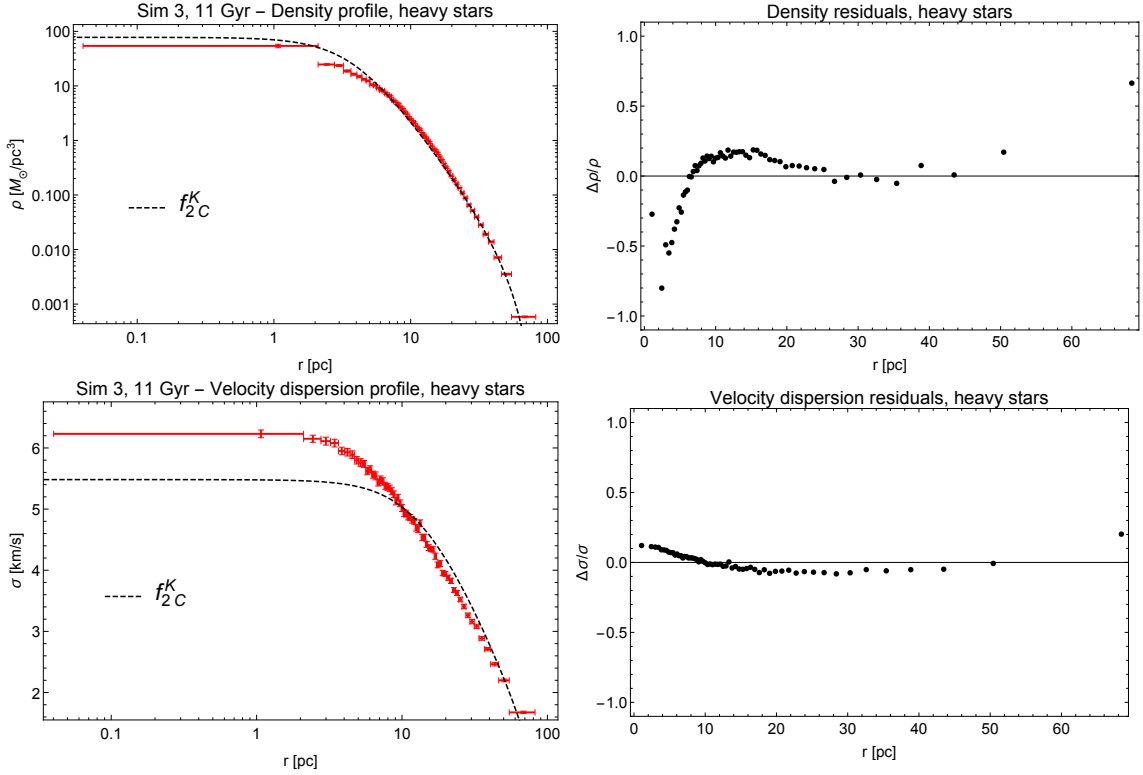


Figure 3.17: Best-fit profiles and residuals for the heavy component of Sim 3 at 11 Gyr from two-component King models. In the upper panels we show the density profile (left) and the density residuals (right). In the lower panel we show the velocity dispersion profile (left) and the velocity dispersion residuals (right).

Two-component $f_T^{(\nu)}$ models

For the $f_T^{(\nu)}$ models, the length scale is (with the notation introduced in Sect. 2.2.2):

$$\lambda = \frac{1}{a_1^{1/4} d_1} \quad (3.36)$$

Thus physical scales can be assigned in the same as in one-component models, replacing a , A and d by a_1 , A_1 and d_1 . We have:

$$a_1 = \frac{\lambda}{M_{s,1} 4\pi G \gamma}, \quad (3.37)$$

$$d_1 = \left[\frac{M_{s,1}}{\lambda^5} (4\pi G \gamma) \right]^{1/4}, \quad (3.38)$$

$$A_1 = [M_{s,1} (4\pi G \lambda \gamma)^3]^{-1/2}. \quad (3.39)$$

Combining Eq. (3.37) and Eq. (3.39) with Eq. (3.29) and Eq. (3.30) we can find the values of a_1 , d_1 and A_1 and thus of $\rho_{s,1} = A_1/a_1^{3/2}$ and $\sigma_{s,1} = a_1^{-1/2}$.

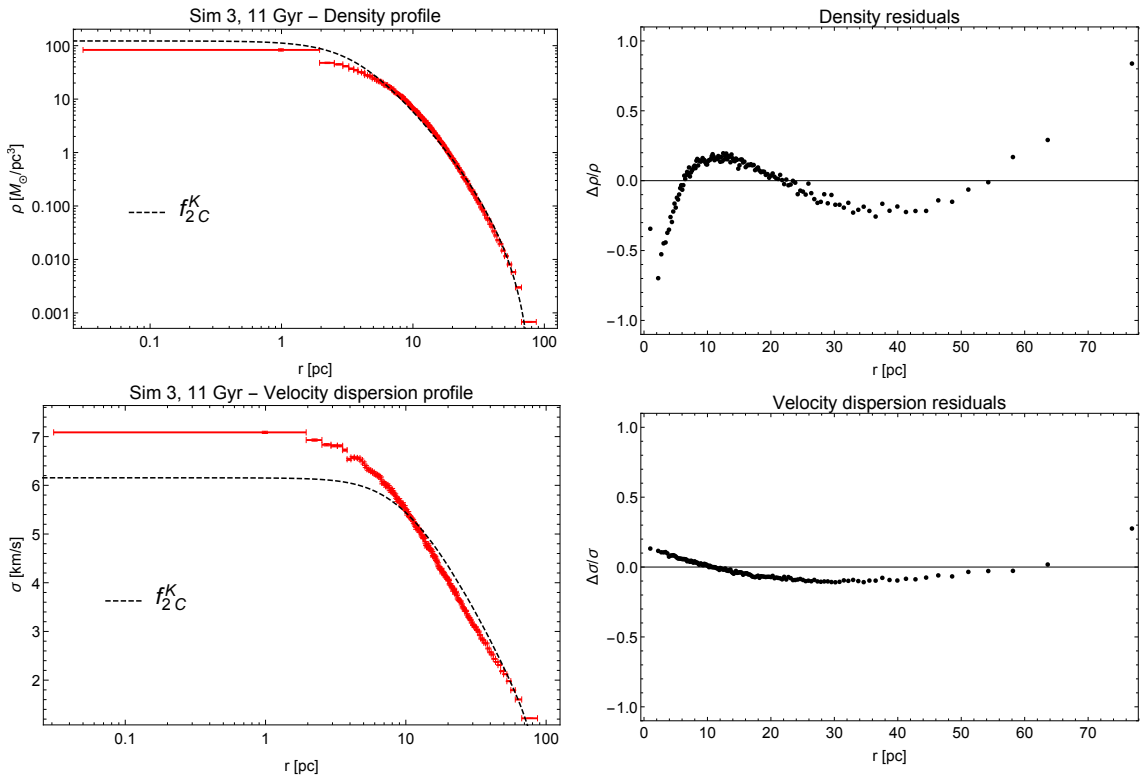


Figure 3.18: Total profiles and residuals of the best-fit result for Sim 3 at 11 Gyr with two-component King models. In the upper panels we show the density profile (left) and the density residuals (right). In the lower panel we show the velocity dispersion profile (left) and the velocity dispersion residuals (right).

The best-fit results for two-component $f_T^{(\nu)}$ models are reported in Tab. 3.16. By comparing $\tilde{\chi}_{tot}^2$ obtained with these models with that in Tab. 3.15, we notice a significant improvement with respect to King models also in the case of the two-component models. There is a good agreement between models and simulated systems. In particular, we can notice that the values for $\chi_{\rho_1}^2$ and $\chi_{\rho_2}^2$ are low: these models are a good representation of the density profiles of the simulated states.

The best-fit result with minimum chi-square, Sim 5 at 7 Gyr (Fig. 3.19 and Fig. 3.20), shows a good matching with the density profiles of the simulated states: this model intercepts all the uncertainty bars. The velocity dispersion profiles of the model show, in this case too, quite different shapes with respect to those of the simulated state, with differences of the order of 5% in central regions and of the order of 20% for the outermost point. As opposed to the one-component $f_T^{(\nu)}$ models, two-component models reproduce the peak of the velocity dispersion profile. The total density and velocity dispersion profiles (defined in Eq. (3.34) and Eq. (3.35), respectively) of the best-fit two-component $f_T^{(\nu)}$ model exhibit a good matching with total profiles of the simulated state, as shown in Fig. 3.21. Finally, the anisotropy

Table 3.16: Best-fit parameters for two-component $f_T^{(\nu)}$ models.

	Ψ	γ	$\chi^2_{\rho_1}$	$\chi^2_{\sigma_1}$	$\chi^2_{\rho_2}$	$\chi^2_{\sigma_2}$	χ^2_{tot}	N_{free}
Sim 3, 11 Gyr	3.85 ± 0.01	28.4 ± 0.1	18.90	21.90	5.25	15.58	16.82	358
Sim 1, 11 Gyr	4.467 ± 0.002	47.8 ± 0.2	13.58	18.05	7.73	15.89	14.46	360
Sim 6, 4 Gyr	4.103 ± 0.009	67.4 ± 0.2	9.65	20.82	8.15	8.81	12.52	442
Sim 5, 4 Gyr	4.708 ± 0.001	67.0 ± 0.2	7.02	30.92	8.11	13.22	16.70	336
Sim 6, 7 Gyr	4.115 ± 0.003	56.6 ± 0.2	3.68	21.35	7.05	6.59	10.23	422
Sim 5, 7 Gyr	5.46 ± 0.02	49.0 ± 0.2	7.13	20.76	16.34	13.05	13.89	334

profiles of the best-fit model (Fig. 3.22) can reproduce the local degree of anisotropy for the both components. Only in the outermost regions the degree of anisotropy predicted by the model is too high ($\alpha \rightarrow 2$) with respect to that found in the simulated state. This analysis seems to confirm the picture according to which collisions tend to drive the system to a velocity distribution similar to that generated by means of violent relaxation.

The complete set of results for the two-component $f_T^{(\nu)}$ models is recorded in Appendix B.2.2. Two-component $f_T^{(\nu)}$ models give a good description of the density and the velocity dispersion profiles for the two components of the simulated states. In addition, they are able to reproduce the central peak in the velocity dispersion profiles. There is also a good agreement between the anisotropy profiles of the simulated states and those obtained from the best-fit models but only for more relaxed systems.

We can conclude that two-components $f_T^{(\nu)}$ provide a good representation of the simulated states, in particular for more relaxed systems. They are able to reproduce the different behaviors of the density profiles and the central velocity dispersions of the two components, thus incorporating mass segregation and central energy equipartition. For this reason, in Sect. 3.4, these models are considered to take into account the variation of the M/L ratio generated by mass segregation.

3.4 M/L ratio and comparison with observations

In Sect. 1.3.4 we explained that mass segregation has important consequences on the local value of the mass-to-light ratio, M/L. In this respect, we also referred to the results found by Bianchini et al. (2017) [10] by considering the set of simulations studied in the present thesis. Giants and stellar remnants both segregate towards the center of clusters, but they obviously generate opposite variations of the M/L ratio: dark remnants increase the M/L value, whereas bright red giants tend to

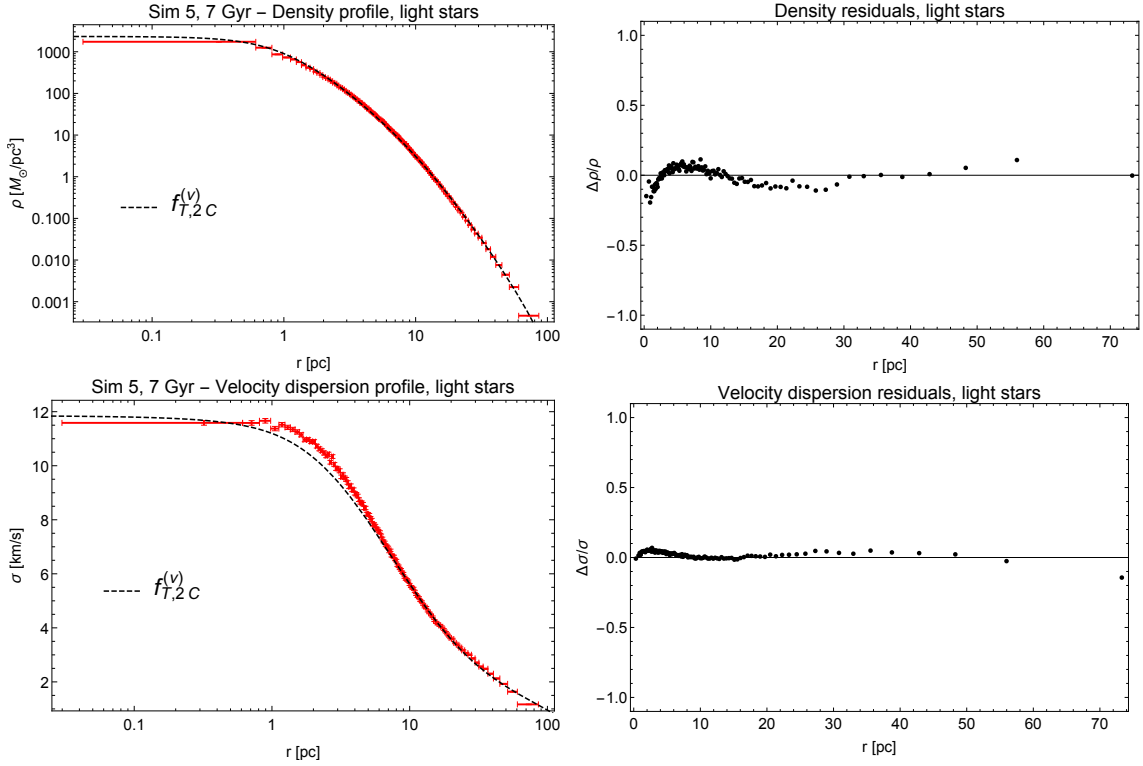


Figure 3.19: Best-fit profiles and residuals for the light component of Sim 5 at 7 Gyr from two-component $f_T^{(\nu)}$ models. In the upper panels we show the density profile (left) and the density residuals (right). In the lower panel we show the velocity dispersion profile (left) and the velocity dispersion residuals (right).

lower it. The combined effects of mass segregation can thus lead to variations of the M/L ratio in central regions, that is a radial gradient in its profile. Bianchini et al. (2017) [10] noted that the projected M/L profiles may exhibit a dip in the very central regions, reach a minimum and then increase as we move outward.

We could wonder if two-component $f_T^{(\nu)}$ models which, as described in Sect. 3.3.2, incorporate mass segregation and give a good representation of the density profile, are also able to reproduce the complex behavior of the M/L ratio. I have constructed intrinsic M/L profiles (of the total system and of the single components) of each simulated state by dividing the system into shells (as described in Sect. 3.3.1) and evaluating the ratio between total mass and the total luminosity in the V-band in each shell. I then assigned to the two components of $f_T^{(\nu)}$ models a representative luminosity equal to the mean luminosity of that component in the simulated state. In Tab. 3.17 I list the mean luminosities of each component in the simulated states and their M/L ratios. Values of the M/L ratio for the heavy component are generally lower than those for the light component because of the high luminosity of giant stars (see also Tab. 3.4).

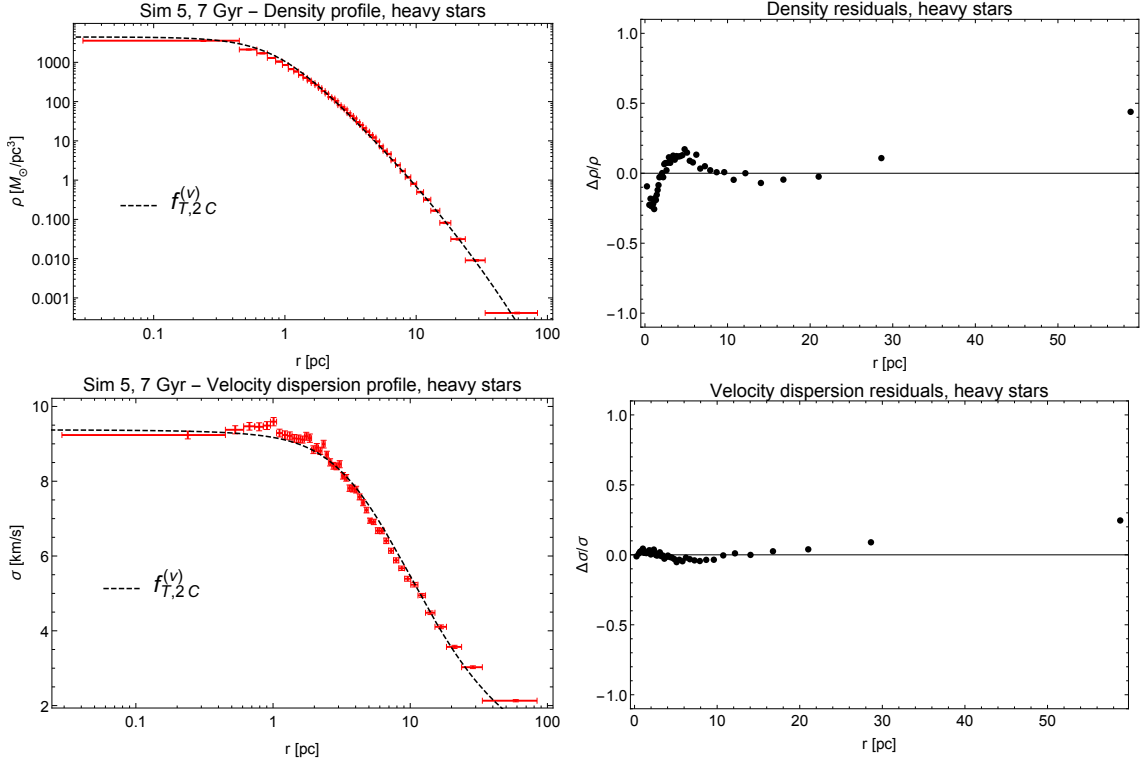


Figure 3.20: Best-fit profiles and residuals for the heavy component of Sim 5 at 7 Gyr from two-component $f_T^{(\nu)}$ models. In the upper panels we show the density profile (left) and the density residuals (right). In the lower panel we show the velocity dispersion profile (left) and the velocity dispersion residuals (right).

Table 3.17: Mean star luminosities and M/L ratios of two components

	Sim 1, 11 Gyr	Sim 3, 11 Gyr	Sim 5, 4 Gyr	Sim 6, 4 Gyr	Sim 5, 7 Gyr	Sim 6, 4 Gyr
$\bar{L}_{\text{light}} [L_\odot]$	0.09	0.09	0.19	0.205	0.13	0.13
$\bar{L}_{\text{heavy}} [L_\odot]$	1.15	0.84	3.78	2.29	2.26	1.34
$(M/L)_{\text{light}} [M_\odot/L_\odot]$	3.26	3.48	1.72	1.66	2.54	2.44
$(M/L)_{\text{heavy}} [M_\odot/L_\odot]$	0.65	0.92	0.21	0.35	0.33	0.56

I evaluated the total M/L ratio of the two-component $f_T^{(\nu)}$ models by dividing the models into 400 radial shells and evaluating the ratio between the total mass and the total luminosity in each shell.

In Fig. 3.23 I illustrate the M/L ratios for four simulated states (black line), compared with those obtained from the best-fit from two-component $f_T^{(\nu)}$ models (red lines). The models under consideration cannot reproduce the M/L profiles of the simulated states. There is a mild agreement only in the central parts of the system, usually out to a distance of the order of the half-mass radius (see Tab. 3.7) but the models predict too low values for the M/L ratio in the outer regions. The reason behind this discrepancy is mass segregation within the light component. As

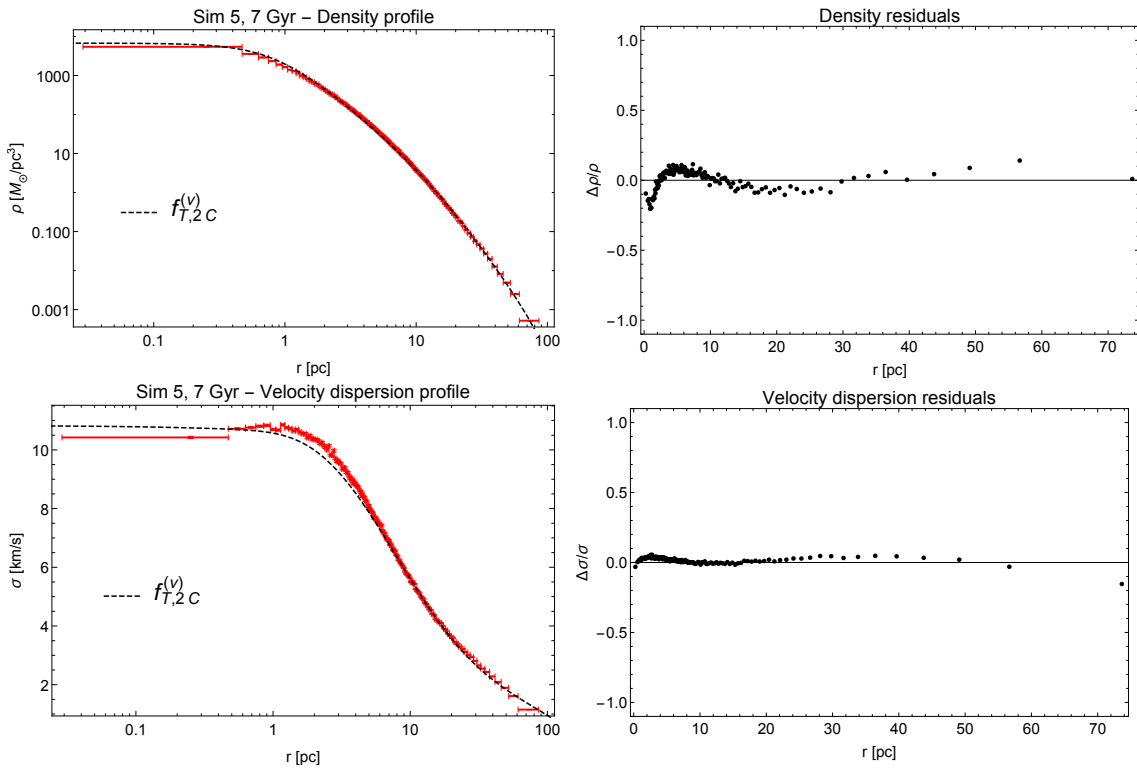


Figure 3.21: Total profiles and residuals of Sim 5 at 7 Gyr from the best-fit result of two-component $f_T^{(\nu)}$ model. In the upper panels we show the density profile (left) and the density residuals (right). In the lower panel we show the velocity dispersion profile (left) and the velocity dispersion residuals (right).

already shown in Fig. 3.8 and Fig. 3.9, main sequence stars (the light component of the models) are affected by mass segregation, which generates a gradient in the M/L profile within the light component itself. In fact, if we consider the M/L profiles of the single components (Fig. 3.24), we find that the profile of the light component of the simulated system (black line) exhibits a remarkable increase from the center to the outermost regions. As we assigned a single constant value of M/L to the light component, our simple dynamical model cannot incorporate this feature. Similarly, all previous studies based on one-component King models cannot incorporate M/L gradients and would naturally fail if gradients are present. In this respect, the heavy component shows less significant gradients, as its luminosity is dominated by giants which, as explained in Sect. 3.2.2, are less affected by mass segregation.

3.4.1 Application to observed globular clusters

The application of models which do not take into account mass segregation properly could lead to misleading results in observational studies. For example,

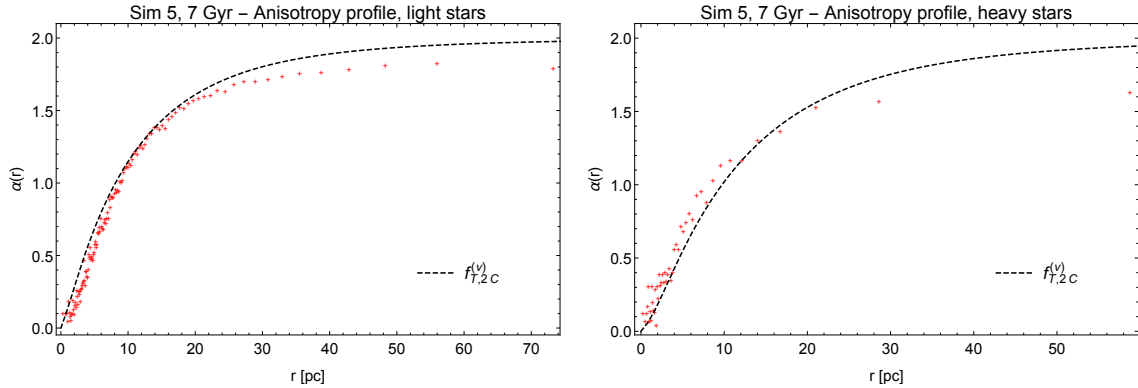


Figure 3.22: Anisotropy profiles of Sim 5 at 7 Gyr for the light component (left panel) and the heavy component (right panel) compared with those obtained from the best-fit two-component $f_T^{(\nu)}$ model.

Di Cecco et al. (2013) [17] studied the density distribution of stars in the cluster M92 (NGC 6341) in two different ways: by means of the projected surface brightness (SB) and of the number density projected profile (ND). They performed a fit to these profiles separately by means of one-component King models (see Sect. 2.1.3) and found that, even if the number density and the surface brightness profiles considered came from the same systems, best-fit parameters turned out to be significantly different. In fact, the number density profile is well-fitted by a King model with $\Psi = 6.91 \pm 0.02$ whereas the surface brightness profile best-fit result gives $\Psi = 8.40 \pm 0.01$. The authors argued that this contradictory result might be due to the fact that each profile represents the density distribution of different stars: the number density profile, derived by considering the radial distribution of both luminous and faint stars, is dominated by main sequence stars, which greatly outnumber evolved giant stars. On the other hand, the surface brightness profile is heavily affected by the presence of the brighter giant stars. The differences in the best-fit models thus reflect the intrinsic differences in the radial distribution of the stellar tracer that determines each profile, which is different in the presence of mass segregation.

I verified that, as suggested by Di Cecco et al. (2013) [17], the number density profile is largely determined by the light component and that the surface brightness profile is instead dominated by the heavy stars. I considered Sim 5 at 7 Gyr and constructed the projected number density profiles and the surface brightness profiles for the total system and for each component. To this purpose, I divided the plane perpendicular to a certain direction (indicated as z in the output file) into radial shells, keeping the number of stars constant in each shell (as was done in the case of the intrinsic profiles, see Sect. 3.3). As my objective is to construct “observable” profiles, I ignored remnants. For each shell, I calculated the number density as the

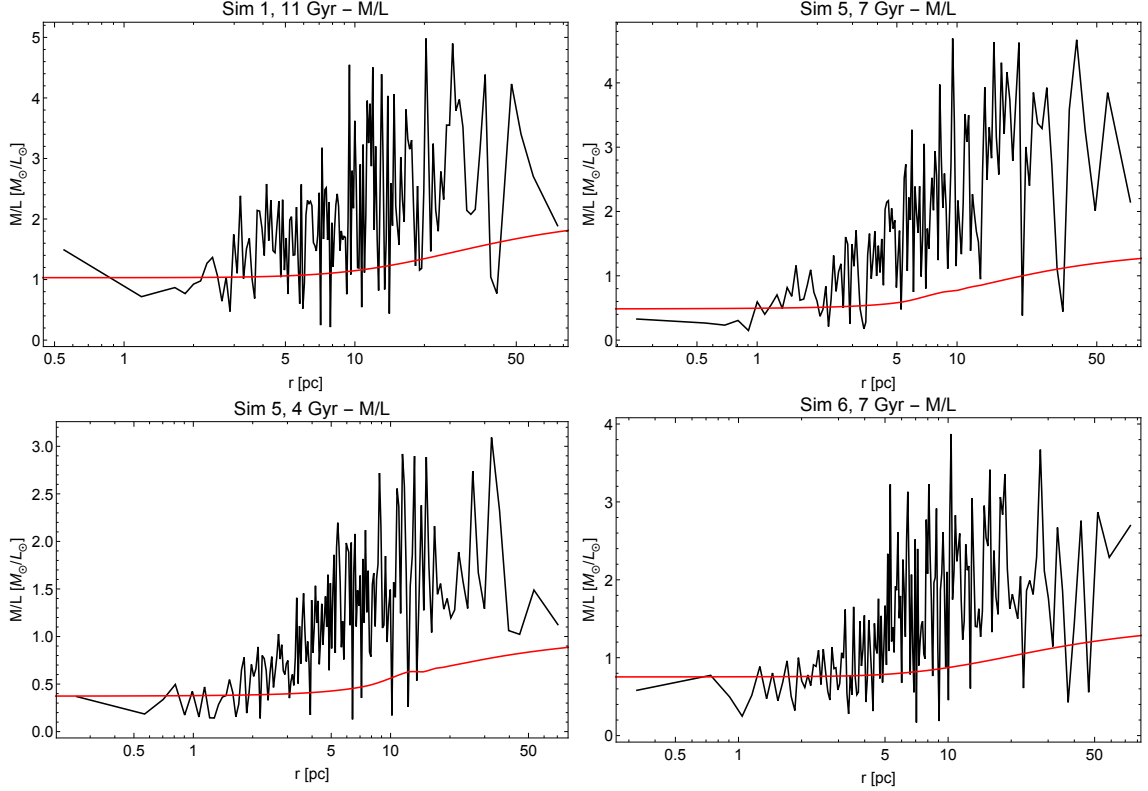


Figure 3.23: Total M/L profiles (black lines) for Sim 1 at 11 Gyr (left upper panel), Sim 5 at 7 Gyr (right upper panel), Sim 5 at 4 Gyr (left lower panel), Sim 6 at 7 Gyr (right lower panel) compared with those obtained from best-fit models for two-component $f_T^{(\nu)}$ models. The profiles of the simulated states are jagged because, in each shell, great contribution to luminosity comes from giant stars. As the number of giants is very small, the total luminosity could vary very much from shell to shell.

ratio between the number of stars and the area $A_{shell} = \pi(R_{out,shell}^2 - R_{in,shell}^2)$, where $R_{in,shell}$ and $R_{out,shell}$ are the projected inner and outer radii of the shell, respectively. The surface brightness profile was calculated by dividing the total luminosity of each shell by the area A_{shell} . The uncertainties were calculated by means of a bootstrap resampling as for the intrinsic profiles (see Appendix A).

I compared the profile of the total system and that of the single components, as illustrated in Fig. 3.25. The projected number density profile, $n(R)$, obtained by considering all the stars (black points), nearly overlaps with that obtained by considering only the light component (red points). On the other hand, the total surface brightness profile, $I(R)$, of the system reflects that of the heavy component (green points), confirming the argument by Di Cecco et al. (2013) [17]. This means that the best-fit concentration parameter obtained from the fit to the number density profile mainly describes the distribution of light stars, whereas the surface brightness

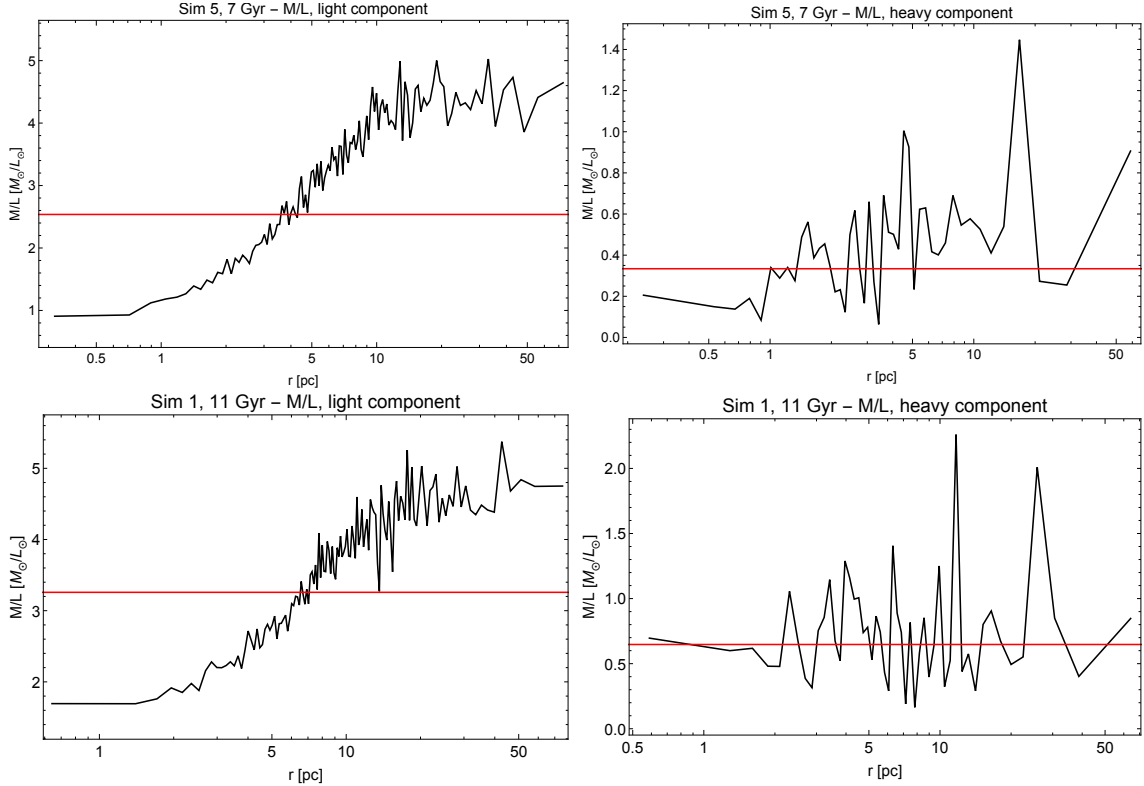


Figure 3.24: M/L profiles for the light component (left) and for the heavy component (right) for Sim 5 at 7 Gyr (upper panels) and Sim 1 at 11 Gyr (lower panels). In these graphics, the profiles of the simulated systems (black lines) are compared to the values assigned to each component in the two-component $f_T^{(\nu)}$ models (red lines).

gives mainly information about the heavy stars.

I then tried to understand which observed profile allows to obtain a better representation of the underlying mass density profile. To this purpose, I considered Sim 5 at 7 Gyr and, in particular, the profiles that we could ideally observe, that is the total projected number density profile (without remnants) and the total surface brightness profile. I then compared these profiles to those obtained from the best-fit result for two-component $f_T^{(\nu)}$ models by converting the projected mass density profile.

I constructed the projected mass profile of the simulated state by dividing the system into projected shells and by evaluating the ratio between the total mass of each shell and the area A_{shell} . The projected density profile for the i -th component $\rho_{p,i}(R)$ of the best-fit $f_T^{(\nu)}$ model was constructed by integrating:

$$\rho_{p,i}(R) = \int_{-\infty}^{\infty} \rho_i(r) dz = \int_{-\infty}^{\infty} \rho_i(\sqrt{R^2 + z^2}) dz. \quad (3.40)$$

This projected mass density profiles of the best-fit two-component $f_T^{(\nu)}$ model, com-

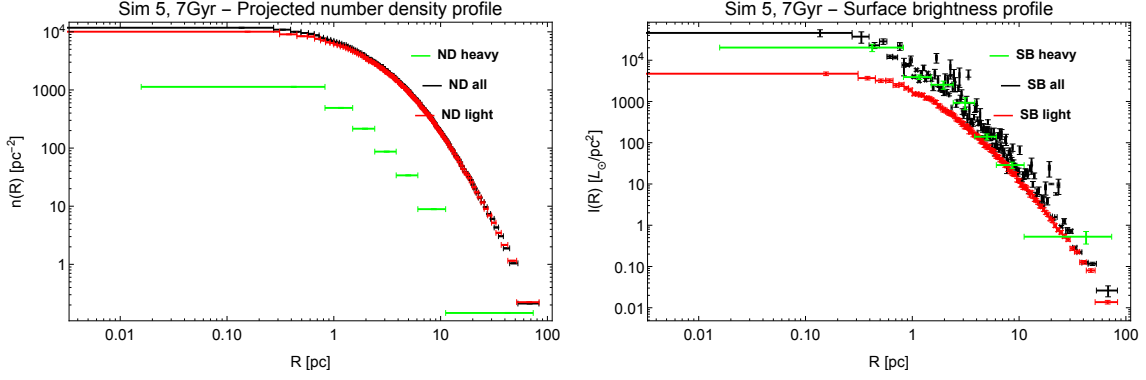


Figure 3.25: The projected number density profile (left panel) and the surface brightness profile (right panel) for simulation Sim 5 at 7 Gyr. Black points correspond to the total profiles, red points correspond to the profiles of the light component and green points correspond to the profiles of the heavy component. The number density is mainly determined by the light component whereas the surface brightness is mainly determined by the heavy component. Large uncertainties in the total surface brightness profile are due to the presence of very different luminosities between giant stars and main-sequence stars, that affect the bootstrap estimate of standard error (see Appendix A).

pared with those of Sim 5 at 7 Gyr, are illustrated in Fig. 3.26. This model provides a very good description of the projected mass density profile for the total profile and for each component.

I converted the projected total mass density profile into a projected number density profile. I divided the profile of each component by the respective mass and calculated the total number density as the sum of the two number densities (two-component conversion). To remove the contribution of remnants from the number density profile, I multiplied the number density profile of the heavy component by the fraction of non-remnant heavy stars. Analogously, I converted the total mass profile into a surface brightness profile. In this case I divided each component by the respective mass-to-light ratio (see Tab. 3.17) and then calculated the total surface brightness profile as the sum of the profiles of the two components.

As shown in Fig. 3.27, the number density profile obtained from this conversion overestimates the number density of the system at the center, as a result of mass segregation: in fact, if we convert the mass density profile into a number density profile by dividing by the mean mass, at the center we divide by a value which is smaller than the actual mean mass of the system in that region. The number density profile obtained in this way will thus overestimate the value of the central density. On the other hand, the surface brightness profile obtained from a one-component

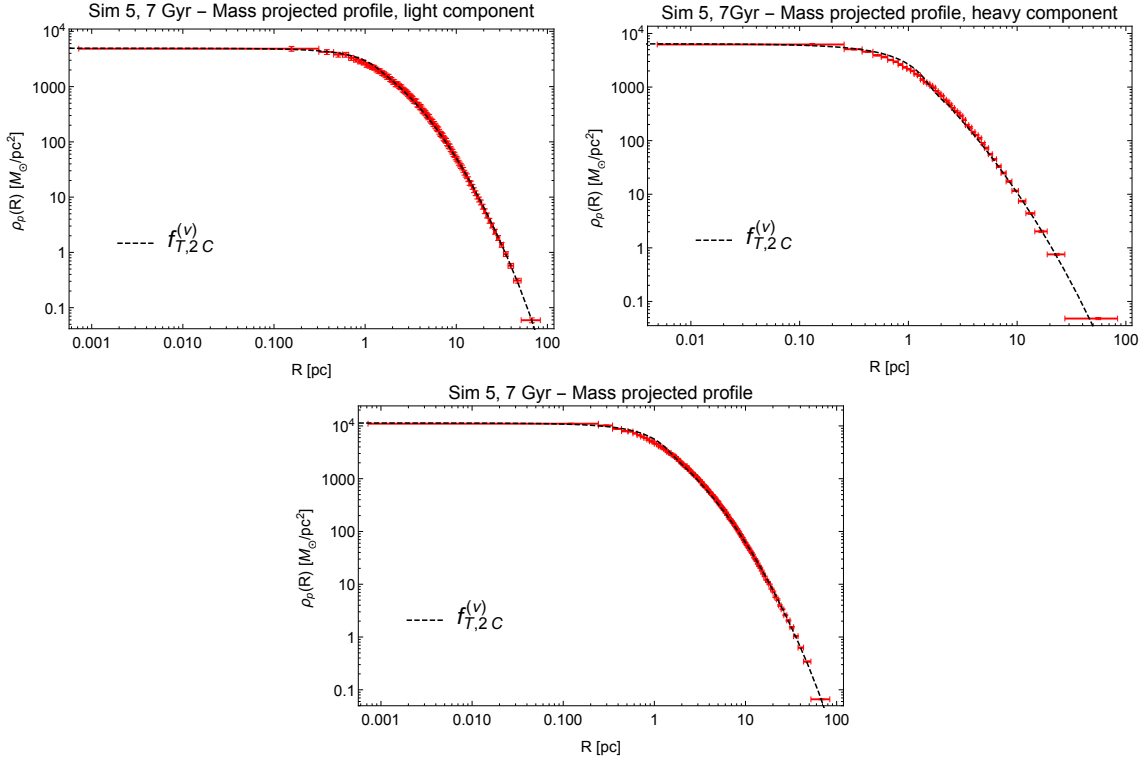


Figure 3.26: Projected mass density profiles of Sim 5 at 7 Gyr (red points) compared to the projected two-component profiles obtained from the best-fit two-component $f_T^{(\nu)}$ model (black line). Left upper panel shows the profile of the light component. Right upper panel shows the profile of the heavy component. Lower panel shows the total profile. There is a very good agreement in all the cases.

conversion overestimates the profile of the simulated state. This is, in particular, a consequence of the gradient in the M/L ratio of the light component, as shown in Fig. 3.24. In this case, when we make the conversion from the mass profile to the surface brightness profile, in the central regions we divide by a M/L ratio higher than the actual value in that region.

This discussion suggests that the result obtained by Di Cecco et al. (2013) [17] by fitting the number density profile underestimates the central concentration of the system, whereas the result obtained from the total luminosity profile overestimates it. We can also say that the concentration parameter which probably best traces the mass density of the system ranges between the two values found by Di Cecco et al. (2013) [17] as the both profiles that they considered are affected by mass segregation with gradients in opposite directions.

Thus, mass segregation has to be taken into account in observational studies, as it could lead to misleading results in the conversion from projected number density profiles and surface brightness profiles to projected mass profiles. As main sequence

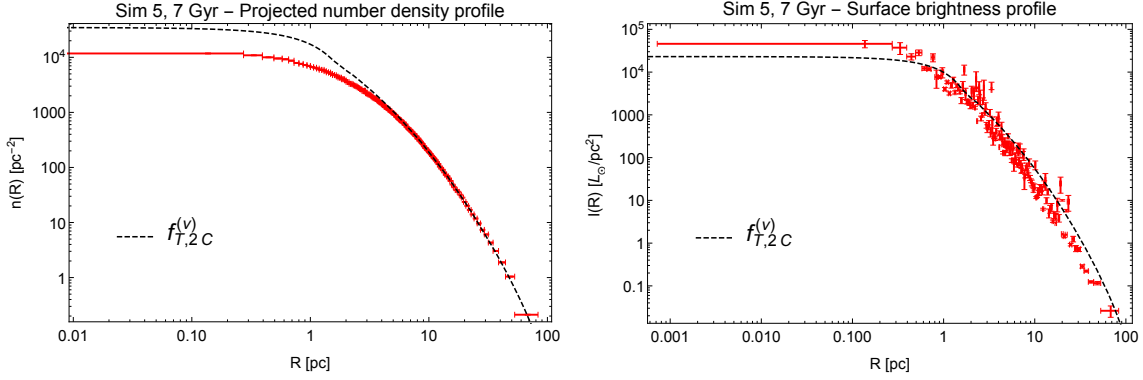


Figure 3.27: Projected number density (left panel) and surface brightness profile (right panel) profile of Sim 5 at 7 Gyr compared with those obtained from the best-fit result for two-component $f_T^{(\nu)}$ models. The profiles obtained from the model cannot reproduce those of the simulation state because of mass segregation.

stare are more affected by mass segregation, a possible solution to this problem could be to try to restrict the attention the surface brightness profile of the red giants, which seems to be less affected by mass segregation and gradients in the M/L ratio. To understand if this procedure may lead to results less affected by mass segregation, I constructed the projected number density and surface brightness profiles for the single components of Sim 5 at 7 Gyr and compared them to those obtained by converting the projected mass profiles of the single components of the best-fit $f_T^{(\nu)}$ models. As illustrated in Fig. 3.28, the number density and surface brightness profile of the light component do not match that obtained from the models. On the other hand, the surface brightness of the best-fit model heavy component show a good matching with that of the simulated state. I point out that the number of shells is very small for the heavy component because of the very small number of giant stars in the simulated state. This aspects causes more statistical fluctuations with respect to measurements on the main-sequence stars.

This discussion suggests that a method to reduce the bias generated by mass segregation could be obtained by considering the surface brightness profile of the heavy component, which is less affected by gradients in the M/L profile. We can conclude that measures on the heavy component surface brightness profile seem to be less affected by mass segregation. On the other hand, unfortunately, measures of giant stars are more affected by fluctuations.

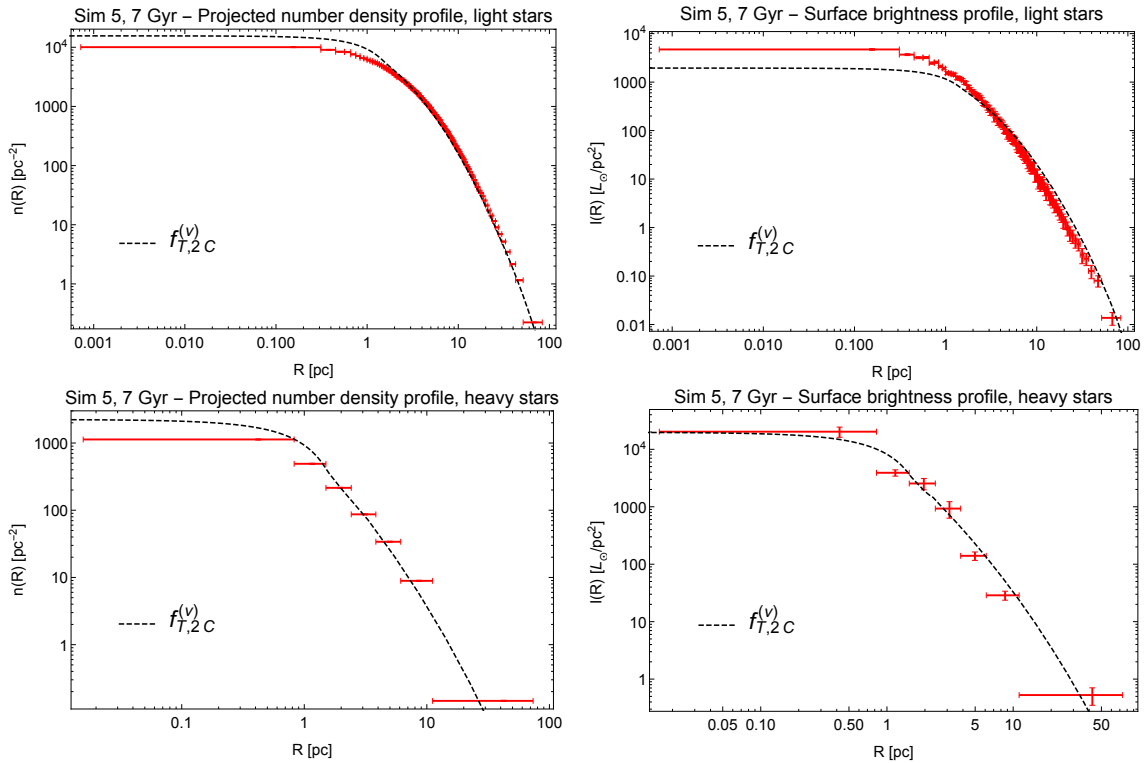


Figure 3.28: The projected number density profiles (left panels) and the projected surface brightness profiles (right panels) for the two components of Sim 5 at 7 Gyr. We can notice that the only profile which seems to be matched by the best-fit profile two-components $f_T^{(\nu)}$ model is the heavy component surface brightness profile.

Chapter 4

Conclusions and perspectives

In this thesis I have studied energy equipartition and mass segregation in globular clusters focusing on a set of simulated states, that is selected “snapshots” taken from realistic Monte Carlo simulations that incorporate both dynamical and stellar evolution. Energy equipartition and mass segregation have been investigated by means of two-component King models (1966) [34] and $f_T^{(\nu)}$ models [16], in which the two components represent light (main sequence) stars and heavy stars (giants, remnants, and binaries) respectively. I also performed a critical discussion of the so called Spitzer “instability”. I finally considered the consequences of mass segregation on the local value of mass-to-light M/L ratio, and, in particular, how gradients in its profile can affect the observations. The main results of this thesis are:

- A condition of only partial global energy equipartition is attained in systems generated by simulations, as already observed by Bianchini et al. (2016) [12]. Energy equipartition is not reached strictly even by limiting the attention to regions of the system close to the center, where relaxation is more effective. Only a condition of partial local equipartition is met at the center of the cluster, where can be quantified by means of the parameter η introduced by Trenti & van der Marel (2013) [58]. All the simulated states that we have considered show values $\eta \leq 0.27$, smaller than expected in case of full central energy equipartition ($\eta = 0.5$).
- For these systems, the Vishniac criterion fails, consistent with the fact that global energy equipartition is not reached. In addition, density profiles of these simulations are well described by two-component $f_T^{(\nu)}$ models (see below) which are found to violate the condition of homology at the basis of Vishniac’s argument.
- Mass segregation is present also in the least relaxed systems, which indicates

that this process is very efficient. Mass segregation characterizes not only the stellar system as a whole, but also main sequence stars, dark remnants and binaries. Only giant stars do not exhibit mass segregation, because the giant phase is so short that, at every snapshot, only stars in a very small range of masses are in this evolutionary phase.

- One-component King models do not offer a good representation of the simulated states. The density profiles of these models present a sharp truncation and high central densities, and velocity dispersion profiles are not compatible with those measured in the simulations. On the other hand, one-component $f_T^{(\nu)}$ models provide a reasonable description of the density profiles of the simulated states, except for the very central regions. Velocity dispersion profiles are generally characterized by a rapid decline, not well captured by the $f_T^{(\nu)}$ models. The anisotropy profiles of more relaxed systems are well fitted by the models, suggesting that collisions drive systems toward a velocity distribution similar to that generated by violent relaxation.
- The two components defined in the way described and justified in the thesis do not fulfill the Spitzer criterion.
- Two-component King models present the same limitations as the one-component case. On the other hand, two-component $f_T^{(\nu)}$ models give an even better representation of these systems with respect to one-component models, in particular for the density distributions. Velocity dispersion profiles still present some differences, but two-component $f_T^{(\nu)}$ models are able to reproduce the central peak in the velocity dispersion shown by simulations and the increase in anisotropy profiles in more relaxed systems. I conclude that these models offer a reasonable representation of the simulations, also in relation to mass segregation and central energy equipartition.
- The variation of the mass-to-light M/L ratio generated by mass segregation cannot be reproduced by two-components $f_T^{(\nu)}$ models. This is due primarily to the mass segregation within the light component (main sequence stars). This aspect can influence the measurement of the relevant parameters obtained by means of optical observations. In particular, the characterization of the mass density profile by means of the observed number density profile underestimates the central concentration of the system whereas the surface brightness profile overestimates it. A possible solution to this problem could be to try to restrict the attention the surface brightness profile of the red giants, which seems to

be less affected by mass segregation and gradients in the M/L ratio, but is, unfortunately, more affected by fluctuations..

In conclusion, two-components $f_T^{(\nu)}$ models appear to offer a realistic representations of globular clusters and a reasonably starting point to investigate dynamical mechanisms related to mass segregation and energy equipartition inside these stellar systems.

One future goal that is encouraged by the results of the present thesis is to make an attempt at using the two-component $f_T^{(\nu)}$ models to interpret the real data of the new globular clusters diagnostics made possible by GAIA.

On the theoretical point of view, a natural and interesting development of this work could be the construction of models able to take into account different degrees of anisotropy in the outer regions, following in detail the indications provided by the simulations. For this, a better understanding of the mechanisms leading to the anisotropy profiles resulting from collisionality would be desired.

Finally, the development of anisotropy in relaxed systems is still a not much understood problem which has been studied almost exclusively by means of numerical simulations and a theoretical comprehension of this process is still lacking.

Bibliography

- [1] Abramowitz, M. and Stegun, I. *Handbook of mathematical functions with formulas, graphs, and mathematical tables*. United States Department of Commerce, National Bureau of Standards (NBS), 1964.
- [2] Anderson J. PhD Thesis. University of California, Berkeley, 1997.
- [3] Anderson, J. and King, I.R. *The rotation of the globular cluster 47 Tucanae in the plane of the sky*. *Astronom J.* 289, p. 772, 2003.
- [4] Bedin, L. G. and Piotto, G. *Omega Centauri: the population puzzle goes deeper*. *Astrophys. J. Letters* 605, p. L125, 2004.
- [5] Bellini, A., Anderson, J., et al. *Hubble Space Telescope proper motion (HST-PROMO) catalogs of galactic globular clusters. I. Sample selection, data reduction, and NGC 7078 results*. *Astrophys. J.* 798, p. 115, 2014.
- [6] Bellini, A., Bianchini, P., et al. *Hubble Space Telescope proper motion (HST-PROMO) catalogs of galactic globular clusters. V. The rapid rotation of 47 Tuc traced and modeled in three dimensions*. *Astrophys. J.* 844, p. 167, 2017.
- [7] Bertin, G. *Dynamics of Galaxies*. Second Edition. Cambridge University Press, 2014.
- [8] Bertin, G. and Varri, A. L. *The construction of non-spherical models of quasi-relaxed stellar systems*. *Astrophys J.* 689, p. 1005, 2008.
- [9] Bianchini, P. et al. *Rotating globular clusters*. *Astrophys J.* 772, p. 67, 2013.
- [10] Bianchini, P., Sills, A., et al. *The relation between the mass-to-light ratio and the relaxation state of globular clusters*. *Mon. Not. R. Astron. Soc.* 469, p. 4359, 2017.
- [11] Bianchini, P., Sills, A., and Miholics, M. *Characterization of the velocity anisotropy of accreted globular clusters*. *Mon. Not. R. Astron. Soc.* 471, p. 1181, 2017.
- [12] Bianchini, P., van de Ven, G., et al. *A novel look at energy equipartition in globular clusters*. *Mon. Not. R. Astron. Soc.* 458, p. 3644, 2016.

- [13] Bianchini, P., Webb, J. J., et al. *Kinematic fingerprint of core-collapsed globular clusters*. *Mon. Not. R. Astron. Soc.* 475, p. L96, 2017.
- [14] Cova, F. “L’instabilità di Spitzer negli ammassi globulari alla luce di studi recenti di dinamica stellare”. Tesi triennale in fisica. Università degli studi di Milano, 2014.
- [15] Da Costa, G. S. and Freeman, K. C. *The structure and mass function of the globular cluster M3*. *Astrophys. J.* 206, p. 128, 1976.
- [16] de Vita, R., Bertin, G., and Zocchi, A. *A class of spherical, truncated, anisotropic models for application to globular clusters*. *Astronomy and Astrophysics* 590, A16, 2016.
- [17] Di Cecco, A., Zocchi, A., et al. *On the density profile of the globular cluster M92*. *Astronom. J.* 145, pp. 103–113, 2013.
- [18] Djorgovski, S. *Physical parameters of galactic globular clusters*. *Publ Astronomical Society of the Pacific* 50, p. 373, 1993.
- [19] Downing, J. M. B., Benacquista, M. J., et al. *Compact binaries in star clusters I - Black Hole binaries inside globular clusters*. *Mon. Not. R. Astron. Soc.* 407, p. 1946, 2010.
- [20] Efron, B. and Tibshirani, R., J. *An introduction to the Bootstrap*. First Edition. Chapman and Hall/CRC, 1993.
- [21] Fregeau, J. M., Ivanova, N., and Rasio, F. A. *Evolution of the binary fraction in dense stellar systems*. *Astrophys J.* 707, pp. 1533–1540, 2009.
- [22] Giersz, M. *Monte-Carlo simulations of star clusters – I. First results*. *Mon. Not. R. Astron. Soc.* 298, p. 1239, 1998.
- [23] Giersz, M. *Monte Carlo simulations of star clusters – III. A million body star cluster*. *Mon. Not. R. Astron. Soc.* 371, p. 484, 2006.
- [24] Giersz, M. and Heggie, D. C. *Statistics of N-body simulations - I. Equal masses before collapse*. *Mon. Not. R. Astron. Soc.* 268, p. 257, 1994.
- [25] Giersz, M., Heggie, D. C., and Hurley, J. R. *Monte-Carlo simulations of star clusters – IV. Calibration of the Monte-Carlo code and comparison with observations for the open cluster M67*. *Mon. Not. R. Astron. Soc.* 388, p. 429, 2008.
- [26] Gunn, E. J. and Griffin, R. F. *Dynamical studies of globular clusters based on photometric radial velocities of individual stars. I. M3*. *Astrophys. J.* 84, p. 752, 1979.

- [27] Harris, W. E. *A new catalog of globular clusters in the Milky Way*. 2010. URL: <http://physwww.mcmaster.ca/~harris/mwgc.dat>.
- [28] Heggie, D. C. and Hut, P. *The gravitational million-body problem: A multidisciplinary approach to star cluster dynamics*. Cambridge University Press, 2003.
- [29] Heggie, D. C., Inagaki, S., and McMillan S. L. *Gravothermal expansion in an N-body system*. *Mon. Not. R. Astron. Soc.* 271, p. 706, 1994.
- [30] Heggie, D.C. and Vesperini, E. *On the effects of dynamical evolution on the initial mass function of globular clusters*. *Mon. Not. R. Astron. Soc.* 289, p. 898, 1997.
- [31] Hénon, M. *Monte Carlo models of star clusters*. *Astrophysics and Space Science* 13, p. 284, 1971.
- [32] Hypki, A. and Giersz, M. *MOCCA code for star cluster simulations – I. Blue stragglers, first results*. *Mon. Not. R. Astron. Soc.* 429, p. 1221, 2013.
- [33] Ivanova, N., Fregeau, J. M., et al. *The evolution of binary fractions in globular clusters*. *Mon. Not. R. Astron. Soc.* 358, p. 572, 2005.
- [34] King, I. R. *The structure of star clusters. III. Some simple dynamical models*. *Astronom J.* 71, p. 64, 1966.
- [35] Kondrat'ev, B. P. and Ozeroy, L. M. *A two component model of a spherical stellar system*. *Mon. Not. R. Astron. Soc.* 84, p. 431, 1982.
- [36] Libralato, M., Bellini, A., et al. *Hubble Space Telescope proper motion (HST-PROMO) catalogs of galactic globular cluster. VI. Improved data reduction and internal-kinematic analysis of NGC 362*. *Astrophys. J.* 861, id:99, 2018.
- [37] Lynden-Bell, D. and Wood, R. *The gravo-thermal catastrophe in isothermal spheres and the onset of red-giant structure for stellar systems*. *Mon. Not. R. Astron. Soc.* 138, p. 495, 1968.
- [38] McLaughlin, D. E. et al. *Hubble Space Telescope proper motions and stellar dynamics in the core of the globular cluster 47 Tucanae*. *Astrophys. J. Supp. Series* 166, p. 249, 2006.
- [39] Merritt, D. *Two component stellar systems in thermal and dynamical equilibrium*. *Astronom J.* 86, p. 318, 1981.
- [40] Michie, R. W. *On the distribution of high energy stars in spherical stellar systems*. *Mon. Not. R. Astron. Soc.* 125, p. 127, 1962.

- [41] Miocchi, P. *Central energy equipartition in multimass models of globular clusters*. *Mon. Not. R. Astron. Soc.* 366, p. 227, 2006.
- [42] Noyola, E., Gebhardt, L., and Bergmann, M. *Gemini and Hubble Space Telescope evidence for an intermediate-mass black hole in ω Centauri*. *Astrophys J.* 676, p. 1008, 2008.
- [43] Oh, K. S. and Lin, D. N. C. *Tidal evolution of globular clusters. II. The effects of galactic tidal field and diffusion*. *Astrophys. J.* 386, p. 519, 1992.
- [44] Peterson, C. and King, I. R. *The structure of star clusters. VI. Observed radii and structural parameters in globular clusters*. *Astronom J.* 80, p. 427, 1975.
- [45] Piotto, G. *Observational evidence of multiple stellar populations in globular clusters*. *Proceedings of the International Astronomical Union No 258 3*, p. 141, 2007.
- [46] Plummer, H. C. *On the problem of distribution in globular star clusters*. *Mon. Not. R. Astron. Soc.* 71, p. 460, 1911.
- [47] Sormani, M. C. and Bertin, G. *Gravothermal catastrophe: the dynamical stability of a fluid model*. *Astronomy and Astrophysics* 552, A37, 2013.
- [48] Spitzer, L. *Equipartition and the formation of compact nuclei spherical stellar systems*. *Astrophys. J.* 159, p. L139, 1969.
- [49] Spitzer, L. *Dynamical evolution of globular clusters*. Princeton University Press, 1987.
- [50] Spitzer, L. and Hart, M. H. *Random gravitational encounters and the evolution of spherical systems. II. Models*. *Astrophys. J.* 166, p. 483, 1971.
- [51] Spitzer, L. and Shapiro, S. L. *Random gravitational encounters and the evolution of spherical systems. III. Halo*. *Astrophys. J.* 173, p. 529, 1972.
- [52] Stiavelli, M. and Bertin, G. *Statistical mechanics and equilibrium sequences of ellipticals*. *Mon. Not. R. Astron. Soc.* 229, p. 61, 1987.
- [53] Stodółkiewicz, J. S. *Dynamical evolution of globular clusters. II. Binaries - Method*. *Acta Astronomica* 36, p. 19, 1986.
- [54] Takahashi, K. *Fokker-Planck models of stars clusters with anisotropic velocity distributions. I. Pre-collapse evolution*. *Publ. Astron. Soc. Jap.* 47, p. 561, 1995.
- [55] Tiongco, M. A., Vesperini, E., and Varri, A. L. *Velocity anisotropy in tidally limited star clusters*. *Mon. Not. R. Astron. Soc.* 455, p. 3693, 2015.

- [56] Trenti, M. and Bertin, G. *A family of models of partially relaxed stellar systems - I. Dynamical properties.* *Astronomy and Astrophysics* 429, p. 161, 2005.
- [57] Trenti, M., Bertin, G., and van Albada, T. S. *A family of models of partially relaxed stellar systems - II. Comparison with the products of collisionless collapse.* *Astronomy and Astrophysics* 433, p. 57, 2005.
- [58] Trenti, M. and van der Marel, R. *No energy equipartition in globular clusters.* *Mon. Not. R. Astron. Soc.* 435, p. 3272, 2013.
- [59] van den Bergh, S. *The luminosity-diameter relations for globular clusters and dwarf spheroidal galaxies.* *Mon. Not. R. Astron. Soc.* 390, p. L51, 2008.
- [60] van den Marel, R. and Anderson, J. *New limits on an intermediate-mass black hole in Omega Centauri. II. Dynamical Models.* *The Astrophysical Journal* 710, p. 1063, 2010.
- [61] Vishniac, E. T. *No Energy Equipartition in Globular Clusters.* *Astrophys. J.* 223, p. 986, 1978.
- [62] Zocchi, A., Bertin, G., and Varri, A. L. *A dynamical study of galactic globular clusters under different relaxation conditions.* *Astronomy and Astrophysics* 539, A65, 2012.
- [63] Zocchi, A., Gieles, M., et al. *Testing lowered isothermal models with direct N-body simulations of globular clusters.* *Mon. Not. R. Astron. Soc.* 462, p. 696, 2016.

Appendix A

Bootstrap estimate of standard error

Let \hat{F} be an empirical distribution with observed values x_i , $i = 1, 2, \dots, n$. A bootstrap sample is defined as a random sample of size n drawn from \hat{F} , indicated as $\mathbf{x}^* = (x_1^*, x_2^*, \dots, x_n^*)$,

$$\hat{F} \rightarrow (x_1^*, x_2^*, \dots, x_n^*). \quad (\text{A.1})$$

The star notation indicates that \mathbf{x}^* is not the actual data set \mathbf{x} , but rather a randomized, or resampled, version of \mathbf{x} . Bootstrap data points $x_1^*, x_2^*, \dots, x_n^*$ are a random sample of size n drawn with replacement from the empirical population of n objects (x_1, x_2, \dots, x_n) . We might have $x_1^* = x_7$, $x_2^* = x_3$, $x_3^* = x_3$, $x_4^* = x_{22}$, ..., $x_n^* = x_4$. The bootstrap data set consists of members of the original data set, some appearing once, some appearing twice, etc.

Let $\tilde{\theta}$ be a statistics obtained by applying a function $s(\cdot)$ to x . The bootstrap replication of $\hat{\theta}$, corresponding to a bootstrap data set \mathbf{x}^* is:

$$\hat{\theta}^* = s(\mathbf{x}^*), \quad (\text{A.2})$$

where the quantity $s(\mathbf{x}^*)$ is the result of applying the same function $s(\cdot)$ to \mathbf{x}^* as was applied to \mathbf{x} . For example if $s(\mathbf{x})$ is the sample mean, then $s(\mathbf{x}^*)$ is the mean on the bootstrap data. Now, let $se_F(\hat{\theta})$ be the standard error of a statistics $\hat{\theta}$. Unfortunately, for virtually any estimate other than the mean, there is no formula that enables to compute the numerical value of the ideal estimate exactly. A common method used to obtain a good approximation to the numerical value of $se_{\hat{F}}(\hat{\theta})$ is the so-called bootstrap method, which is based on the creation of multiple random samples for a certain empirical distribution.

To implement the bootstrap method, a random number device selects integers i_1, i_2, \dots, i_n , each of which equals any value between 1 and n . The bootstrap sample

consists of the corresponding members of \mathbf{x} ,

$$x_1^* = x_{i_1}, x_2^* = x_{i_2}, x_n^* = x_{i_n}. \quad (\text{A.3})$$

The bootstrap method works by drawing many independent bootstrap samples, evaluating the corresponding bootstrap replications, and estimating the standard error of $\hat{\theta}$ as the empirical standard deviation of replications:

$$\hat{se}_B(\hat{\theta}) = \left\{ \sum_{b=1}^B \frac{[\hat{\theta}^*(b) - \hat{\theta}^*(\cdot)]^2}{B-1} \right\}^{1/2}, \quad (\text{A.4})$$

where $\hat{\theta}^*(\cdot) = \sum_{b=1}^B \hat{\theta}^*(b)/B$ is the mean value of replications of the selected statistics. The result is called the bootstrap estimate of standard error, denoted by \hat{se}_B , where B is the number of bootstrap samples used.

We may now wonder how large should be B , the number of bootstrap replications used to evaluate \hat{se}_B . The ideal number of bootstrap estimates one should take is $B \rightarrow \infty$. Actually, time constraints may dictate a small value of B if $\hat{\theta}$ is a very complicated function of \mathbf{x} (the amount of computer time increases linearly with B). As observed by Efron and Tibshirani (1993) [20], even a small number of bootstrap replications, $B = 25$, is usually informative. $B = 50$ is often enough to give a good estimate of $se_F(\hat{\theta})$. Very seldom are more than $B = 200$ replications needed for estimating standard error. For the determination of uncertainties of density and velocity distribution profiles described in Sect. 3.3.1, I considered $B = 200$ bootstrap replication.

Appendix B

Fit results

B.1 One-component models

B.1.1 One-component King models

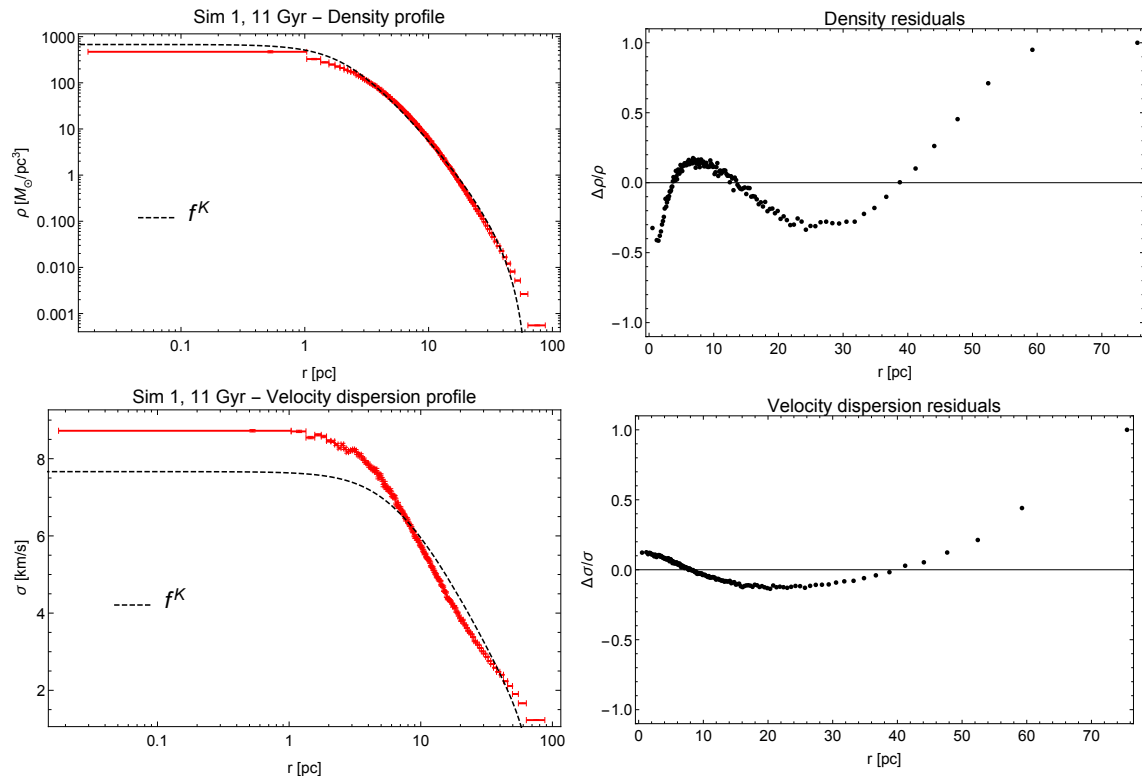


Figure B.1: Best-fit result for Sim 1 at 11 Gyr obtained from one-component King models.

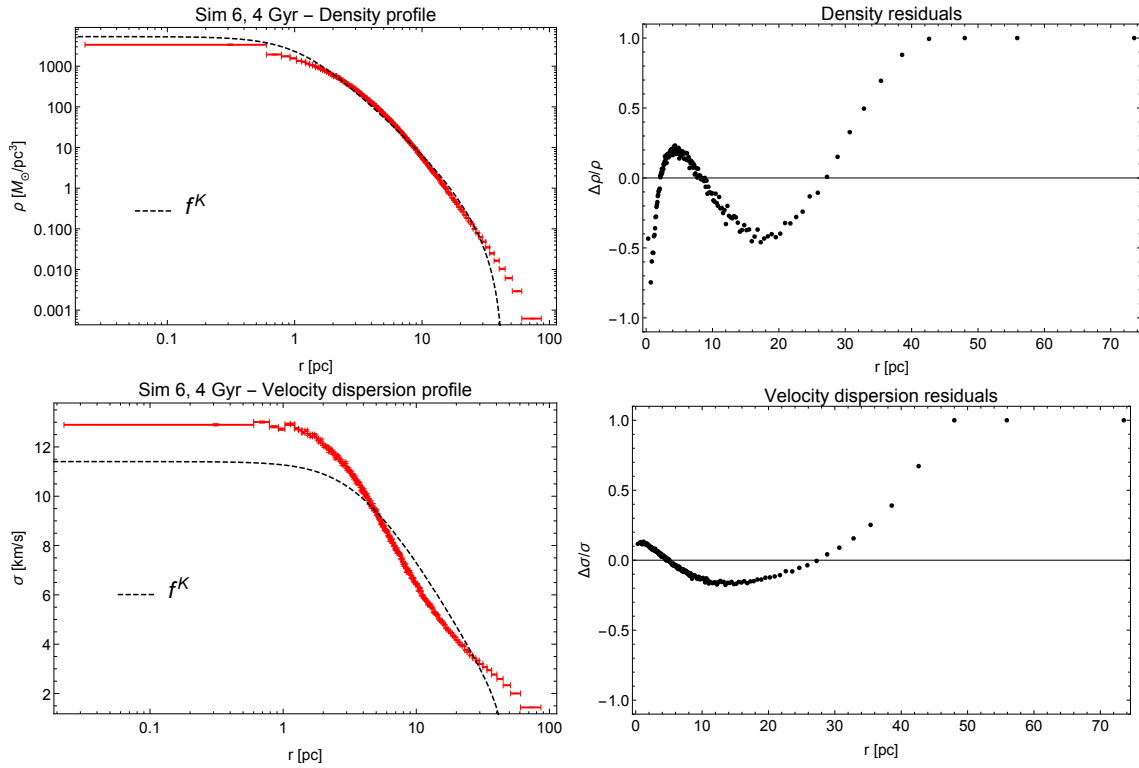


Figure B.2: Best-fit result for Sim 6 at 4 Gyr from one-component King models.

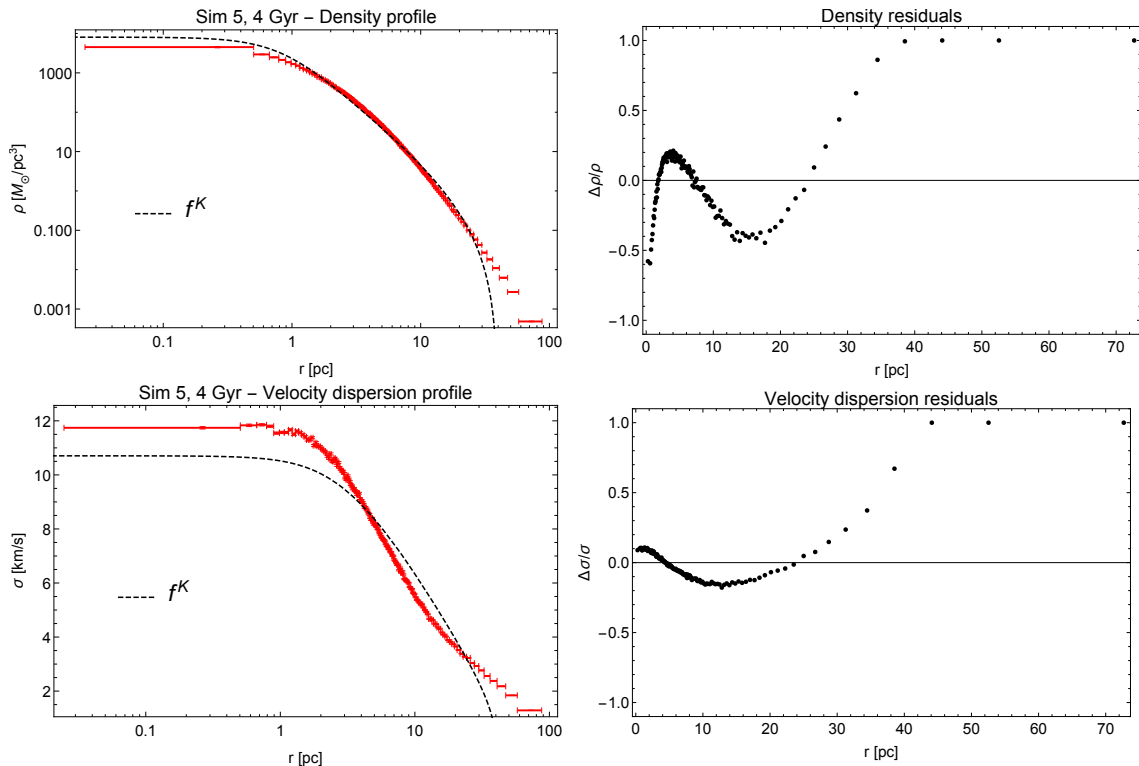


Figure B.3: Best-fit result for Sim 5 at 4 Gyr from one-component King models.

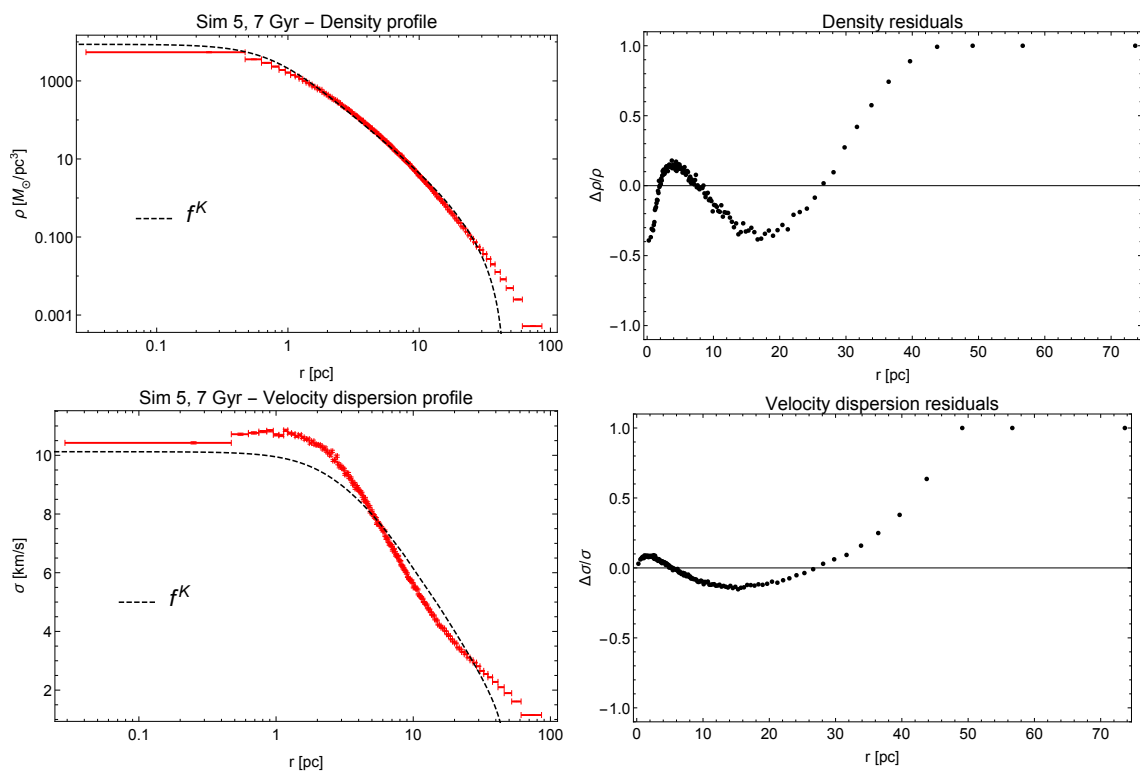


Figure B.4: Best-fit result for Sim 5 at 7 Gyr from one-component King models.

B.1.2 One-component $f_T^{(\nu)}$ models

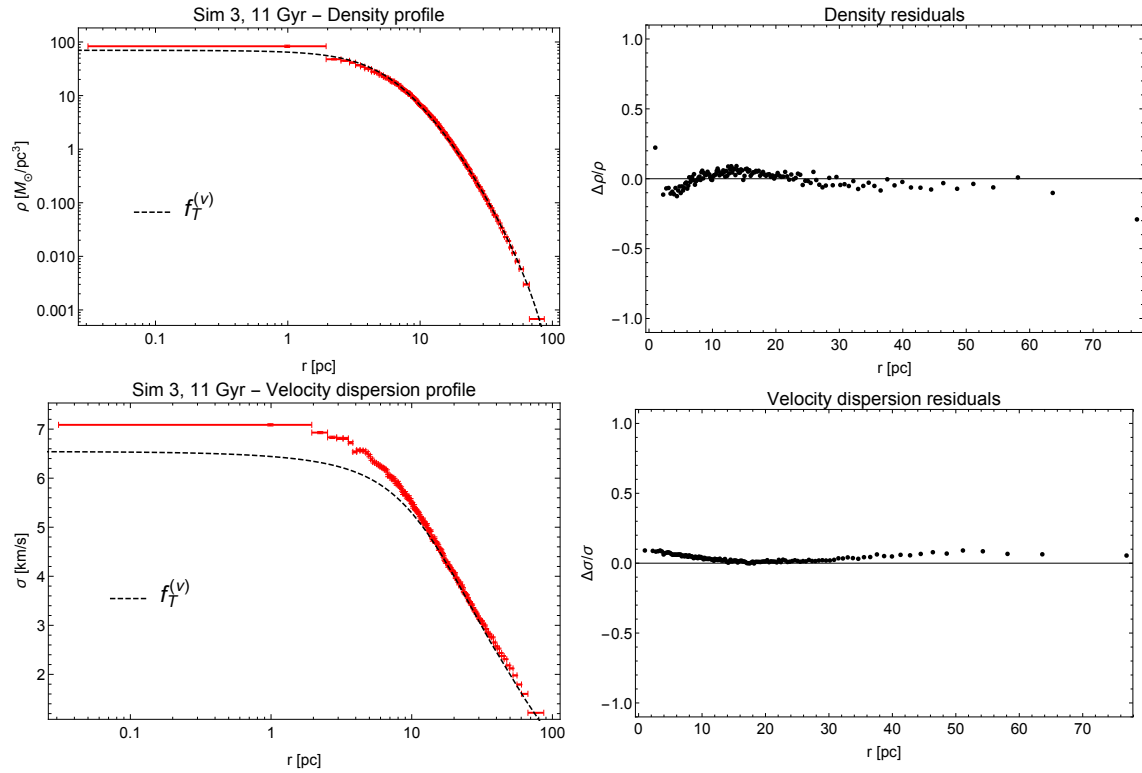


Figure B.5: Best-fit result for Sim 3 at 11 Gyr obtained from one-component $f_T^{(\nu)}$ models.

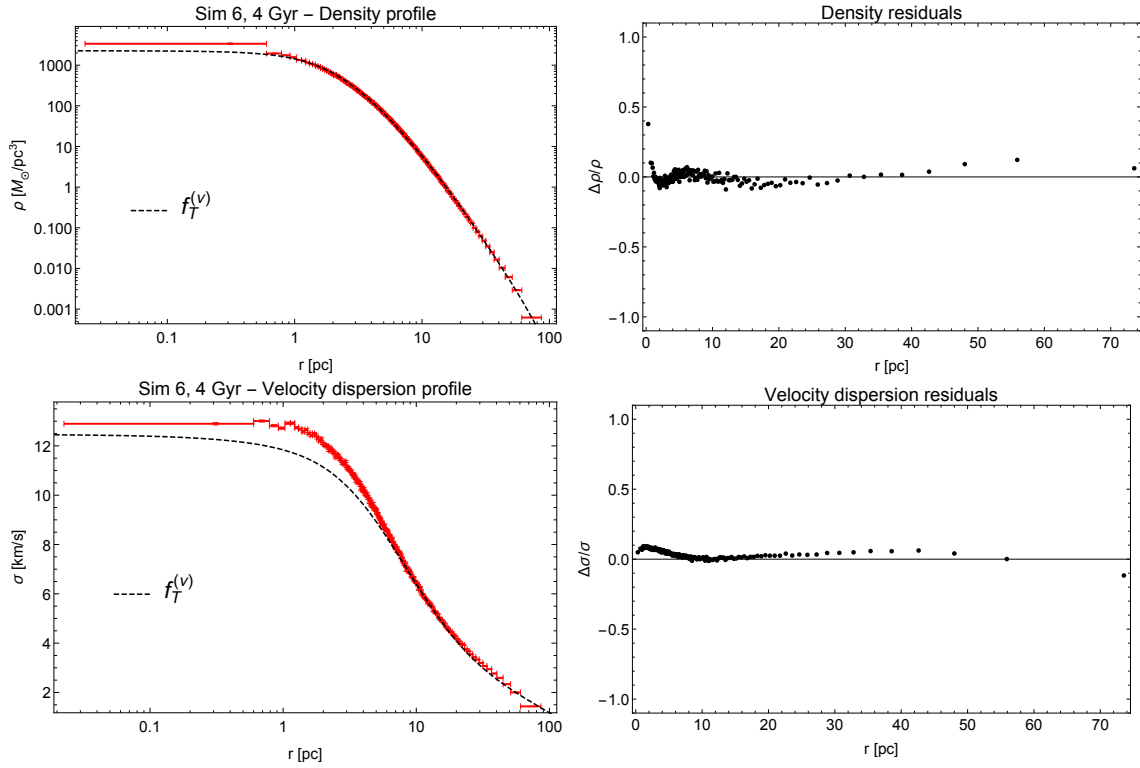


Figure B.6: Best-fit result for Sim 6 at 4 Gyr obtained from one-component $f_T^{(\nu)}$ models.

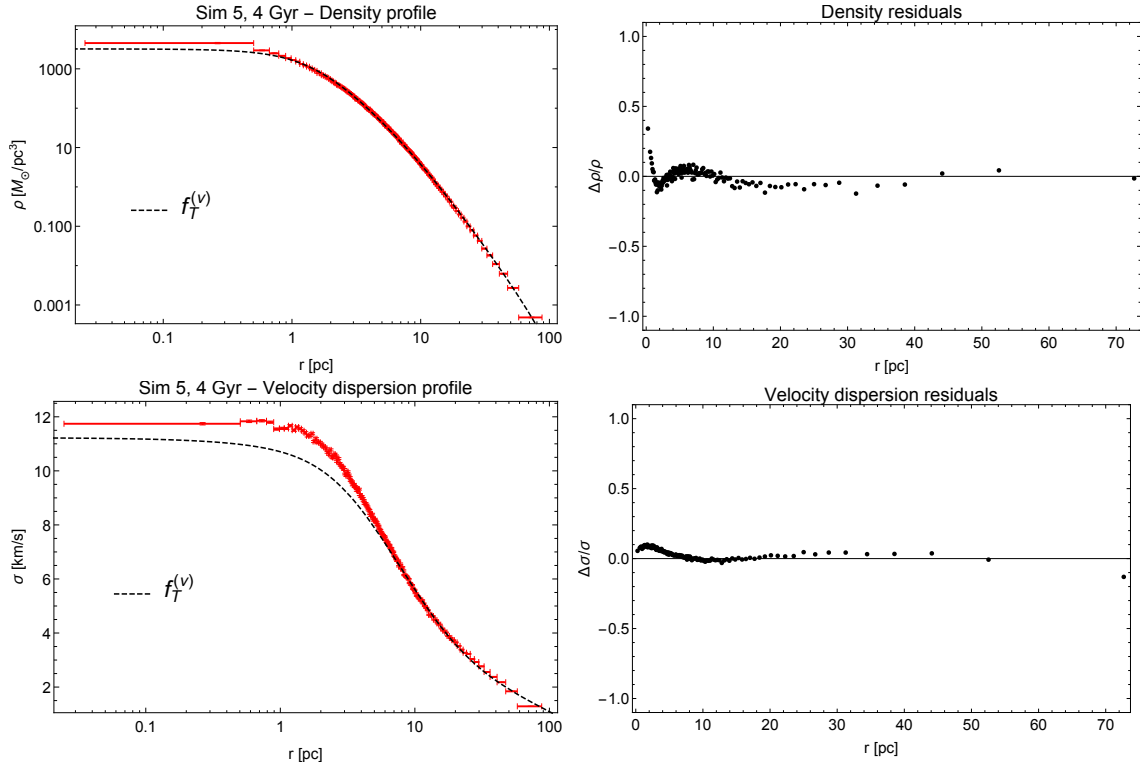


Figure B.7: Best-fit result for Sim 5 at 4 Gyr obtained from one-component $f_T^{(\nu)}$ models.

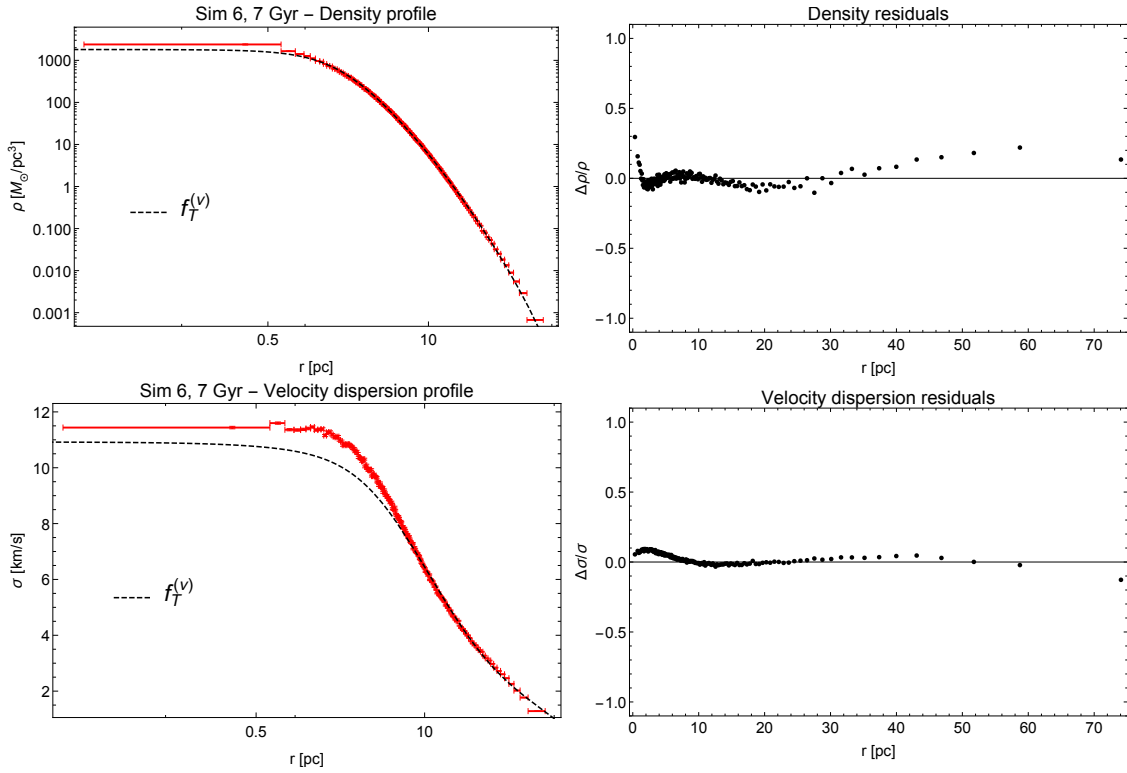


Figure B.8: Best-fit result for Sim 6 at 7 Gyr obtained from one-component $f_T^{(\nu)}$ models.

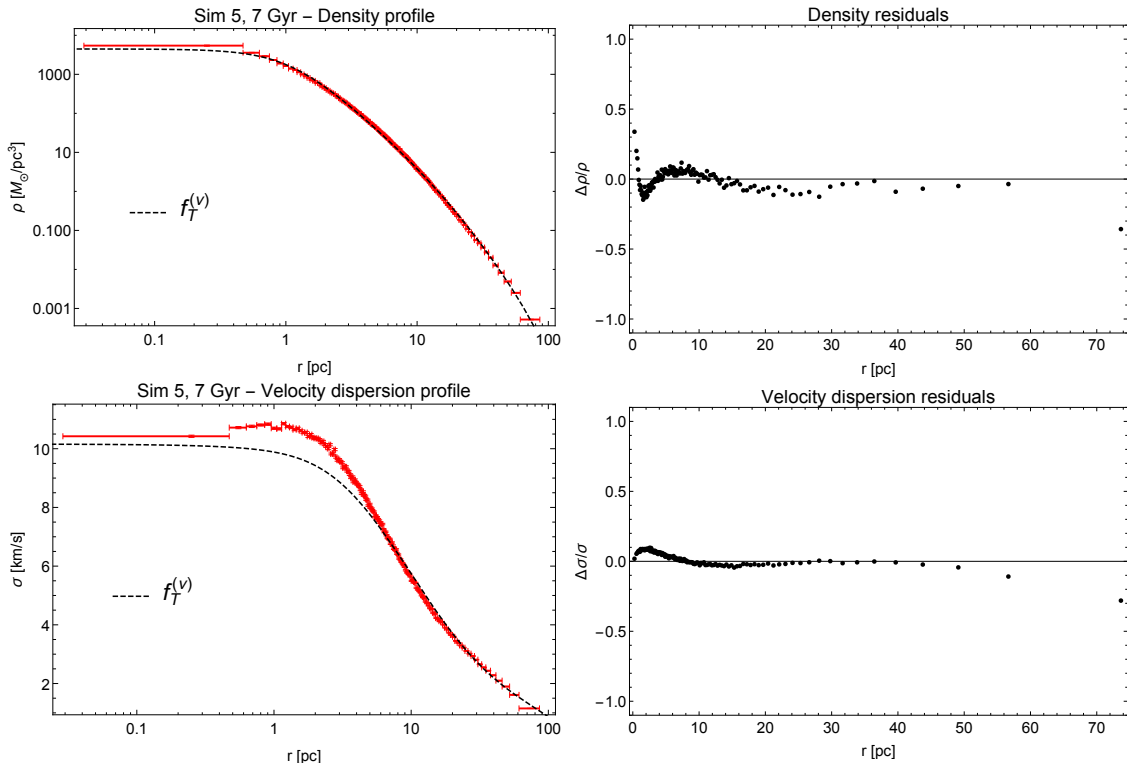


Figure B.9: Best-fit result for Sim 5 at 7 Gyr obtained from one-component $f_T^{(\nu)}$ models.

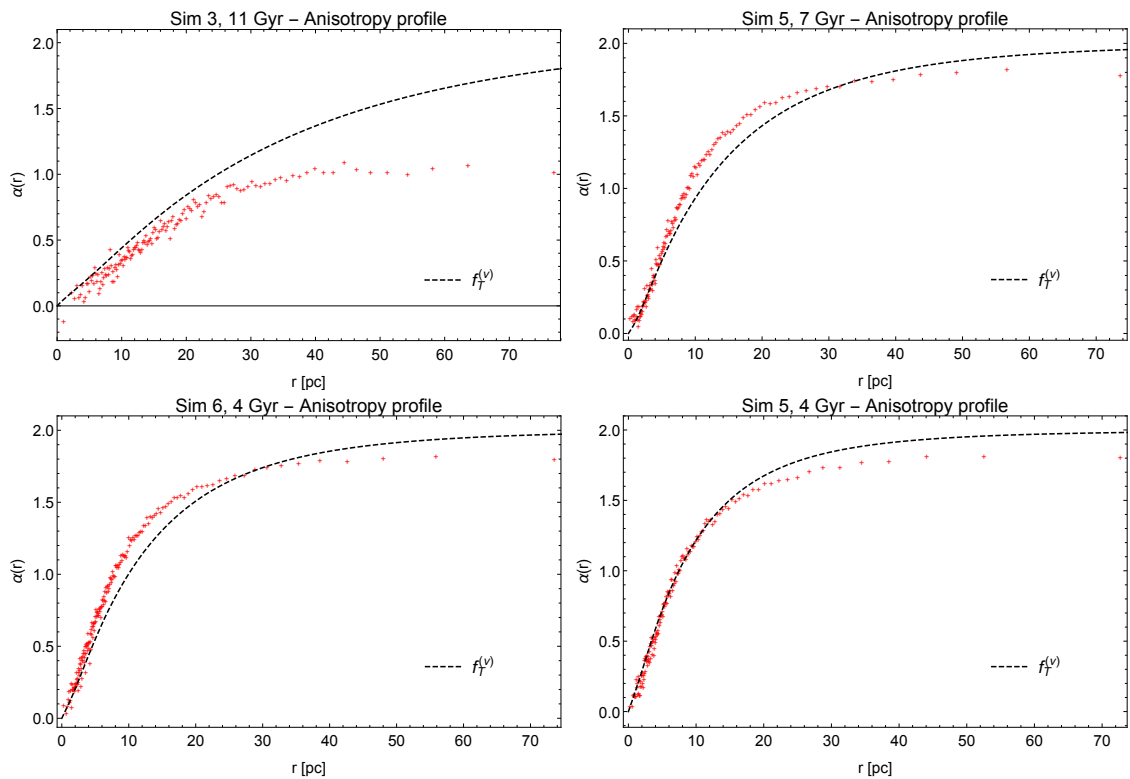


Figure B.10: Anisotropy profiles for the best-fit models obtained from one-component $f_T^{(\nu)}$ models.

B.2 Two-component models

B.2.1 Two-component King models

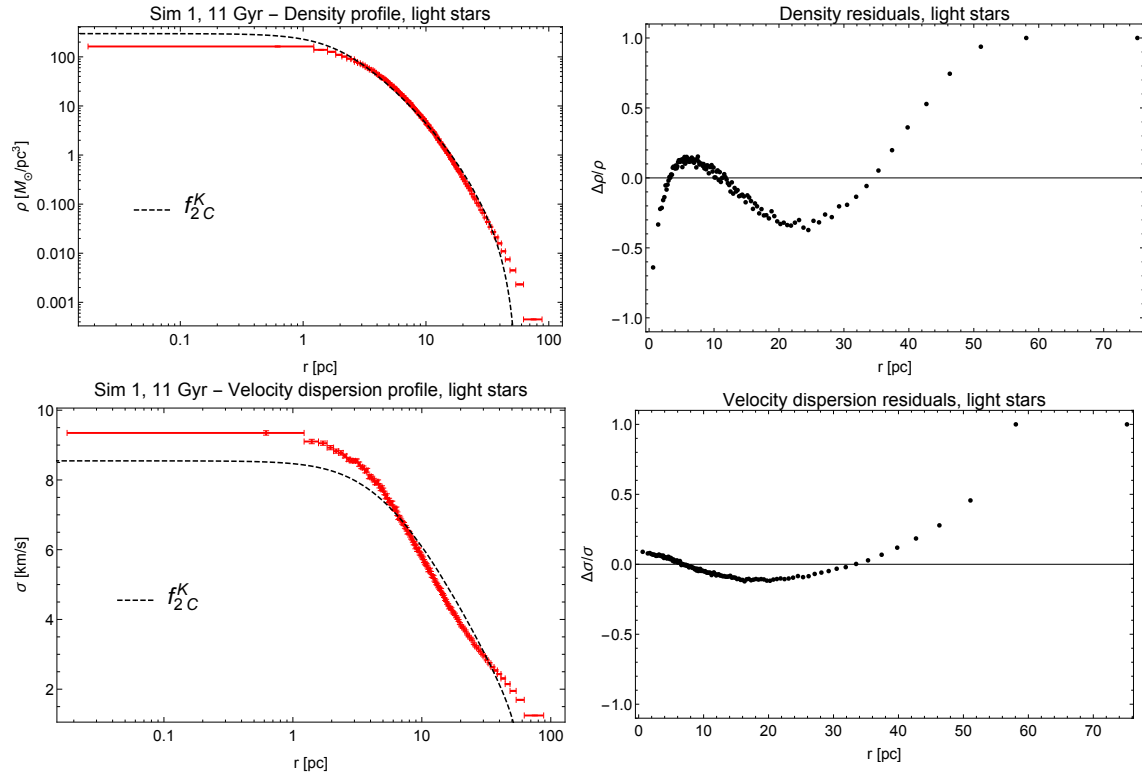


Figure B.11: Best-fit result for the light component of Sim 1 at 11 Gyr obtained from two-component King models.

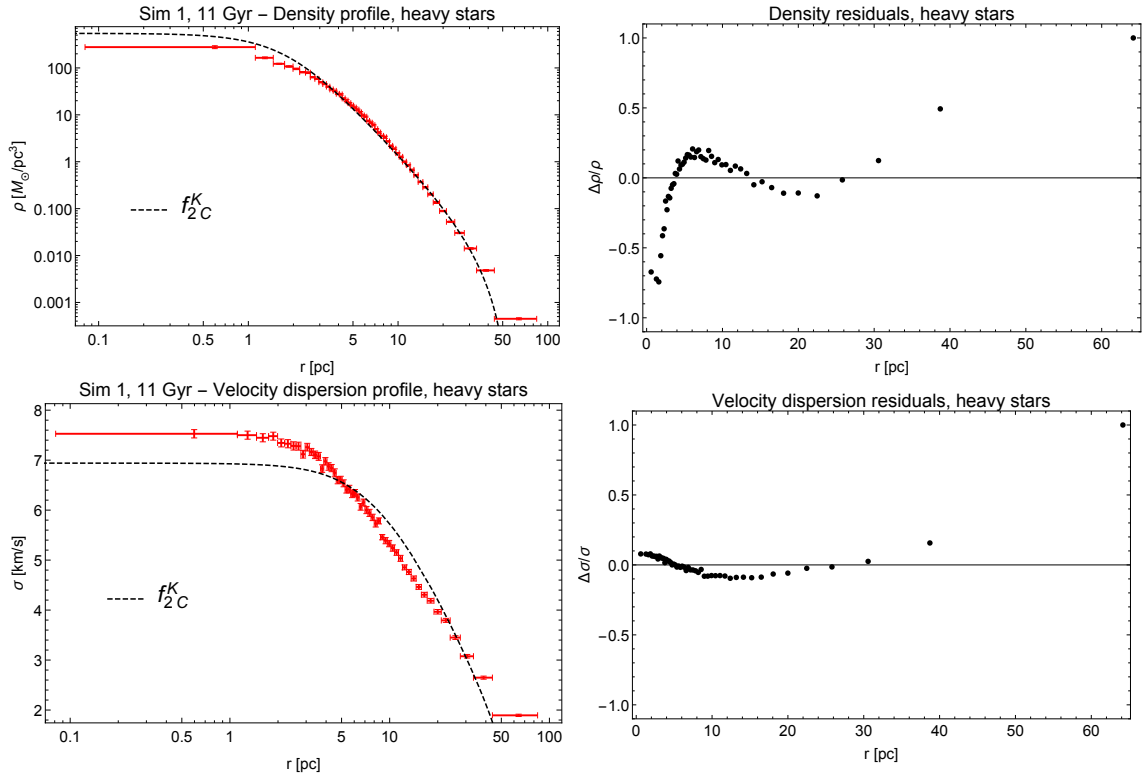


Figure B.12: Best-fit result for the heavy component of Sim 1 at 11 Gyr obtained from two-component King models.

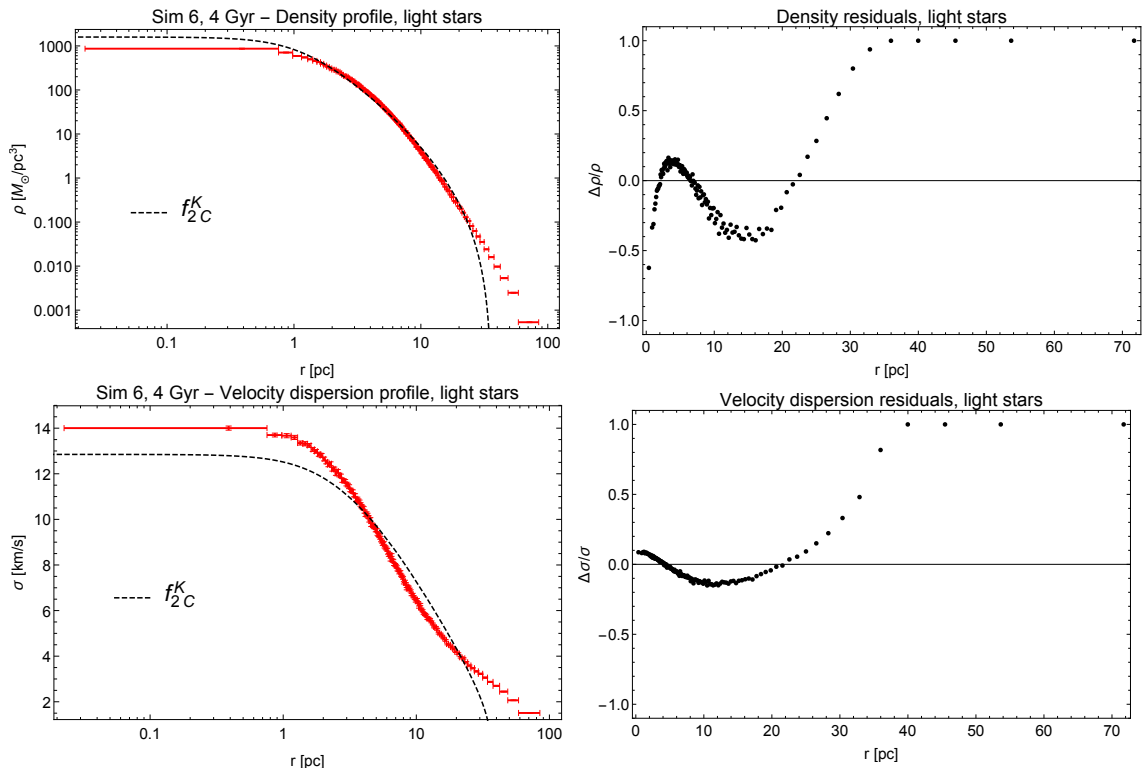


Figure B.13: Best-fit result for the light component of Sim 6 at 4 Gyr obtained from two-component King models.

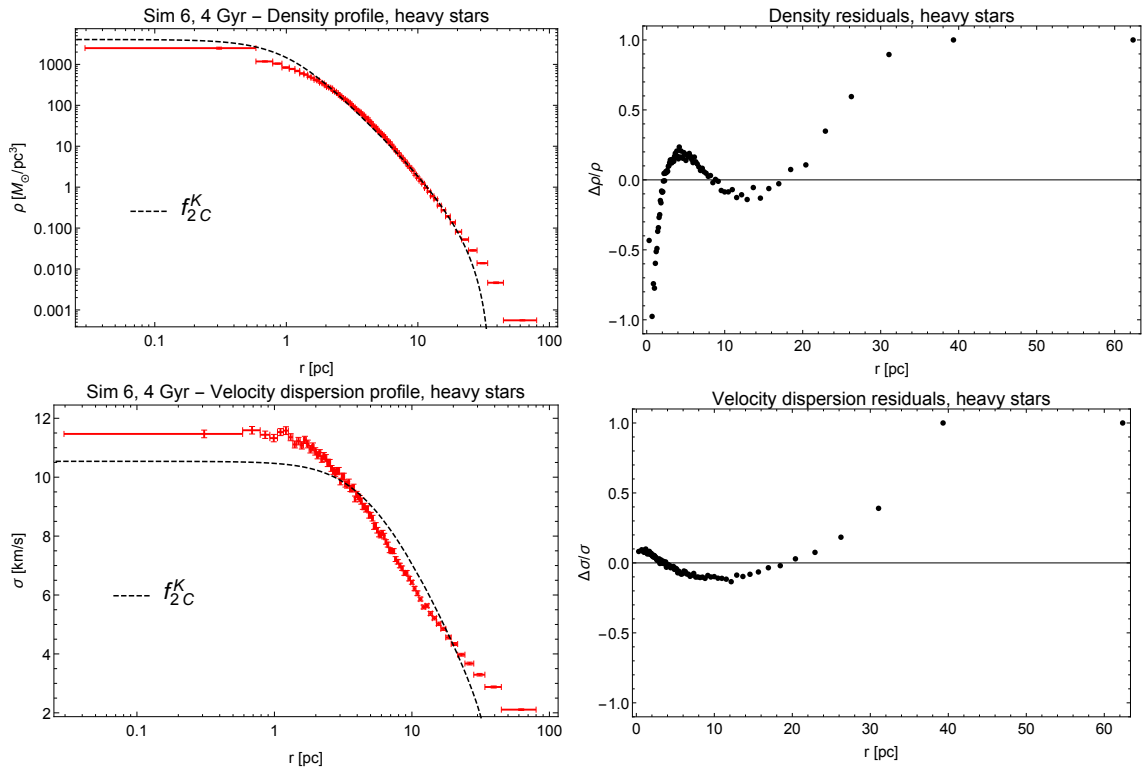


Figure B.14: Best-fit result for the heavy component of Sim 6 at 4 Gyr obtained from two-component King models.

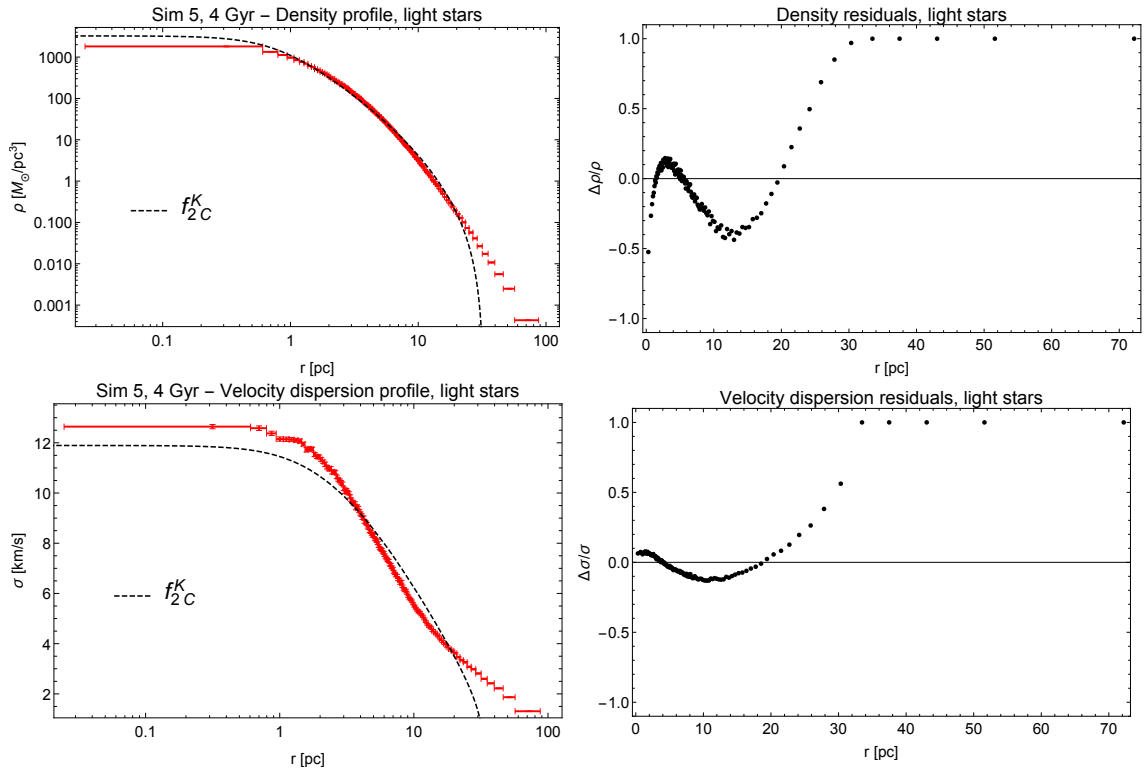


Figure B.15: Best-fit result for the light component of Sim 5 at 4 Gyr obtained from two-component King models.

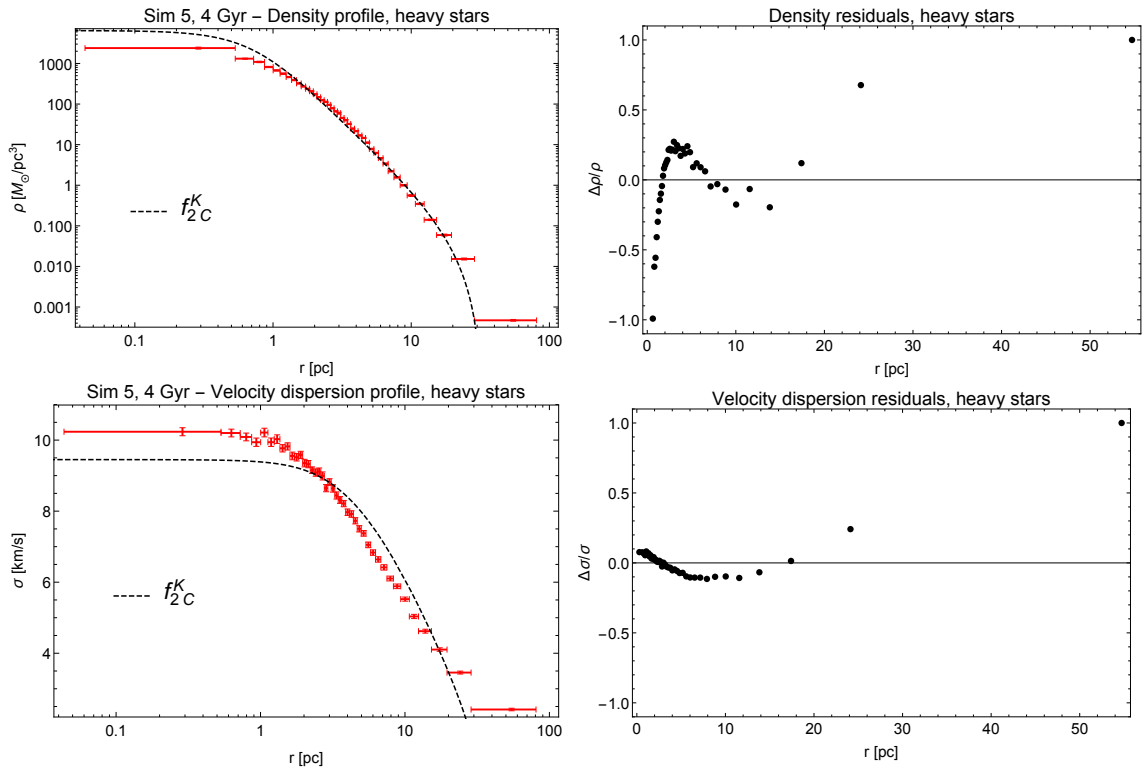


Figure B.16: Best-fit result for the heavy component of Sim 5 at 4 Gyr obtained from two-component King models.

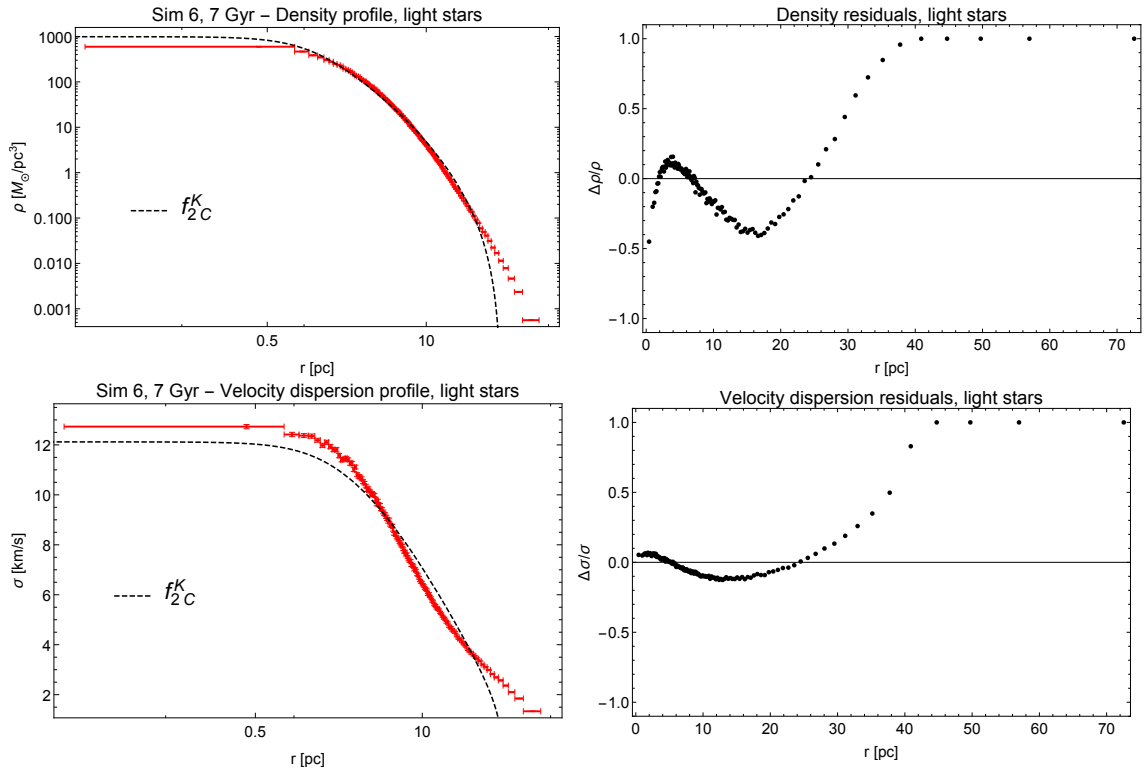


Figure B.17: Best-fit result for the light component of Sim 6 at 7 Gyr obtained from two-component King models.

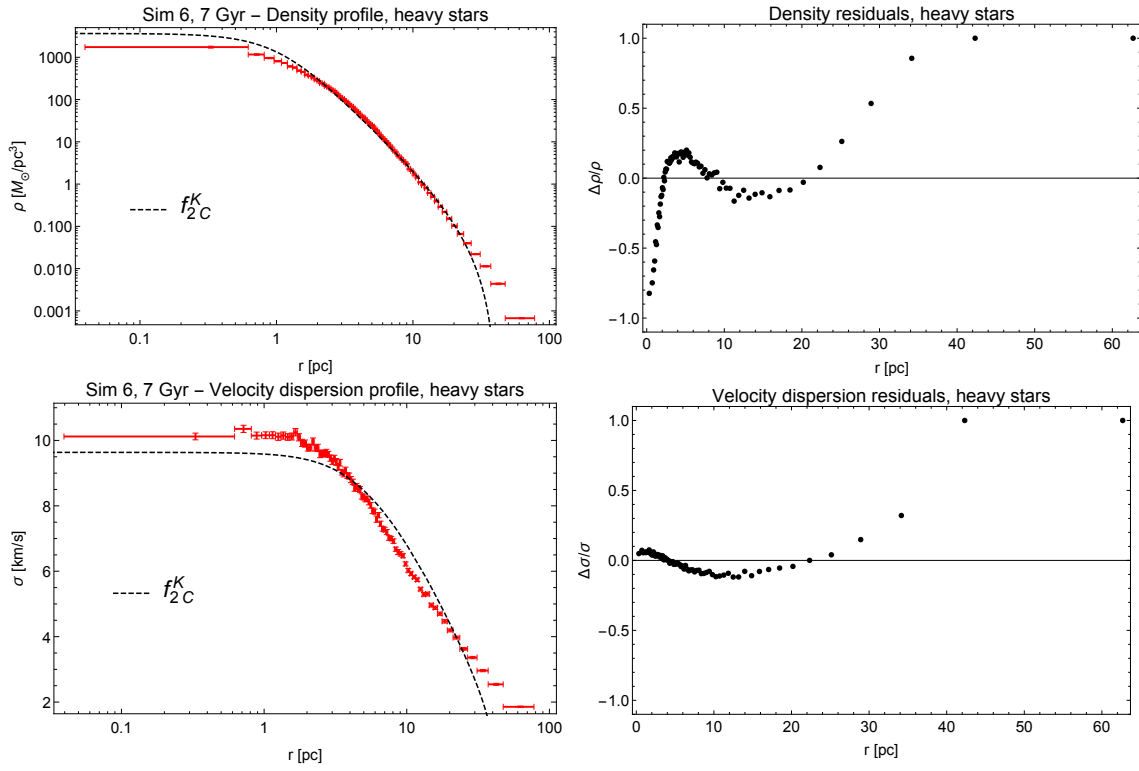


Figure B.18: Best-fit result for the heavy component of Sim 6 at 7 Gyr obtained from two-component King models.

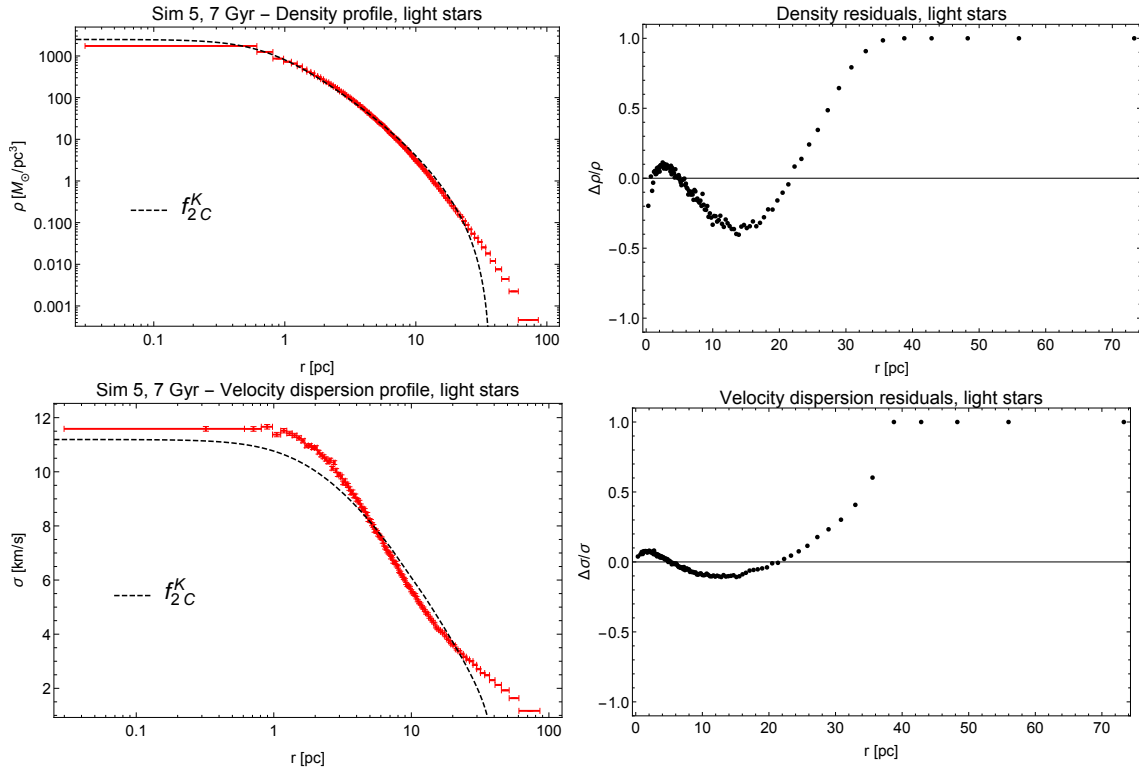


Figure B.19: Best-fit result for the light component of Sim 5 at 7 Gyr obtained from two-component King models.

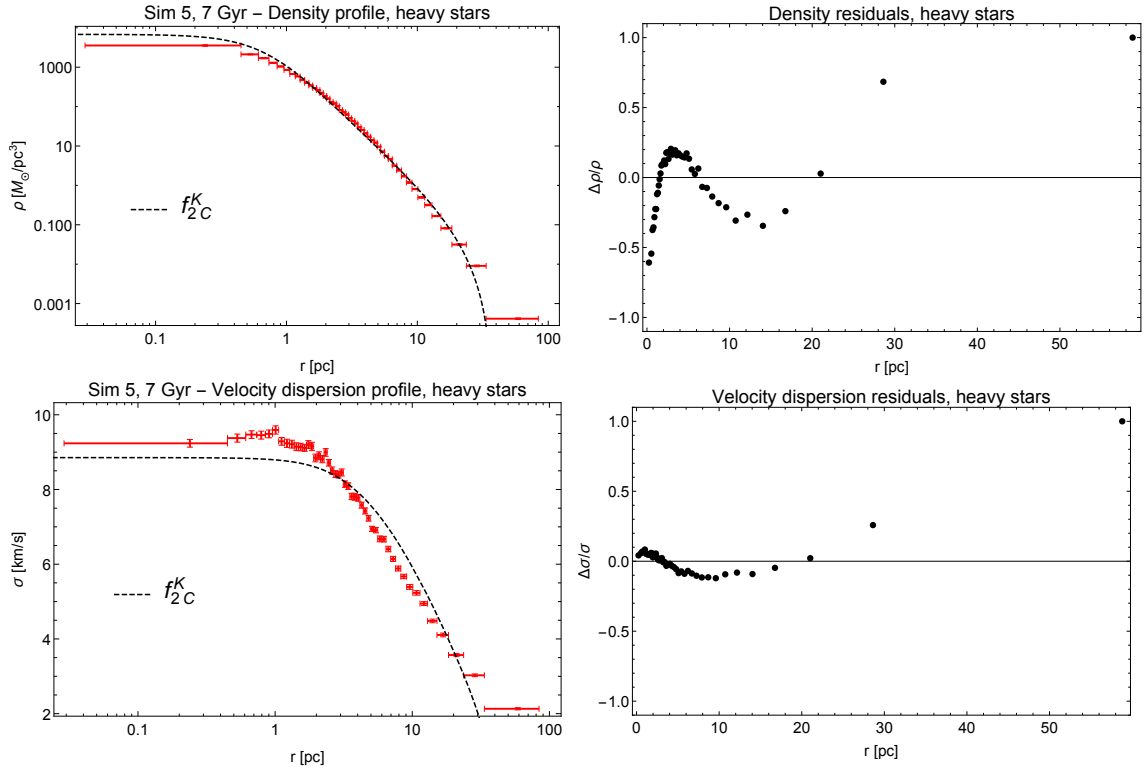


Figure B.20: Best-fit result for the heavy component of Sim 5 at 7 Gyr obtained from two-component King models.

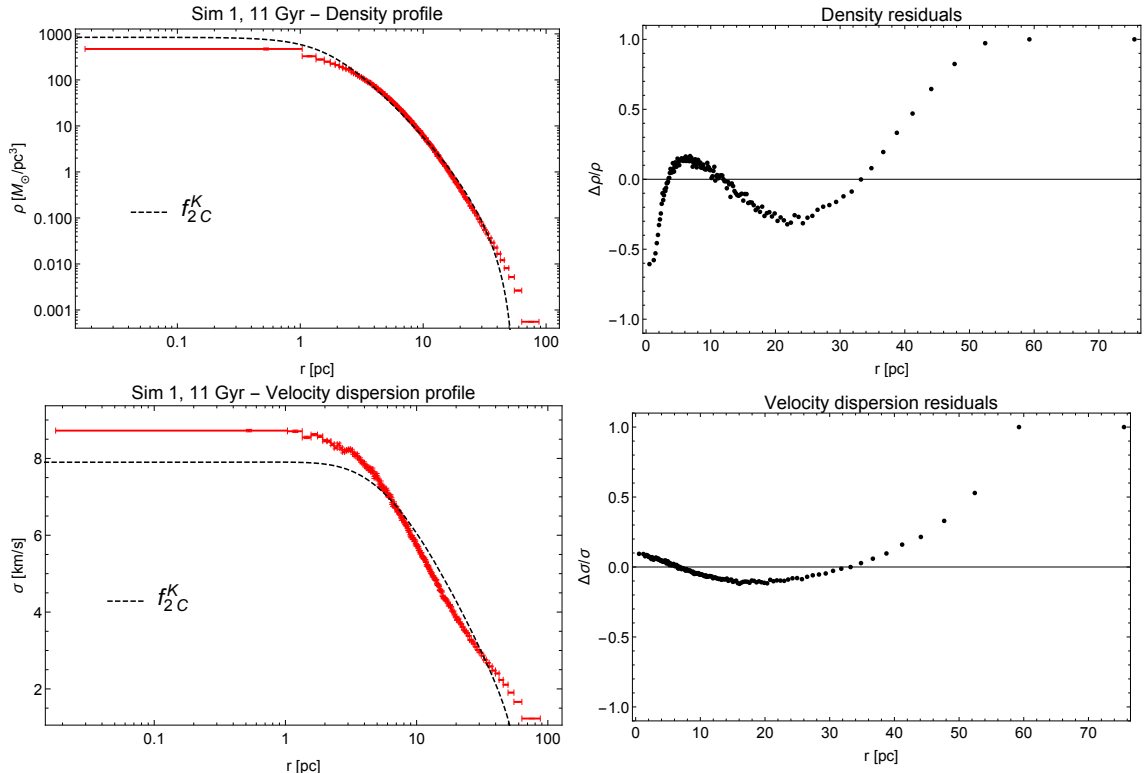


Figure B.21: Total density and velocity dispersion profiles for the best-fit model of Sim 1 at 11 Gyr obtained from two-component King models.

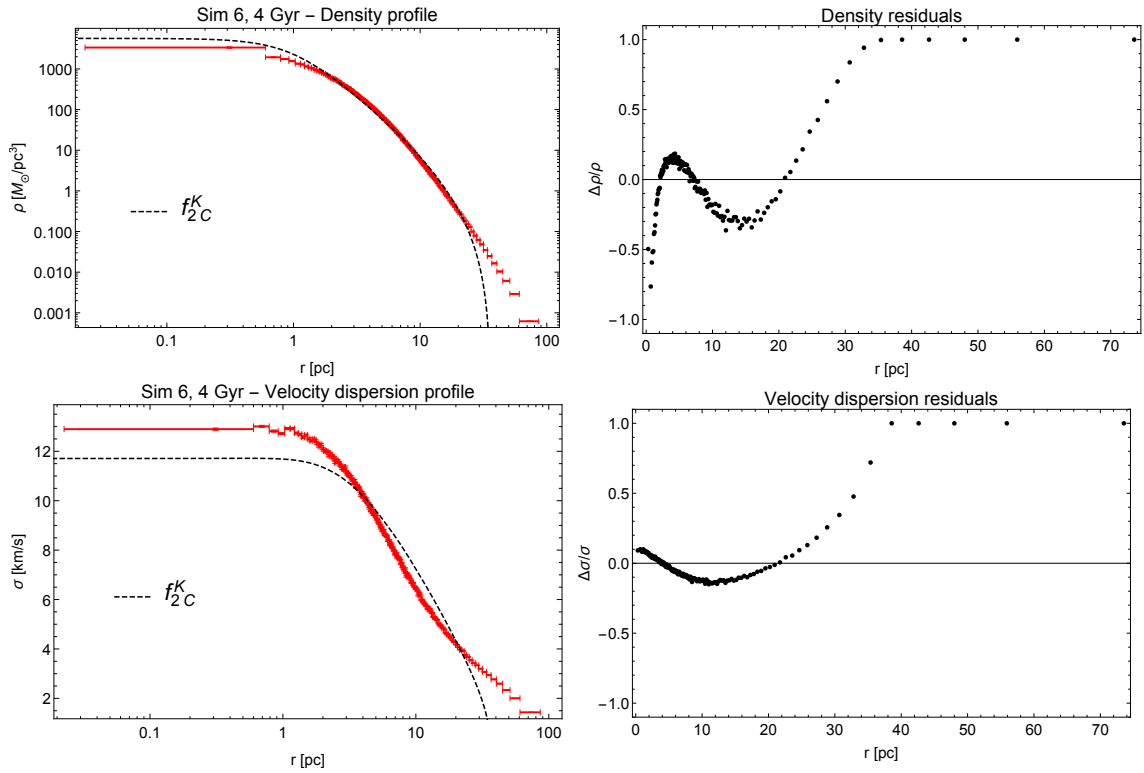


Figure B.22: Total density and velocity dispersion profiles for the best-fit model of Sim 6 at 4 Gyr obtained from two-component King models.

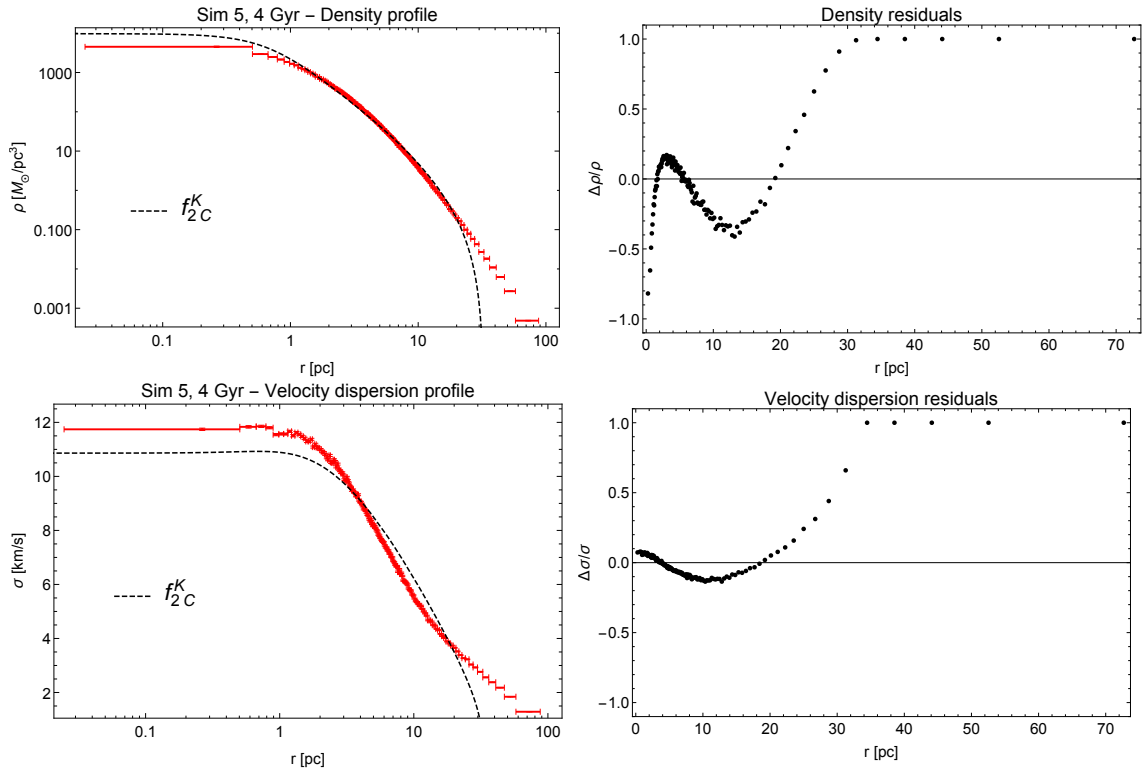


Figure B.23: Total density and velocity dispersion profiles for the best-fit model of Sim 5 at 4 Gyr obtained by means of a two-components King model.

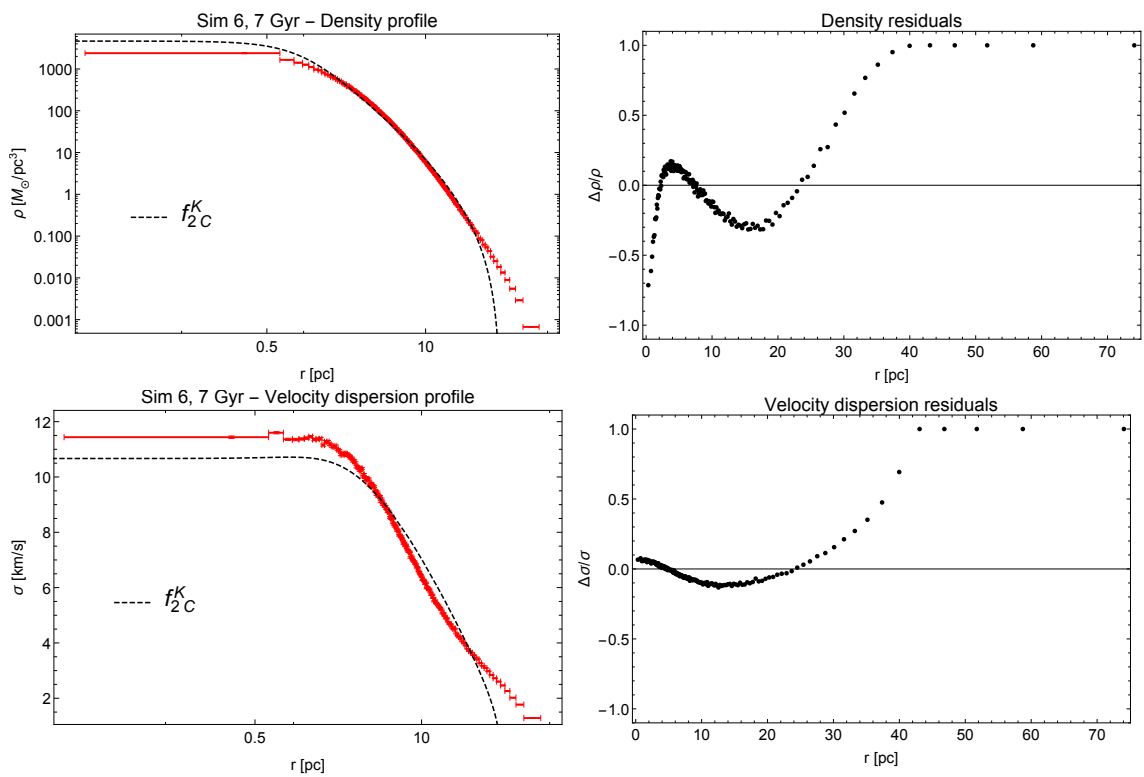


Figure B.24: Total density and velocity dispersion profiles for the best-fit model of Sim 6 at 7 Gyr obtained from two-component King models.

B.2.2 Two-component $f_T^{(\nu)}$ models

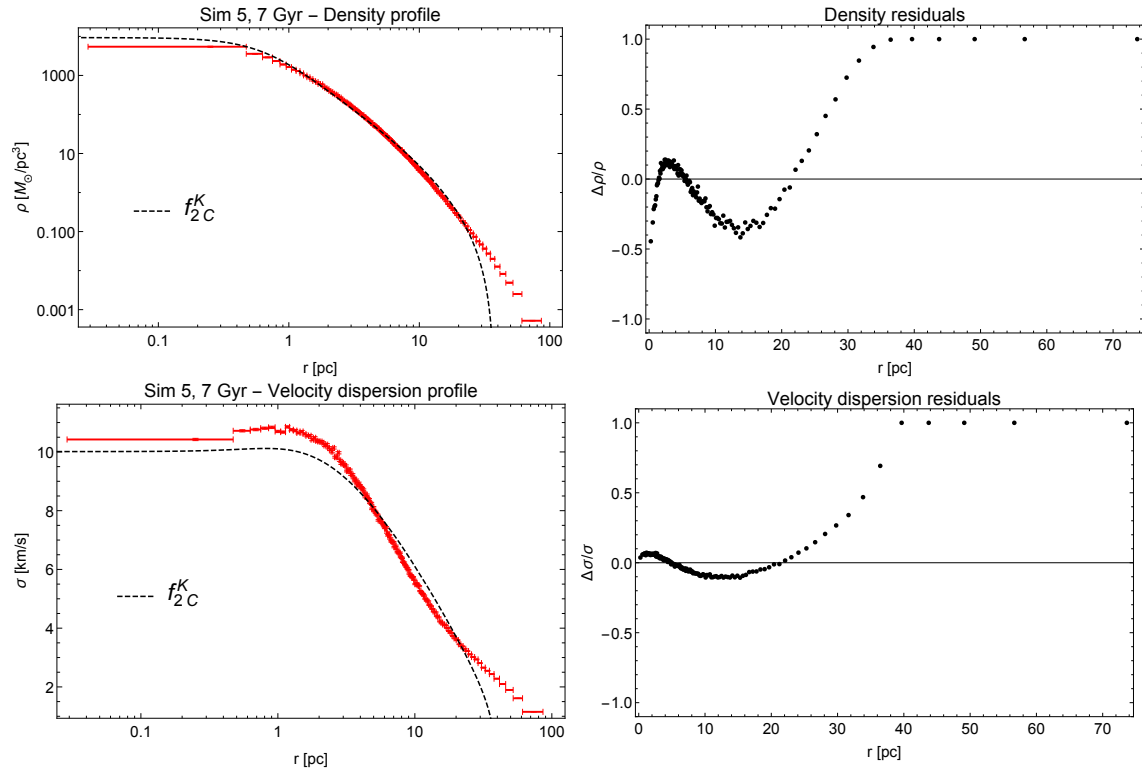


Figure B.25: Total density and velocity dispersion profiles for the best-fit model of Sim 5 at 7 Gyr obtained from two-component King models.

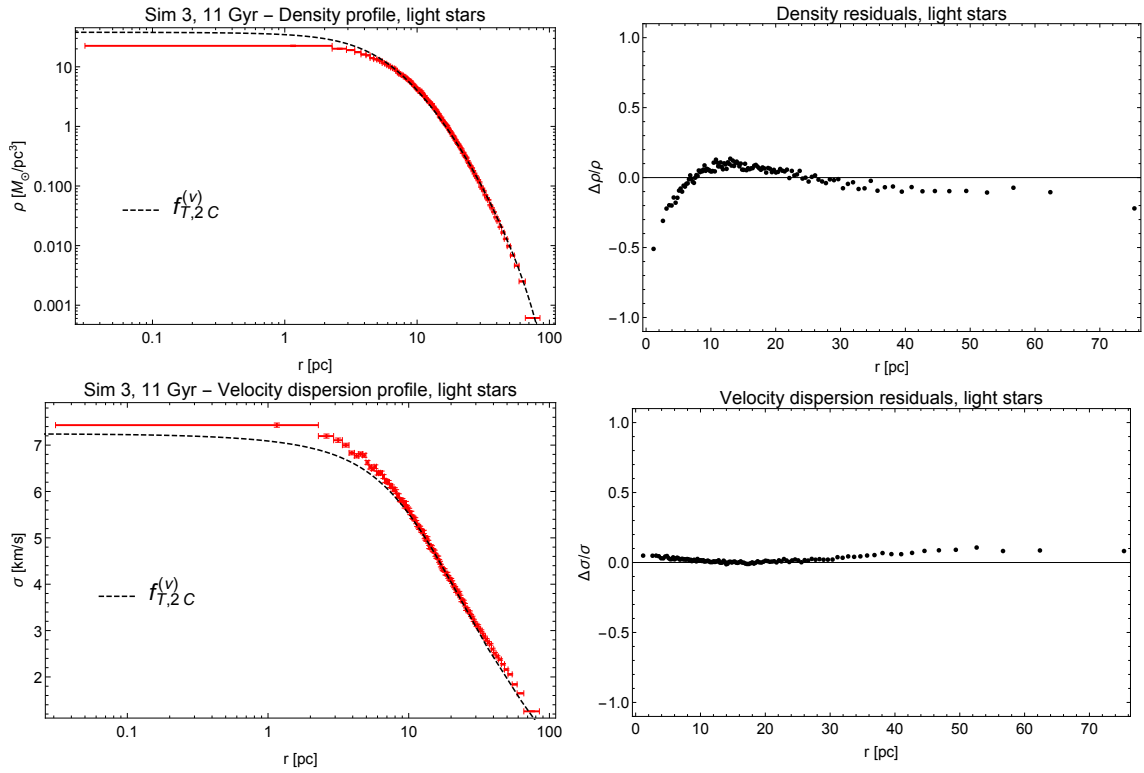


Figure B.26: Best-fit result for the light component of Sim 3 at 11 Gyr obtained from two-component $f_T^{(\nu)}$ models.

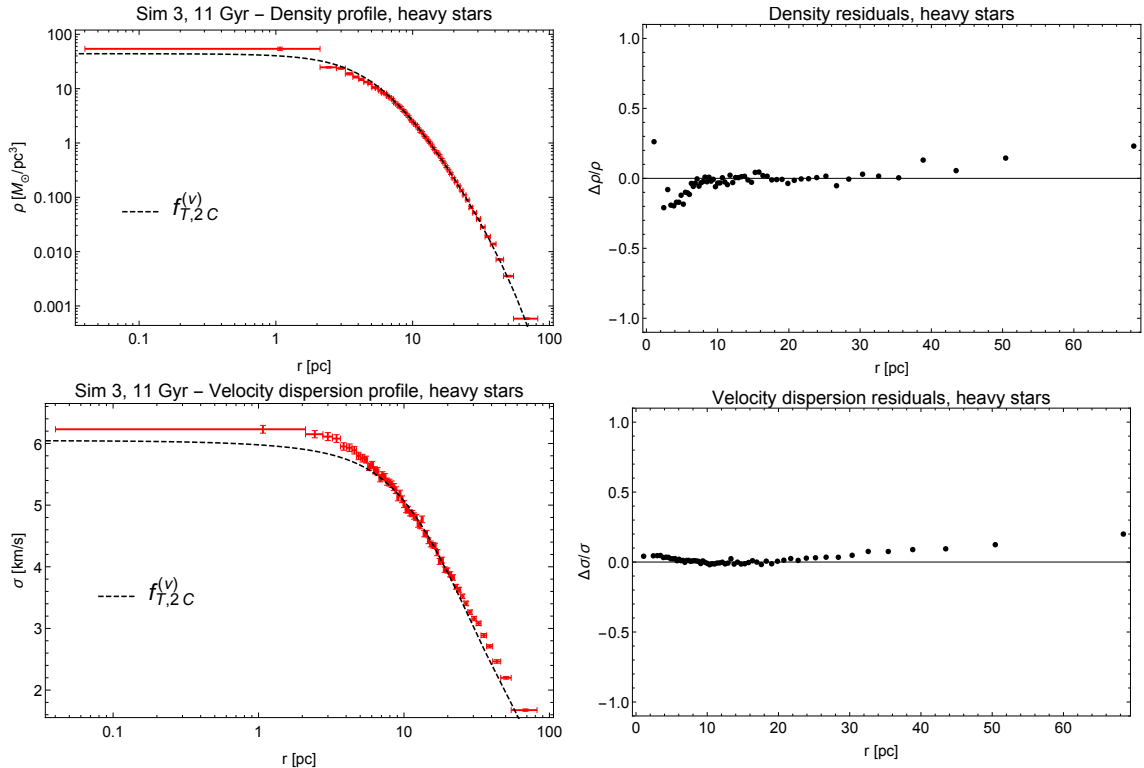


Figure B.27: Best-fit result for the heavy component of Sim 3 at 11 Gyr obtained from two-component $f_T^{(\nu)}$ models.

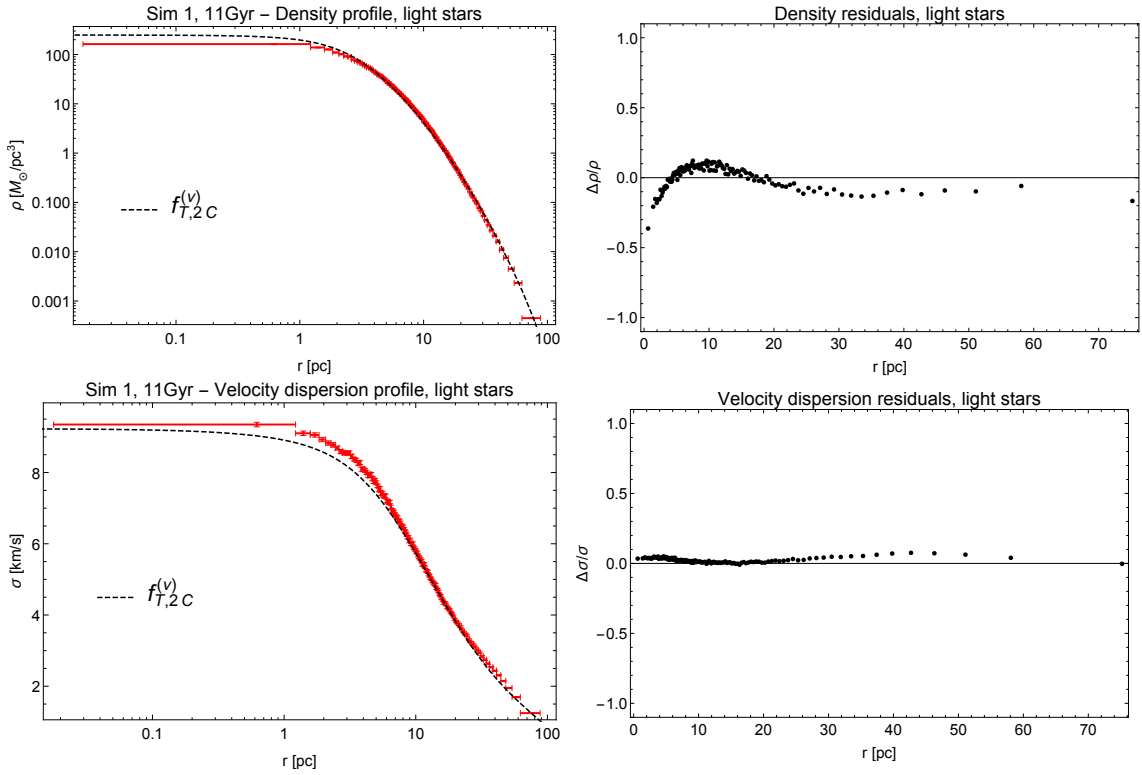


Figure B.28: Best-fit result for the light component of Sim 1 at 11 Gyr obtained from two-component $f_T^{(\nu)}$ models.

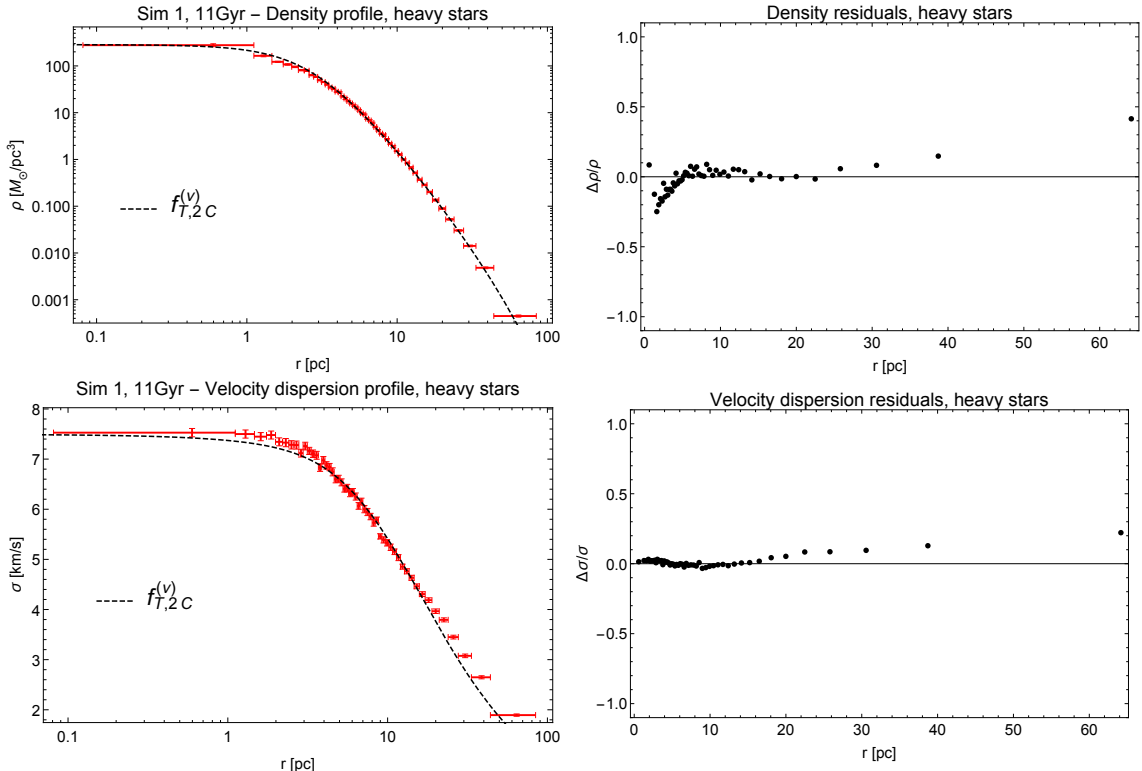


Figure B.29: Best-fit result for the heavy component of Sim 1 at 11 Gyr obtained from two-component $f_T^{(\nu)}$ models.

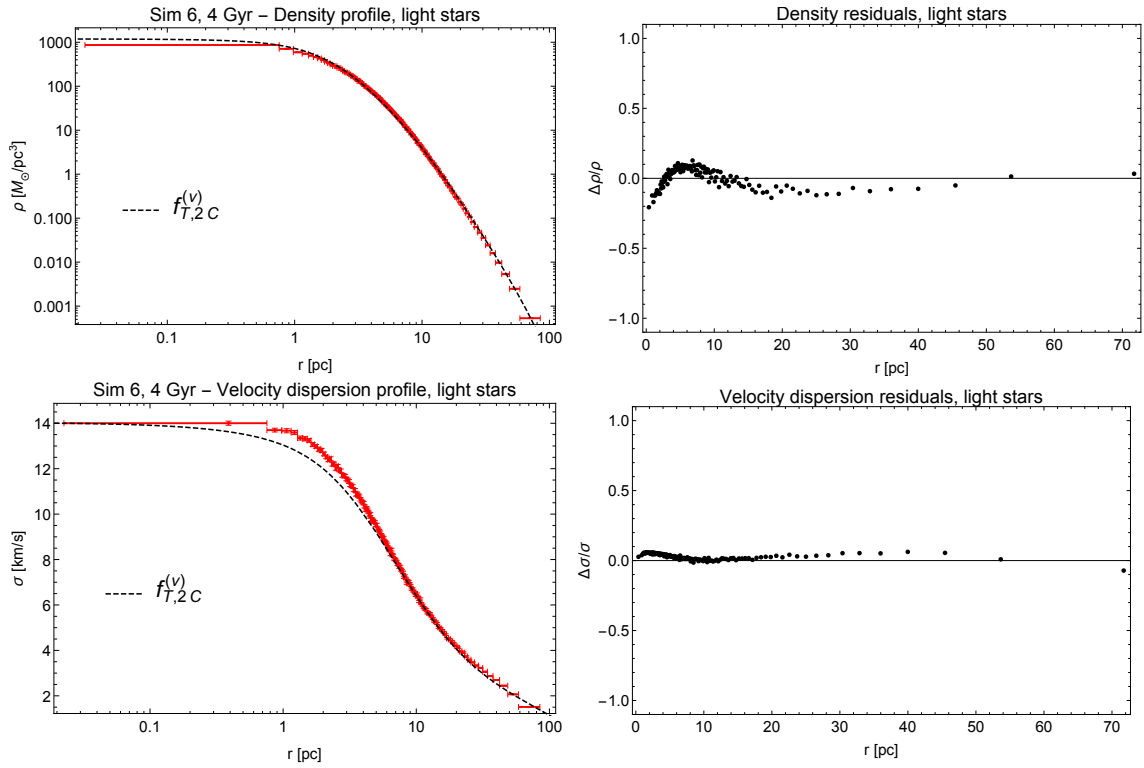


Figure B.30: Best-fit result for the light component of Sim 6 at 4 Gyr obtained from two-component $f_T^{(\nu)}$ models.

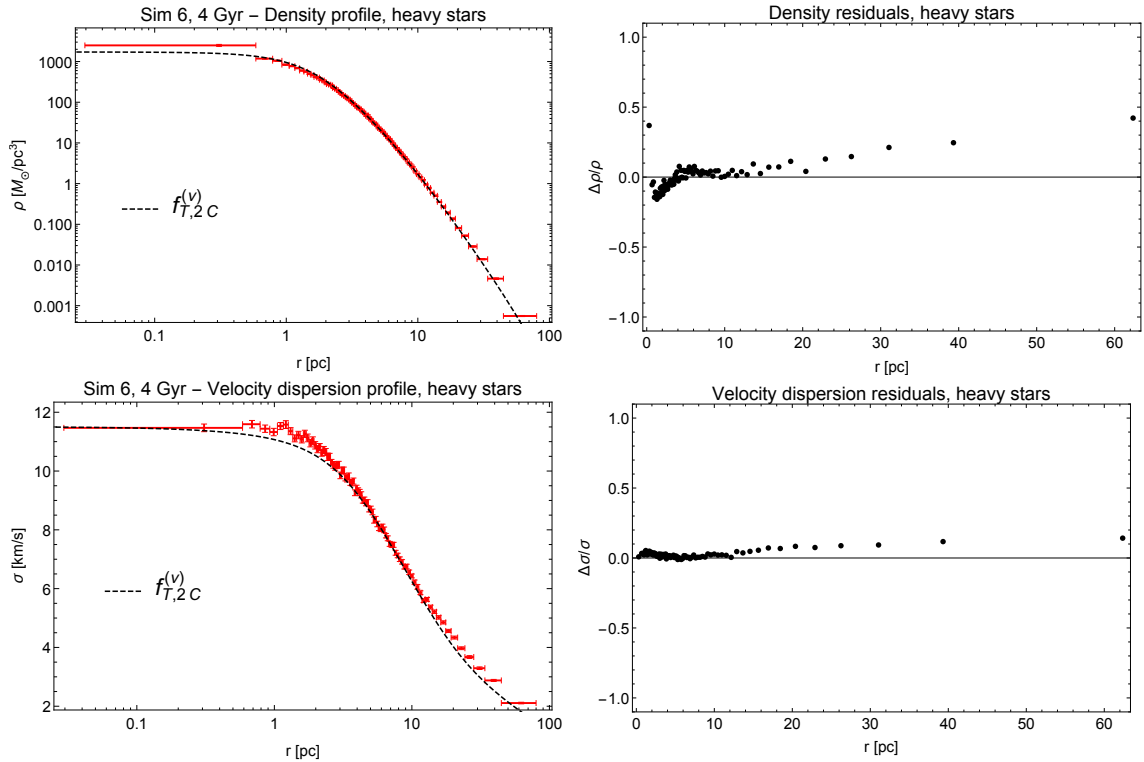


Figure B.31: Best-fit result for the heavy component of Sim 6 at 4 Gyr obtained from two-component $f_T^{(\nu)}$ models.

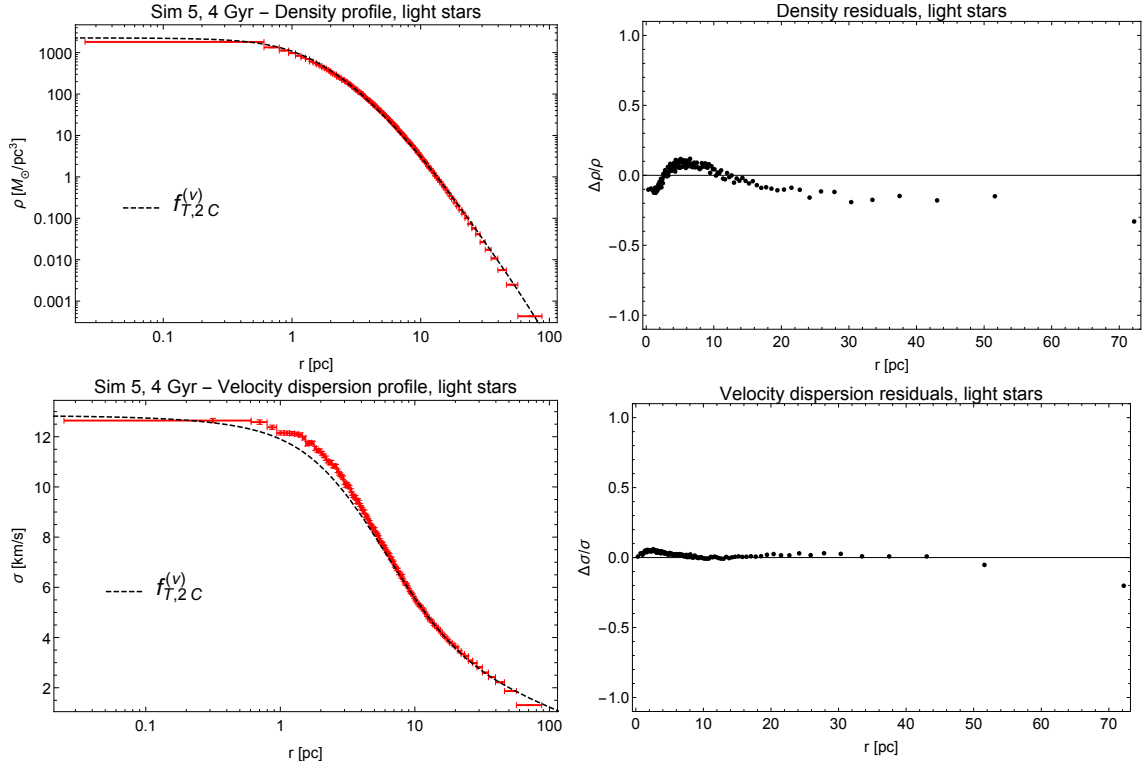


Figure B.32: Best-fit result for the light component of Sim 5 at 4 Gyr obtained from two-component $f_T^{(\nu)}$ models..

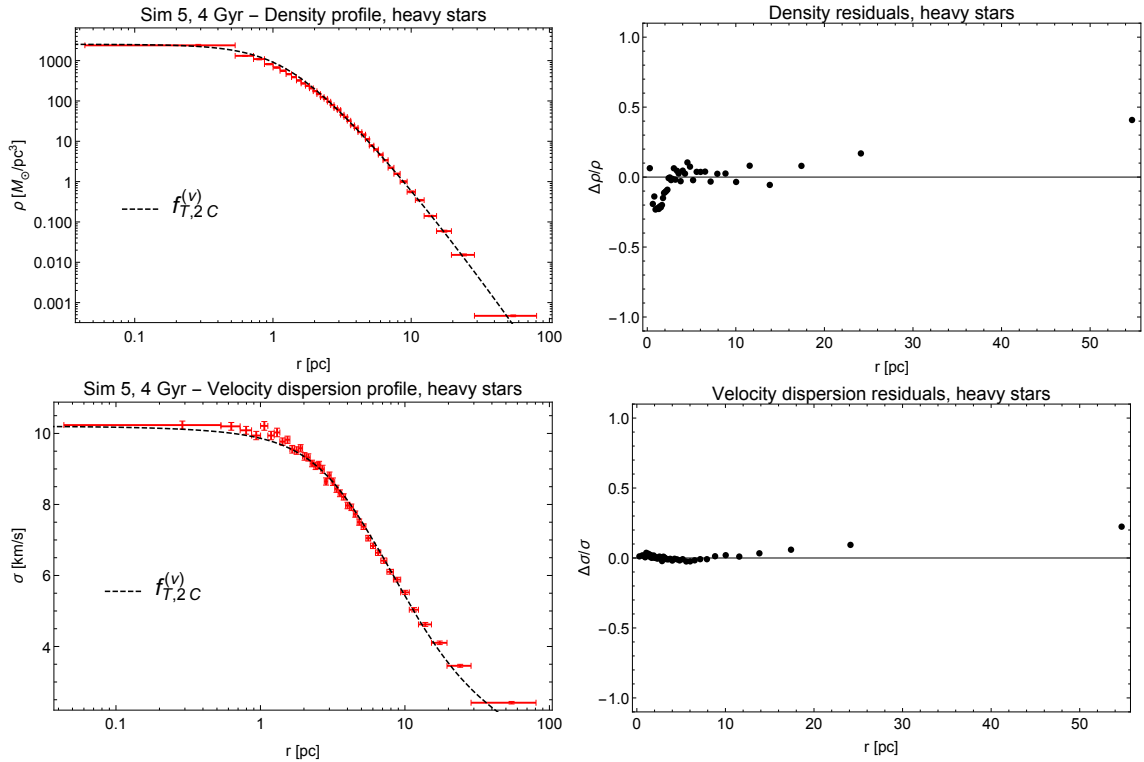


Figure B.33: Best-fit result for the heavy component of Sim 5 at 4 Gyr obtained from two-component $f_T^{(\nu)}$ models.

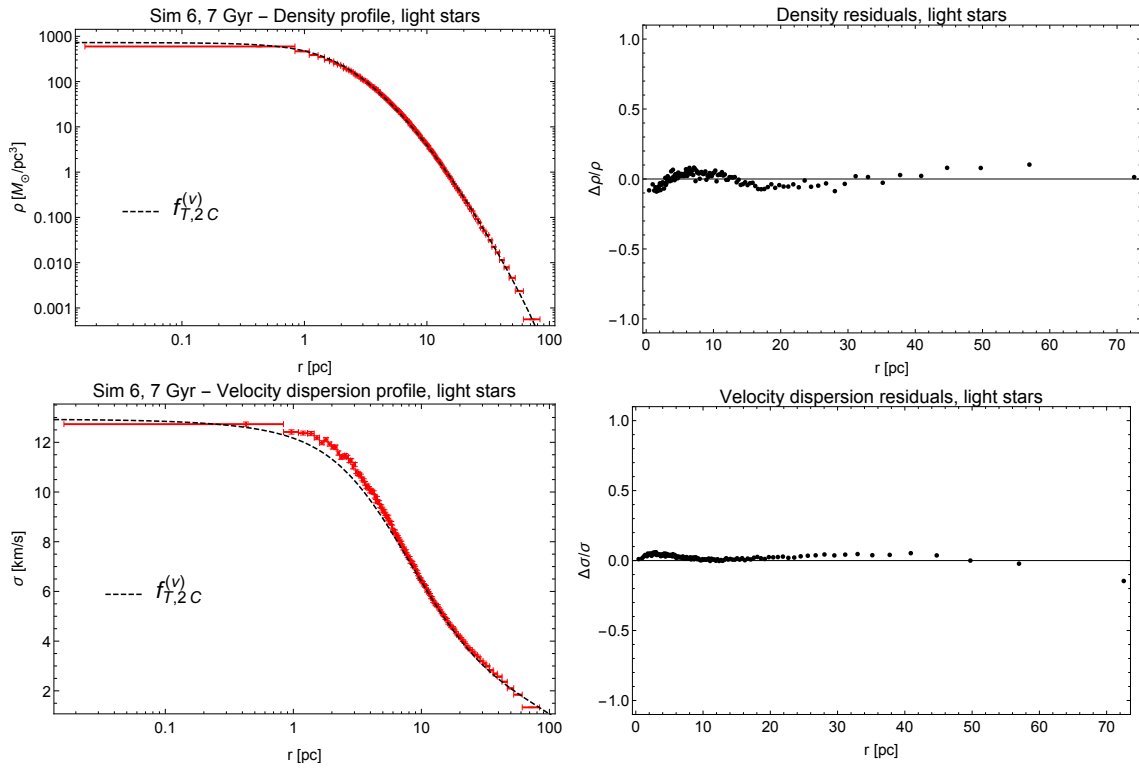


Figure B.34: Best-fit result for the light component of Sim 6 at 7 Gyr obtained from two-component $f_T^{(\nu)}$ models.

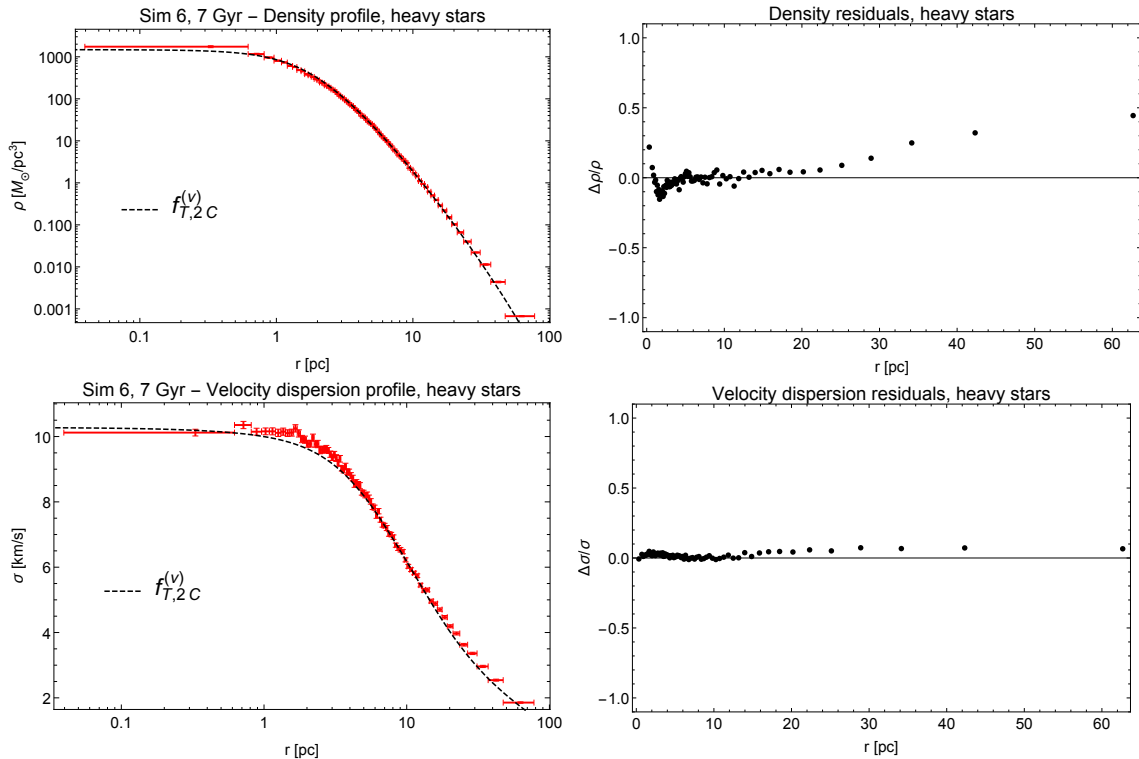


Figure B.35: Best-fit result for the heavy component of Sim 6 at 7 Gyr obtained from two-component $f_T^{(\nu)}$ models.

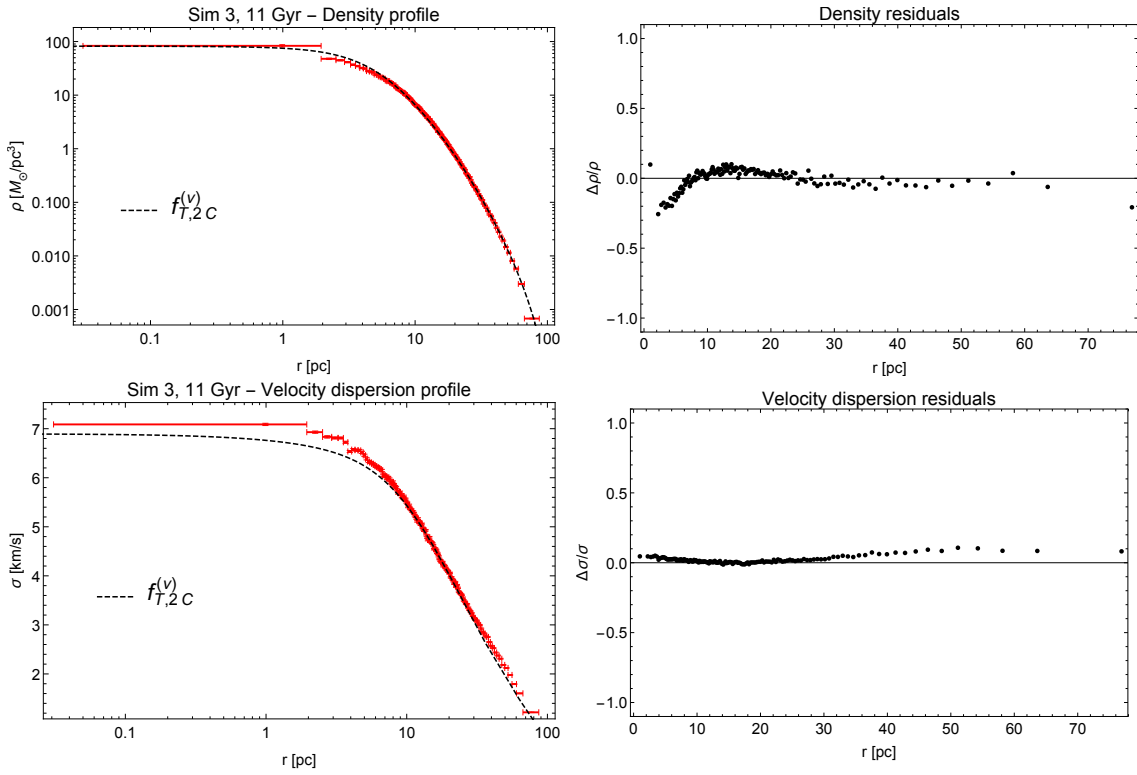


Figure B.36: Total density and velocity dispersion profiles for the best-fit model of Sim 3 at 11 Gyr obtained from two-component $f_T^{(\nu)}$ models.

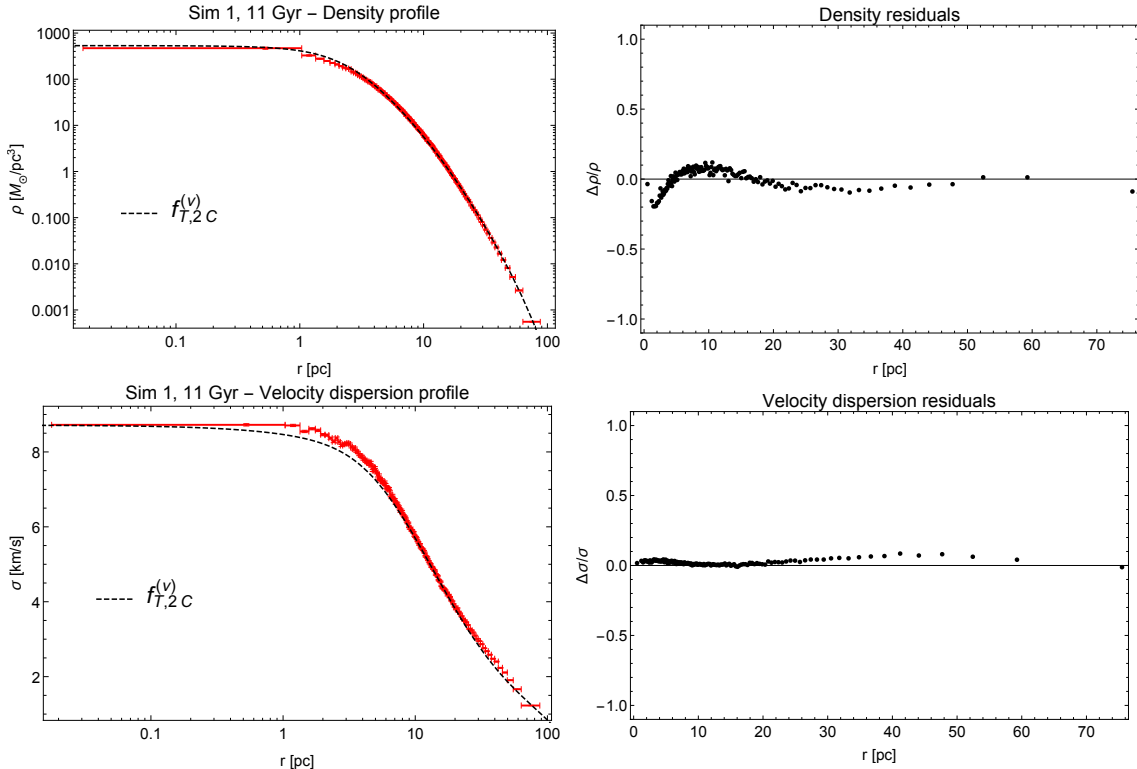


Figure B.37: Total density and velocity dispersion profiles for the best-fit model of Sim 1 at 11 Gyr obtained from two-component $f_T^{(\nu)}$ models.

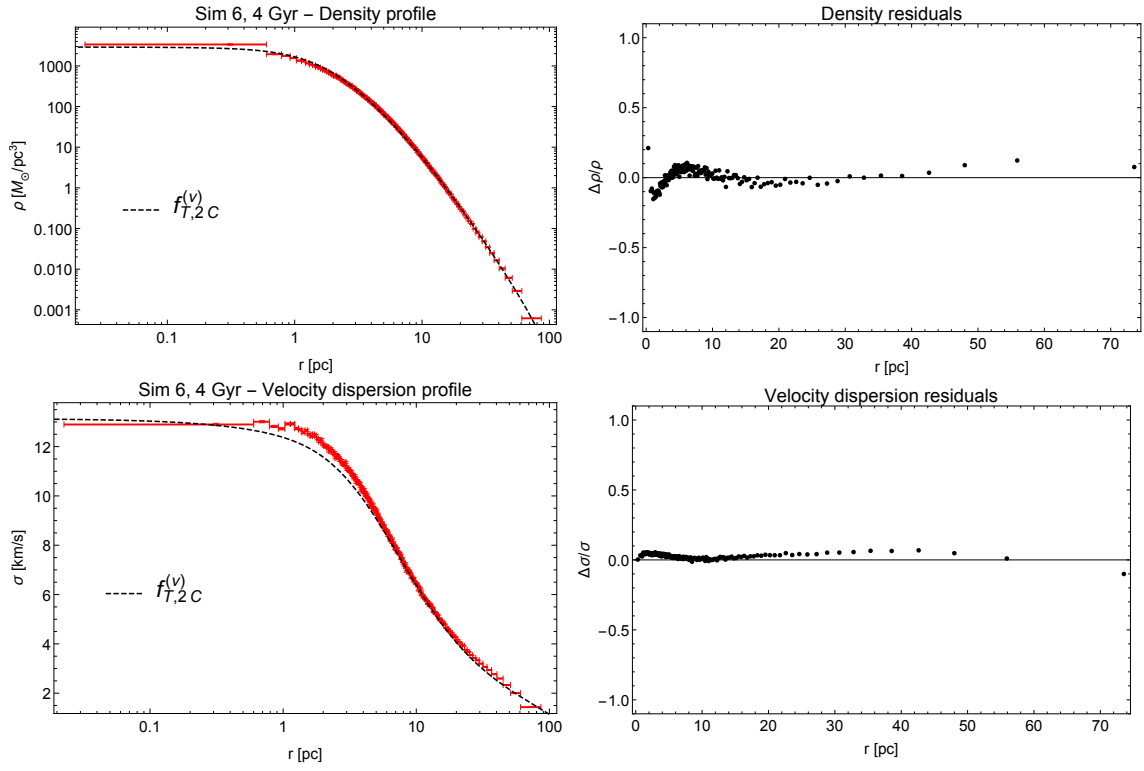


Figure B.38: Total density and velocity dispersion profiles for the best-fit model of Sim 6 at 4 Gyr obtained from two-component $f_T^{(\nu)}$ models.

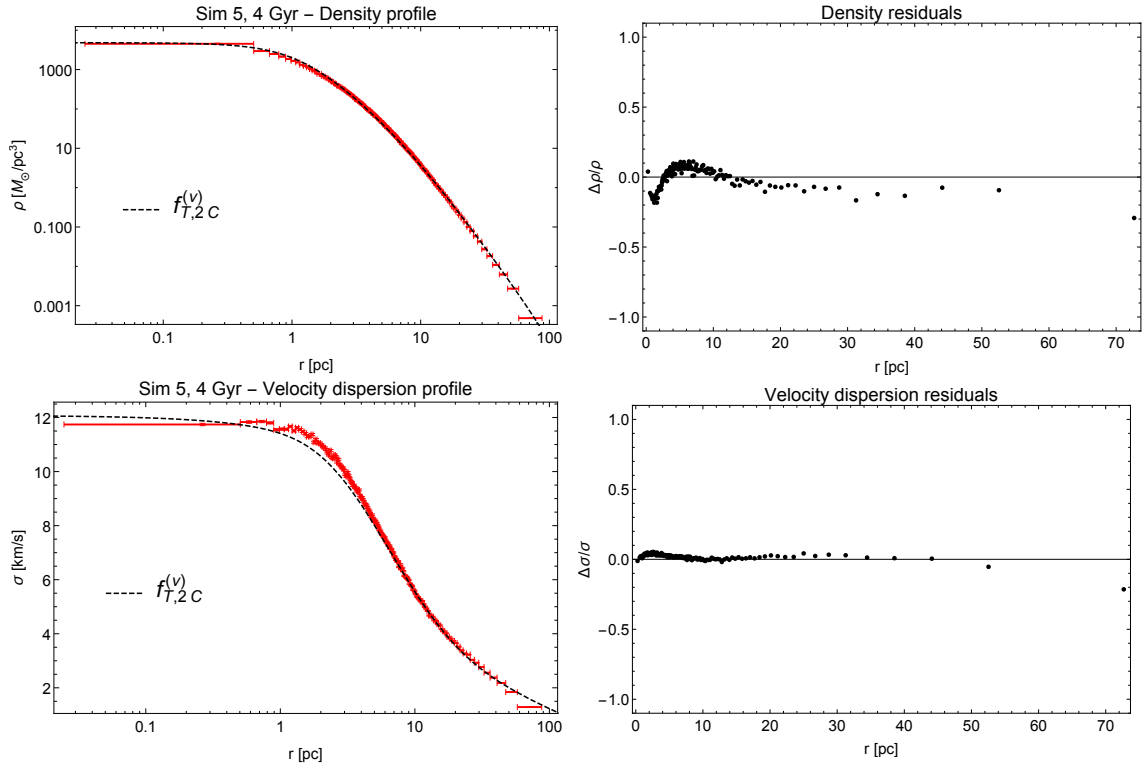


Figure B.39: Total density and velocity dispersion profiles for the best-fit model of Sim 5 at 4 Gyr obtained from two-component $f_T^{(\nu)}$ models.

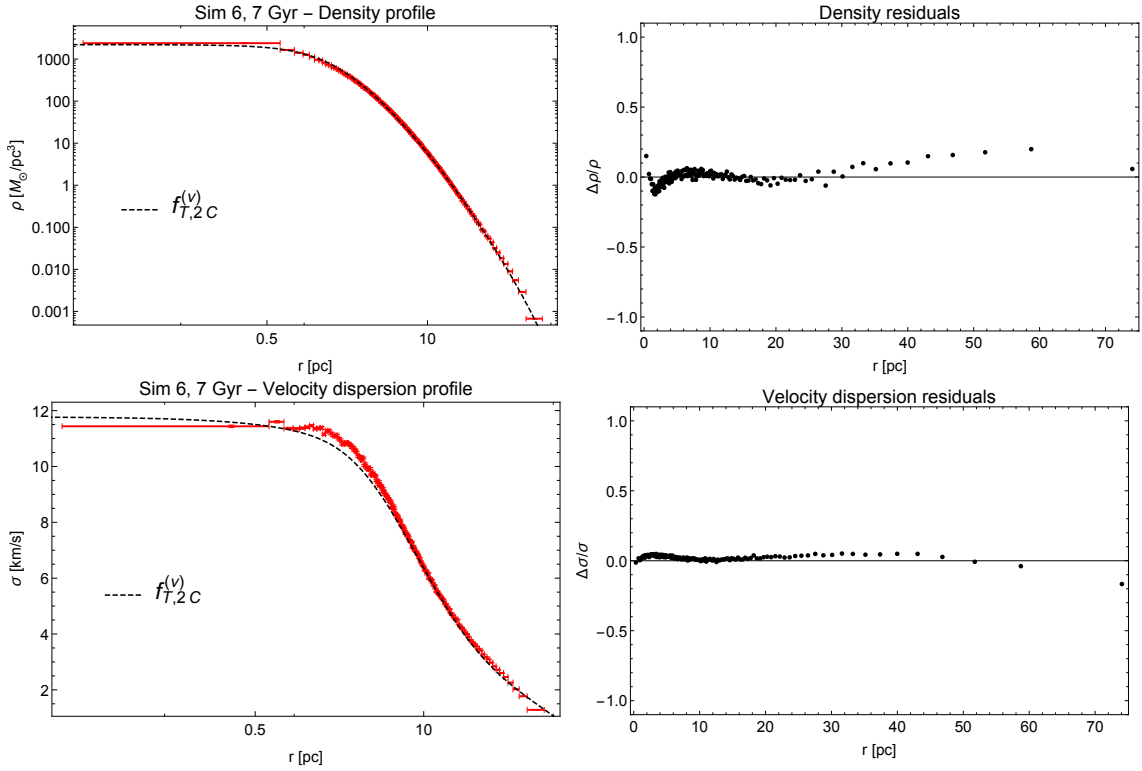


Figure B.40: Total density and velocity dispersion profiles for the best-fit model of Sim 6 at 7 Gyr obtained from two-component $f_T^{(\nu)}$ models.

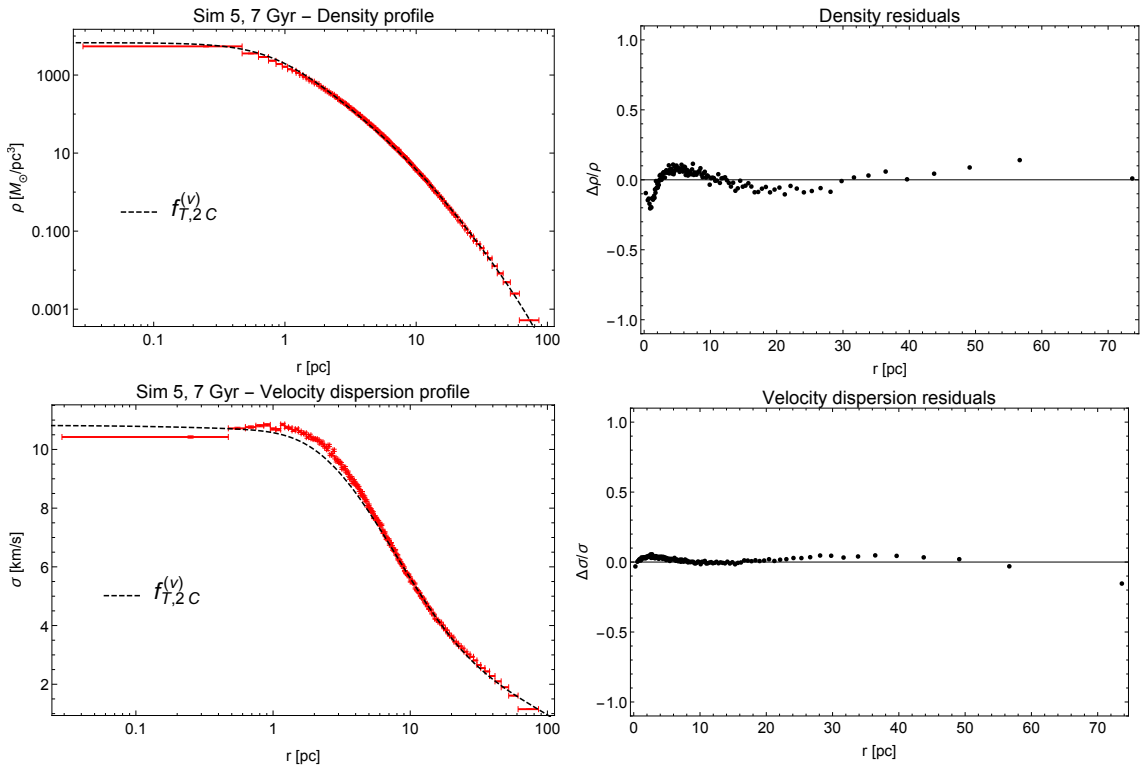


Figure B.41: Total density and velocity dispersion profiles for the best-fit model of Sim 5 at 7 Gyr obtained from two-component $f_T^{(\nu)}$ models.

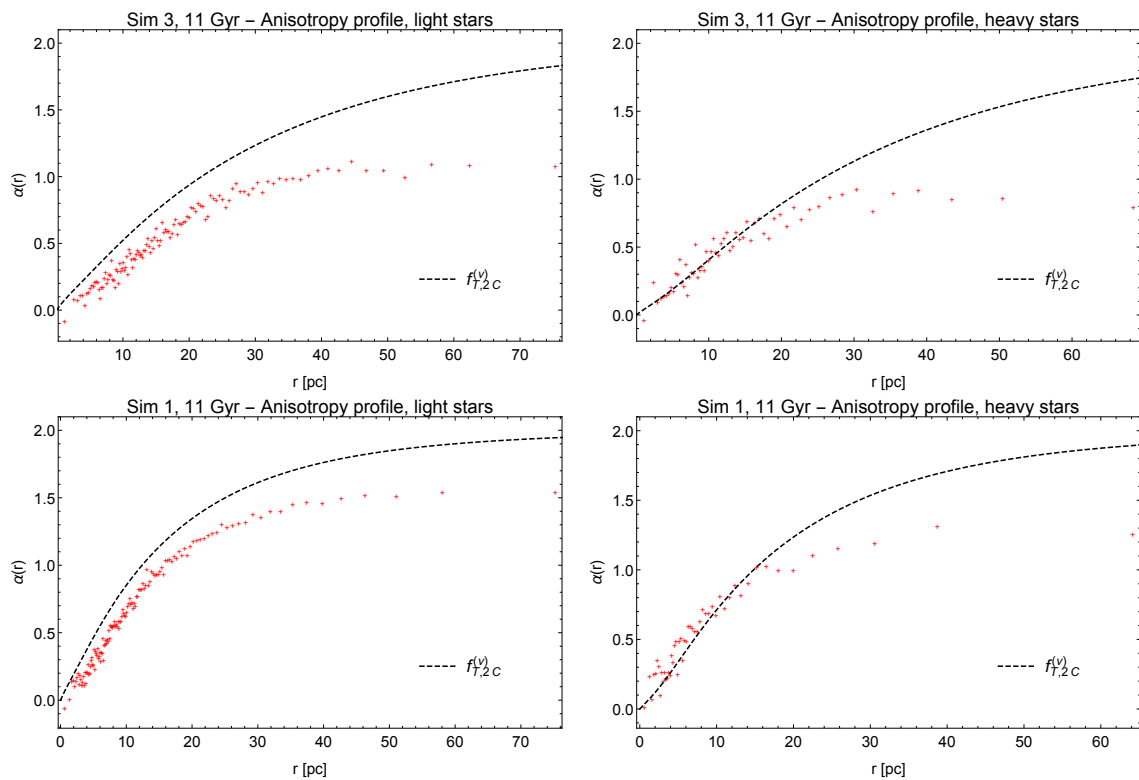


Figure B.42: Light component and heavy component anisotropy profiles for the best-fit models of Sim 3 at 11 Gyr and Sim 1 at 11 Gyr obtained from two-component $f_T^{(\nu)}$ models.

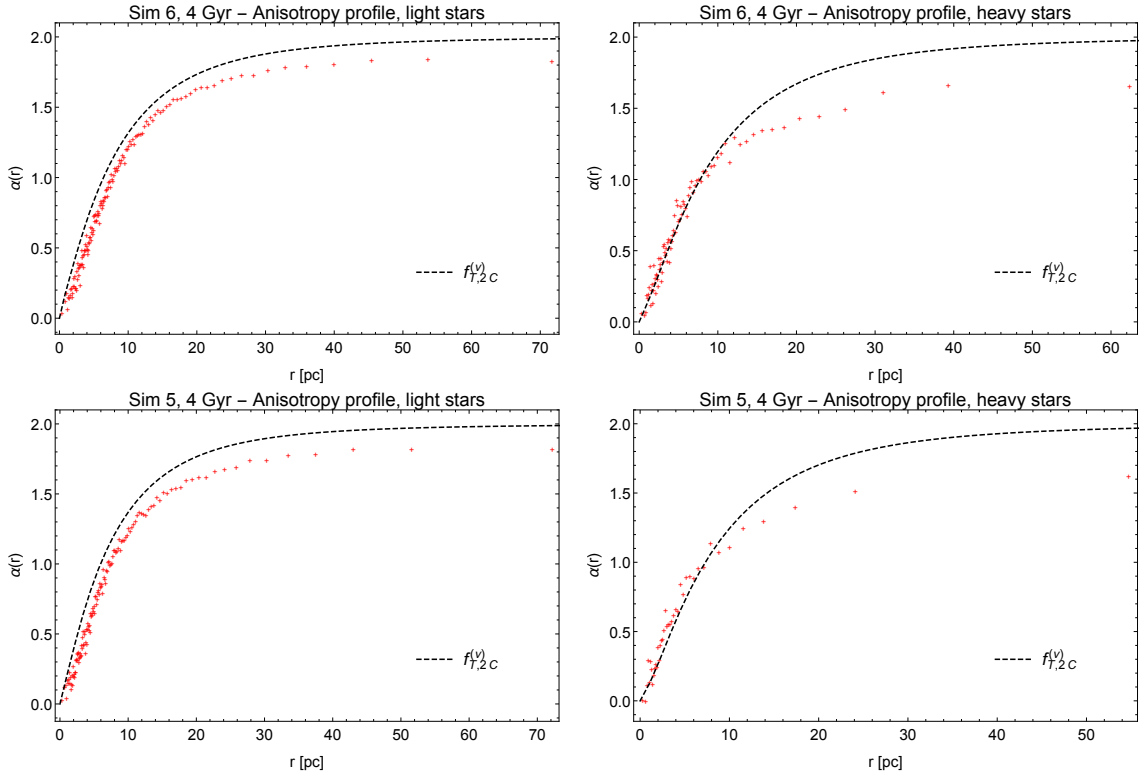


Figure B.43: Light component and heavy component anisotropy profiles for the best-fit models of Sim 6 at 4 Gyr and Sim 5 at 4 Gyr obtained from two-component $f_T^{(\nu)}$ models..

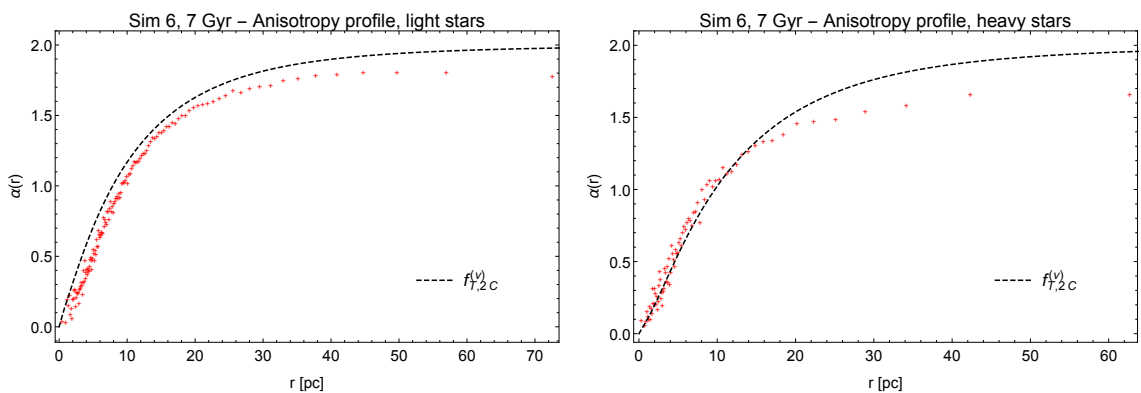


Figure B.44: Light component and heavy component anisotropy profiles for the best-fit model of Sim 6 at 7 Gyr obtained from two-component $f_T^{(\nu)}$ models.

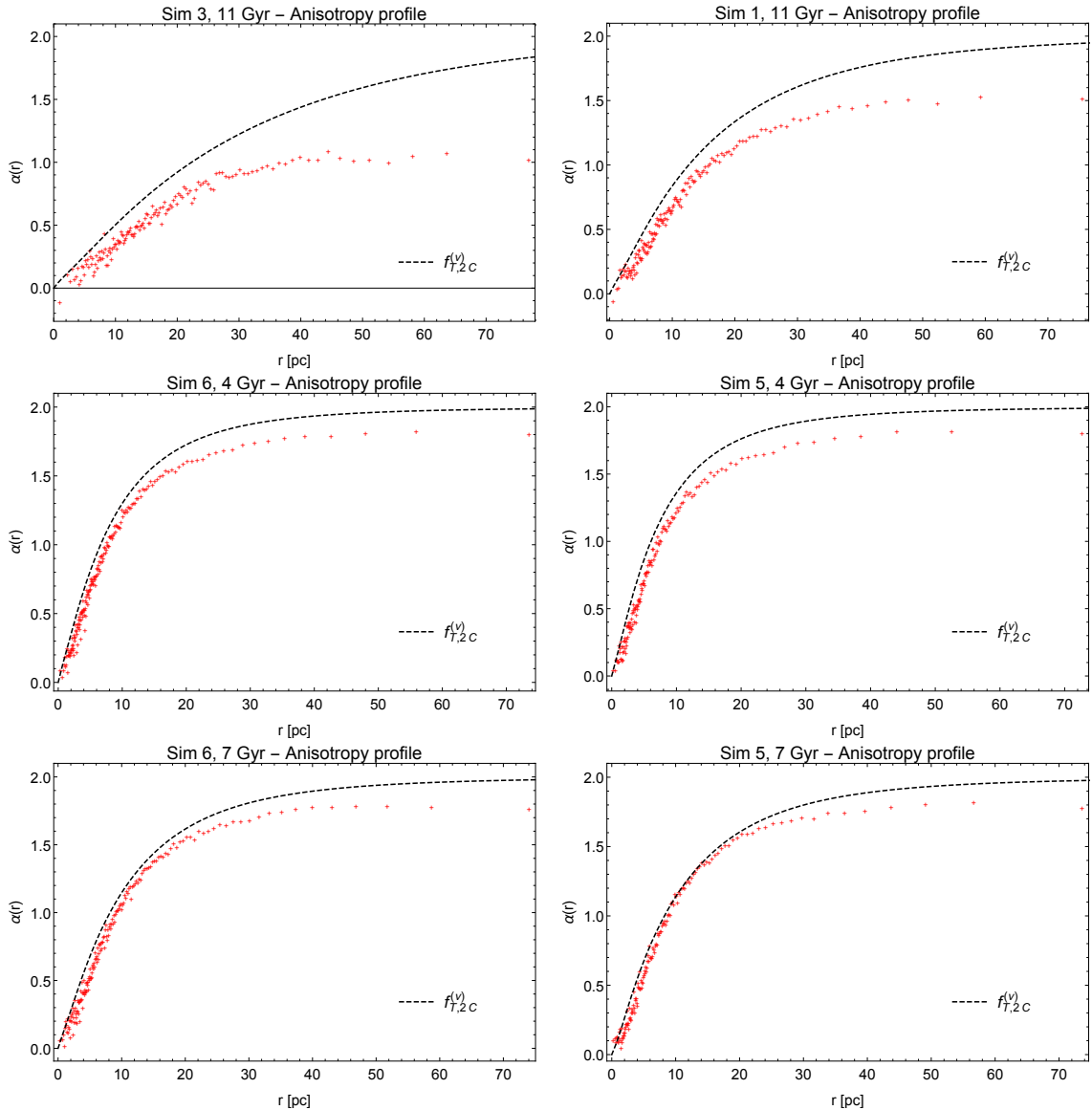


Figure B.45: Total anisotropy profiles for the best-fit models obtained from two-component $f_T^{(\nu)}$ models.

Ringraziamenti

Desidero ringraziare in primo luogo il professor Bertin per la grande disponibilità mostrata durante lo svolgimento della tesi, per i preziosi consigli, e per avermi dato la possibilità di appassionarmi allo studio di questa disciplina. Vorrei inoltre ringraziare il dottor Grillo per la gentilezza e la disponibilità mostrate durante lo svolgimento del progetto. Un sentito grazie a Paolo Bianchini per avermi fornito i dati che hanno permesso la realizzazione di questa tesi e per il costante aiuto durante questi mesi. Vorrei inoltre ringraziare Anna Lisa Varri per l'aiuto e per l'entusiasmo trasmesso durante il nostro confronto.

Un grazie speciale va a tutta la mia famiglia che mi è sempre stata vicina durante gli anni di studio, senza mai farmi mancare il proprio supporto e l'affetto necessario per andare avanti.

Ringrazio Ale per il suo continuo e immancabile amore e per esserci in ogni momento, dal meno importante a quando c'è veramente bisogno.

Un grazie sentito anche a chi mi ha accompagnato durante questo percorso universitario; chi mi ha aiutato, chi ha saputo consigliarmi, e chi mi ha tenuto compagnia durante le lunghe ore di studio. In particolare, un grazie ad Andre R. e Edo S., che con me hanno condiviso le prime ore di lezione, e ad Andre O., con cui ho vissuto le avventure di questi ultimi due anni e in cui ho scoperto un amico fidato.

Infine vorrei ringraziare i miei amici, i più sinceri, che mi stanno vicini e mi sopportano. In particolare un grazie a Ricky, Edo R., Bubu, Cami, Dalmo, Denny, Pami, Samu che ci sono sempre da molti anni ormai.

Grazie